

Doctoral School in Environmental Engineering

Coupled water and heat transfer in permafrost modeling

Matteo Dall'Amico



UNIVERSITÀ DEGLI STUDI DI TRENTO

**Dipartimento di Ingegneria Civile
e Ambientale**

2010

Doctoral Thesis in Environmental Engineering (XXI cycle)
defended at the Faculty of Engineering of the University of Trento

Supervisors: Prof. Riccardo Rigon¹, Dr. Stephan Gruber²

¹: University of Trento, Italy

²: University of Zurich, Switzerland

On the cover: Matterhorn (German name) or Cervino (Italian name) seen from Breithorn (photo Dall'Amico)

© Matteo Dall'Amico (text and images when not differently specified)

Università degli Studi di Trento, Italia

Ai miei genitori,
che sempre mi hanno incoraggiato
a seguire i miei talenti

Acknowledgements

I would like to thank my supervisors for their precious and stimulating thinking and guidance throughout this long journey. Stephan, your enthusiasm and deep insight were a source of inspiration for directing the research. Riccardo, thank you for your precise help and suggestions in the world of thermodynamics and of equations. You taught me the importance of going back to fundamentals. A special thank to Dr. Stefano Endrizzi, for teaching the secrets of the GEOtop source code.

I would like to thank to all friends from the Department of Civil and Environmental Engineering and in particular to Dr. Emanuele Cordano, for sharing nice talks on Richards' equation and to Dr. Michael Dumbser, for his precious help in the numerical part of the thesis. A big thank also to the Department of Physical Geography of the University of Zurich, where I spent beautiful moments of my research. Thanks to Prof. Haeberli and to the staff of Stephan (Dr. Jeannette Noetzli, Andi Hasler, Lorenz Boeckli and Stefanie Gubler).

Thanks also to Dr. Silvia Simoni and Fabrizio Zanotti, my colleagues and partners in the next part of my professional life.

Some results have been presented in preliminary form at international and national conferences: Nicop 2008 in Fairbanks, Alaska; AGU Fall meeting 2008 in San Francisco, California; EGU 2009 in Vienna; AGU 2009 Fall meeting in San Francisco, California.

Abstract

Permafrost degradation in high mountain environments is one of the effects of climate change in the Alpine region (*IPCC*, 2007). The consequences may be manifold, ranging from rock falls and debris flows, to structural damages in infrastructures located on high mountains. The exceptional rock-fall activity during the summer 2003 is likely an indication of this rapid destabilization that takes place as an almost immediate reaction to extreme warming (*Gruber et al.*, 2004a).

The understanding and prediction of such phenomena requires first the localization of permafrost affected areas, and then the monitoring of permafrost sites through proper measurement and modeling techniques. However, the modeling of alpine permafrost is not an easy task because of a variety of causes that contribute to increase the complexity. In particular, the crucial factors dominating alpine permafrost are (1) topography and soil type heterogeneity, (2) snow insulating effect, (3) presence of ice in the ground and (4) high thermal inertia for temperature change at depth. These disturbances could be dealt with through a physically based approach that accounts for the topographical characteristics of the basin, allows heterogeneous parameterization of thermal and hydraulic properties of the ground, solves snow accumulation and melting, and calculates temperature, water and ice content in the ground.

GEOtop (*Rigon et al.*, 2006) is a distributed physically-based hydrological model that appears suitable to deal with the above outlined requirements, as it solves coupled water and energy budgets, allows heterogeneous input parameters in the form of maps and includes a snow module that calculates accumulation-melting of snow through a multilayer discretization of the snowpack (*Endrizzi*, 2007). The model, at the beginning of this work, was lacking of a freezing-soil module capable to account for phase change and heat advection in the soils, extremely important in permafrost affected areas (*Roth and Boike*, 2001). The inclusion of this part, however, needs a deep thermodynamical analysis of the system, in order to derive the relations between pressure and temperature in a ground subject to freezing conditions. Furthermore, the solution of the energy equation requires a robust numerical scheme, which has to cope with the high non-linearities present in the apparent heat capacity formulation for phase change (*Hansson et al.*, 2004). Finally, the snow-soil thermal interactions require a special attention, as they command the energy flux in input to the ground when the snow is present.

The objectives of this thesis are to develop a new freezing soil module inside GEOtop, to test the model against analytical solutions, experimental data and field observations, and to apply the model to investigate the influence of coupled heat and water flow in arctic and alpine permafrost areas.

Contents

1	Introduction	1
1.1	Permafrost and freezing soil modeling	1
1.1.1	Permafrost proneness models	2
1.1.2	Freezing-soil evolution models	3
1.2	Freezing-soil models and hydrology	3
1.3	Freezing-soil algorithms	5
1.4	Objectives of this work	7
1.5	Overview of the chapters	8
2	Equilibrium thermodynamics	11
2.1	Introduction	11
2.2	Postulates	11
2.3	Variables	13
2.4	Gibbs-Duhem identity	16
2.5	Interfaces	17
2.6	Thermodynamical Potentials	18
2.6.1	Variations and Differentials	20
2.6.1.1	Enthalpy	20
2.6.1.2	Gibbs Free Energy	21
2.6.1.3	Helmoltz Free Energy	21
2.7	Quantities for unit of mass	22
2.7.1	A note on potentials as dependent on temperature and pressure	24
2.8	Thermodynamic equilibrium	24
2.8.1	Equilibrium of two phases with flat interfaces	25
2.9	Conclusions	28
3	Freezing soil	29
3.1	Introduction	29
3.2	Equilibrium of two phases in a capillary	29

Contents

3.3	Ice pressure and “freezing=drying” assumption	32
3.4	The generalized Clausius-Clapeyron relation	35
3.5	The freezing point depression	36
3.6	The soil freezing characteristic curve	41
3.6.1	The Van Genuchten based SFC	44
3.7	Conclusions	48
4	Mass and heat conservation	53
4.1	Introduction	53
4.2	The volume conservation	53
4.3	Mass conservation	56
4.4	The internal energy	57
4.5	Heat conservation	60
4.6	Conclusions	61
5	Thermal and hydraulic parameters of soils and rocks	63
5.1	Introduction	63
5.2	Thermal conductivity	63
5.3	Thermal capacity	69
5.4	Hydraulic conductivity	74
5.5	Apparent heat capacity	79
5.6	Conclusions	84
6	The freezing-soil model in GEOTop	85
6.1	Introduction	85
6.2	The decoupled solution	85
6.3	The numerical scheme	88
6.3.1	The discretization	90
6.3.2	Iterative scheme	92
6.3.3	Boundary conditions	95
6.3.3.1	Neumann condition	96
6.3.3.2	Dirichlet condition	99
6.4	Conclusions	100
7	Model validation	103
7.1	Introduction	103

7.2	Pure conduction	103
7.2.1	Linear conduction equation	103
7.2.2	Non-linear conduction equation	105
7.3	Conduction and phase change without water movement	105
7.3.1	Freezing case	106
7.3.2	Comparison between the numerical and the analytical solution	110
7.4	Conduction and phase change with water movement	114
7.5	Conclusions	114
8	Case study 1: water- and frost-table evolution	117
8.1	Introduction	117
8.2	Factors influencing hydrology in organic permafrost terrains	118
8.3	Study site	120
8.3.1	The climate at Siksik	120
8.4	Field measurements	122
8.5	Thaw depth simulation	124
8.5.1	Point simulation	127
8.5.2	Distributed simulation	127
8.6	Conclusions	130
9	Case study 2: snow-soil thermal interactions	133
9.1	Introduction	133
9.2	Interface problem	133
9.2.1	Snow-soil interface thermal conductivity	134
9.2.2	Snow layer modeling	136
9.3	Applications	138
9.4	Conclusions	142
10	Conclusions	145
	References	159

List of Figures

1.1	<i>Permafrost proneness model in Trentino</i>	2
2.1	<i>Legendre transform among thermodynamics potentials</i>	18
2.2	<i>Clausius-Clapeyron thermodynamic equilibrium</i>	27
3.1	<i>Effect of curvature on liquid-air interface</i>	30
3.2	<i>Freezing=drying schematization</i>	34
3.3	<i>Freezing soil schematization</i>	37
3.4	<i>Freezing soil schematization in a capillary</i>	38
3.5	<i>Pore radius related to freezing pressure and temperature</i>	41
3.6	<i>Unfrozen water and temperature</i>	43
3.7	<i>Soil freezing curve according to Van Genuchten model</i>	45
3.8	<i>Freezing soil schematization with soil freezing curve</i>	47
3.9	<i>Combined effect of pressure and temperature on unfrozen water</i>	48
3.10	<i>Effect of temperature and pressure on unfrozen water</i>	49
3.11	<i>3D plot of water and ice content related to temperature and pressure</i>	51
3.12	<i>Unfrozen water dependance on Van Genuchten parameters</i>	52
4.1	<i>Frozen soil constituents and control volume</i>	54
4.2	<i>Internal energy dependance on temperature and pressure</i>	59
5.1	<i>Dry soil (rock) thermal conductivity and porosity</i>	65
5.2	<i>Saturated soil (rock) thermal conductivity and porosity</i>	66
5.3	<i>Unsaturated soil thermal conductivity and pressure-temperature (2D)</i>	67
5.4	<i>Unsaturated thermal conductivity against temperature and pressure</i>	68
5.5	<i>Unsaturated thermal conductivity and porosity</i>	69
5.6	<i>Unsaturated thermal conductivity and Van Genuchten parameters</i>	70
5.7	<i>Thermal capacity and porosity</i>	72
5.8	<i>Thermal capacity against temperature and pressure</i>	73
5.9	<i>Thermal capacity and temperature-pressure (2D)</i>	73

List of Figures

5.10	<i>Thermal capacity and Van Genuchten parameters</i>	75
5.11	<i>Unsaturated hydraulic conductivity against temperature and pressure</i>	78
5.12	<i>Unsaturated hydraulic conductivity and Van Genuchten parameters</i>	80
5.13	<i>Apparent heat capacity and porosity</i>	81
5.14	<i>Apparent heat capacity against temperature and pressure</i>	82
5.15	<i>Apparent heat capacity and Van Genuchten parameters</i>	83
6.1	<i>Schematization of the geometry along an inclined plane</i>	86
6.2	<i>Flow chart of freezing soil module in GEOtop</i>	87
6.3	<i>Discretization scheme of energy balance equation</i>	90
6.4	<i>Schematization of a non convergent Newton-Raphson method</i>	96
7.1	<i>Comparison with analytical solution of linear heat equation</i>	104
7.2	<i>Comparison with analytical solution of non-linear heat equation</i>	106
7.3	<i>The problem of Neumann</i>	107
7.4	<i>Analytical solution of Neumann problem</i>	109
7.5	<i>Step function with Van Genuchten parameters</i>	110
7.6	<i>Comparison with analytical solution of Neumann problem (1)</i>	111
7.7	<i>Comparison with analytical solution of Neumann problem (2)</i>	112
7.8	<i>Comparison with analytical solution of Neumann problem (3)</i>	113
7.9	<i>Comparison with experimental results of Hansson et al. (2004) (1)</i>	115
7.10	<i>Comparison with experimental results of Hansson et al. (2004) (2)</i>	116
8.1	<i>Frost- and water-table depth</i>	119
8.2	<i>Study area of Siksik creek</i>	121
8.3	<i>Peat depth at Siksik</i>	123
8.4	<i>Frost table in organic soil against distance from main stream and time (2D)</i>	125
8.5	<i>Thaw depth frequency distribution</i>	126
8.6	<i>Simulated and measured temperature at the meteo tower</i>	127
8.7	<i>Frost- and water-table depth evolution</i>	128
8.8	<i>Measured and simulated thaw-depth comparison</i>	129
8.9	<i>Spatial variability of frost-depth (1)</i>	131
8.10	<i>Spatial variability of frost-depth (2)</i>	132
9.1	<i>Snow-soil interface thermal conductivity against snow density and snow depth</i>	135
9.2	<i>Different snow schematizations</i>	137
9.3	<i>Simulated and measured snow depth and soil temperatures</i>	140
9.4	<i>Simulated and measured snow depth comparison with two soil schematizations (1)</i>	141

9.5 *Simulated and measured snow depths, density and temperatures* 142

List of Tables

1.1	<i>Features of freezing soil models in bibliography</i>	7
2.1	<i>Thermodynamic intensive variables</i>	15
2.2	<i>Functional dependence of the potentials</i>	20
2.3	<i>Specific thermodynamic variables</i>	22
3.1	<i>Pressure-Temperature relation in bibliography</i>	39
3.2	<i>Unfrozen water dependance on Van Genuchten parameters</i>	49
4.1	<i>Notation of mass and volume in the soil/rock schematization</i>	54
5.1	<i>Unsaturated thermal conductivity and Van Genuchten parameters</i>	68
5.2	<i>Unsaturated thermal conductivity formulations in bibliography</i>	71
5.3	<i>Thermal capacity and Van Genuchten parameters</i>	74
5.4	<i>Hydraulic conductivity formulations in bibliography</i>	76
5.5	<i>Unsaturated hydraulic conductivity and Van Genuchten parameters</i>	79
5.6	<i>Apparent heat capacity and Van Genuchten parameters</i>	84
6.1	<i>Non linear diffusion-advection equations</i>	89
6.2	<i>Boundary fluxes according to Neumann and Dirichlet</i>	99
8.1	<i>Weekly aggregation of measured data</i>	124
8.2	<i>Hydraulic and thermal parameters of peat</i>	126
9.1	<i>Snow-soil interface thermal conductivity against snow density and snow depth</i>	136
9.2	<i>Snow and soil temperatures at the interface</i>	139

1 Introduction

As reported by the Intergovernmental Panel on Climate Change (*IPCC*, 2007), the warming of the climate system is unequivocal, as is now evident from observations of increases in global average air and ocean temperatures, widespread melting of snow and ice, and rising global mean sea level. The effects for the Alpine region are not easy to determine, because climate models are running on continental scale, and consequently the orographic effect and the variability due to local factors are hardly taken into account. As far as permafrost degradation is concerned, evidence from European monitoring sites indicates that active layer thickness has been the greatest in the summers of 2002 and 2003, approximately 20% greater than in previous years (*Harris et al.*, 2003). The implications in high mountain environments mostly depend on the type of ground. On bedrock, for example, the thermal response of rock faces to individual extreme events is fast compared to debris-covered slopes, which are often insulated by blocky surface (*Harris and Pedersen*, 1998) and have a high ice-content. Therefore one can expect local degradation of frozen slopes within mountain permafrost areas (*Haeblerli et al.*, 1993) and loss of stability within ice-filled rock discontinuities, even at temperatures still below the freezing point (*Davies et al.*, 2001). On debris covered slopes, on the other hand, accelerated permafrost creep (*Kääb et al.*, 2007) and stability issues in rock glaciers (*Arenson and Springman*, 2000) are likely to be expected, together with an enhanced probability of debris flow triggering (*Zimmermann and Haeblerli*, 1992). The understanding and prediction of such phenomena have become a current issue for local administrations and the European community, as demonstrates the recently approved PermaNET project (<http://www.permanet-alpinespace.eu>) of the Alpine Space program. The objectives of this project are the quantification of the extent of the territory affected by perennially frozen ground for the entire alpine chain, and the monitoring of permafrost sites through direct and indirect measurements. These objectives address the importance of permafrost modeling.

1.1 Permafrost and freezing soil modeling

Permafrost and freezing soil modeling have a long history of application. *Zhang et al.* (2008) and *Riseborough et al.* (2008) provide a detailed bibliography and description of the applications

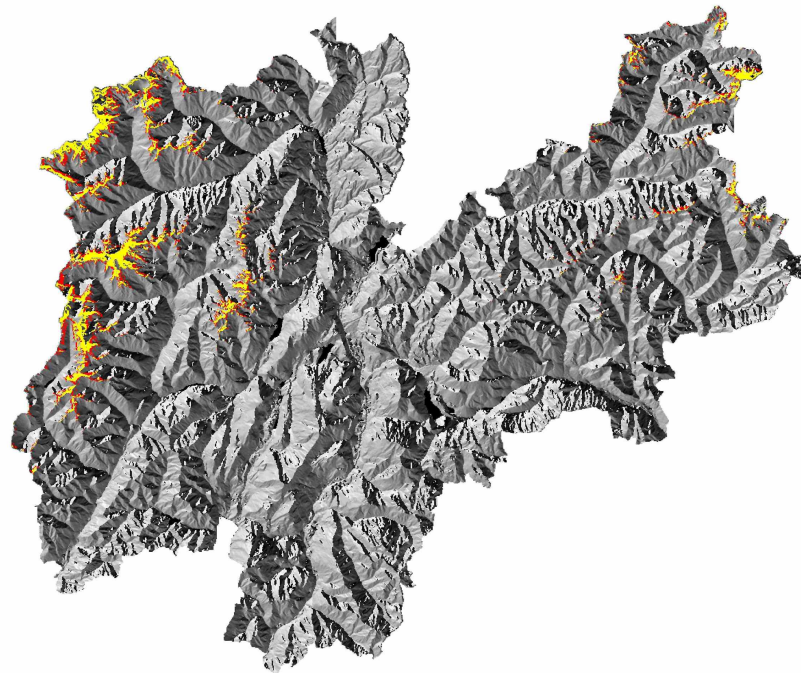


Figure 1.1: *Permafrost proneness model of Trentino according to Keller (1992). Yellow: permafrost probable. Red: permafrost possible, even though not probable*

and typology of approaches. In general, one could say that permafrost modeling may be divided into two main fields of application: *permafrost proneness modeling* and *freezing soil evolution modeling*.

1.1.1 Permafrost proneness models

Permafrost proneness models aim at localizing and quantifying the extent of a territory which is subject to permafrost conditions. They can be viewed as yes/no functions about the occurrence of permafrost, primarily applicable to the area where the model is calibrated and assuming steady-state conditions. Therefore extrapolations in time and space may lead to uncertain or even misleading results. Permafrost proneness is calculated through the estimation of the mean annual ground temperature (MAGT) according to three main approaches (Etzelmüller *et al.*, 2001): (i) *physically based*, in which MAGT is derived directly by the solution of the surface energy balance and the heat equation in the soil (Stocker-Mittaz *et al.*, 2002); (ii) *empirical-statistical*, in which the MAGT is based on proxy-variables of selected factors, which reflect a simplified relation between climate and permafrost distribution (Keller, 1992); (iii) *thermal offset model* that focuses on the heat fluxes within the active layer, using empirical relationships (Wright *et al.*, 2003 and Juliussen and Humlum, 2007). An example of this type of application is given in Fig. 1.1, that reports the

permafrost proneness of the Province of Trento (Italian eastern Alps) based on the empirical statistical approach of *Keller (1992)*. The yellow color represents the *permafrost probable* area, and the red color the *permafrost possible* area. In this case the proneness to permafrost is made dependent on (1) elevation, which can be considered as a proxy of MAAT, (2) slope, which accounts for local snow presence due to avalanches, and (3) aspect, that is a simplified proxy of the incoming solar radiation. This approach has the advantage to be easily obtainable from a digital elevation model (DEM). However, it doesn't consider the full contribute given by the incoming potential solar radiation, it doesn't consider the heterogeneity of the surface characteristics (rock/debris) and it doesn't account for the snow presence that represents a major insulating effect.

1.1.2 Freezing-soil evolution models

Freezing-thawing soil evolution models allow to represent the ground temperature and water/ice content in time and space, and therefore are usually used to simulate measured patterns of temperatures and to create future scenarios. As *Zhang et al. (2008)* point out, there are three categories of algorithms for simulating ground thawing and freezing depths: *empirical and semiempirical*, *analytical*, and *numerical*. Empirical and semiempirical algorithms relate ground thawing-freezing depth to some aspect of surface forcing by one or more experimentally established coefficients (e.g. *Anisimov et al., 2002*). Analytical algorithms are specific solutions to heat conduction problems under certain assumptions. The most widely applied analytical solution is Stefan's formulation, which simulates the freezing/thawing front using accumulated ground surface degree-day (either the freezing or thawing index) (*Lunardini, 1981*). Numerical algorithms determine the ground thawing-freezing depths by numerically solving the heat transfer equation. The latent term $C_{ph} := \rho_w L_f d\theta_w/dT$ (where L_f is the latent heat of fusion and θ_w is the volumetric water content) is generally treated according to two approaches: (i) the pure conduction heat equation is first solved, and then the soil temperature is readjusted by the ratio of liquid and solid water given by energy conservation during phase change (*Shoop and Bigl, 1997*); (ii) C_{ph} is related to temperature and unfrozen water content by an apparent heat capacity formulation (*Lukyanov and Golovko, 1957*). The physically based numerical approach, according to *Zhang et al. (2008)*, should give the best performance in simulating the ground thawing and freezing depths.

1.2 Freezing-soil models and hydrology

The analysis of freezing/thawing depths and the ice content in the ground are extremely important for hydrological models. Studies have shown that proper frozen soil schemes help improve land surface and climate model simulations (e.g. *Viterbo et al., 1999* and *Smirnova et al., 2000*). For example, comparisons of results from the Project for Intercomparison of Land Surface Parame-

terization Schemes Phase 2(d) [PILPS 2(d)] have shown that the models with an explicit frozen soil scheme give a much more realistic soil temperature simulation during winter than those without a frozen scheme (*Luo et al.*, 2003). However, the inclusion of freezing-soil algorithms in hydrological models is challenging, for a series of reasons like:

1. high topographical and surface type heterogeneity. Topographical features may drastically vary in short distances, and represent important parameters that can influence the presence and degradation timing of permafrost (*Gruber et al.*, 2004b). Surface characteristics may affect the insulation property and the temperature profile, like vegetation, surface type (debris, rock), and soil texture. Also the soil type characteristics (e.g. rock, coarse grained soil, fine grained soil) have a high spatial variability and deeply affect the thermal conductivity of the material and therefore the thermal behavior of the soil (*Gruber and Hoelzle*, 2008);
2. snow insulating effect: in high alpine environments the snow is present about eight months per year, and cannot be excluded if a detailed analysis has to be performed. Given its good insulating properties and high albedo, snow is one of the critical parameter influencing the energy exchange processes between the atmosphere and the ground (*Keller and Gubler*, 1993). A proper representation of the snow evolution can provide the right time window of direct soil exposure to solar radiation, and, in turn, a reliable quantification of the soil energy fluxes. Conversely, a poor representation may lead to significant errors that propagate and increase deeper we go in the ground;
3. phase change in the ground: water in the the active layer of permafrost is subject to continuous freezing-thawing cycles and is consequently a enormous source-sink term of energy due to the presence of latent heat. Furthermore, phase change also leads to changing thermo-physical properties, conductivity and thermal offset. Consequently phase change is a crucial term in the heat equation and has to be accounted to produce a reliable ground thermal analysis;
4. high thermal inertia: permafrost is a long-term phenomenon and often formed by freezing conditions over hundreds of years or millennia. Modeling its evolution at depth is challenging, because phase change and the slow velocity of the temperature signal provide the system with a high inertia. One of the main difficulties lies therefore in the derivation of the initial conditions of temperature and ice content in the ground. In fact, an unrealistic temperature initialization may take several hundred or thousands of years (of simulated time) to equilibrate with surface conditions. In this case, it becomes difficult (if not impossible) to distinguish between real transient effects represented by a model and the delayed response to an initialization that did not correspond to real conditions.

Numerous are the hydrological models that attempt to include freeze-thaw algorithms in a full hydrological cycle. Among the many, the models SHAW and COUP may be shortly cited. The Simultaneous Heat And Water (SHAW) model was developed by *Flerchinger* (1987) as a comprehensive model to describe heat and mass transfer under freezing conditions. Originally developed to simulate soil freezing and thawing, it simulates heat, water and solute transfer within a one-dimensional profile which includes the effects of plant cover, dead plant residue and snow. The model solves both heat, water and chemical transfer in the soil of both the solid, liquid and vapor phase. The model has been tested under a wide range of conditions (*Flerchinger and Saxton*, 1989 and *Flerchinger and Pierson*, 1991 to cite just a few) and has been proven to work well for freezing soil (*Flerchinger*, 1991 and *Hayhoe*, 1994), also in the presence of solutes in the soil (*Nassar et al.*, 2000). The COUP model is a new updated version of the previous WinSoil model (*Jansson*, 1998). The name “coup” stems from the word coupled, and the model actually consists of different sub-models, which have been integrated into a system of models. The model, initially developed to simulate conditions in forest soils, has recently been generalized to elucidate water and heat processes in any soil independent of plant cover. Recently nitrogen and carbon cycles have also been included in the model. The one dimensional COUP model represents water and heat dynamics in a layered soil profile covered with vegetation. Two coupled differential equations for water and heat flow represent the central part of the model. These equations are discretized with a finite difference scheme and solved with an explicit forward difference method (Euler integration).

1.3 Freezing-soil algorithms

One of the first attempts to include soil freeze-thaw cycles into a numerical model is the work of *Nakano and Brown* (1971) who have assumed the advance of the freezing front as a moving boundary condition. They apply the analytical solution derived by *Carslaw and Jaeger* (1959) to a soil of a given porosity, and introduce the effect of an artificial freezing zone of finite width between the frozen and the unfrozen parts, in order to avoid the problem of shock wave propagation in the transition between the frozen and thawed state typical of the classical “freezing front” assumption. No water flow, i.e. no mass balance equation, is taken into account and the energy balance is expressed through the apparent heat capacity formulation as proposed by *Lukyanov and Golovko* (1957). *Harlan* (1973) is probably the first to attempt to solve coupled mass and energy balance equations for the freezing soil by making an analogy between the mechanism of water transport in partially frozen soils and those in unsaturated soils. He solves the system on a homogeneous rigid porous medium through a fully implicit finite difference scheme, where the unknowns are temperature and soil water potential; phase change in the water balance appears in the source/sink term. He also uses the apparent heat capacity formulation in the energy balance. The results show

that the freezing process induces the movement of both heat and mass from warm to cold regions, inducing the moisture content in the unfrozen soil zone to decrease sharply toward the freezing front. Soil texture and initial moisture conditions seem to be crucial in affecting the availability and mobility of water. *Guymon and Luthin (1974)* describe a one-dimensional model for freeze-thaw processes based on an equivalent quasi-linear variational functional for the Richards equation and the heat conduction equation including convective components. *Fuchs et al. (1978)* develop a theory of soil freezing applicable to unsaturated conditions with solute presence in the soil. They state that solutes tend to depress the freezing point temperature and modify the relationship between temperature, moisture content and apparent thermal properties of the soil. Phase change is taken into account in the apparent heat capacity formulation, and the water flow contribution is accounted for in the apparent thermal conductivity, thus the simultaneous heat and water transport equations result in a merged single differential equation for heat. *Jame and Norum (1980)* further develop the model of *Harlan (1973)* and highlight that the effect of mass transfer on the thermal state of soil is an important factor to be considered. *Newman and Wilson (1997)* propose a theoretical formulation for unsaturated soils using soil-freezing and soil-water characteristic curve data to combine the heat and mass transfer relationships into a single equation for freezing or frozen regions of the soil. *Christoffersen and Tulaczyk (2003)* have constructed a high-resolution numerical model of heat, water, and solute flows in sub-ice stream till subjected to basal freeze-on. They propose a formulation of the equilibrium relation without assuming $p_i = 0$ through the full version of the Clapeyron equation, which enable them to model segregation ice onto the freezing interface and so develop stratified basal ice layers. *Hansson et al. (2004)* introduce a new method for coupled heat transport and variably saturated water flow using the Richards' equation. They account for water flow due to gravity, pressure gradient and temperature gradient, both for liquid and vapor phase. *McKenzie et al. (2007)* propose the freezing module of the SUTRA code that works under complete saturated conditions, which represents a limitation as the thermal and hydraulic properties of soils are much dependent on the saturation degree. *Daanen et al. (2007)* develop a 3D model to analyze the horizontal effects that lead to the formation of nonsorted circles, an example of a relatively stable patterned-ground system. Their model is very similar to *Hansson et al. (2004)* but it differs in the linkage between ice content and temperature. *Watanabe (2008)* also uses a similar model to *Hansson et al. (2004)* and reproduces directional freezing experiments on silty soil and compares with the experimental data.

In Table 1.1 the features of the various freezing soil algorithms are summarized. Some important aspects in freezing soil algorithms may be highlighted:

1. generally all the authors use the same closure relationship between pressure and temperature in the form of a generalized Clapeyron equation. However, after the first attempt of *Loch (1978)*, this equation has never been fully derived from a thermodynamical point of view,

Author	Dim	Num	B.E.	Vap	Sol	F.H.	WFTG
<i>Harlan (1973)</i>	1D	IFD					
<i>Guymon and Luthin (1974)</i>	1D	FE					
<i>Fuchs et al. (1978)</i>	1D	/			X		X
<i>Zhao et al. (1997)</i>	1D	IFD	X	X			
<i>Christoffersen and Tulaczyk (2003)</i>	1D	IFD			X	X	
<i>Hansson et al. (2004)</i>	1D	FE space IFD time	X	X			X
<i>Daanen et al. (2007)</i>	3D	IFD	X			X	
<i>Watanabe (2008)</i>	1D	IFD	X				X

Table 1.1: *Freezing soil models features from various authors. Vap stands for vapor, Sol for solutes, B.E. for blocking effect, F.H. for frost heave or ice lenses, IFD for implicit finite difference, EFD for explicit finite difference, FE for finite element, WFTG for water flow due to thermal gradient*

therefore leaving numerous doubts on its limitations.

2. generally all the authors, sometimes explicitly, sometimes implicitly, utilize the “freezing=drying” assumption as suggested by *Miller (1963)*. On the one hand this speculation simplifies the modeling, as it allows to use the same relationships used for unsaturated soils to freezing soils. On the other hand, however, has a profound meaning on the pressures for the water and the ice phase, and therefore requires a careful analysis in order to understand the type of processes (e.g. frost heave) that can be dealt with.
3. often in literature the soil saturation level the models are dealing with is not specified. Sometimes the pressure-temperature relationships are given for a fully saturated soil, sometimes for a dry soil, leaving to the reader the doubt about the validity of the hypothesis.

1.4 Objectives of this work

In dealing with permafrost and freezing ground modeling, the following research questions were considered crucial to provide a robust and reliable modeling applicable to the cryosphere:

1. What are the thermodynamic equilibrium relations behind the soil heat equation?
2. What is the field of validity of the “freezing=drying” hypothesis?
3. How sensible are the thermal and hydraulic parameters of soil according to the saturation degree and the temperature?
4. What numerical scheme is suited to solve the heat equation with phase change and advection in the soil?
5. What are the thermal issues at the snow-soil interface and how can they be dealt with?
6. How can the spatial variability of thaw depth in the arctic tundra be explained and what are the driving parameters?

The objective of this work is answering these research questions, which means to disclose the blanket which is laid over the soil heat equation, and to dig into the thermodynamics to understand the validity of the relationships. Furthermore, it means to develop a freezing soil algorithm and to insert it into an hydrological model in order to test it and apply to real conditions. The above described hydrological models (SHAW and COUP), however, have been disregarded in this work because they are one-dimensional models, and in this work a distributed application was sought-after, in order to try to describe the high spatial heterogeneity of soil surface and soil properties typical of permafrost affected areas.

The model chosen for this dissertation is GEOtop (*Rigon et al., 2006*), a physically based hydrological model that solves the energy and mass balance of the ground. This model accounts for the topographical characteristics of the basin, allows heterogeneous input parameters in the form of maps and includes a snow module that calculates accumulation-melting of snow through a multilayer discretization of the snowpack (*Zanotti et al., 2004* and *Endrizzi, 2007*). GEOtop is integrated with the GIS environment JGrass (www.jgrass.org), a free open source multi-platform GIS that calculates the topographical maps (aspect, slope, convexity) and hydrographic maps (drainage directions, river networks...). GEOtop at the beginning of this work was suffering from two important limitations: (i) the model was conceived to work in a distributed way, in order to allow an easy interface with GIS systems, and had been designed to analyze gentle slopes, e.g. up to 40°, typical of mid-altitude ranges. This has shown to be a shortcoming for simulations in high alpine environments, because of the extreme topography (e.g. 80° steepness) typical of the elevated rock faces; (ii) the model was neglecting phase change and the ice content in the soil. For these reasons a 1D version of GEOtop has been developed: the surrounding topography is encapsulated by a horizon file that permits to calculate the cast shadow at the simulation point (*Gruber et al., 2003*). Furthermore, a new freezing soil module been developed. The algorithm is physically based and

includes the latent heat term in the apparent heat capacity (*Lukyanov and Golovko, 1957*). The new version of the model has then been applied to an alpine permafrost site, to analyze the thermal problems existing between the snow and the ground. Eventually, the model was applied to an arctic permafrost site, to study the coupled thermal and hydraulic interactions responsible for the frost depth variation in time and space in the arctic tundra.

1.5 Overview of the chapters

The thesis has been divided into ten chapters, that are briefly summarized.

Chapter 1 “Introduction” is meant to introduce the scope of this work, to state the research questions and define the objectives.

Chapter 2 “Equilibrium thermodynamics” is meant to give an overall view of the thermodynamics law, variables and potentials, with the intent to give a coherent notation that will be useful throughout the work.

Chapter 3 “Freezing soil” provides a derivation of the equilibrium relation between ice and water in a porous media, under the assumption *freezing=drying*. This will allow to derive the soil freezing characteristic curve.

Chapter 4 “Mass and heat conservation” derives the equations for mass and heat conservation in a soil/rock.

Chapter 5 “Thermal and hydraulic parameters of soils and rocks” gives an overview on the modeling techniques for the thermal conductivity, thermal capacity and hydraulic conductivity of soils and rock. A sensitivity study on porosity and the shape of the soil water retention curve is also provided.

Chapter 6 “The freezing-soil model in GEOtop” illustrates the decoupling procedure of the mass and heat equations and describes the numerical details.

Chapter 7 “Model validation” is meant to prove the numerical stability of the model comparing it against the analytical solutions typical of the heat equation. Furthermore, a comparison with experimental data will be also provided to evaluate the behavior of the coupled heat and mass equation.

Chapter 8 “Case study 1: water- and frost-table evolution” is intended to show the model application in a peat-covered arctic catchment, in order to investigate the source of variability of frost table depth.

Chapter 9 “Case study 2: snow-soil thermal interactions” regards the application of the model to an alpine catchment, with the objective to analyze the thermal interactions between the snow cover and the soil below.

Chapter 10 “Conclusions” summarizes the overall work and draws the main findings.

2 Equilibrium thermodynamics

2.1 Introduction

This chapter is meant to give an overall view of the thermodynamics laws, with the intent to review the use and the notation of function, laws and potentials. As starting point we use the *Callen* (1985) book and postulates that are suitably modified below. They assume:

- an understanding of the distinctions between macroscopic and microscopic variables, and between extensive and intensive macroscopic variables;
- the concept of a system surrounded by boundaries that restrict (hold constant) some or all of the extensive variables of the system;
- the definitions of internal energy and work, and the concept of heat defined through the First Law of thermodynamics.

As far as the notation is concerned, throughout the text, we will use:

- a the parenthesis to indicate that a variable, for instance $S()$, is actually a function of some other variables that can be deduced from the context;
- b the in-line notation for derivatives $\partial_X S$ which actually stands for:

$$\partial_X S() := \frac{\partial S()}{\partial X} \quad (2.1)$$

These notes modify those by *Ingersent* (2000).

2.2 Postulates

For convenience, Callen formulates the postulates only for simple systems, defined as systems that are macroscopically homogeneous, isotropic and uncharged, that are large enough that surface effects can be neglected, and that are not acted on by electric, magnetic, or gravitational

fields. Extension to the more general systems dealt with in this dissertation is straightforward, and included below.

Postulate I. *There exist particular states (called equilibrium states) of the systems that, macroscopically, are characterized completely by the internal energy U_c , which depends upon volume V_k , the mass of the phase components, M_k , and the surface energy that pertain to the boundaries of area A_k between phases. Internal energy depends also on entropy, to be defined in postulate II*

The subscript k indicates either ice $k \leftarrow i$, liquid water $k \leftarrow w$ or water vapor $k \leftarrow v$. Subscript c stand for "canonical" of, if preferred, "Callen". When no subscript is present, the generic phase is intended, according to the phrase context. The symbol " \leftarrow " indicates an *assignment*, which differs conceptually from an equality, a definition, and an identity, which are usually denoted by the same " $=$ ". In this dissertation " $=$ " means *equality*, in the sense that $x = y + 3$ identifies a line in the $x - y$ plane; " $:=$ " means *a definition*, as in the $T := \partial_S U$ below in the text; " \equiv " means *identity*, as in $\cos^2 x + \sin^2 x \equiv 1$, which is valid for any x ; the final specification of a symbolic expression to numbers is an assignment.

(1) The phase composition refers to the number of each type of particle considered to be important to the system (e.g. molecules, electrons, quarks, photons) belonging to each phase.

(2) A composite system can be formed from multiple subsystems, i.e. phase parts, each of which has equilibrium states that are characterized by their own values of $U_c^{(\alpha)}, S^{(\alpha)}, V^{(\alpha)}, M^{(\alpha)}$. The composite system (soil in this case) contains ground particles ($\alpha \leftarrow g$), air ($\alpha \leftarrow a$), and water ($\alpha \leftarrow w$) either in condensed forms or vapor). It is said to be *closed* if the total energy, its total volume, its total mass are restricted.

$$U_c(\cdot) = \sum_{\alpha} U_c(\cdot)^{(\alpha)} \quad (2.2)$$

$$V = \sum_{\alpha} V^{(\alpha)} \quad (2.3)$$

$$M = \sum_{\alpha} M^{(\alpha)} \quad (2.4)$$

Each subsystem can, in principle, contain several phases. So, for instance:

$$U^{(w)} = \sum_k U_k^{(w)} \quad (2.5)$$

superscripts are omitted when unnecessary. Internal constraints may prevent free flow of energy, volume, or matter between the subsystems and/or phase.

The first postulate is equivalent to the first principle of thermodynamics.

Postulate II. *There exists a function of time (called the entropy S) defined for all equilibrium*

states and non equilibrium states T . (2008), that is maximized during any physical process. Eventually entropy can be made dependent of the extensive variables of any (*closed*) composite system. Thus, in the absence of an internal constraint, the extensive variables of the system in a physical process are those which maximize the entropy over the manifold of constrained equilibrium states.

This key postulate is equivalent to part of the Second Law of Thermodynamics (see Eq. 2.65 and 2.66) and implies that the equilibrium theory has nothing to say about non equilibrium states. In the following of the dissertation, however, this theory will be extended to non equilibrium situations.

Postulate III. *-The entropy of a composite system is additive over the constituent subsystems. The energy is continuous and differentiable and is a monotonically increasing function of the entropy.*

(1) Usually this postulate is written as: "The entropy of a composite system is additive over the constituent subsystems. The **entropy** is continuous and differentiable and is a monotonically increasing function of the **energy**". In an experiment, in fact, usually energy can be controlled but entropy can not. However, the statement above allows for a simpler and clear notation of the equilibrium thermodynamics.

(2) The first sentence implies that the entropy is extensive.

(3) The differentiability condition requires the existence of the first partial derivative of internal energy with respect to each extensive parameter X upon which the internal energy depends, including entropy.

(4) It can be shown that thermodynamic stability also requires that the second partial derivative of S on each variable X is negative.

(5) The second sentence states that U_c is a very well-behaved function of S , V , and M . A few artificial systems, out of our topics, can violate this assumption.

Postulate IV. *The entropy of any system (is non-negative and) vanishes in the state for which $\partial_S U_c(\) = 0$ (that is, at the zero of temperature).*

(2) This is a restatement of the Third Law of Thermodynamics or the *Nernst* postulate.

(3) It is the least important postulate because we generally look at entropy differences.

2.3 Variables

Accordingly to the previous section:

$$U_c(\) = U_c(S, V, A, M) \quad (2.6)$$

or, the internal energy in its canonical form is a function of entropy, volume, area of separation between constituents, and mass of the constituents (sub-super-scripts of constituent omitted for simplicity, and similar term exist for any constituent). These are therefore the **independent variables** of the system. The total variation of internal energy in time “ t ” is then expressed as:

$$\frac{dU_c(S, V, A, M)}{dt} = \frac{\partial U_c(\cdot)}{\partial S} \frac{\partial S}{\partial t} + \frac{\partial U_c(\cdot)}{\partial V} \frac{\partial V}{\partial t} + \frac{\partial U_c(\cdot)}{\partial A} \frac{\partial A}{\partial t} + \frac{\partial U_c(\cdot)}{\partial M} \frac{\partial M}{\partial t} \quad (2.7)$$

As usual in thermodynamics, the dependence of the variation on time is omitted, which can create some embarrassing situation when dealing with system assumed to vary with time, and the variation is presented (*Bohren and Albrecht (1998)* argue unnecessarily) as a differential:

$$dU_c(S, V, A, M) = \frac{\partial U_c(\cdot)}{\partial S} dS + \frac{\partial U_c(\cdot)}{\partial V} dV + \frac{\partial U_c(\cdot)}{\partial A} dA + \frac{\partial U_c(\cdot)}{\partial M} dM \quad (2.8)$$

One can simply consider the differential as a short notation for the complete derivative with time. The experienced reader should also notice that the above is not the traditional thermodynamical notation where, for instance, the partial derivative of the internal energy versus entropy would have been written:

$$\left(\frac{\partial U_c}{\partial S} \right)_{V, A, M} \quad \text{instead of} \quad \frac{\partial U_c(\cdot)}{\partial S} \quad (2.9)$$

This is usually explained in textbooks by saying that the variable “ V, A, M ” are kept constant, which has a meaning when thinking to experiments, but is a nonsense from an algebraic point of view. The real mathematical meaning is that U_c is a function of S , and of the other variables V, A, M , and the notation is necessary because, as we will see, the internal energy is sometimes used as function of the above extensive variables, and sometimes of other variables, which are introduced below, but in the traditional textbooks or treatises, it maintains the same symbol.

According to *Callen (1985)*, the partial derivatives of the internal energy versus the independent variables have the names as in table 2.1 which, in turn is a consequence of the second principle of thermodynamics (see eq.2.65 and 2.66) that states that at equilibrium these quantities are uniform (through space) and constant (through time) in the whole system, in the case of a system with a single constituent, and variable in space (heterogeneous) and constant in time, in the multiple constituents case. These quantities, being constant in time and locally homogeneous at some spatial scale large enough to dump quantum mechanical fluctuations, can be measured. Some of these dependent variables have a meaning which is commonly accepted in everyday life, with less concern of the associate extensive independent variables, but, as a matter of fact, they represent just the derivative of the internal energy in the canonical form.

Thus the variation of internal energy can be written as:

$$dU_c(S, V, A, M) = T(\)dS - p(\)dV + \gamma(\)dA + \mu(\)dM \quad (2.10)$$

The form of the above differential without parenthesis is a common source of misunderstanding since, without them, it is not redundantly clear which are the independent variable and which are the dependent ones. The independent variables are called *extensive*, since they depend linearly on the mass amount of the phase/substance. The dependent variables are, on the contrary, *intensive*. Say X , the generic intensive variable, each one of them is, in principle, function of the whole set of the extensive variables. Thus for example (Callen, 1985):

$$T = T(S, V, A, M) \quad (2.11)$$

A particular system, for instance an ideal gas, can be dependent on just a subset of the extensive variables (for instance, just S).

The volume of a system can be measured directly by comparison, with standard samples of length, and the mass too. In principle also the extent of the separation surfaces can be measured the same way. Equilibrium thermodynamics suggests that also temperature, pressure and chemical potential can be measured by putting a system in equilibrium with a set up device of reference (for instance, ice melting into liquid water). Thus, it can be convenient to express the internal energy as a function of temperature (T) and pressure (p), instead of their *conjugate* extensive variables, respectively the entropy S , that we can evaluate only indirectly, and the volume V . It can be seen as a strange change of variable, which reads:

$$p \rightarrow -\frac{\partial U_c(\)}{\partial V} \quad (2.12)$$

and:

$$T \rightarrow \frac{\partial U_c(\)}{\partial S} \quad (2.13)$$

Expression	Symbol	Name of the dependent variable
$\partial_S U_c$	T	temperature
$-\partial_V U_c$	p	pressure
$\partial_A U_c$	γ	surface energy
$\partial_M U_c$	μ	chemical potential

Table 2.1: *Dependent variables resulting from the derivative of the internal energy on the independent variables. Pressure refers to the pressure exerted to the environment on the system (and this explain the minus sign)*

where the notation “ $X \rightarrow Y$ ” means “ Y substitutes X ”, which mathematically would implies the knowledge of the functional form of the partial derivative of $U_c(\)$ and its inversion with respect to V and S . In practice, through experiments where T and p are controlled, the form of the internal energy is accessed directly as a function of the intensive variables. Thus, we can define the internal energy U (without the subscript “c”) as:

$$U := U(T, p, A, M) \quad (2.14)$$

where the value of U are the same of U_c when the appropriate association between T and S , and p and V are made, according to Eq. (2.12, 2.13). The subscript “c” has been dropped to avoid confusion about the functional dependence. U_c is a function of entropy, volume, interfacial area and mass; U is a function of temperature, pressure, interfacial area and mass.

A third internal energy function could be used:

$$U_v := U(T, V, A, M) \quad (2.15)$$

since volumes are easily measured, and experiments can be prepared with fixed volumes. The above definition avoids ambiguities and allows for the exploiting of normal algebra also in thermodynamics.

2.4 Gibbs-Duhem identity

Internal Energy is usually decomposed into its part left explicit according to Eq. 2.10. Thus, it can be written as:

$$U(\) := T(\)S - p(\)V + \gamma(\)A + \mu(\)M \quad (2.16)$$

where, in order to reconcile the above expression with calculus, the following identity, called in literature Gibbs-Duhem equation, must be assumed:

$$SdT(\) - Vdp(\) + Md\mu(\) \equiv 0 \quad (2.17)$$

where the interfacial forces have been neglected. Thus whenever Eq. 2.16 is used, also Eq. 2.17 must be kept. It says that intensive variables are not independent. When considering a single phase (free water or free ice) the above equation becomes:

$$d\mu_j(\) = \frac{V_j(\)}{M_j} dp - \frac{S_j(\)}{M_j} dT = v_j(\)dp - s_j(\)dT \quad (2.18)$$

and, as soon as volume and entropy are linear functions of mass (e.g. *Callen*, 1985), the chemical potential of a single phase is just a function of pressure and temperature.

2.5 Interfaces

In the previous sections, it was assumed that the internal energy depends on both volume, V and surfaces, A . In reality, interfaces should be better treated as phases by themselves, where the surface energy, $\gamma(\)$ plays the role of pressure, and area plays the role of volume (*Safran*, 1994). In this view, the dependence from A in the expression of the previous section should be dropped, and it should be:

$$U_B(\) := U_B(S, V, M) \quad U_I := U_I(S, A, M) \quad (2.19)$$

for the "bulk" phase and the "interface" respectively.

However, at equilibrium of the bulk phase with the interface:

$$\begin{cases} \mu_B(\) = \mu_I(\) \\ T_B = T_I \end{cases} \quad (2.20)$$

Thus, at equilibrium, the total internal energy of the bulk plus the interface phase is:

$$\begin{aligned} U(\) &= U_B(\) + U_I(\) = \\ T_B(\)S_B - p(\)V + \mu_B(\)M_B + T_I(\)S_I + \gamma(\)A + \mu_I(\)M_I &= \\ T(\) [S_B + S_I] - p(\)V + \gamma(\)A + \mu(\) [M_B + M_I] &= \\ T(\)S - p(\)V + \gamma(\)A + \mu(\)M & \end{aligned} \quad (2.21)$$

where S and M are respectively the total (bulk plus interface) entropy and mass. The last expression recovers the structure of the internal energy used in the previous section. In multiphase systems interfaces can be as many as the number of constituents in contact, and there could be more than one $\gamma(\)A$ terms, each for any interface.

In the dissertation, accordingly to convenience, the former or the last notation will be used. However, the section below conforms to the idea that the bulk of a substance and its boundaries are different phases.

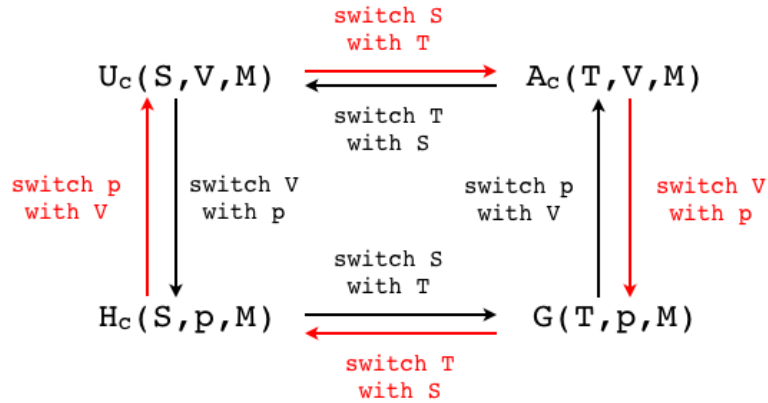


Figure 2.1: Legendre transform among the four thermodynamics potentials

2.6 Thermodynamical Potentials

In classical thermodynamics the internal energy is not just the unique representation of the energetic state of the system. At least other three are used through time with different scopes. They are based on:

- Enthalpy

$$H_c(\cdot) := H_c(S, p, M) \quad (2.22)$$

- Gibbs free energy

$$G(\cdot) := G(T, p, M) \quad (2.23)$$

- Helmholtz free energy

$$A_c(\cdot) := A_c(T, V, M) \quad (2.24)$$

It is clear, that keeping fixed the dependence on M variables, each of the above *potentials* represents an exchange of one (or two) extensive independent variable with its conjugate intensive variable. Including the internal energy, the scheme works as in Fig. 2.1.

When dealing with interfaces, the same rules apply but using the conjugate $\gamma(\cdot)$ and A in place of $p(\cdot)$ and V . Any of these potential contains the same information about the system as one of the other, and, in principle, it is possible to build the entire thermodynamics just on one of them. However, the information is presented in a different form that can be more suitable to understand some peculiar thermodynamics features. They can be obtained one from each other by a *Legendre transform*. A clear treatment of the subject can be found in *Zia et al. (2009)*, that can be summarized as follows:

Given a function Z of variable X and Y , with the appropriate smoothness properties, say:

$$Z = Z(X, Y) \quad \text{with } x := \partial_X Z(\) \quad \text{and } y := \partial_Y Z(\) \quad (2.25)$$

a Legendre transform of $Z(\)$, say $A(\)$, is defined by:

$$A(x, Y) := Z(X(x, Y), Y) - xX(x, Y) \quad (2.26)$$

This implies that:

- 1 The change of coordinates $X \rightarrow x$ is made, i.e.:
 - a) the expression for the derivative (2.25)_b is obtained as function of X and Y ;
 - b) it is inverted for getting X as a function of x and Y ;
 - c) it is finally reintroduced in the original expression
- 2 $A(x, Y)$ represents the original quantity $Z(\)$, now function of x and Y , subtracted by the product $xX(\)$

The new function $A(\)$ does not have the same values as the original $Z(\)$ for corresponding values of x and X , and differs exactly from it by “ $-xX(\)$ ”, which has a simple geometrical interpretation, e.g. (Zia *et al.*, 2009). This special type of change of coordinates, is pretty common in Classical Mechanics e.g. *Gantmacher* (1975)) and, obviously in Thermodynamics.

Thus, the following Legendre transform connects the various potentials:

$$U_c(\) \rightarrow H_c(\) : \quad H_c(S, p, M) := U_p(S, p, M) + pV(S, p, M) \quad (2.27)$$

$$H_c(\) \rightarrow G(\) : \quad G_c(T, p, M) := H_T(T, p, M) - TS(T, p, M) \quad (2.28)$$

$$G(\) \rightarrow A_c(\) : \quad A_c(T, V, M) := G(T, V, M) - Vp(T, V, M) \quad (2.29)$$

$$A_c(\) \rightarrow U_c(\) : \quad U_c(S, V, M) := A(S, V, M) - ST(S, V, M) \quad (2.30)$$

The subscript “c” stands for Callen’s, or canonical form of the potentials. Because Gibbs free energy is in the form function of T and p , it has not subscripts. In the following of the text, all the above potentials, except when specified, will be function of T, p, A, M and written without any subscript. Thus:

$$U(\) := U(T, p, M) \quad H(\) := H(T, p, M) \quad (2.31)$$

$$G(\) := G(T, p, M) \quad A_H := A(T, p, M) \quad (2.32)$$

where A_H has a subscript to avoid confusion with area. In table 2.2 is reported a summary of the notation of the potentials according to the functional dependence on variables.

	Functional Dependence			
	(S,V,M)	(S,p,M)	(T,p,M)	(T,V,M)
Internal energy	$U_c()$	$U_p()$	$U()$	$U_v()$
Enthalpy	$H_v()$	$H_c()$	$H()$	$H_{Tv}()$
Gibbs free-energy	$G_{sv}()$	$G_S()$	$G()$	$G_v()$
Helmoltz free-energy	$A_S()$	$A_{Sp}()$	$A_H()$	$A_c()$

Table 2.2: *Functional dependence of the potentials*

Thus, the following Legendre transforms connect the various potentials:

$$U_c() \rightarrow H_c(): H_c() := U_p() + pV() \quad (2.33)$$

$$H_c() \rightarrow G(): G_c() := H_T() - TS() \quad (2.34)$$

$$G() \rightarrow A_c(): A_c() := G_v() - Vp() \quad (2.35)$$

$$A_c() \rightarrow U_c(): U_c() := A_S() - ST() \quad (2.36)$$

2.6.1 Variations and Differentials

Variations of the thermodynamics potential during a generic transformation follow from the definition above. Only the calculations about enthalpy are fully performed, being the algebra, in fact, straightforward, once the notation is understood.

2.6.1.1 Enthalpy

The variation of Enthalpy is:

$$\begin{aligned} dH_c &= d[U_p() + pV()] = dU_p() + d[pV()] = \\ &T()dS - pdV() + \mu()dM + V()dp + pdV() = \\ &T()dS + \mu()dM + V()dp \end{aligned} \quad (2.37)$$

where the Gibbs-Duhem identity has been used. The reader should notice that, by definition, the following identities hold:

$$T() \equiv \frac{\partial H_c()}{\partial S} \quad \mu() \equiv \frac{\partial H_c()}{\partial M} \quad V() \equiv \frac{\partial H_c()}{\partial p} \quad (2.38)$$

When dealing with an interface phase, the enthalpy of the interface, according to Eq. 2.37 and, considering that $\gamma(\cdot)$ replaces $-p(\cdot)$ and $A(\cdot)$ replaces $V(\cdot)$, it is:

$$\begin{aligned} dH_c &= d[U_\gamma(\cdot) - \gamma A(\cdot)] = dU_\gamma(\cdot) - d[\gamma A(\cdot)] = \\ T(\cdot)dS + \gamma dA(\cdot) + \mu(\cdot)dM - A(\cdot)d\gamma - \gamma dA(\cdot) &= \\ T(\cdot)dS + \mu(\cdot)dM - A(\cdot)d\gamma & \end{aligned} \quad (2.39)$$

With the consequent identity:

$$A(\cdot) \equiv -\frac{\partial H_c}{\partial \gamma} \quad (2.40)$$

2.6.1.2 Gibbs Free Energy

Any variation of Gibbs Free Energy is:

$$dG(\cdot) = dH_c(\cdot) - d[T(\cdot)S] = V(\cdot)dp - S(\cdot)dT + \mu(\cdot)dM \quad (2.41)$$

As in the case of Entalphy, the following identities hold by definition:

$$S(\cdot) \equiv -\frac{\partial G(\cdot)}{\partial T} \quad \mu(\cdot) \equiv \frac{\partial G(\cdot)}{\partial M} \quad V(\cdot) \equiv \frac{\partial G(\cdot)}{\partial p} \quad (2.42)$$

Considering a system of a bulk phase plus its interface phase, it is:

$$dG(\cdot) = dH_c(\cdot) - d[T(\cdot)S] = V(\cdot)dp - A(\cdot)d\gamma - S(\cdot)dT + \mu(\cdot)dM \quad (2.43)$$

where:

$$A(\cdot) \equiv -\frac{\partial G(\cdot)}{\partial \gamma} \quad (2.44)$$

However, by definition, it is also:

$$G(T, p, M) := U(T, p, M) - TS(\cdot) + pV(\cdot) - \gamma A(\cdot) \equiv \mu(\cdot)M \quad (2.45)$$

Thus, it is also:

$$d(G(\cdot) = d[\mu(\cdot)M] \quad (2.46)$$

2.6.1.3 Helmholtz Free Energy

Variations of the Helmholtz free Energy can be obtained by the same rules as above. It is:

$$dA_c(\cdot) = d[G_V(\cdot)] - d[Vp(\cdot)] = -p(\cdot)dV - S(\cdot)dT + \mu(\cdot)dM \quad (2.47)$$

with the following identities:

$$p(\cdot) \equiv -\frac{\partial A_c(\cdot)}{\partial V} \quad S(\cdot) \equiv -\frac{\partial A_c(\cdot)}{\partial T} \quad \mu(\cdot) \equiv \frac{\partial A_c(\cdot)}{\partial M} \quad (2.48)$$

2.7 Quantities for unit of mass

All the above extensive quantities, $S, V, A, U_c, H_c, A_c, G$ can be divided by the mass of the system to obtain the relative specific quantities: specific entropy, specific volume, specific area, specific internal energy, specific enthalpy, specific Helmholtz energy, specific Gibbs' free energy. As outlined in table 2.3, they will be denoted by the lower-case symbols.

One special note needs to be issued for the term:

$$G := \mu(\cdot)M \quad (2.49)$$

In fact dividing both the members for the mass term, it is:

$$g(\cdot) \equiv \mu(\cdot) \quad (2.50)$$

which means that, for a single-substance-single-phase system, the chemical potential is the specific Gibbs free energy. However, for a system where multiple phases are present, say ice and liquid water:

Symbol	Name
$s_k(\cdot)$	specific entropy
$v_k(\cdot)$	specific volume
$a_{jl}(\cdot)$	specific area
$u_k(\cdot)$	specific internal energy
$h_k(\cdot)$	specific entalphy
$a_k(\cdot)$	specific Helmholtz's energy
$g_k(\cdot)$	specific Gibbs' free energy

Table 2.3: *Specific variables (for unit mass). The subscript k stands for any of the permitted subscript for the same quantities, or for no subscript, to denote the functional dependence of the quantity specified; subscript "jl" stands for the two substances which the interface separates.*

$$G(\cdot) := \mu_i(\cdot)M_i + \mu_w(\cdot)M_w \quad (2.51)$$

where the subscripts indicate respectively ice and liquid water. The specific quantity now can be

obtained by dividing for the total mass $M_i + M_w$ and

$$g(\cdot) := \mu_i(\cdot)f_i + \mu_w(\cdot)f_w \quad (2.52)$$

where f_i is the ice fraction and f_w is the water fraction in the total mass. In this case the specific Gibbs' free energy is the weighted mean of ice and water chemical potential.

A conundrum also arises when considering the differentials of the quantities. In fact if (2.10) is valid, then:

$$du_c(s, v, a, m) = T(\cdot)ds - p(\cdot)dv + \gamma(\cdot)da + \mu(\cdot)dm \quad (2.53)$$

is the equation for specific internal energy in the canonical form, where:

$$dm := \frac{dM}{M} \quad (2.54)$$

which is the variation of the given phase mass with respect to the mass itself. This is really a non-sense in a single phase system (where, by the way, this term is null), but acquires meaning when there are two phases. Then:

$$\begin{aligned} du_c(s, v, a, m) = & T(\cdot)ds_i - p_i(\cdot)dv_i + \gamma_{iw}(\cdot)da_{iw} + \mu_i(\cdot)dm_i + \\ & T(\cdot)ds_w - p_w(\cdot)dv_w + \mu_w(\cdot)dm_w \end{aligned} \quad (2.55)$$

where

$$dm_i := \frac{dM_i}{M_i + M_w} \quad dm_w := \frac{dM_w}{M_i + M_w} \quad (2.56)$$

It is eventually interesting to notice (see section 3.2 from *Bohren and Albrecht, 1998*) that, given the definition of the internal energy $U_v = U(T, V, M)$, one can define:

$$\frac{\partial U_v(\cdot)}{\partial T} := C_v \quad (2.57)$$

as the heat capacity at constant volume. At the same manner:

$$\frac{\partial H(\cdot)}{\partial T} := C_p \quad (2.58)$$

is the heat capacity at constant pressure.

2.7.1 A note on potentials as dependent on temperature and pressure

When, as in most of the dissertation, potentials dependent on pressure and temperature will be chosen, the differential written in the previous section maintains the same formal structure. Thus, when switching to T and p as independent variable (from $U_c(\cdot)$ to $U(\cdot)$), (2.10) remains:

$$dU(T, p, A, M) = TdS(\cdot) - pdV(\cdot) + \gamma dA(\cdot) + \mu(\cdot) dM \quad (2.59)$$

where the difference is in the position of (\cdot) which denotes a different functional dependence of the terms appearing in the functional. The differential $dS(\cdot)$, $dV(\cdot)$ and $dA(\cdot)$ must obviously be expanded according to their functional dependence. For instance, if $S = S(T, p, \gamma, M)$, then:

$$dS(\cdot) = \frac{\partial S}{\partial T} dT + \frac{\partial S}{\partial p} dp + \frac{\partial S}{\partial \gamma} d\gamma + \frac{\partial S}{\partial M} dM \quad (2.60)$$

The existence of all of these terms depends on the system under analysis. Finally (2.59) becomes

$$dU(T, p, A, M) = \alpha(\cdot) dT - \beta(\cdot) dp - \delta(\cdot) d\gamma - m(\cdot) dM \quad (2.61)$$

where $\alpha(\cdot)$, $\beta(\cdot)$, $\delta(\cdot)$, $m(\cdot)$ are the appropriate quantities that come out from the derivation chain rule. What exactly they do depends on the system under analysis, however, usually the function dependence in Eq. 2.59 does not need to be really expanded.

2.8 Thermodynamic equilibrium

Let us now review the conditions for equilibrium of a thermodynamical system. The conservation of energy applied to a system states that *the rate of change of energy of the body - internal energy $U(\cdot)$ and kinetic energy $K(\cdot)$ and the potential energy $P(\cdot)$ of the flow field - is equal to the sum of the fluxes, Φ of energy through the boundaries coming from radiation, advection, convection and conduction.*

$$\frac{d[U(\cdot) + K(\cdot) + P(\cdot)]}{dt} = \Phi(\cdot) \quad (2.62)$$

Besides, the internal energy can be expanded as in Eq. 2.16, and in cases of closed systems, fluxes are null.

$$\dot{Q}(\cdot) := TS(\cdot) \quad (2.63)$$

represents the rate of exchange of thermal energy through heating/cooling and

$$\dot{L}(\cdot) := -pV(\cdot) \quad (2.64)$$

(work) is the power of stresses acting on the boundary of the body (*Muller and Weiss, 2005*). As stated, by the second postulate, one part of the second law of thermodynamics states that *the effects of the thermal energy fluxes can be described, at equilibrium, by a state function called entropy, $S(\cdot)$* . In particular, it is:

$$\dot{Q}(\cdot) = T(\cdot) \frac{dS}{dt} \quad (2.65)$$

and during a process, for an isolated system:

$$\frac{dS(\cdot)}{dt} \geq 0 \quad (2.66)$$

In fact, in the last expression, the internal energy expression is inverted to obtain entropy as a function of internal energy (or equivalently another potential) and the other extensive quantities, as the problem under studies requires.

This statement reads that the entropy of a closed system tends to a maximum:

$$dS(U, V, M) = 0 \quad (2.67)$$

or, stated differently, under variety of cases, the Gibbs free energy, $G(\cdot)$ of a closed system tends to a minimum:

$$dG(T, p, M) = 0 \quad \text{given } T=\text{cost } p=\text{cost} \quad (2.68)$$

The above equation is true also the trivial condition where the temperature and the pressure at the boundaries of the system are kept constant.

2.8.1 Equilibrium of two phases with flat interfaces

Let us consider a homogeneous substance in two phases (e.g. water and ice, denoted by subscripts "w" and "i" respectively) in equilibrium, and let us suppose the separation interfaces are flat. One can apply the equilibrium condition given by Eq. 2.67 to Eq. 2.10: considering both phases:

$$\begin{cases} dU_w(\cdot) = T_w dS_w(\cdot) - p_w dV_w(\cdot) + \mu_w(\cdot) dM_w \\ dU_i(\cdot) = T_i dS_i(\cdot) - p_i dV_i(\cdot) + \mu_i(\cdot) dM_i \end{cases} \quad (2.69)$$

Considering that in a closed system $dU_w(\cdot) = -dU_i(\cdot)$, $dM_w = -dM_i$, $dV_w(\cdot) = -dV_i(\cdot)$, and that $dS(\cdot) = dS_w(\cdot) + dS_i(\cdot)$, one obtains:

$$dS(\cdot) = \left(\frac{1}{T_w} - \frac{1}{T_i} \right) dU_w(\cdot) + \left(\frac{p_w}{T_w} - \frac{p_i}{T_i} \right) dV_w(\cdot) - \left(\frac{\mu_w(\cdot)}{T_w} - \frac{\mu_i(\cdot)}{T_i} \right) dM_w = 0 \quad (2.70)$$

2. Equilibrium thermodynamics

Once observed that, at equilibrium, the kinetic energy $K(\cdot)$ must be null, the above implies that at equilibrium is also:

$$\begin{cases} T_i = T_w \\ p_i = p_w \\ \mu_i = \mu_w \end{cases} \quad (2.71)$$

Therefore at equilibrium T , p and $\mu(\cdot)$ are constants throughout the system. Another important property of equilibrium can be derived subtracting the two Equations 2.69:

$$(dU_w + p_w dV_w) - (dU_i + p_i dV_i) = T d(S_w - S_i) + \mu_w dM_w - \mu_i dM_i \quad (2.72)$$

Let us notice that because on Gibbs free energy, $\mu_w = \mu_i$ and, for the mass conservation during phase change, $dM_w = -dM_i$. Because $H_c(\cdot) := U(\cdot) + p(\cdot)V$, eventually one obtains:

$$d(H_w - H_i) = T d(S_w - S_i) \quad (2.73)$$

and, for each constituent, j :

$$T(\cdot) dS_j = dH_j \quad (2.74)$$

The Gibbs-Duhem identity, applied to the two phases, in turn, reads:

$$\sum_{j \in \{w,i\}} M_j d\mu_j(\cdot) = \sum_{j \in \{w,i\}} [V_j(\cdot) dp - S_j(\cdot) dT] \quad (2.75)$$

In experiments where pressure is kept constant, and the mass is constant, the relation between enthalpy and entropy is:

$$dH(\cdot) = T dS(\cdot) := \dot{Q}(\cdot) \quad (2.76)$$

and, besides, the enthalpy variation is the heating/freezing of the body (the thermal energy).

Thermodynamical equilibrium in the case of homogeneous substance with flat interfaces and no gravity, according to Eq. 2.71, implies $dp_i = dp_w := dp$, i.e. the pressure is the same in both phases and,

$$\mu_i(T, p) = \mu_w(T, p) \quad (2.77)$$

i.e. the chemical potentials of two substances, are equal, such that there is no net material transformation passing from one phase to the other. The equality among the chemical potential allow for obtaining a curve in the plain T, p which is known as Calusius-Clapeyron (CC) equation. The relation can be obtained according to the following arguments: if the pressure is changed, then also the chemical potential will change accordingly, until a new equilibrium will be found at a new (p, T) . Generalizing this for each point in the (p, T) plane, this means that the differential of

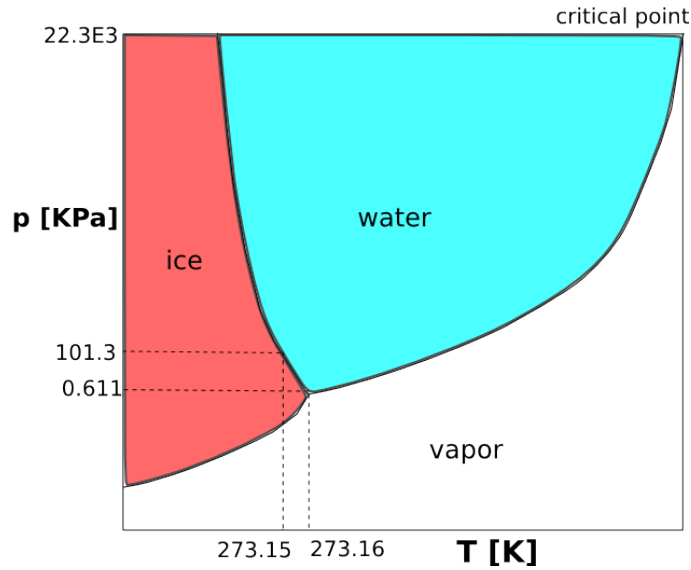


Figure 2.2: Clausius-Clapeyron thermodynamic equilibrium

the chemical potential of the two substances must be equal, i.e.:

$$d\mu_w(T, p) = d\mu_i(T, p) \quad (2.78)$$

Applying Eq. 2.18 for expliciting the above differentials the equality turns into:

$$-\frac{h_w(\cdot)}{T}dT + v_w(\cdot)dp = -\frac{h_i(\cdot)}{T}dT + v_i(\cdot)dp \quad (2.79)$$

from which follows that:

$$\Rightarrow \frac{dp}{dT} = \frac{s_w(\cdot) - s_i(\cdot)}{v_w(\cdot) - v_i(\cdot)} = \frac{h_w(\cdot) - h_i(\cdot)}{T [v_w(\cdot) - v_i(\cdot)]} \equiv \frac{L_f(\cdot)}{T [v_w(\cdot) - v_i(\cdot)]} \quad (2.80)$$

where $L_f(\cdot) := h_w(\cdot) - h_i(\cdot)$ [J Kg⁻¹] is the latent heat of fusion (or just enthalpy of fusion).

This equation represents the equilibrium relation for phase change between the liquid and the solid phase. In a (T, p) diagram, as in Fig. 2.2, this curve separates the ice (red region) between the liquid water (cyan region).

In a stable-equilibrium situation all the water in the ideal system under analysis (a large mass of water with constant pressure and temperature at the boundary - and no gravity), will be either liquid water or ice, but during the passage between the two phases are usually considered to exist a meta-stable equilibrium, in which the equilibrium thermodynamics can still be used to infer the values

of the thermodynamic variables. The atomic structure of the water allows for many arrangements of the molecules, and, in correspondence to each one of them, there is ideally an expression of the chemical potential (as a function of T and p). In this context the three arrangements that we are interested in are those called traditionally ice, liquid water and water vapor close to ordinary pressure and temperature at the Earth's surface, but, for instance, many forms of ice are known (e.g. *Bentley and Humphreys*, 1962 and *Nakaya*, 1956). The thermodynamics of equilibrium requires that the phase present at a certain (T, p) is the one with lowest chemical potential (*Hudson*, 1996). Thus, assuming we have the three surfaces representing the three chemical potentials, the lowest envelope of them represent the thermodynamic equilibrium reality. The curves of the Clausius - Clapeyron relation on the phase diagrams represent the intersection of these surfaces.

2.9 Conclusions

In this section the basic notation and concept of thermodynamics of equilibrium have been introduced. These concepts and equalities will be used in the next chapter to delineate the equations used for approaching the freezing process in soils.

3 Freezing soil

3.1 Introduction

In this chapter a throughout derivation of the soil freezing process is performed, starting from thermodynamic equilibrium to the derivation of the water and ice content in the ground given the temperature and pressure. The findings of *Loch* (1978) and the thermodynamic formulation of the previous chapter allow to derive a generalised form of the Clapeyron equation, in which mechanical equilibrium at the ice/water interface is not assumed but rather the chemical potentials in the ice and liquid are equated. This formulation will be made assuming a capillary tube schematization for the soil and the assumption “freezing=drying” as suggested by *Miller* (1963). This assumption, often used in the literature, has a precise meaning on the pressure of the water and the ice phase, and limitations on the physical processes that may be dealt with. Then a freezing pressure will be defined, to account for the freezing/thawing process. This will eventually allow, through the combined use of the soil water retention curves and the thermodynamical equilibrium, to derive the soil freezing characteristic curve and therefore the ice content.

3.2 Equilibrium of two phases in a capillary

The capillary tube is characterized by the presence of curved interfaces between the phases and thus the thermodynamical equilibrium depends by the curvature of the interface, i.e. the surface tension existing between the two phases. Let us imagine a single capillary where liquid water is in equilibrium with its vapor and air as in Fig. 3.1. In this case, by a simple equilibrium of forces, one obtains:

$$p_a \pi r^2 = p_w \pi r^2 + 2\pi r \gamma_{wa} \cos \alpha \quad (3.1)$$

where p_a , p_w [Pa] are the pressures of the gaseous portion and of water respectively, α is the contact angle and γ_{wa} [N m⁻¹] is the surface tension between air and water. Dividing all by πr^2 one obtains:

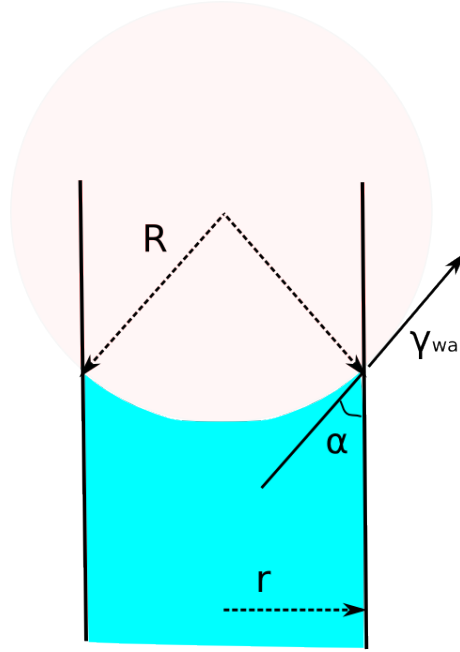


Figure 3.1: Effect of curvature on liquid-air interface

$$p_a = p_w + 2 \gamma_{wa} \frac{\cos \alpha}{r} = p_w + 2 \gamma_{wa} \frac{1}{R} \quad (3.2)$$

where $R = r / \cos \alpha$ is the curvature radius. Considering $R = r$ the water pressure p_w becomes:

$$p_w = p_a - \gamma_{wa} \frac{2}{r} \quad (3.3)$$

The same equation may be derived by the more general formulation, if the surface area of the interface separating water and air is assumed to be just a function of the water volume, $A_{wa}(\cdot) := A(V_w)$, where A_{wa} is the area of the separation surface between water and air, and V_w is the volume of the water droplet. Then:

$$p_w = p_a - \gamma_{wa} \frac{\partial A_{wa}(\cdot)}{\partial V_w} \quad (3.4)$$

Considering a sphere of water inside the capillary, the volume is $4/3\pi r^3$ and the surface area is $4\pi r^2$, therefore the same equation may be obtained as:

$$p_w = p_a - \gamma_{wa} \frac{\partial A_{wa}(r)}{\partial V_w(r)} = p_a - \gamma_{wa} \frac{\partial A_{wa}/\partial r}{\partial V_w/\partial r} = p_a - \gamma_{wa} \frac{2}{r} := p_a - p_{wa}(r) \quad (3.5)$$

where $p_{wa}(r) := \gamma_{wa} \partial A_{wa}(r) / \partial V_w$ may be defined as the pressure drop due to the interface and is, according to the capillary equation, a function of the radius r . Eq. 3.5, usually known as Laplace's

equation, says that the pressure drop across the air-water interface in any pore is inversely proportional to the size of the pore. This means that, with increasing negative pressures, increasingly smaller pores are being emptied. Assuming the same relation applies for water-air and water-ice interface one obtains:

$$\begin{cases} p_w = p_a - \gamma_{wa} \frac{\partial A_{wa}}{\partial V_w} = p_a - p_{wa}(r) \\ p_w = p_i - \gamma_{iw} \frac{\partial A_{iw}}{\partial V_w} = p_i - p_{iw}(r) \end{cases} \quad (3.6)$$

The above considerations are assumed to be valid for a representative elementary volume. A more rigorous treatment of the topic can be found in *Gray and Miller (2007)*. The internal energy should be modified to account for the component of the internal energy given by the interfaces. Therefore Eq. 2.69 becomes:

$$\begin{cases} dU_w(\cdot) = T_w dS_w(\cdot) - p_w dV_w(\cdot) + \mu_w(\cdot) dM_w \\ dU_i(\cdot) = T_i dS_i(\cdot) - p_i dV_i(\cdot) + \mu_i(\cdot) dM_i \\ dU_{iw}(\cdot) = \gamma_{iw} \frac{\partial A_{iw}(\cdot)}{\partial V_w} dV_w(\cdot) \end{cases} \quad (3.7)$$

Considering that in a closed system $dU(\cdot) = 0$ one obtains:

$$dU_w(\cdot) + dU_i(\cdot) + dU_{iw}(\cdot) = 0 \quad (3.8)$$

which means that:

$$dU_w(\cdot) + dU_{iw}(\cdot) := dU_w^*(\cdot) = -dU_i(\cdot) \quad (3.9)$$

Accounting for the interfacial forces in the internal energy budget, of water one obtains:

$$\begin{cases} dU_w^*(\cdot) = T_w dS_w(\cdot) - \left(p_w + \gamma_{iw} \frac{\partial A_{iw}(\cdot)}{\partial V_w} \right) dV_w(\cdot) + \mu_w(\cdot) dM_w \\ dU_i(\cdot) = T_i dS_i(\cdot) - p_i dV_i(\cdot) + \mu_i(\cdot) dM_i \end{cases} \quad (3.10)$$

Thus, finally, considering that: $dM_w = -dM_i$, $dV_w = -dV_i$, (neglecting at this stage the differences in liquid water and ice densities), and that $dS = dS_w + dS_i$, one obtains:

$$dS = \left(\frac{1}{T_w} - \frac{1}{T_i} \right) dU_w + \left(\frac{p_w + \gamma_{iw} \frac{\partial A_{iw}}{\partial V_w}}{T_w} - \frac{p_i}{T_i} \right) dV_w - \left(\frac{\mu_w}{T_w} - \frac{\mu_i}{T_i} \right) dM_w = 0 \quad (3.11)$$

which implies that, at equilibrium, besides having $K(\cdot) = 0$, it is:

$$\begin{cases} T_i = T_w \\ p_i = p_w + \gamma_{iw} \frac{\partial A_{iw}}{\partial V_w} \\ \mu_i = \mu_w \end{cases} \quad (3.12)$$

3.3 Ice pressure and “freezing=drying” assumption

In a saturated soil all the pores are filled with water and no air-water separation surface is present. In this case the water pressure totals $p_w = p_a + \rho_w g h$, where h is the water column height above the point, and depends just on the gravitational gradient. In an unsaturated soil, on the other hand, the presence of the menisci creates a negative pressure according to Eq. 3.4. This pressure, divided by ρ_w and g , represents the energy, up to the Darcy scale, belonging to the water in the capillaries. Integrating this energy in a representative elementary volume and dividing by the the total volume, one obtains the mean energy of the water in the volume, considering all the radius in the various capillaries. This value is called soil *suction* and is usually referred to as ψ_w .

Let us suppose an unsaturated soil where the water invades the pores having menisci of radius $r \leq r_0$. The water pressure at the macroscale is given by the surface tension between water and air:

$$p_{w0} = p_a - \gamma_{wa} \frac{\partial A_{wa}(r_0)}{\partial V_w} = p_a - p_{wa}(r_0) \quad (3.13)$$

where p_{w0} [Pa] is the water negative pressure due to the menisci surfaces created by the water-air interface in the pores with radius $r < r_0$, p_{wa} [Pa] is the interface water-air pressure, γ_{wa} [N m^{-1}] is the water-air surface tension, V_w [m^3] is the water volume and p_a is the air pressure. Let us suppose to freeze some water in the soil: this means that the water-air interface present at r_0 is replaced by an ice-air interface, and that a new ice-water interface is created at a smaller radius r_1 . Consequently the water in the capillary of radius r_1 will be subject to a new pressure p_{w1} , and the ice will be subject to the pressure p_i , as explained in Fig. 3.2. Following the capillary preceptual model developed above, one gets:

$$\begin{aligned} p_{w1} &= p_i - \gamma_{iw} \frac{\partial A_{iw}(r_1)}{\partial V_w} := p_i - p_{iw}(r_1) \\ p_i &= p_a - \gamma_{ia} \frac{\partial A_{ia}(r_0)}{\partial V_w} := p_a - p_{ia}(r_0) \end{aligned} \quad (3.14)$$

This implies:

$$p_{w1} = p_a - \gamma_{ia} \frac{\partial A_{ia}(r_0)}{\partial V_w} - \gamma_{iw} \frac{\partial A_{iw}(r_1)}{\partial V_w} \quad (3.15)$$

If we consider the assumption *freezing=drying* (Miller, 1963), we should think that the ice in the capillary behaves like air, i.e. the water below receives an increment in negative pressure (suction) as if the water was evaporated or drained. In this case the water pressure p_{w1} would be the same as no ice would be present, and the ice pressure is equal to air pressure. Therefore this model implies

that:

$$p_{w1} = p_a - p_{wa}(r_1) \quad (3.16)$$

$$p_i = p_a - p_{ia}(r_0) \equiv p_a \quad (3.17)$$

or, stated differently:

$$p_{iw}(r) = p_{wa}(r) \quad (3.18)$$

$$p_{ia}(r) \leftarrow 0 \quad (3.19)$$

which says that the interface pressure ice-water is equal to the interface pressure air-water and that the interface pressure ice-air is zero if the pressure gauge of air is taken to be null.

Rearranging Eq. 3.16 considering that liquid water is now confined in pores of radius less than r_1 , it is:

$$p_{w1} = p_a - \gamma_{wa} \frac{\partial A_{wa}(r_1)}{\partial V_w} = p_a - \gamma_{wa} \frac{\partial A_{wa}(r_0)}{\partial V_w} + \gamma_{wa} \frac{\partial A_{wa}(r_0)}{\partial V_w} - \gamma_{wa} \frac{\partial A_{wa}(r_1)}{\partial V_w} \quad (3.20)$$

that implies:

$$p_{w1} = p_{w0} - \gamma_{wa} \frac{\partial}{\partial V_w} (A_{wa}(r_1) - A_{wa}(r_0)) = p_{w0} + p_{wa}(r_0) - p_{wa}(r_1) \quad (3.21)$$

where A_{wa}^1 is the surface area of the water-air interface at the radius r_1 when the ice is formed between the radius r_0 and r_1 . Defining:

$$\Delta p_{freez} := -\gamma_{wa} \frac{\partial \Delta A_{wa}}{\partial V_w} = p_{wa}(r_0) - p_{wa}(r_1) \quad (3.22)$$

as the *freezing pressure* triggered by the formation of ice, one obtains that the new water pressure becomes:

$$p_{w1} = p_{w0} + \Delta p_{freez} \quad (3.23)$$

The hypothesis *freezing=drying* therefore means that the new water pressure, after the ice formation, is reduced by a quantity Δp_{freez} that depends on the specific surface area of the ice in the pores and the type of soil, as ice would not exist. Summarizing, the pressures of water and ice

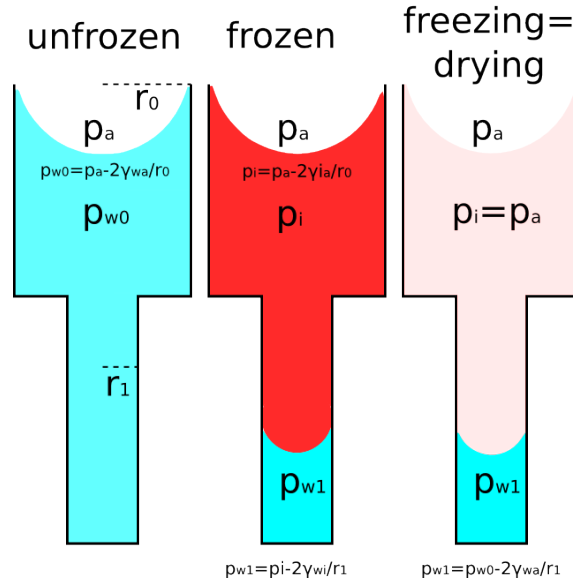


Figure 3.2: *Freezing=drying schematization*

become:

$$\begin{cases} p_{w1} = p_a - p_{wa}(r_1) \equiv p_{w0} + \Delta p_{freez} \\ p_i = p_a \leftarrow 0 \end{cases} \quad (3.24)$$

Under this notation, one can say that p_{w0} is the pressure of water in the capillary under unfrozen conditions, that depends on the air-water interfaces and thus on the saturation content of the soil. On the other hand, p_{w1} is the pressure of water in the capillary under freezing conditions, that depends on the negative temperature of the soil. Finally p_i is the pressure of ice that, under the assumption of *freezing=drying*, is equal to $p_a \leftarrow 0$. The difference between p_i and p_{w1} is the so-called freezing pressure (or freezing suction) Δp_{freez} .

Therefore from the assumptions *freezing=drying* and the capillary tube representation, straightly derives that the ice phase has a “zero-gauge” pressure. This finding is often, if not always, used in literature. However, most authors have not a clear view of the motivations behind it. *Spaans and Baker* (1996), when presenting an integrated form of the Clapeyron equation for total water potential, they write: “the broad assumption of zero gauge pressure in the ice phase has been questioned under certain conditions (*Miller* 1973 and 1980), but thus far there is scant evidence against it, except in obvious cases (heaving)”. Also *Hansson et al.* (2004) advance doubts on the source of the *zero ice pressure*. They say: “Usually in soil science the ice pressure is sometimes assumed to equal the zero gauge pressure, with the reference pressure being atmospheric. While this assumption has often been debated, no consensus has yet been reached. In particular, if a soil

is unsaturated the potential of heaving is reduced such that the assumption of zero ice pressure is more likely to hold." It is evident that the zero gauge pressure for ice is a *consequence* of the *freezing=drying* assumption, and is also a convenient hypothesis. In fact, it allows to get rid of the ice density from the Gibbs-Duhem relation. Otherwise, the ice pressure would remain at the denominator as in the Clausius-Clapeyron equation 2.80.

On the other hand *Christoffersen and Tulaczyk* (2003) propose a formulation of the equilibrium relation without assuming $p_i = 0$. They say that ice lens and therefore frost heave may be triggered when the ice pressure head ϕ_i exceeds the sum of gravitational overburden pressure and ice-water interfacial pressure. Frost heave, in fact, cannot be modeled under the *freezing=drying* condition, but needs a more complete approach (*Rempel et al.* 2004, *Rempel*, 2007).

3.4 The generalized Clausius-Clapeyron relation

For any substance (water or ice) taken alone, assuming a process at constant pressure, and therefore using enthalpy for approximating entropy, the Gibbs-Duhem equation becomes:

$$d\mu_j(\cdot) = -\frac{h_j(\cdot)}{T}dT + v_j(\cdot)dp_j \quad j \in \{i, w\} \quad (3.25)$$

where is either $j \leftarrow w$ or $j \leftarrow i$, and h and v are the specific enthalpy and specific volume respectively. If h and v can be considered well approximated as a constant (function of a reference temperature, T_0 , and pressure p_0), which seems reasonable, in the cases studied in this dissertation, then:

$$d\mu_j(\cdot)|_p \approx -\frac{h_j(T_0, p_0)}{T}dT + v_j(T_0, p_0)dp_j \quad j \in \{i, w\} \quad (3.26)$$

where $h_j(T_0, p_0)$ is the value of enthalpy and $v_j(T_0, p_0)$ specific volumes of the substance at temperature T_0 and pressure p_0 .

The equilibrium condition can be obtained by equalizing the differential of the chemical potentials $d\mu_w(\cdot) = d\mu_i(\cdot)$ as in Eq. 2.78:

$$-\frac{h_w(T_0, p_0)}{T}dT + v_w(\cdot)dp_w = -\frac{h_i(T_0, p_0)}{T}dT + v_i(\cdot)dp_i \quad (3.27)$$

As we know from 3.24 that $p_i = p_a$ and $p_w = p_i + p_{freez}$ one gets:

$$\begin{cases} dp_w = dp_{freez} \\ dp_i = 0 \end{cases} \quad (3.28)$$

The last equality being a consequence of $p_a \leftarrow \text{const} = 0$. Therefore:

$$L_f \frac{dT}{T} = v_w(\cdot) dp_{\text{freez}} = g d\Psi_{\text{freez}} \quad (3.29)$$

as $p = \rho_w g \Psi$ where Ψ is the pressure head. Furthermore:

$$L_f \ln \frac{T}{T_0} \approx L_f \frac{T - T_0}{T_0} = g (\Psi_{\text{freez}} - \Psi_{\text{freez}_0}) \quad (3.30)$$

Putting as reference $T_0 = 273.15 \text{ K}$ and $\Psi_{\text{freez}_0} = 0$ one obtains:

$$\Psi_{\text{freez}} = \Psi_{\text{freez}}(T) = \frac{L_f}{g T_0} (T - T_0) \quad (3.31)$$

and the water pressure at the radius r_1 becomes:

$$p_{w1} = p_{w0} + \rho_w \frac{L_f}{T_0} (T - T_0) \quad (3.32)$$

Eq. 3.31 is called Clapeyron equation. It was first introduced by *Edlefsen and Anderson* (1943) in the attempt to describe the mutual dependence of temperature, water content and solutes by means of a generalized and extended Clapeyron equation using thermodynamic equilibrium theory. A potential problem with the equilibrium assumption of this theory is that equilibrium may take a long time to establish (*Spaans and Baker*, 1996). In table 3.1 are reported several representations of the Clapeyron equation by various authors. According to the “freezing=drying” assumption, the freezing of soil may be schematized as in Fig.3.3. Adding the capillary tube representation, the freezing process may be represented as in Fig. 3.4.

3.5 The freezing point depression

From Clausius-Clapeyron Eq. 2.78 one knows that at $p_w = p_a \leftarrow 1 \text{ atm}$ the melting temperature is 273.15 K . However, when interfacial forces are present (e.g. in a capillary tube), the melting temperature decreases, due to a combination of surface energy and interface curvature. Suppose an unsaturated soil with $p_w = p_{w_0}$: solving Eq. 3.31 with respect to temperature, one obtains:

$$\Psi_{\text{freez}} \equiv \Psi_{w_0} = \frac{L_f}{g T_0} (T - T_0) \quad (3.33)$$

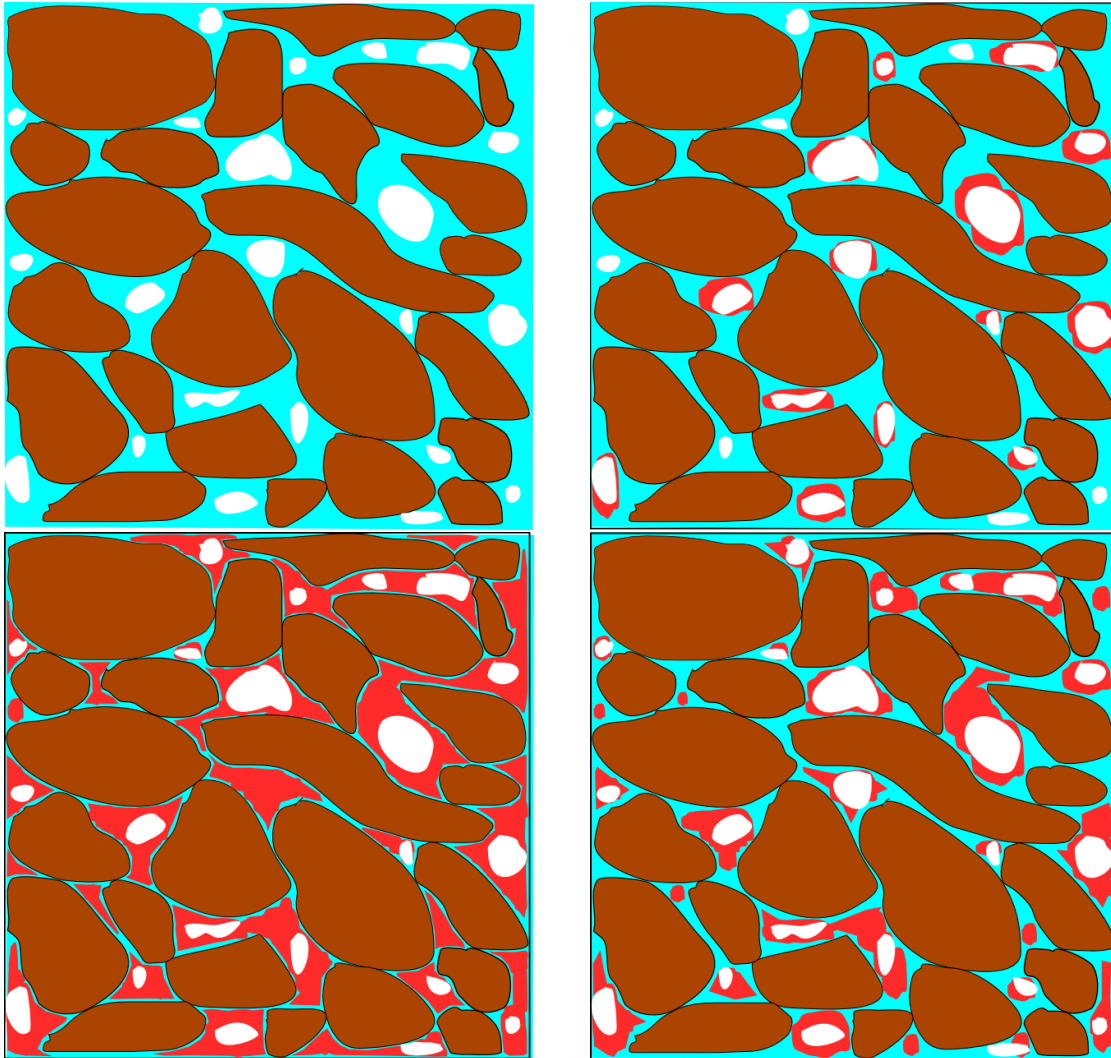


Figure 3.3: Freezing process schematization for an unsaturated soil (assuming equal density of water and ice, and no frost heave process acting). The color brown represents the soil particles, the light blue the water, the red the ice and the white the air. The ice, from a complete unfrozen-unsaturated condition (top left), starts forming in the bigger pores (top right), then reaches the smaller pores (bottom left) until all the water is frozen (bottom right)

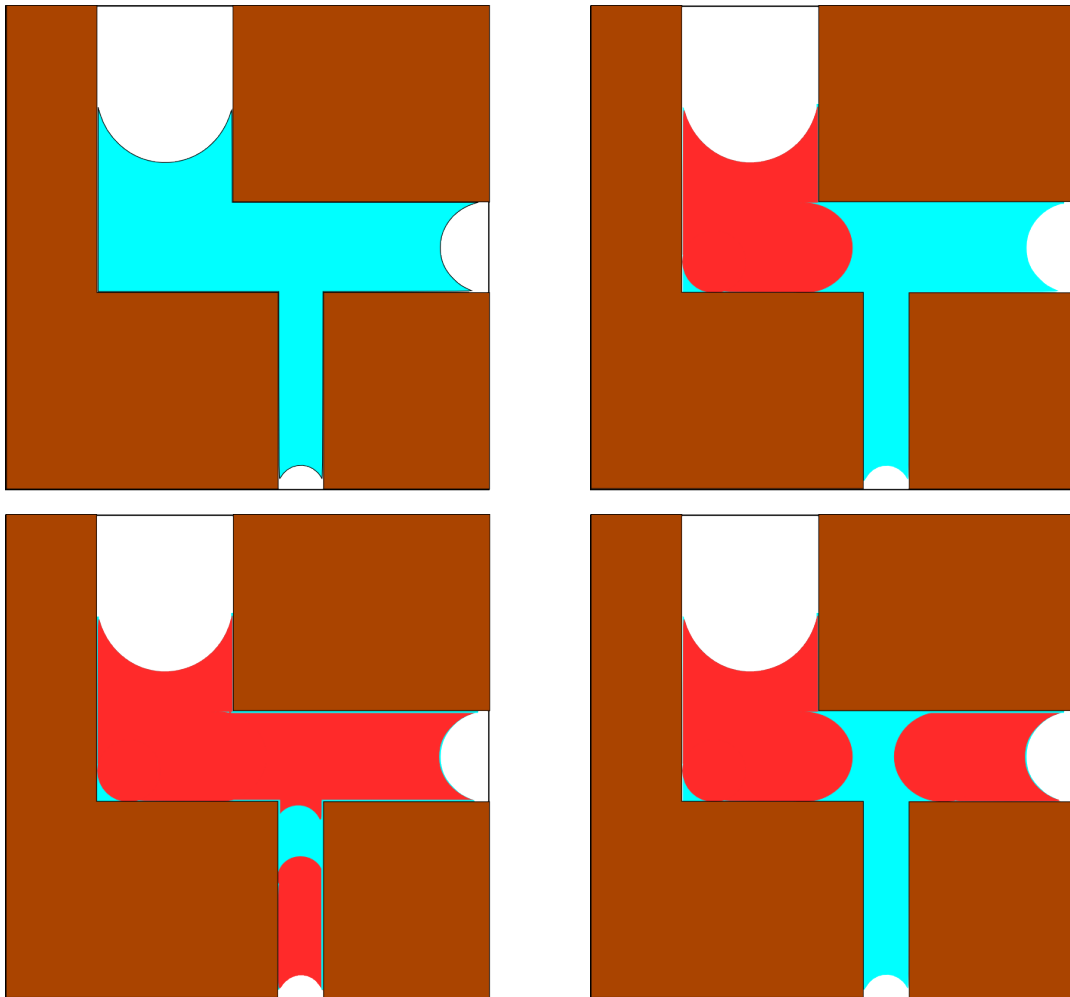


Figure 3.4: *Capillary tube freezing process schematization, according to the freezing=drying approximation. The color brown represents the soil particles, the light blue the water, the red the ice and the white the air. An unsaturated unfrozen soil (top left) starts freezing from the biggest pores, than the freezing advance to the medium (bottom left) until reaches the smallest pores (bottom right)*

Author	Equilibrium formulation	Unit
<i>Williams</i> (1964)	$\Psi = \frac{L_f}{gT} \Delta T$	[m]
<i>Guymon and Luthin</i> (1974), <i>Hansson et al.</i> (2004), <i>Koren et al.</i> (1999)	$d\Psi = \frac{L_f}{(T+273.15)g} \cdot dT$	[m]
<i>Fuchs et al.</i> (1978)	$\Psi + \pi = \frac{L_f}{(T+273.15)g} \cdot (T - T_m)$	[m]
<i>Christoffersen and Tulaczyk</i> (2003)	$\Psi - \phi_i = \frac{L_f}{273.15g} \cdot T + \pi$	[m]
<i>Spaans and Baker</i> (1996)	$\Psi + \pi = -712.38 \ln\left(\frac{T}{T_m}\right) + 5.545(T - T_m) - 3.14E-3(T - T_m^2)$	[J Kg ⁻¹]
<i>Flerchinger et al.</i> (2006)	$d[\Psi(T) + \pi(T)] = \frac{L_f}{(T+273.15)g} \cdot dT + d\phi_i$	[m]
<i>Daanen et al.</i> (2007), <i>Zhang et al.</i> (2007)	$\Psi(T) = \frac{L_f}{273.15g} \cdot T$	[m]
<i>Watanabe</i> (2008)	$\Psi(T) = \frac{L_f}{g} \cdot \ln \frac{T}{T_m}$	[m]
<i>Luo et al.</i> (2009)	$\Psi = \frac{L_f (T - T_m)}{g T}$	[m]

Table 3.1: $\Psi = \Psi(T)$ relations from various authors. π is the osmotic suction and ϕ_i is the ice pressure head.

and :

$$T^* := T_0 + \frac{g T_0}{L_f} \Psi_{w_0} \quad (3.34)$$

where T^* is the temperature of phase change under unsaturated conditions, due to interfacial forces. It is clear that the freezing pressure Ψ_{freez} is actually working just for temperature inferior to T^* . For saturated soils, $T^* = T_0$ as $\Psi_{w_0} = 0$. Eventually:

$$\begin{cases} T^* = T_0 + \frac{g T_0}{L_f} \Psi_{w_0} \\ \Psi_{freez}(T) = \frac{L_f}{g T_0} (T - T_0) \cdot H(T - T^*) \end{cases} \quad (3.35)$$

where H is the Heaviside function. At the same manner, one can also use Eq. 3.13 and 3.32 and the Laplace Equation 3.5 to derive the radius r_1 where the freezing process has arrived.

$$\begin{cases} r_0 = \frac{2 \gamma_{wa}}{p_a - p_{w0}} \\ p_{w1} = p_{w0} + \rho_w \frac{L_f}{T_0} (T - T_0) = p_a - \gamma_{wa} \frac{2}{r_1} \end{cases} \quad (3.36)$$

therefore:

$$\Rightarrow r_1 = \frac{2 \gamma_{wa}}{p_a - p_{w0} - \rho_w \frac{L_f}{T_0} (T - T_0)} \quad (3.37)$$

or equivalently:

$$\frac{1}{r_1} = \frac{1}{r_0} - \frac{\rho_w L_f}{2 \gamma_{wa} T_0} (T - T_0) = f(r_0, T) \quad (3.38)$$

Therefore the radius r_0 is a function of the negative water pressure given by the unsaturation degree, whereas the radius r_1 is a function of both r_0 and the negative temperature. Under the *freezing=drying* hypothesis, the air will be present in the biggest pores i.e. between an infinite radius (saturated conditions) and r_0 , the ice will be placed between r_0 and r_1 and the water from r_1 to the smallest pores. As visible in Fig.3.5, if $r = \infty$, $p_w = p_a$ and the freezing temperature is equal to the bulk melting temperature $T = T_m \leftarrow 273.15K$. Decreasing the pore radius, the pore water pressure becomes more negative and the freezing temperature is depressed according to Eq. 3.35. Considering $\gamma_{wa} \leftarrow 76E-3$ [N/m] at $0^\circ C$ (Armstrong and Brun, 2008), if the initial pore water pressure in unsaturated conditions is $p_{w0} \leftarrow -100$ [KPa], one obtains that $r_0=1.52$ [μm] and the freezing temperature becomes $T^* \leftarrow -0.008^\circ C$. If the freezing process starts, as $L_f \leftarrow 333.7$ [KJ/Kg] and considering a temperature $T_1 \leftarrow -10^\circ C$, one obtains that the ice is advanced until the pore radius $r_1 \leftarrow 1.23E-2$ [μm].

According to this scheme, one could say that there is an "air region" in the biggest pores, then an "ice region" in the medium pores and finally a "water region" in the smallest pores. This is coherent to Eq. 9 and 10 of Staehli et al. (1996), which hypothesize the existence of two macro regions according to pore radius corresponding the water-ice and ice-air interfaces:

$$r_{wi} = -\frac{2\gamma_{wi}T_m}{\rho_w L_f (T - T_m)} \quad (3.39)$$

$$r_{ia} = \frac{2\gamma_{ia}T_m}{\rho_w g \rho_w (\theta_{init})} \quad (3.40)$$

where θ_{init} is the initial water content at freezing and γ_{ia} is the surface tension of the ice-air interface. Thus, for pores with a radius less than r_{wi} , the pores are filled with unfrozen water, whereas larger pores are ice-filled, or, if they are large enough, air-filled. It follows that, given the total water content, the only variable affecting the amount of ice in the soil is the temperature: a lowering of temperature leads to a decrease in r_{wi} and a raised temperature leads to an increase in r_{wi} . *Thaw-*

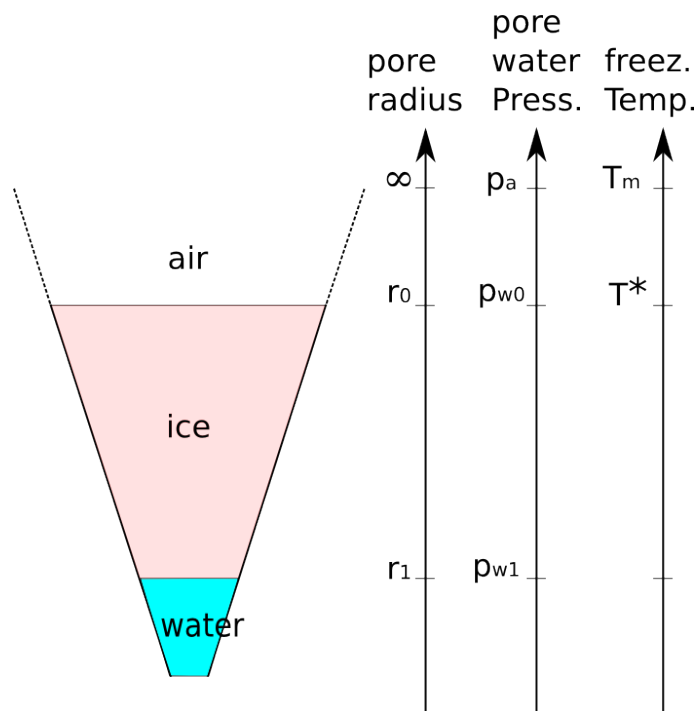


Figure 3.5: Pore radius in relationship with pore water pressure and freezing temperature: decreasing the radius, the pore water pressure becomes more negative and the freezing temperature decreases.

ing of the soil can thus only occur from finer towards coarser pores. They call *lowflow domain* the region where $r < r_{wi}$, since the water in that domain is tightly bound by the solid particles and moves slowly. On the other hand, the *highflow domain* is considered to coincide with the initially air-filled pore region, where $r > r_{ia}$, since it allows rapid conduction of infiltrating water. In the lowflow domain the water is unfrozen due to a low water potential, and it flows slowly according to Darcy's law. In the highflow domain, the air-filled pores allow a rapid water flow based on a unit gravitational flow.

3.6 The soil freezing characteristic curve

The *soil water characteristic curve* (SWC) (or water retention curve) is the relationship between the water content, θ_w , and the soil water potential, ψ and is characteristic for different types of soil. *Brooks and Corey* (1964), *Clapp and Hornberger* (1978), *Gardner* (1958) and *Van Genuchten* (1980) represent the most popular SWC currently used. When ice is present in the soil, heat and water flux are tightly coupled, i.e. ψ and θ_w are strongly dependent on temperature because the ice formation in the pores affects the phases equilibrium. The relation between soil freezing temperatures and unfrozen water content is usually referred to as *soil freezing characteristic curve* (SFC).

3. Freezing soil

In Fig.3.6 an experimental SFC is reported, considering two different types of soils: silty clay (dotted line) and sandy loam (plain line). Decreasing the temperature, the decrease of unfrozen water content depends on the soil type: for coarse grain materials, as sandy loam, the decrease is almost instantaneous, i.e. at -1°C all the water is transformed into ice. For silty clay, on the other hand, even at very negative temperatures part of the water is still unfrozen, thanks to the strong bonds and surface energy of the molecules.

Various are the attempts to derive the SFC. One of the first attempt to study the moisture content of soil samples subject to freezing is the work of *Schofield* (1935). Arguing that a "pressure deficiency" or suction of the soil water is mainly responsible for the observed freezing point depression, he proposed that a relationship exists between the suction at a given moisture content and the temperature at which the water in the soil begins to freeze. *Miller* (1963), studying the equilibrium condition between phase (e.g. water-vapor, air-water and ice-water), formulates an analogy between air-water and the ice-water case and suggests that a soil freezing characteristic, i.e. a relation between soil liquid water content and pressure conceptually measured inside the pores, may be hypothesized that resembles the soil water characteristic in unfrozen unsaturated soils. *Williams* (1964) plots the experimental results of suction ψ [m] and temperature [$^{\circ}\text{K}$], and finds that the values have a good agreement with the relationship $\psi = L_f \Delta T / (g T)$, and reports in favor of the simple interpretation of the physical facts based on capillarity presented in this dissertation. demonstrated that for certain soils the SWCC and SFC are similar. They also point out the advantages of using SFC to determine water retention properties at low matric potentials, and that for certain soils the water characteristic curve is not significantly affected by temperature. They assumed the same pressure difference between unfrozen water-ice interfaces and water-air interfaces, i.e. under these assumptions the SFC can be estimated from the SWC. *Guymon and Luthin* (1974) also assume the similarity between freezing and unsaturated soils, and propose to use the soil characteristic curve and Clausius-Clapeyron equation to infer the relative proportion of ice.

Flerchinger et al. (2006) illustrate an approach to derive the SFC from in situ measurements of unfrozen water content with time-domain reflectometry (TDR), and to deduce the SWC from the SFC for simulation of both frozen and unfrozen soils. They advise that the SFC can be used if the soil is sufficiently wet to allow water to freeze. In fact, if the soil is too dry, the soil water potential is below the equilibrium potential (see Eq. 3.31) and therefore water will not freeze. Furthermore, for soils too wet, the osmotic potential becomes a relatively larger component of the total water potential and therefore the SFC may have limitation. The results of *Watanabe* (2008) highlight the existence of water flow both in the frozen and unfrozen area, and confirm that SWC can be applied as the SFC in the numerical simulation.

The SFC can be derived by imposing a relation between θ_w and T . This is usually done by

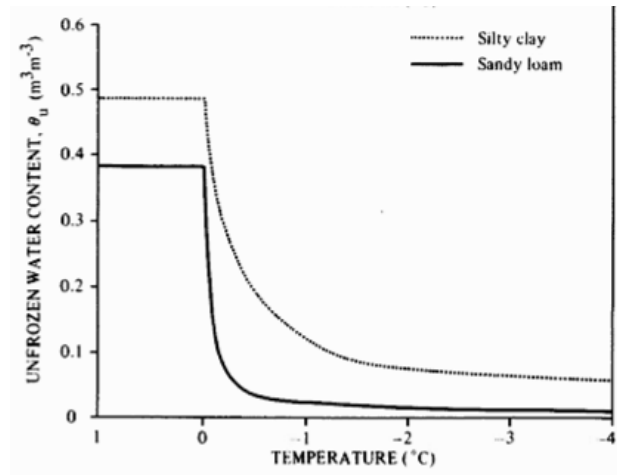


Figure 3.6: Unfrozen water and temperature relationship for two different soil textures. Picture taken from Williams and Smith (1989)

relating the soil pressure head $\psi := p_w / (\rho_w g)$ [m], with T , usually through the Clapeyron relation. Then the SWC allows to find the relation $\theta_w = \theta_w(\psi)$. Finally one can derive the SFC by imposing $\theta_w = \theta_w(\psi(T))$.

Luo *et al.* (2009) and Niu and Yang (2006) model the SFC using the Clapp and Hornberger (1978) model for the water-suction relation and the Clapeyron equation to relate suction-temperature relation. They obtain:

$$\theta_w^{max} = \theta_s \cdot \left(\frac{L_f(T - T_m)}{g T \psi_{sat}} \right)^{-1/b} \quad (3.41)$$

where ψ_{sat} is the “saturation” suction and b a calibration parameter. Zhang *et al.* (2007) propose a suction-water content relation based on Clapp and Hornberger (1978) with the correction for the ice effect (Koren *et al.*, 1999):

$$\theta_w = \theta_s \cdot \left(\frac{L_f(T - T_m)}{g T \psi_{sat}} \right)^{-1/b} \cdot (1 + C_k \theta_i)^2 \quad (3.42)$$

where C_k represents the effect of soil specific surface on matric potential due to the presence of ice. Koren *et al.* (1999) proposes a value of 8 for C_k . Shoop and Bigl (1997) use the Gardner (1958) formulation for the water-suction relationship as:

$$\theta_w = \frac{\theta_s}{A_w |\psi|^{\alpha + 1}} \quad (3.43)$$

where A_w is the Gardner’s multiplier of the moisture characteristics and α is the Gardner’s exponent for the moisture characteristics. McKenzie *et al.* (2007) parametrize directly the SFC as

$\theta_w = \theta_w(T)$ with a linear or exponential function and no specification is given about the coupling between the water content and soil water pressure.

3.6.1 The Van Genuchten based SFC

The *Van Genuchten* (1980) formulation of the SWC is defined as:

$$\theta_w = f_{VG}(\psi) = \theta_r + (\theta_s - \theta_r) \cdot \{1 + [-\alpha(\psi)]^n\}^{-m} \quad (3.44)$$

where θ_r is the adimensional residual and θ_s is the saturated water content, i.e. the soil porosity. α [m^{-1}], m [-] and n [-] are fitting parameters reflecting the inverse of the air entry point and the grain size distribution respectively. Usually one puts $m=1-1/n$ in order to get rid of one parameter. As well as the saturated hydraulic conductivity, α and n , can be derived from the soil texture through the Pedotransfer Functions (PTFs) (*Vereecken et al.*, 1989 and *Schaap et al.*, 2001) or measured (sampled) in sites. One knows that the pressure p_{w0} , according to the capillary conceptualization, indicates the maximum pore radius r_0 where the water (be it liquid or solid) is present. When the freezing process sets in, the water pressure p_{w1} becomes a function of the temperature T (see Eq. 3.32) and indicates the new pore radius $r_1 < r_0$ where the liquid water content is present. Therefore one could state that $\psi_{w1} = f(\psi_{w0}, T)$:

$$\psi_{w1} = \psi_{w0} + \frac{L_f}{g T_0} (T - T^*) \cdot H(T - T^*) \quad (3.45)$$

where H is the Heaviside function. According to 3.44 one can calculate the total water content (liquid and solid) present in a capillary:

$$\Theta = f_{VG}(\psi_{w0}) \quad (3.46)$$

Θ is independent on temperature and is linked just to the infiltration/evaporation cycles in the soil. At the same manner, when the freezing process sets in, the new liquid water content becomes:

$$\theta_w = f_{VG}(\psi_{w1}) \quad (3.47)$$

Substituting Eq. 3.45 in ψ_{w1} one obtains:

$$\theta_w = \theta_r + (\theta_s - \theta_r) \cdot \left\{ 1 + \left[-\alpha \psi_{w0} - \alpha \frac{L_f}{g T_0} (T - T^*) \cdot H(T - T^*) \right]^n \right\}^{-m} \quad (3.48)$$

which represents the equation for the SFC. The difference between the water content at ψ_{w0} and ψ_{w1} is the water subject to phase change. Therefore one can derive the relationship for the ice

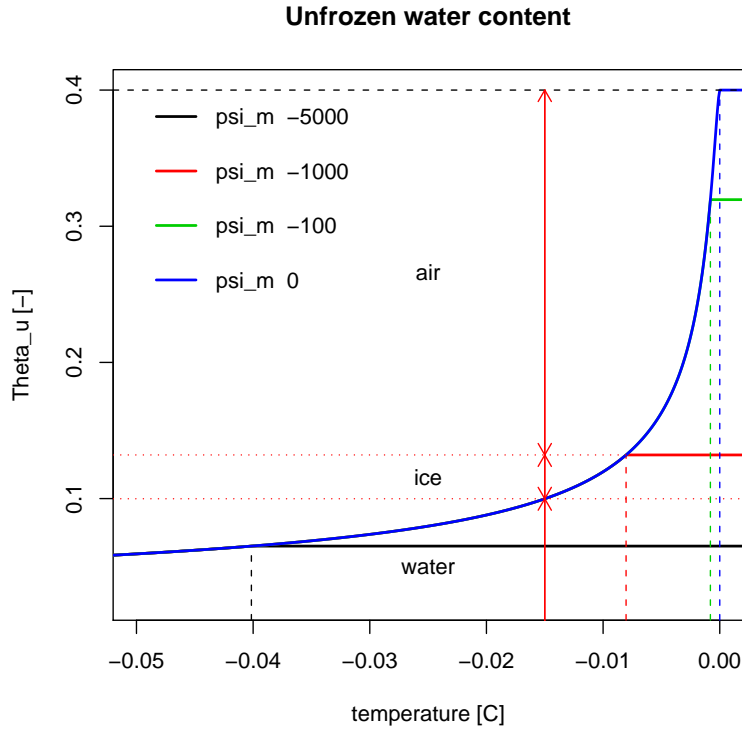


Figure 3.7: SFC according to Van Genuchten model: under the curve just liquid water is allowed, over the curve ice is allowed until the maximum value given by ψ_{m0} , over which only air is allowed. The vertical dotted line represent $T^*(\psi_m)$ at various saturation content. In this plot $\theta_s = 0.4$

content:

$$\theta_i = \frac{\rho_w}{\rho_i} (\Theta - \theta_w) = \frac{\rho_w}{\rho_i} (f_{VG}(\psi_0) - f_{VG}(\psi_1)) \quad (3.49)$$

Combining Eq. 3.46, 3.47 and 3.49 one can obtain the liquid and solid water content in a pore, given the unsaturated water pressure p_{w0} and the negative temperature T_1 responsible for p_{w1} . The process of freezing in a soil can be visualized in Fig.3.7. Looking at the y coordinate of the plot, representing θ_w , one can isolate three regions:

- $\theta_w < \theta_r$: perennial unfrozen water region because of the strong bonding of the unfrozen water with the soil skeleton (common for very fine grain soils);
- $\theta_r < \theta_w \leq \theta_w(\psi_{m0}, T_1)$: unfrozen water region;
- $\theta_w(\psi_{m0}, T_1) < \theta_w \leq \Theta$: frozen region;
- $\Theta < \theta_w \leq \theta_s$: air region;

3. Freezing soil

- $\theta_w > \theta_s$: soil region.

Therefore one obtains several *Soil Freezing Characteristic Curves* (SFC): $\theta_w = \theta_w(T)|_{\psi_{m0}}$ that represent the allowed unfrozen water content at a given ψ_{m0} as a function of temperature. The colder it gets, the lower the allowed water content at the equilibrium. At $T = T_m$ the water content reaches the maximum allowed water content given by the porosity θ_s .

The freezing process may then be visualized through the use of the SFC as in Fig. 3.8. At the top left an unsaturated unfrozen soil is depicted. Then the temperature decreases, and the ice forms in the bigger pores (top right), then the ice advances (bottom left) until the residual water content is reached that will never freeze (bottom right).

From Eq. 3.48 it is evident that, under the assumption *freezing=drying* and the capillary representation, the unfrozen water and ice content are a function of:

- the porosity θ_s of the material;
- the type of the SWC representation, and so the parameters α and n and θ_r according to the *Van Genuchten* (1980) model;
- the total water content at the onset of freezing given by ψ_{w0} ;
- the temperature decrement $T - T^*$ when $T < T^*$.

The combined effect of temperature and ψ_{w0} is well summarized in Fig. 3.9, where on the x axis is reported the variation of the total water content ψ_{w0} , on the y axis the variation of temperature, and the colors represent the ratio θ_w/θ_s (top) and θ_i/θ_s (bottom). It is apparent that at positive temperatures the water content decreases slowly with ψ_{w0} according to the SWC, whereas at negative temperatures the decrease is very quick due to the freezing process that rapidly decreases ψ_{w1} . The ice content (bottom figure) is the difference between the total water content given by ψ_{w0} and the unfrozen water content. The same process is described in Fig.3.10.

It is also possible to visualize a 3D plot of the unfrozen water content as a function of ψ_{m0} and T as depicted in Fig. 3.11. The red surface therefore represents the maximum unfrozen water content given a certain temperature and an initial water suction ψ_{m0} . If we plotted the total water content Θ we could derive also the ice content as the difference between the two surfaces. This is done in Fig. 3.11 where the total water content $\Theta = \Theta(\psi_{m0})$ is represented by the blue surface. The blue line represents the SWC, i.e. the relation $\theta_w = \theta_w(\psi_{m0})$ independent on temperature; the red line represent the SFC at saturation level, i.e. the relation $\theta_w = \theta_w(\psi_{m0} = 0, T)$.

The influence of the parameters α and n on the SFC are reported in Fig. 3.12. One can notice that, given ψ_{w0} , the liquid water content decreases sharply with increasing α . As visible in table 3.2, given $\psi_{w0} = -1000$ [mm], the liquid water content depends strongly on the van genuchten

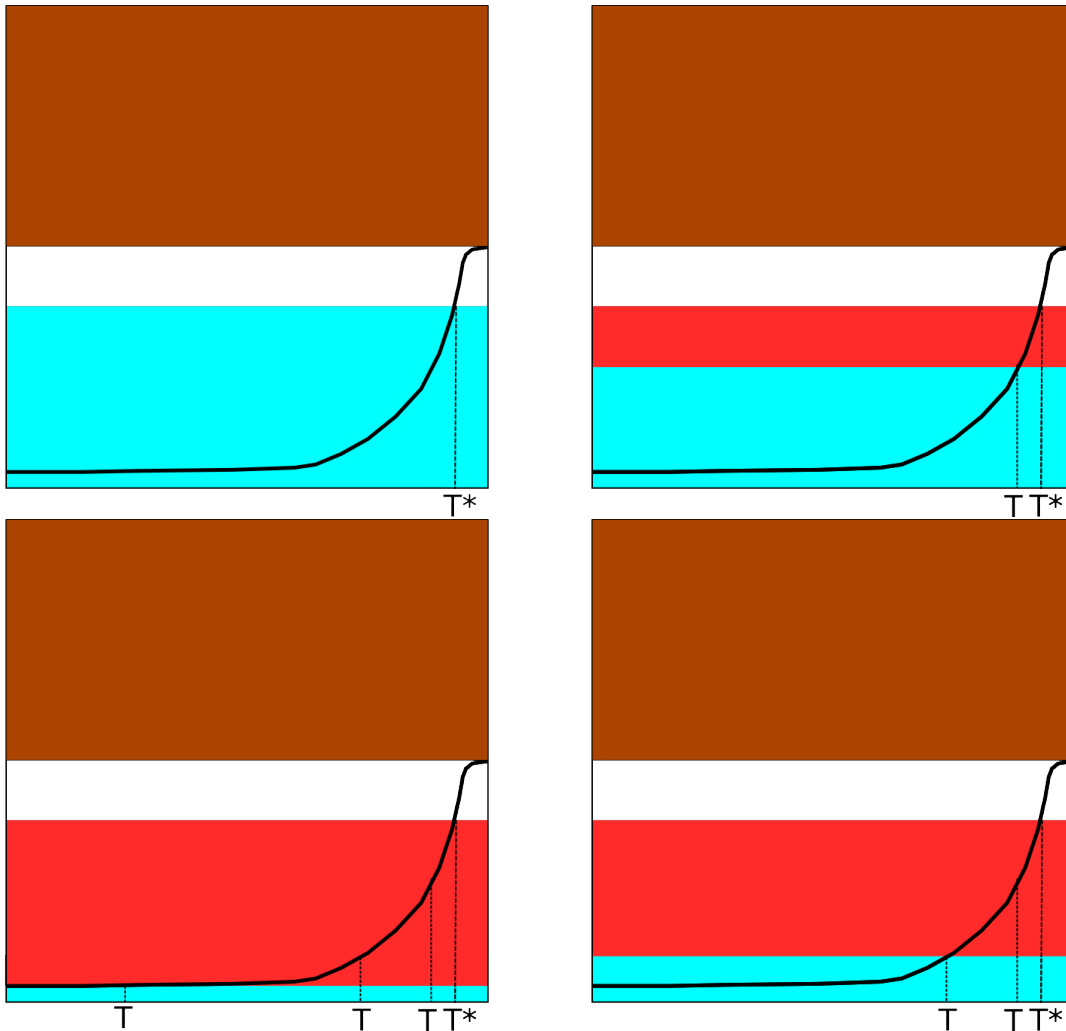


Figure 3.8: Freezing process schematized using the SFC (black line). On the x axis is the temperature, on the y axis is θ_w . Top left: unsaturated unfrozen soil. top right: the freezing process begins when $T < T^*$; bottom right: freezing process in an advanced state; bottom left: end of the freezing process when $\theta_w = \theta_r$

3. Freezing soil

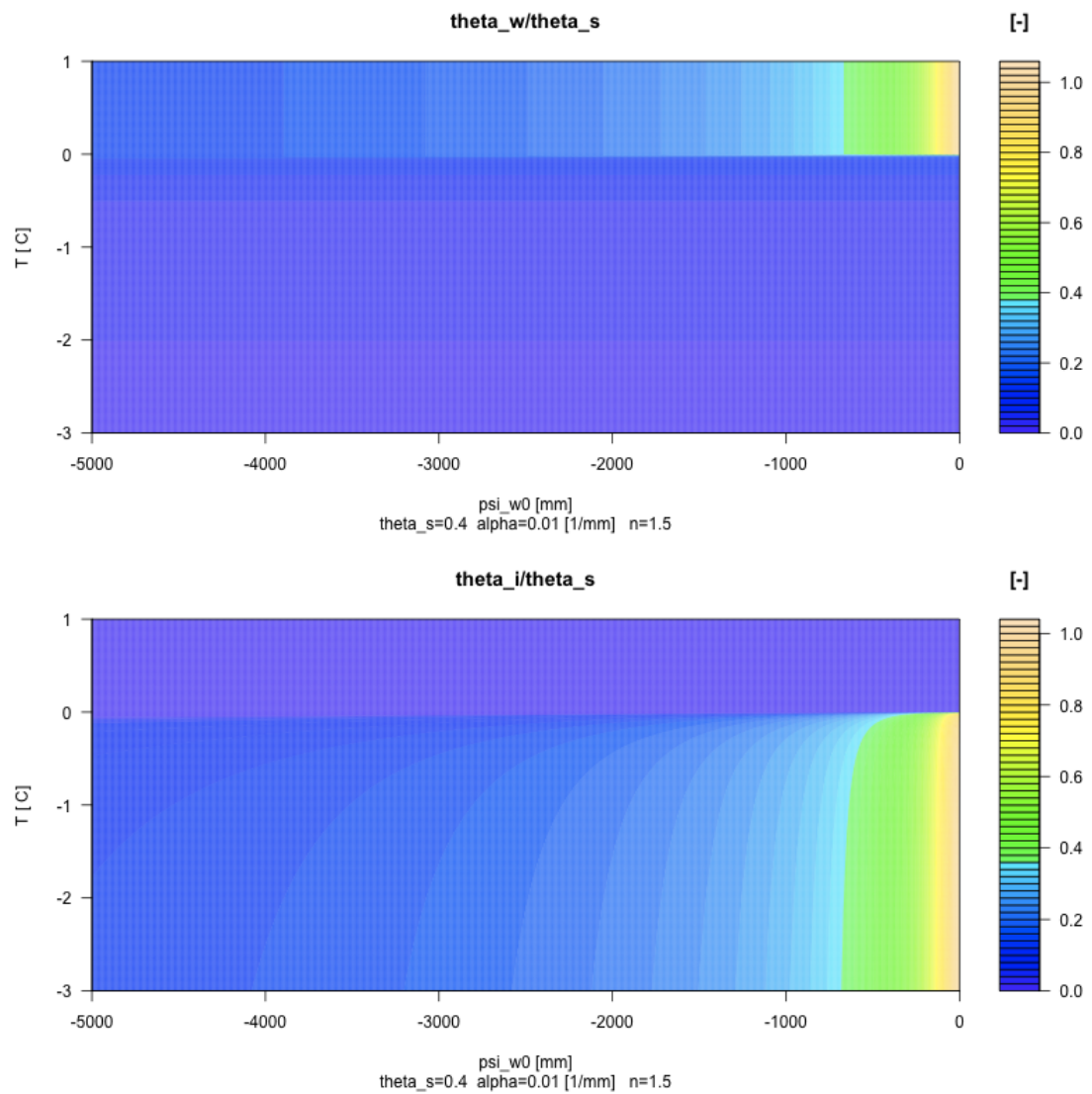


Figure 3.9: Combined effect of T and ψ_{w0} on liquid water content (top) and ice content (bottom). The colors represent the ratio θ_w/θ_s and θ_i/θ_s respectively to get rid of the porosity effect

parameters and on the temperature. Depending on the combination (α, n) , the ratio θ_w/θ_s may vary of 4 orders of magnitude for positive temperatures, and of 8 orders of magnitude at $T = -2$ °C.

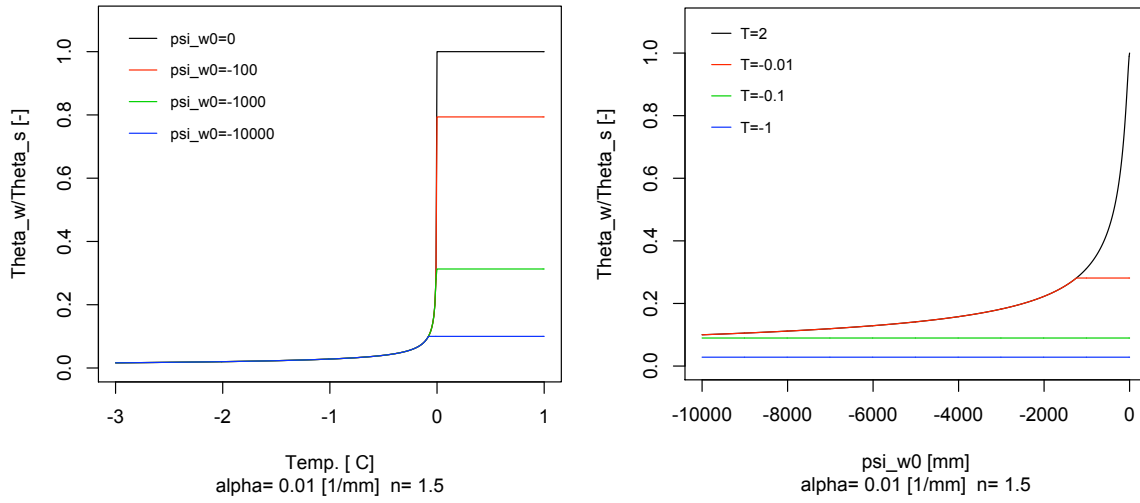


Figure 3.10: Effect of T on water content at various ψ_{w0} level (left); effect of ψ_{w0} on water content at various T (right)

$T > 0$				
$\alpha [mm^{-1}]$				
n	0.001	0.01	0.1	0.4
1.1	0.939	0.789	0.631	0.549
1.5	0.794	0.313	0.099	0.049
2.0	0.707	0.099	0.009	0.002
2.5	0.659	0.032	0.001	1.2E-4

$T = -2^\circ C$				
$\alpha [mm^{-1}]$				
n	0.001	0.01	0.1	0.4
1.1	0.576	0.457	0.363	0.316
1.5	0.063	0.020	0.006	0.003
2.0	4E-3	4E-4	4E-5	1E-5
2.5	2.5E-4	8E-6	2.5E-7	3.2E-8

Table 3.2: Ratio θ_w/θ_s at $\psi_{w0} = -1000 [mm]$ for positive temperatures (top) and at $T = -2^\circ C$ (bottom) as function the combination (α, n) In the calculation θ_r was set to 0.

3.7 Conclusions

In this section the theory of freezing soil has been revisited, on the basis of the thermodynamic equilibrium relations derived in the previous section. The assumption *freezing=drying* (Miller,

1963) is often used in literature. This hypothesis allows to represent the freezing process as a desaturation process and thus to schematize the soil as a capillary tube. It is thus possible to derive the thermodynamic equilibrium for curved interfaces, and, thanks to the Gibbs-Duhem equation, derive the equilibrium relation between water and ice. This is often called generalized Clapeyron equation. However, the *freezing=drying* relations implies that:

- the pressure at the ice-water interface is equal to the air-water interface $p_{iw}(r) = p_{wa}(r)$;
- the pressure at the ice-air interface $p_{ia}(r) \leftarrow 0$;
- $p_i = p_a \leftarrow 0$.

Thanks to these simplifications, $dp_i = 0$ and so, from the Gibbs-Duhem equation, it is possible to derive the generalized Clapeyron equation for the equilibrium between the ice and water phase where the term related to the pressure of ice is absent. A freezing suction ψ_{freez} may be defined, as the negative pressure due to negative temperature T . This suction is added to the negative pressure $\psi_{w,0}$ due to the saturation degree and gives the total suction of the water phase. The values of ice and water content in the ground can be derived by the the soil water retention curve and are very sensitive to the shape of the curve. According to the Van Genuchten model, results show that different combinations of α and n may result in a variation of the liquid water content of more then eight orders of magnitude. The limitation of the *freezing=drying* assumption is that phenomena like frost heave cannot be modeled. In this case, a more complete approach should be used (Rempel *et al.* 2004, Rempel, 2007). A interesting contribution on this side is given by Christoffersen and Tulaczyk (2003), who propose a formulation of the equilibrium relation without assuming $p_i = 0$. A further step could be to account for non-equilibrium interphase mass and heat transfer (Niessner and Hassanizadeh, 2009).

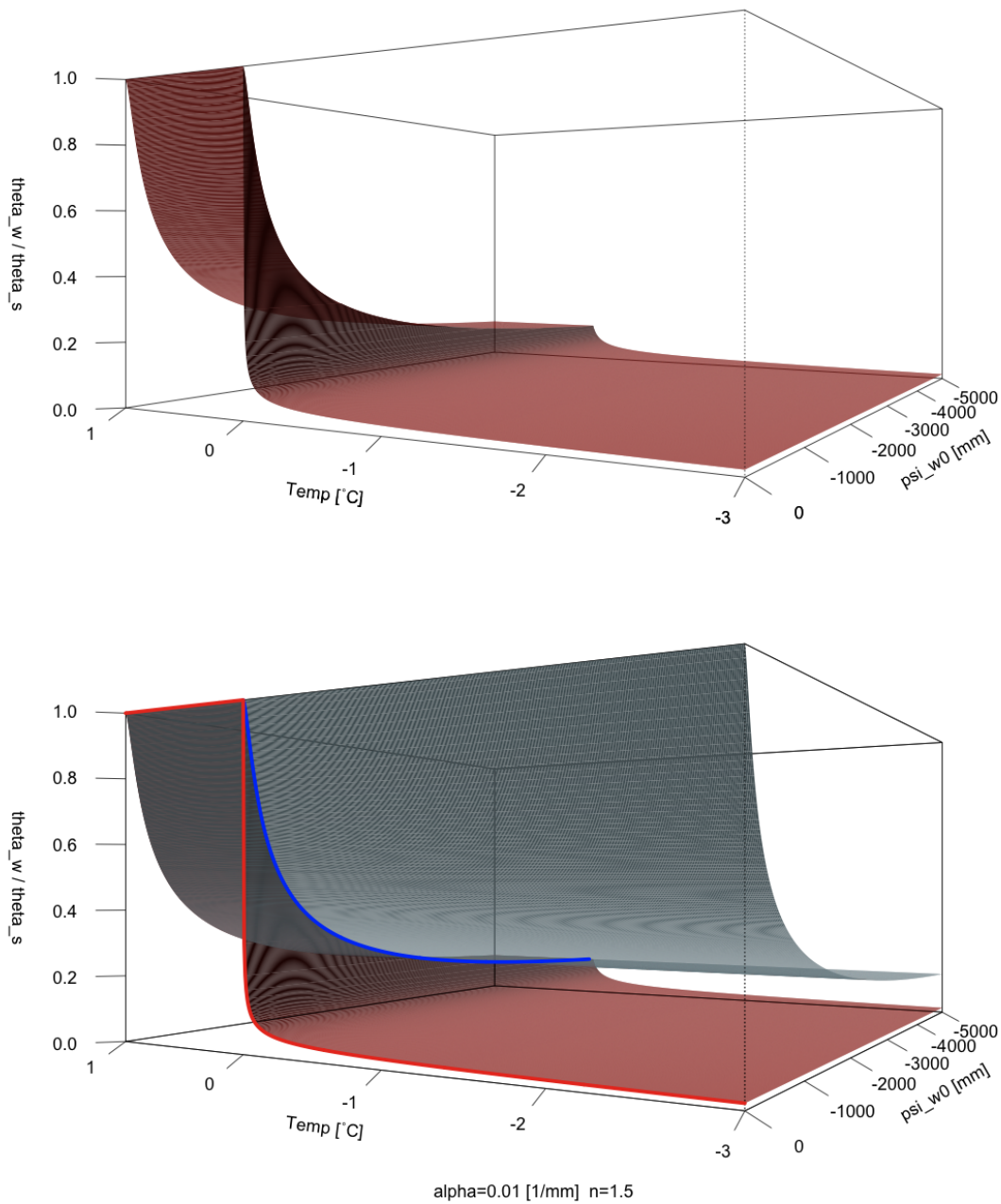


Figure 3.11: Top: the red surface represents the ratio $\frac{\theta_w}{\theta_s}$ at different temperatures and various total water content given by Ψ_{w0} . Bottom: the blue surface represents the total (liquid + solid) water content admitted by Ψ_{w0} , i.e. the upper boundary of the liquid water. Among the surfaces lies the ice region. Red line: SFC at complete saturation, i.e. when $\Psi_{w0} = 0$. Blue line: SWC at positive temperatures

3. Freezing soil

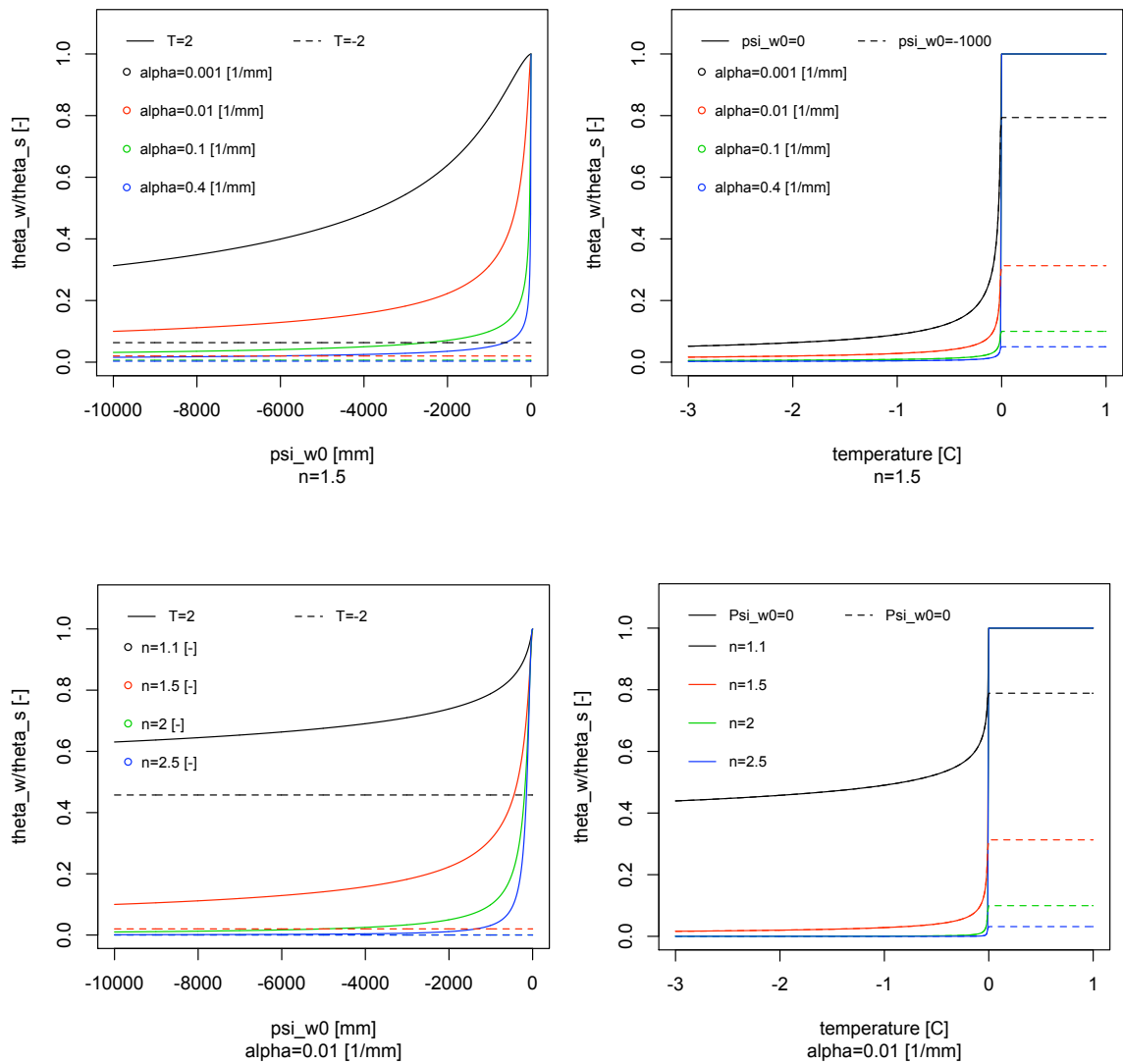


Figure 3.12: Influence of Van Genuchten parameters α and n on liquid water content according to the SFC. Top left: influence of ψ_{w0} at different α . Top right: influence of temperatures at different α . Bottom left: influence of ψ_{w0} at various n and Bottom right: influence of T at various α . Plain line: positive temperatures; dotted line: negative temperatures

4 Mass and heat conservation

4.1 Introduction

This section is intended to give an overview on the equations for the heat and mass conservation that must be applied to a hypothetical soil/rock volume. The mass conservation involves phase change and the water fluxes due to infiltration. The heat conservation includes phase change, conduction and convection of heat. The two equations will be thoroughly developed directly from the continuity equation and the conservation of total mass and internal energy.

4.2 The volume conservation

Frozen soil is a multiphase, complex material which generally is a composite of four different constituents: (i) solid grains (mineral particles, organic or both), (ii) ice, of different grain size and orientation (*Pihlainen and Johnston, 1963*), (iii) unfrozen water (*Williams, 1967*), and (iv) gas or air. A soil schematization is reported in Fig. 4.1) and the notation is summarized in table 4.1. Given a rigid control volume V_c [m^3], the volume conservation requires:

$$V_g + V_{voids} = V_c \quad (4.1)$$

where the voids space is composed by ice, water and air:

$$V_i + V_w + V_a = V_{voids} \quad (4.2)$$

The water in soil is subject to phase change, if the temperature is below the melting point, and to infiltration/evaporation or draining processes, according to the hydraulic and geometric gradient. We can thus ideally think that a volume of water V_w [m^3] in a time interval is composed by:

$$V_w := V_{w0} + \Delta V_w^{ph} + \Delta V_w^{fl} \quad (4.3)$$

where V_{w0} is the initial volume of water at the beginning of the interval, ΔV_w^{ph} is the volume of

4. Mass and heat conservation

Symbol	Name	Unit	Symbol	Name	Unit
V_c	ground control volume	[L ³]	M_c	ground mass	[Kg]
V_a	volume of air gas	[L ³]	M_a	air mass	[Kg]
V_w	volume of water	[L ³]	M_w	water mass	[Kg]
V_i	volume of ice	[L ³]	M_i	ice mass	[Kg]
V_g	volume of ground particle	[L ³]	M_g	ground particle mass	[Kg]

Table 4.1: Notation of mass and volume in the soil/rock schematization

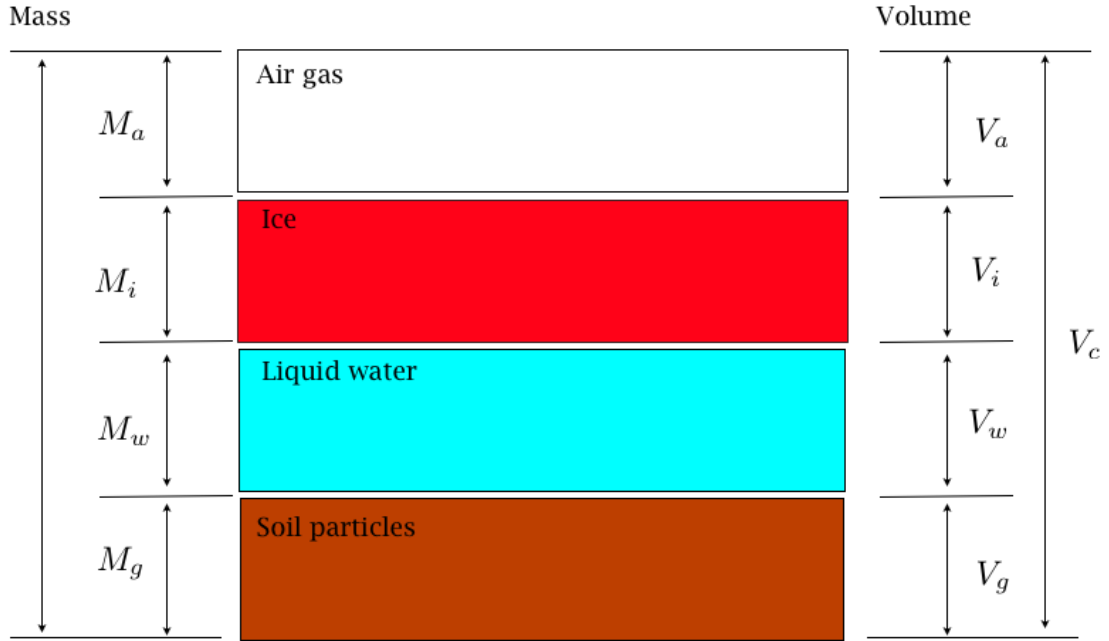


Figure 4.1: Frozen soil constituents and schematization of the control volume V_c (Phukan, 1985)

water subject to phase change during the time interval, and ΔV_w^{fl} is the volume of water subject to variation due to fluxes during the time interval. At the same manner, the volume of ice V_i [m³] may be defined as:

$$V_i := V_{i0} + \Delta V_i^{ph} \quad (4.4)$$

where V_{i0} is the initial volume of ice, ΔV_i^{ph} and is the volume of ice subject to phase change. Notice that we put $\Delta V_i^{fl} \equiv 0$ as ice fluxes are not considered.

Let us define:

$$V_{tot} := V_w + V_i = V_{w0} + V_{i0} + \Delta V_w^{ph} + \Delta V_i^{ph} + \Delta V_w^{fl} \quad (4.5)$$

as the volume of all the water content in the soil, both in liquid and solid state. Let us furthermore

define:

$$\theta_{w0} := \frac{V_{w0}}{V_c} \quad \theta_{i0} := \frac{V_{i0}}{V_c} \quad \Delta\theta_w^{ph} := \frac{\Delta V_w^{ph}}{V_c} \quad \Delta\theta_i^{ph} := \frac{\Delta V_i^{ph}}{V_c} \quad \Delta\theta_w^{fl} := \frac{\Delta V_w^{fl}}{V_c} \quad \Delta\theta_a := \frac{\Delta V_a}{V_c} \quad (4.6)$$

as the volumetric variables. One obtains:

$$\frac{V_{tot}}{V_c} := \Theta = \theta_{w0} + \theta_{i0} + \Delta\theta_w^{ph} + \Delta\theta_i^{ph} + \Delta\theta_w^{fl} \quad (4.7)$$

and:

$$0 \leq \theta_r \leq \Theta \leq \theta_s \leq 1 \quad (4.8)$$

In the rigid soil schematization the porosity is constant and the total water contents allowed to change respecting that upper limit given by the porosity and the residual water content.

At the same manner as was done for the volume, one can define the mass of water M_w [Kg] as:

$$M_w := M_{w0} + \Delta M_w^{ph} + \Delta M_w^{fl} \quad (4.9)$$

where M_{w0} is the initial mass of water, M_w^{ph} is the mass of water subject to phase change and M_w^{fl} is the mass of water subject to variation due to fluxes. At the same manner, the mass of ice M_i [Kg] becomes:

$$M_i := M_{i0} + \Delta M_i^{ph} \quad (4.10)$$

where M_{i0} is the initial mass of ice, and ΔM_i^{ph} is the mass of ice subject to phase change. Notice again that $\Delta M_i^{fl} \equiv 0$ as ice fluxes are not considered. For the mass conservation during phase change, it must be:

$$\Delta M_w^{ph} + \Delta M_i^{ph} = 0 \quad (4.11)$$

The above statement, written with densities and volumes, becomes:

$$\rho_w \Delta V_w^{ph} + \rho_i \Delta V_i^{ph} = 0 \quad \text{or, dividing by } V_c: \quad \rho_w \Delta\theta_w^{ph} + \rho_i \Delta\theta_i^{ph} = 0 \quad (4.12)$$

Substituting Eq. 4.12 in 4.8 after simple calculations one obtains:

$$\rho_w \theta_r \leq \rho_w \theta_{w0} + \rho_w \Delta\theta_w^{fl} + \rho_i \theta_{i0} + (\rho_w - \rho_i) \Delta\theta_i^{ph} \leq \rho_w \theta_s \quad (4.13)$$

From the above equation and Eq. 4.8 derive the upper and lower limit of $\Delta\theta_w^{fl}$:

$$\theta_r - \left[\theta_{w0} + \theta_{i0} + \left(1 - \frac{\rho_i}{\rho_w} \right) \Delta\theta_i^{ph} \right] \leq \Delta\theta_w^{fl} \leq \theta_s - \left[\theta_{w0} + \theta_{i0} + \left(1 - \frac{\rho_i}{\rho_w} \right) \Delta\theta_i^{ph} \right] \quad (4.14)$$

This statement means that the drainage of water in a Δt is restricted by the value of the available pore space, which is given by the initial water and ice content and the rate of freezing/thawing.

4.3 Mass conservation

The mass conservation in a soil volume may be written as:

$$\frac{\partial M_w^{fl}}{\partial t} + \frac{\partial M_w^{ph}}{\partial t} + \frac{\partial M_i^{ph}}{\partial t} + \rho_w V_c \vec{\nabla} \bullet \vec{J}_w + \rho_w V_c S_w = 0 \quad [\text{Kg s}^{-1}] \quad (4.15)$$

or, stated differently:

$$\rho_w \frac{\partial V_w^{fl}}{\partial t} + \rho_w \frac{\partial V_w^{ph}}{\partial t} + \rho_i \frac{\partial V_i^{ph}}{\partial t} + \rho_w V_c \vec{\nabla} \bullet \vec{J}_w + \rho_w V_c S_w = 0 \quad [\text{Kg s}^{-1}] \quad (4.16)$$

where S_w [s^{-1}] a sink term due to evapotranspiration. \vec{J}_w [m s^{-1}] is the water flux within the soil and follows the Darcy-Buckingham formulation:

$$\vec{J}_w = \vec{J}_w(\psi_{w1}) = -K_H \vec{\nabla}(\psi_{w1} + z_f) \quad [\text{m s}^{-1}] \quad (4.17)$$

$K_H = K_H(\psi_{w1})$ [m/s] is the hydraulic conductivity, and z_f is the elevation with respect to a reference elevation and represents the gravitational head. Therefore one observes that $\vec{J}_w = \vec{J}_w(\psi_{w0}, T)$. Notice that is the ice flux \vec{J}_i [m s^{-1}] within the soil is not present. Dividing by V_c one gets:

$$\rho_w \frac{\partial \theta_w^{fl}}{\partial t} + \rho_w \frac{\partial \theta_w^{ph}}{\partial t} + \rho_i \frac{\partial \theta_i^{ph}}{\partial t} + \rho_w \vec{\nabla} \bullet \vec{J}_w + \rho_w S_w = 0 \quad [\text{Kg m}^{-3} \text{s}^{-1}] \quad (4.18)$$

Considering Eq. 4.12 the terms related to phase change vanish, therefore one gets:

$$\rho_w \frac{\partial \theta_w^{fl}(\psi_{w1})}{\partial t} + \rho_w \vec{\nabla} \bullet \vec{J}_w + \rho_w S_w = 0 \quad [\text{Kg m}^{-3} \text{s}^{-1}] \quad (4.19)$$

Eventually the mass conservation becomes:

$$\frac{\partial}{\partial t} \left[\theta_w^{fl}(\psi_{w1}) \right] - \vec{\nabla} \bullet \left(K_H \vec{\nabla} \psi_{w1} + K_H \vec{\nabla} z_f \right) + S_w = 0 \quad [\text{s}^{-1}] \quad (4.20)$$

which is also called Richards equation (*Richards, 1931*).

4.4 The internal energy

The internal energy U referred to the the volume V_c may be written as:

$$U = U_g(T, M_g) + U_i(\Psi_{w0}, T, M_i) + U_w(\Psi_{w0}, T, M_w) \quad [\text{J}] \quad (4.21)$$

where U_g , U_w and U_i are the internal energies [J] of ground particle, water and ice respectively referred to the temperature reference $T_{ref} = 0^\circ\text{C}$. In particular:

$$\begin{cases} U_i(\Psi_{w0}, T, M_w) = TS_i - p_i V_i + \mu_i M_i^{ph} \\ U_w(\Psi_{w0}, T, M_i) = TS_w - p_w V_w + \mu_w M_w^{ph} \end{cases} \quad (4.22)$$

At equilibrium (see Eq. 2.74) one knows that $TS = H$ and $\mu_w = \mu_i$. As far as the internal energy of the ground soil U_g is concerned, the terms referring to the pressure and chemical potential may be neglected; thus $U_g(T) \approx TS_g = H_g$. Therefore Eq. 4.21 becomes:

$$U = H_g + h_w M_w + h_i M_i - (p_w V_w + p_i V_i) + \mu_w M_w^{ph} + \mu_i M_i^{ph} \quad (4.23)$$

This equation may be simplified by noting that:

- at equilibrium $\mu_w = \mu_i$;
- the mass of water and ice subject to phase change are linked by the relation 4.11:

$$M_w^{ph} = -M_i^{ph} \quad (4.24)$$

or stated differently:

$$\rho_w dV_w^{ph} = -\rho_i dV_i^{ph} \quad (4.25)$$

- the assumption “*freezing=drying*” (Eq. 3.24) implies that $p_i = p_a \leftarrow 0$. Thanks to this assumption the work $p_i dV_i \equiv 0$.
- the “rigid volume” scheme implies that the control volume V_c and the volume of soil particles V_g are constant. Following Eq. 4.5 and 4.2 one obtains:

$$dV_{tot} + dV_a = dV_w^{ph} + dV_i^{ph} + dV_w^{fl} + dV_a = 0 \quad (4.26)$$

- Assuming that, during phase change, there is no volume variation due to water flux ($dV_w^{fl} = 0$) one obtains:

$$dV_w^{ph} + dV_i^{ph} + dV_{air} = 0 \quad (4.27)$$

4. Mass and heat conservation

Recalling Eq.4.12 the above becomes:

$$\left(1 - \frac{\rho_w}{\rho_i}\right) dV_w^{ph} + dV_{air} = 0 \quad (4.28)$$

If we assume $\rho_w = \rho_i$, Eq. 4.28 turns in:

$$dV_{air} = 0 \quad \text{and} \quad dV_w^{ph} = 0 \quad (4.29)$$

and consequently:

$$dV_w = 0 \quad (4.30)$$

Thanks to this assumption the work $p_w dV_w \equiv 0$.

- the enthalpy of water and ice may be calculated by integrating Eq. 2.58 in temperature:

$$\int h_w dT = h_{w0} + c_w(T - T_0) \quad ; \quad \int h_i dT = h_{i0} + c_i(T - T_0) \quad (4.31)$$

where c_w and c_i are the specific heat capacities of water and ice respectively; h_{w0} and h_{i0} are arbitrary constants under the assumption that the difference:

$$L_f := h_{w0} - h_{i0} \quad (4.32)$$

equals the latent heat of fusion of water L_f . We choose to put as a reference $h_{i0} = 0$ and $T_0 = 0^\circ\text{C}$. Eventually the enthalpies of water and ice become:

$$H_w = L_f M_w + c_w M_w T = L_f \rho_w V_w + \rho_w c_w V_w T \quad (4.33)$$

$$H_i = c_i M_i T = \rho_i c_i V_i T \quad (4.34)$$

Applying the assumptions above specified, eventually Eq. 4.23 becomes:

$$U = \rho_g c_g V_g T + (L_f + c_w T) \rho_w V_w + \rho_i c_i V_i T \quad (4.35)$$

Dividing by the control volume V_c :

$$U = C_g (1 - \theta_s) T + \rho_w c_w \theta_w T + \rho_i c_i \theta_i T + \rho_w L_f \theta_w \quad [\text{J m}^{-3}] \quad (4.36)$$

where $C_g = \rho_g c_g$ [$\text{J m}^{-3} \text{K}$] is the volumetric heat capacity of soil particles, c_i and c_w are the mass heat capacity of ice and water (2117 and 4188 [$\text{J Kg}^{-1} \text{K}^{-1}$] respectively), L_f is the latent heat of freezing (approximately $3.34 \cdot 10^5$ [J Kg^{-1}]), and ρ_i and ρ_w the densities of ice and water

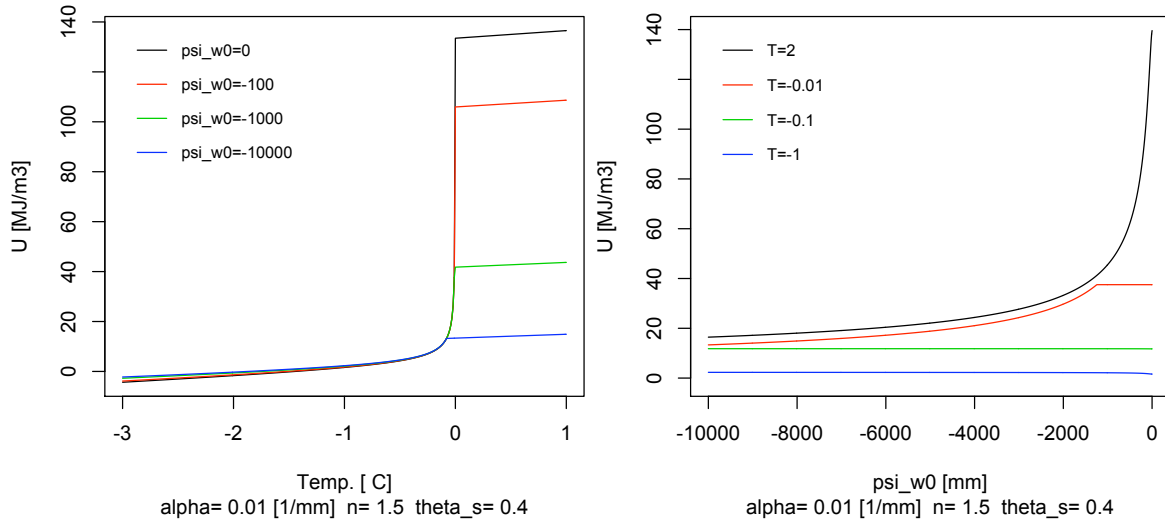


Figure 4.2: Internal energy U as function of temperature (left) and ψ_{w0} (right). In the calculations $T_{ref} := 0^\circ\text{C}$

respectively. Let us define the thermal conductivity of soil as (Farouki, 1981):

$$C_T := C_{gs}(1 - \theta_s) + \rho_w c_w \theta_w + \rho_i c_i \theta_i \quad (4.37)$$

Eq. 4.36 can be written in a more compact term:

$$U = C_T T + \rho_w L_f \theta_w \quad (4.38)$$

The internal energy, therefore, is a function of (ψ_{w0}, T) and may be seen as the sum of two components: $C_T T$ which is the sensible part responsible of the temperature variation of the volume, and $\rho_w L_f \theta_w$ which is the potential part due to the phase change. As visible in Fig. 4.2 on the left, it increases linearly with temperature until the melting point, where there is a sudden increase due to the latent heat effect, then it increases linearly again for positive temperatures. The slope of the line is equal to $\rho_i c_i$ and $\rho_w c_w$ for negative and positive temperatures respectively. On the right is reported the influence of the total water content. It is evident that, increasing the water content, also the internal energy increases.

4.5 Heat conservation

The heat conservation in a control volume may be described as:

$$\frac{\partial U}{\partial t} + \vec{\nabla} \bullet (\vec{G} + \vec{J}) + S_{en} = 0 \quad [\text{J m}^{-3}] \quad (4.39)$$

- \vec{G} is the conduction flux within the soil which, according to Fourier's law, may be written as:

$$\vec{G} = -\lambda_T(\Psi_{w0}, T) \cdot \vec{\nabla} T \quad [\text{W m}^{-2}] \quad (4.40)$$

where λ_T [$\text{W m}^{-1} \text{K}^{-1}$] represents the total thermal conductivity of the soil matrix and depends on the saturation degree and temperature (see section 5.6).

- \vec{J} is the advection heat flux given by the heat transported by water flow. It is calculated by the product between the density of water ρ_w , the water flux \vec{J}_w and the mass unitary internal energy of water $u_w = L_f + c_w T$ [J Kg^{-1}].

$$\vec{J} = \rho_w c_w \vec{J}_w(\Psi_{w0}, T) \cdot T \quad [\text{W m}^{-2}] \quad (4.41)$$

- S_{en} is the sink term related to energy losses due to evapotranspiration.

Deriving Eq. 4.38 with respect to t and considering Eq. 5.7 for the thermal capacity one may write:

$$\frac{dU}{dt} = C_T \frac{dT}{dt} + \rho_i c_i \cdot T \cdot \frac{\partial \theta_i^{ph}}{\partial t} + \rho_w c_w \cdot T \cdot \frac{\partial \theta_w^{ph}}{\partial t} + \rho_w L_f \frac{\partial \theta_w}{\partial t} \quad (4.42)$$

As:

$$\theta_w^{ph} + \frac{\rho_i}{\rho_w} \theta_i^{ph} = 0 \Rightarrow \rho_i \frac{\partial \theta_i^{ph}}{\partial t} = -\rho_w \frac{\partial \theta_w^{ph}}{\partial t} \quad (4.43)$$

one obtains:

$$\frac{dU}{dt} = C_T \frac{dT}{dt} + \rho_w [(c_w - c_i) \cdot T + L_f] \frac{\partial \theta_w}{\partial t} \quad (4.44)$$

From Eq. 3.45 we have that $\theta_w = \theta_w[\Psi_{w1}(T)]$. Therefore:

$$\frac{\partial \theta_w[\Psi_{w1}(T)]}{\partial t} = \frac{\partial \theta_w}{\partial \Psi_{w1}} \cdot \frac{\partial \Psi_{w1}}{\partial T} \cdot \frac{\partial T}{\partial t} = C_H(\Psi_{w1}) \cdot \frac{\partial \Psi_{freez}}{\partial T} \cdot \frac{dT}{dt} \quad (4.45)$$

where Ψ_{freez} is the freezing suction as defined in Eq. 3.35 and

$$\left. \frac{\partial \theta_w}{\partial \Psi_{w1}} \right|_{\Psi_{w0}} := C_H[\Psi_{w1}(T)] = C_H(T) \quad (4.46)$$

is the hydraulic capacity of the soil calculated at $\psi_{w1}(T)$. If one substitutes (4.45) in (4.44) obtains:

$$\frac{dU}{dt} = \left[C_T + \rho_w \left(L_f + (c_w - c_i) \cdot T \right) \cdot C_H(T) \cdot \frac{\partial \psi_{freeze}(T)}{\partial T} \right] \cdot \frac{dT}{dt} \quad (4.47)$$

The term in squared brackets:

$$C_T + \rho_w \left[L_f + (c_w - c_i) \cdot T \right] \cdot C_H(T) \cdot \frac{\partial \psi_{freeze}(T)}{\partial T} = C_T + C_{ph} := C_a \quad (4.48)$$

is usually referred to as the *apparent heat capacity* (Lukyanov and Golovko, 1957) and is the sum of two contributes: C_T which accounts for the sensible heat transmitted to the soil matrix, and C_{ph} which accounts for the latent released by phase change. C_{ph} may be calculated also directly from definition of apparent heat capacity (Williams and Smith, 1989):

$$C_{ph} := \rho_w L_f \left(\frac{d\theta_u}{dT} \right)_{T_{in}} = \rho_w L_f \frac{\partial \theta_w}{\partial \psi} \cdot \frac{\partial \psi}{\partial T} \quad (4.49)$$

If $T > T^*$ then $\psi_{w1} \equiv \psi_{w0} = \text{const}$. Therefore the hydraulic capacity is null and consequently the apparent heat capacity coincides with the thermal capacity.

4.6 Conclusions

In this section the equations for the mass and energy budget have been thoroughly derived. Regarding the mass conservation, the hypothesis of a “rigid volume” was made, which means that the porosity of the system is constant. This assumption limits the pore space available for water freezing and water flow. Furthermore the flow of ice was considered null and the vapor phase is neglected. The water flow in frozen soil is assumed analogous to that in unsaturated soil (Cary and Mayland 1972, Miller 1963). Therefore, the relationships for matric potential and hydraulic conductivity of unsaturated soils are assumed valid for frozen soils.

Regarding the heat conservation, within the local averaging volume, all phases (soil particle, ice and liquid) are in thermal equilibrium, i.e. all phases have the same temperature. During phase change the water flux $\vec{J}_w = 0$ in V_c is null and water expansion upon freezing is not taken into account, i.e. $\rho_w = \rho_i$. Furthermore the assumption *freezing=drying* implies that $p_i = p_a \leftarrow 0$. These two hypothesis allow to neglect the work due to freezing expansion.

The result is a system of two coupled and highly non linear differential equations on the unknowns (ψ_{w0}, T) . The thermal conductivity / capacity, and the hydraulic conductivity are also function of (ψ_{w0}, T) . This dependance will be discussed in the following section.

5 Thermal and hydraulic parameters of soils and rocks

5.1 Introduction

The presence of water and/or ice in the soil has a crucial importance in defining the thermal and hydraulic properties of a soil/rock. In general, one could say that four main characteristics are important:

- porosity θ_s , defining the pore space in which water or ice can reside;
- the negative pressure ψ_{w0} , that defines the total water content and the saturation degree;
- temperature T , influencing the ice content and the viscosity of water;
- the SWC (or SFC) formulation.

This section is intended to give an overview on the thermal and hydraulic property of the ground, i.e. thermal conductivity, thermal capacity and hydraulic conductivity. For each property a review on the current modeling techniques will be given (*Zhang et al.*, 2008), with a special attention on the *Johansen* (1975) and *Farouki* (1981) representation for the thermal conductivity, the *de Vries* (1963) for the thermal capacity and the *Mualem* (1976) model for the hydraulic conductivity. Then, according to the *Van Genuchten* (1980) model for the SWC and the *freezing=drying* assumption, a sensitivity of the thermal and hydraulic properties on each of the previous feature will be addressed. A paragraph will be also dedicated to the apparent heat capacity (ed. 4.48), as its behavior with temperature is a key issue in solving the heat equation.

5.2 Thermal conductivity

The thermal conductivity, λ [$\text{W m}^{-1} \text{K}^{-1}$] is the property of a material that indicates its ability to conduct heat. The thermal conductivity of a composite material like a soil or a rock depends

on the thermal property of its components, i.e. type of ground particle (quartz, granite, limestone, shale and sandstone) and the water/ice content. It is evident that the porosity and the saturation degree have a major impact on the value of λ . One modeling technique is to assess the “dry” and the “humid” thermal conductivities of the material and then to find a proper relation for each saturation degree. *McCumber and Pielke* (1981) propose the following relation for unsaturated thermal conductivity:

$$\lambda(P_f) = \begin{cases} \exp(-(P_f + 2.7)) & \text{if } P_f \leq 5.1 \\ 0.00041 & \text{if } P_f > 5.1 \end{cases} \quad (5.1)$$

The value in this case is given in [$\text{cal s}^{-1} \text{cm}^{-1} \text{K}^{-1}$] and P_f is the base 10 logarithm of the magnitude of the moisture potential ψ which is expressed as a head of water [cm].

Johansen (1975) and later *Farouki* (1981) propose a thermal conductivity model that vary between two extremes: the dry thermal conductivity, with the lowest thermal properties, and the saturated thermal conductivity with the highest value. The unsaturated thermal conductivity is eventually calculated as a linear combination of the dry and saturated thermal conductivity according to the saturation degree. Other authors, as explained in table 5.2, use a weighted mean of the thermal conductivity of each single component (ground particle, water and ice) without calculating the dry and saturation value. A thorough revision of the thermal parameters used in different models can be found in *Zhang et al.* (2008). The approach of *Johansen* (1975) and *Farouki* (1981) is hereafter explained.

Dry thermal conductivity *Johansen* (1975) proposes the following empirical formulation for the dry thermal conductivity:

$$\lambda_{dry} = \begin{cases} 0.05 & \text{unfrozen peat} \\ 0.55 & \text{frozen peat} \\ \frac{0.135 \rho_{dry} + 64.7}{2700 - 0.947 \rho_{dry}} & \text{mineral soil} \\ 0.039 \theta_s^{-2.2} & \text{crushed rock} \end{cases} \quad (5.2)$$

where $\rho_{dry} = 2700 \cdot (1 - \theta_s)$ is the bulk density of soil [Kg m^{-3}]. The dry thermal conductivity, according to this relationship, highly depends on the porosity θ_s and ranges between $\lambda_{dry} \approx 3$ if $\theta_s = 0$, i.e. pure ground particles, and $\lambda_{dry} \approx 0.024$ if $\theta_s = 1$, which corresponds to the thermal

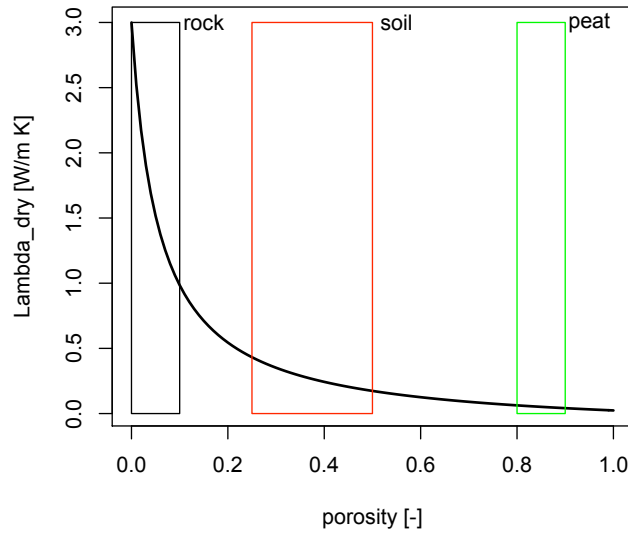


Figure 5.1: Dry soil (rock) thermal conductivity and porosity

conductivity of air (see 5.1).

Saturated thermal conductivity According to *Johansen (1975)* the saturated thermal conductivity may be calculated as a geometric mean of the thermal conductivity of the ground particle λ_g , of ice λ_i and of water λ_w elevated at the respective soil, ice and water content.

$$\lambda_{sat} = \lambda_g^{1-\theta_s} \lambda_w^{\theta_s} \quad \text{if } T > T_{freez}$$

$$\lambda_{sat} = \lambda_g^{1-\theta_s} \lambda_w^{(1-i_r)\theta_s} \lambda_i^{i_r\theta_s} \quad \text{if } T \leq T_{freez} \quad (5.3)$$

where $i_r = \theta_i / (\theta_w + \theta_i)$ is the ice ratio. *Johansen (1975)* proposes to calculate λ_g for soils from:

$$\lambda_g = \lambda_q^q \cdot \lambda_0^{1-q} \quad (5.4)$$

where q is the quartz fraction, and λ_q and λ_0 are the thermal conductivity of quartz and other minerals respectively. $\lambda_q = 7.7 \text{ [W m}^{-1} \text{ K}^{-1}]$ and λ_0 usually vary between $2.0 \div 3.0 \text{ [W m}^{-1} \text{ K}^{-1}]$ if the quartz fraction is less than 20%. Alternatively, a possible formulation for λ_g for soils could be the following proposed by *de Vries (1963)*:

$$\lambda_g = \frac{8.80(\%sand) + 2.92(\%clay)}{(\%sand) + (\%clay)} \quad (5.5)$$

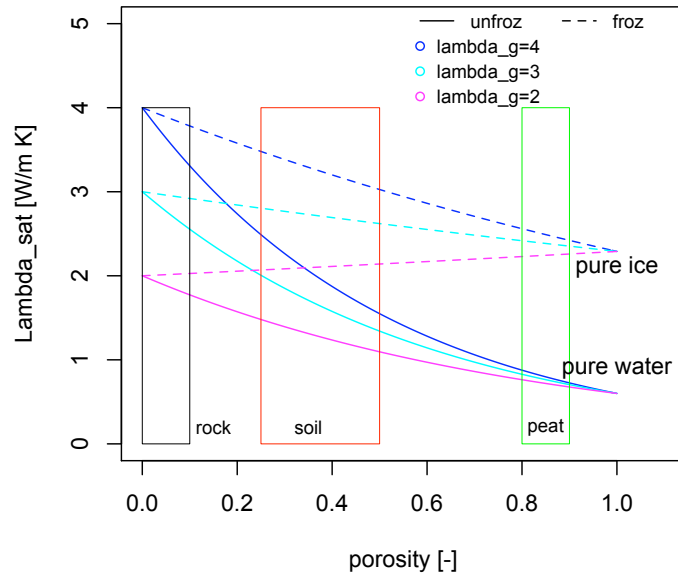


Figure 5.2: Saturated thermal conductivity variation with porosity at different λ_g [$\text{W m}^{-1} \text{K}^{-1}$]. The plain and dotted lines refer to positive and negative temperatures respectively

In general, the thermal conductivity λ_g of soil materials ranges between $1.3 \div 5$ [$\text{W m}^{-1} \text{K}^{-1}$] according to the percentage of quartz, granite, limestone, shale and sandstone (Andersland and Ladanyi, 2003). Given the thermal conductivities of water $\lambda_w = 0.6$ and ice $\lambda_i = 2.2$ [$\text{W m}^{-1} \text{K}^{-1}$], it is possible to calculate the saturated thermal conductivity as a function of the porosity.

As reported in Fig. 5.2, increasing the porosity the unfrozen saturated thermal conductivity rapidly decreases, because $\lambda_w < 1$ and therefore $\lambda_w^{\theta_s} < 1$. The frozen thermal conductivity, on the other hand, increases or decreases with porosity depending on λ_g : if $\lambda_g < \lambda_i$ then the frozen saturated thermal conductivity increases (see green dotted line), otherwise decreases. At $\theta_s = 1$ one has a homogeneous substance (pure ice or water) and therefore the saturated thermal conductivities converge to the respective ice or water thermal conductivities.

Unsaturated thermal conductivity According to Johansen (1975) the unsaturated thermal conductivity may be calculated as a linear combination of the dry and saturated thermal conductivity, depending on the saturation degree and on temperature:

$$\lambda_T(\psi_{w0}, T) = K_e \lambda_{sat} + (1 - K_e) \lambda_{dry} \quad (5.6)$$

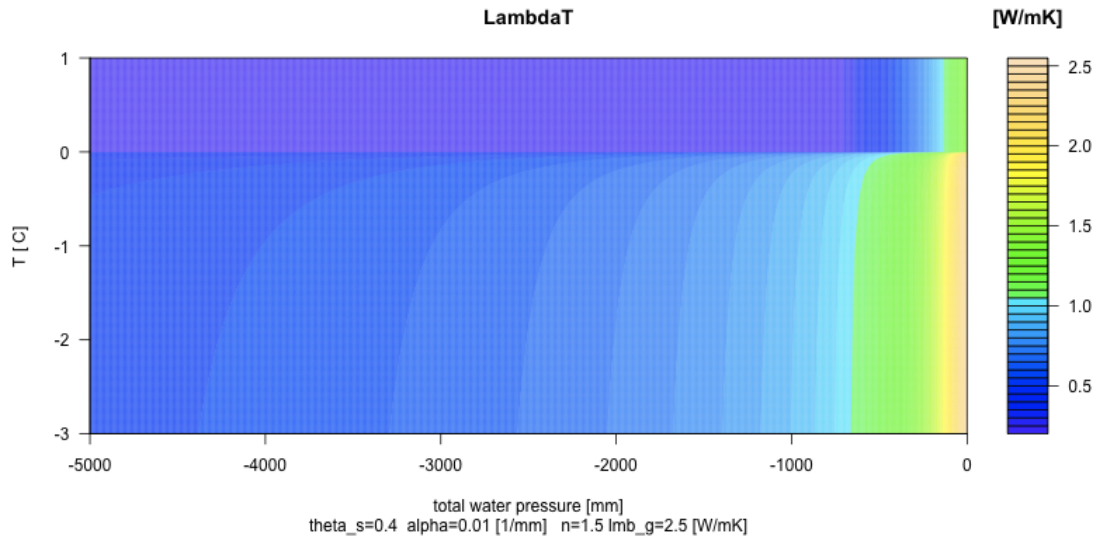


Figure 5.3: Unsaturated thermal conductivity λ_T as function of ψ_m and temperature

The proportion coefficient is K_e , which stands for Kersten number, and is a function of the degree of saturation $S_r = (\theta_w + \theta_i)/\theta_s$ and of temperature:

$$\begin{cases} K_e = \log(S_r) + 1 & \text{if } T \geq T_{freeze} \\ K_e = S_r & \text{if } T < T_{freeze} \end{cases}$$

S_r , according to Eq. 3.45 and 3.47, may be expressed as a function of ψ_{w0} and T . Therefore one could calculate the unsaturated thermal conductivity as in Fig. 5.3 where ψ_{w0} (x axis) represents the total water content, and T (y axis) represents the state of water (liquid or solid) according to the SFC (see section 3.6). It is possible to see an abrupt increase in the thermal conductivity passing from the unfrozen to the frozen condition, due to the higher thermal conductivity of ice. At the same time the thermal conductivity in the unfrozen state increases with the increase of ψ_{w0} . In fact, as shown in the Fig. 5.2, considering $\theta_s = 0.4$ the dry thermal conductivity $\lambda_{dry} \approx 0.243 < \lambda_w$, therefore increasing the water content produces also a moderate increase in the thermal conductivity.

This behavior is also visible in Fig. 5.4. On the left is reported the variation of λ_T at various porosity values, with respect to temperature. One can notice a jump passing from the unfrozen to the frozen state, and the jump increases with the increasing of porosity. At the same time, increasing the total water content (i.e. increasing ψ_{w0}), increases also the thermal conductivity. Looking at the right part of the plot, one can notice the variation with respect to the total water content ψ_{w0} . Increasing ψ_{w0} , the thermal conductivity increases slowly at very dry condition, and

5. Thermal and hydraulic parameters of soils and rocks

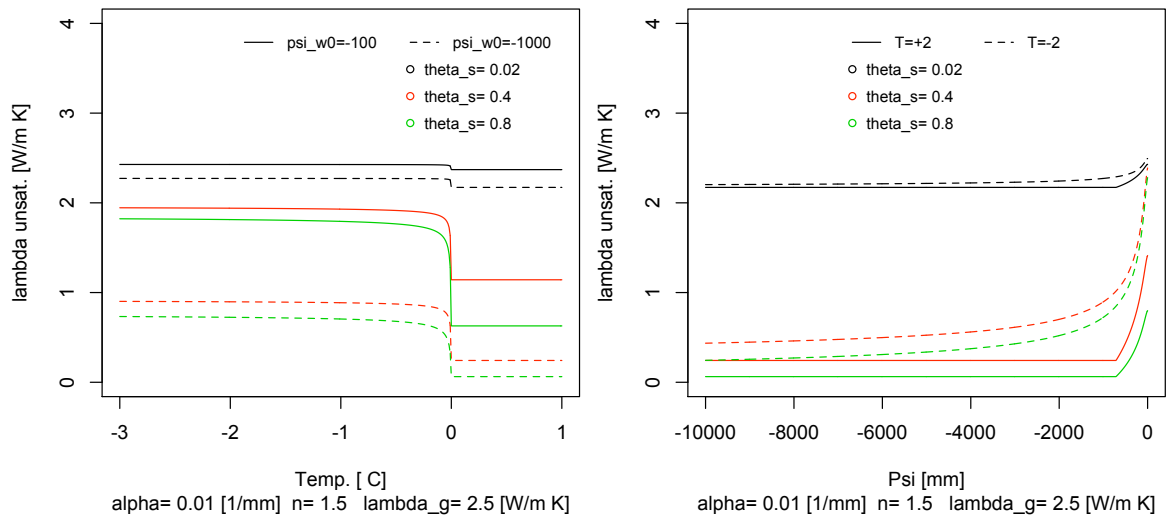


Figure 5.4: *Unsaturated thermal conductivity. Left: influence of temperature at various porosity values. Right: influence of the total water content given by ψ_{w0} .*

then rapidly at higher near saturation.

In Fig. 5.5 is reported the variation of the thermal conductivity with porosity. First of all one can notice a strong decrease in λ_T due to the decrease in water content ψ_{w0} , both in the frozen and unfrozen state. Furthermore, given a value of ψ_{w0} , as $\lambda_w < \lambda_g$, increasing the porosity λ_T decreases. This decrease is much stronger for small values of porosity and then, approximately at $\theta_s \approx 0.5$, λ_T stabilizes.

	$T > 0$				$\psi_{w0} = -1$ [m]	$T = -2$ °C			
	α [mm ⁻¹]					α [mm ⁻¹]			
n	0.001	0.01	0.1	0.4	0.001	0.01	0.1	0.4	
1.1	1.33	1.13	0.87	0.71	1.64	1.45	1.21	1.08	
1.5	1.14	0.24	0.24	0.24	1.89	0.90	0.45	0.35	
2.0	1.01	0.24	0.24	0.24	1.77	0.46	0.26	0.25	
2.5	0.93	0.24	0.24	0.24	1.67	0.31	0.25	0.24	

Table 5.1: *Thermal conductivity in [W m⁻¹ K] of the bulk soil at $\psi_{w0} = -1$ [m] for positive temperatures (left) and at $T = -2$ °C (right), as function the combination (α, n) . In the calculation the method of Johansen (1975) was used with $\theta_s = 0.4$ and $\theta_r = 0$.*

It is also possible to plot the thermal conductivity with respect to the SWC parameters. Using the Van Genuchten (1980) representations, this means the parameters α [mm⁻¹] and n [-] as outlined

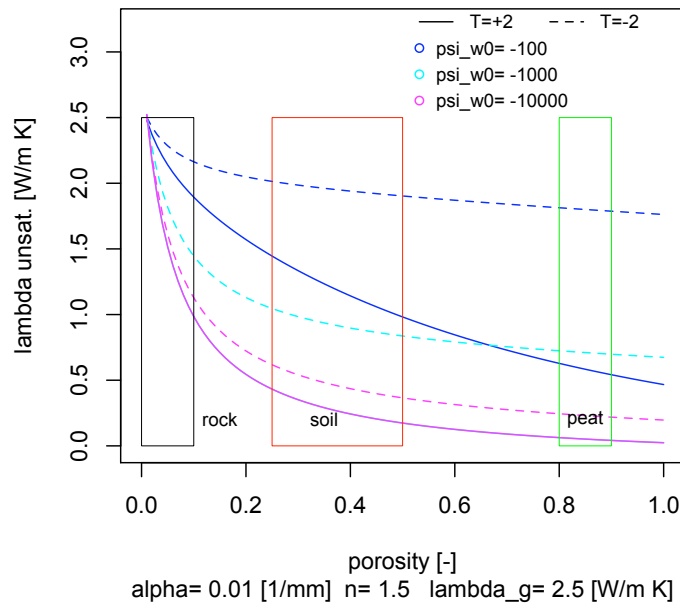


Figure 5.5: Unsaturated thermal conductivity as function of porosity at various ψ_{w0}

in Eq. 3.44. Table 5.1 shows the values of λ_T of a soil with porosity equal to 0.4 at an unsaturated condition given by $\psi_{w0} = -1$ [m]. According to the specific values of (α, n) , the thermal conductivity may vary from 0.24 to 1.33 [$\text{W m}^{-1} \text{K}$] in the unfrozen state, and from 0.24 to 1.64 [$\text{W m}^{-1} \text{K}$] in the frozen state. In Fig. 5.6 at the top is reported the influence of the parameter α in function of ψ_{w0} both in the unfrozen and in the frozen state. Increasing α means decreasing the water content at very negative suction potentials, and this means to decrease the thermal conductivity. At the bottom is shown the influence of the parameter n . High values of n mean a pore distributions with a very low variance. Interesting is the behavior in function of the temperatures (bottom right): at $\psi_{w0} = 0$ this means a rapid freezing with consequent increase in λ_T , whereas at $\psi_{w0} = -1000$ [mm] this means a low saturation degree with consequent low λ_T .

5.3 Thermal capacity

The thermal capacity of a rock/soil sample is the amount of heat required to raise its temperature by one degree. If the “amount” is volume, then it is called volumetric heat capacity [$\text{J m}^{-3} \text{K}^{-1}$]; if it is mass, then it is called specific heat capacity [$\text{J Kg}^{-1} \text{K}^{-1}$]. It can be computed by adding

5. Thermal and hydraulic parameters of soils and rocks

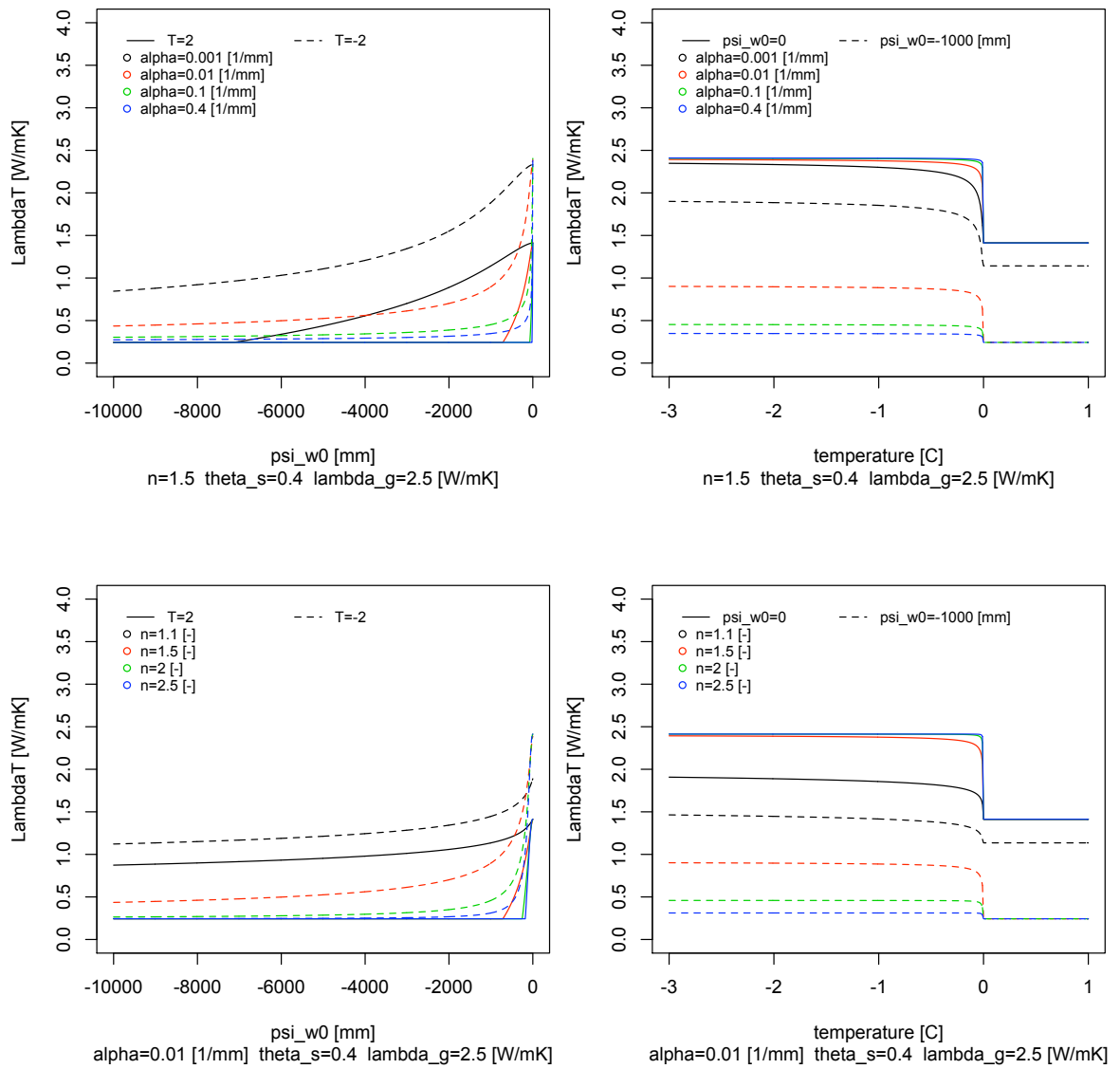


Figure 5.6: Unsaturated thermal conductivity. Top left: influence of α and ψ_{w0} . Top right: influence of α and T . Bottom left: influence of n and ψ_{w0} . Bottom right: influence of α and T

Author	λ_{uns}
Harlan (1973), Fuchs et al. (1978), Guymon and Luthin (1974)	$\frac{\sum_j m_j \lambda_j \theta_j}{\sum_j m_j \theta_j}$
Hansson et al. (2004), Watanabe (2008)	$C_1 + C_2(\theta_w + F\theta_i) - (C_1 - C_4) \exp \left[- (C_3(\theta_w + F\theta_i))^{C_5} \right] + \beta_f C_w q_w $
Daanen et al. (2007)	$\lambda_u(1 - \theta_s) + \lambda_i \theta_i$
Luo et al. (2009), Niu and Yang (2006), Zhang et al. (2007)	$K_e \lambda_{sat} + (1 - K_e) \lambda_{dry}$
Daanen et al. (2007)	$\lambda_u(1 - \theta_s) + \lambda_i \theta_i$
Koren et al. (1999) after McCumber and Pielke (1981)	$\lambda(P_f) \cdot (1 + \theta_i)$
Shoop and Bigl (1997), McKenzie et al. (2007), Zhao et al. (1997)	$\lambda_g(1 - \theta_s) + \lambda_w \theta_w + \lambda_i \theta_i$

Table 5.2: Unsaturated thermal conductivity formulations from various authors.

the heat capacities of the different constituents in a unit mass of soil/rock. Thus (Farouki, 1981):

$$C_T = C_{gs}(1 - \theta_s) + c_i \rho_i \theta_i + c_w \theta_w \rho_w \quad (5.7)$$

where C_{gs} [$\text{J m}^{-3} \text{K}^{-1}$] is the volumetric heat capacity of ground particle and $c_i=2217$ [$\text{J Kg}^{-1} \text{K}^{-1}$], $c_w=4188$ [$\text{J Kg}^{-1} \text{K}^{-1}$] are the specific heat capacity of ice and water respectively. In case of soils, it depends on the type of soil under consideration and may be formulated according to the empirical expression of de Vries (1963):

$$C_{gs} = \frac{2.128(\%sand) + 2.385(\%clay)}{(\%sand) + (\%clay)} \cdot 10^6 \quad (5.8)$$

As both θ_w and θ_i are functions of $\Psi_{w1} = \Psi(\Psi_{w0}, T)$, one could write:

$$C_T(\Psi_{w1}) = C_{gs}(1 - \theta_s) + c_i \rho_i \cdot \theta_i(\Psi_{w1}) + c_w \rho_w \cdot \theta_w(\Psi_{w1}) \quad (5.9)$$

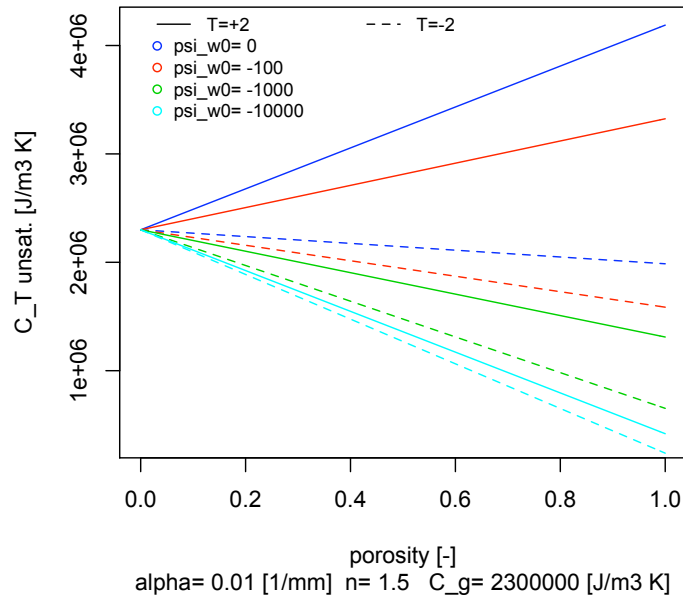


Figure 5.7: Thermal capacity variation with porosity at different ψ_{w0} . The plain and dotted lines refer to positive and negative temperatures respectively

As for the thermal conductivity, it is therefore possible to plot the sensitivity of the thermal capacity to porosity, total water content, temperature and Van Genuchten parameters.

Dependance on porosity As can be seen in Fig. 5.7, at null porosity the thermal capacity coincides with the thermal capacity of the soil grain C_{gs} . Then, increasing the porosity, the thermal capacity assumes a linear behavior: if the temperature is negative (dotted line), it always decreases, no matter the total water content, as the thermal capacity of ice $C_i = 1.95 E6 < C_{gs}$. If the temperature is positive, the linear behavior depends on ψ_{w0} : if the soil is saturated then it always increases as $C_{gs} < C_w = 4.18 E6$. Decreasing the total water content, the rate of increase of C_T decreases. At a certain ψ_{w0} , also the unfrozen unsaturated thermal capacity decreases with increasing porosity as the air doesn't give any contribution.

Dependance on water content and temperature at various porosity As reported in Fig.5.8, the thermal capacity, given a porosity θ_s , increases with increasing ψ_{w0} as the water (or ice) adds a capacity to the soil, and increases with increasing temperature as $C_w > C_i$. The coupled influence of both ψ_{w0} and T may be seen in Fig.5.9.

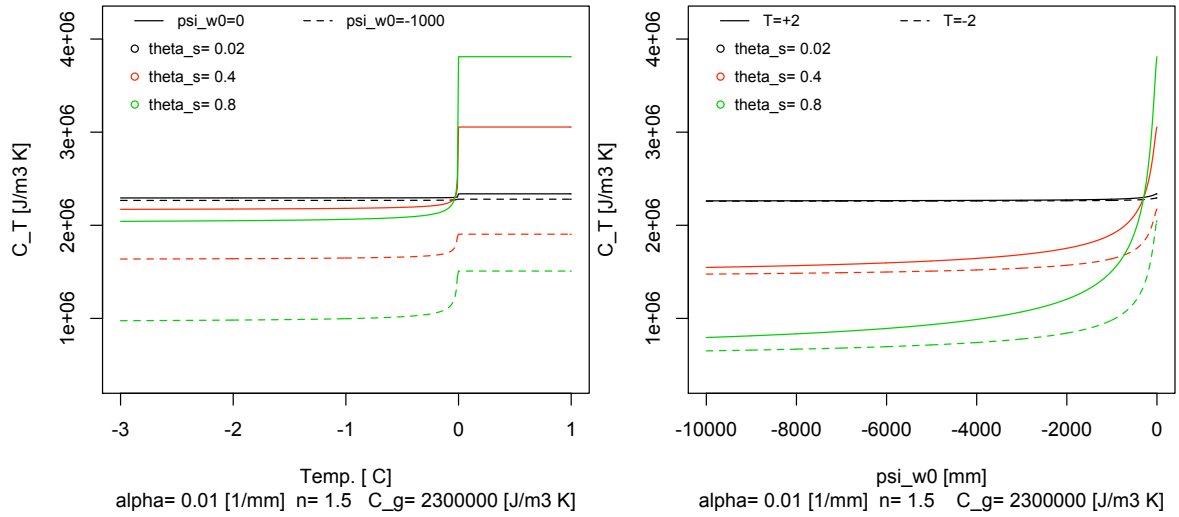


Figure 5.8: Soil bulk thermal capacity C_T as function of temperature (left) and ψ_{w0} (right) at various porosity values

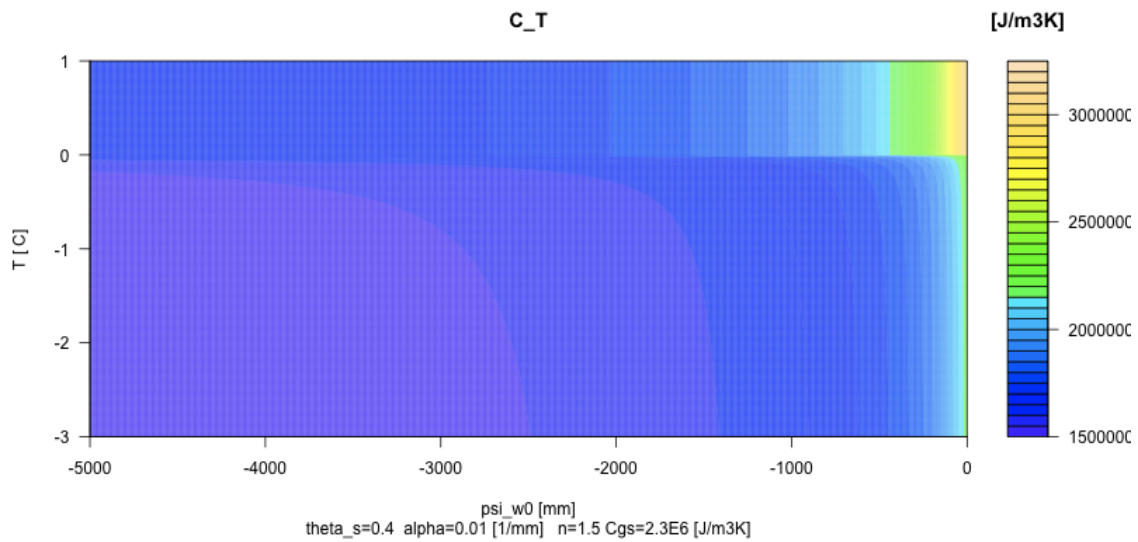


Figure 5.9: Unsaturated thermal capacity as a function of ψ_{w0} and T

Dependance on Van Genuchten parameters at various T and ψ_{w0} In Fig. 5.10 at the top is reported the influence of the parameters α , n , T and ψ_{w0} on the thermal capacity. Increasing α , as outlined in Eq. 3.12, means decreasing the water content for a given ψ_{w0} , and this reflects in a reduction of the thermal capacity (top left), both in the unfrozen and in the frozen state. The same happens increasing temperatures (top right) for every total water content. Also n is highly linked to the water content. High values of n mean low water content, and therefore low thermal capacity, both in the unfrozen and in the frozen state (bottom left). The same is true for increasing temperatures: an increase in n reflects in a reduction of C_T for every saturation level. When $T = 0$ is reached, then C_T remains constant. Table 5.3 shows the values of C_T of a soil with porosity equal to 0.4 at an unsaturated condition given by $\psi_{w0}=-1$ [m]. According to the specific values of (α,n) , the thermal capacity may vary from 1.38 to 2.95 [$\text{MJ m}^{-3} \text{K}$] in the unfrozen state, and from 1.38 to 2.63 [$\text{MJ m}^{-3} \text{K}$] in the frozen state.

	$T > 0$				$\psi_{w0}=-1$ [m]	$T = -2^\circ\text{C}$			
	α [mm^{-1}]					α [mm^{-1}]			
	n	0.001	0.01	0.1		0.4	0.001	0.01	0.1
1.1	2.95	2.70	2.43	2.3	2.63	2.40	2.20	2.09	
1.5	2.71	1.90	1.55	1.46	2.05	1.64	1.46	1.42	
2.0	2.56	1.55	1.40	1.38	1.93	1.46	1.39	1.38	
2.5	2.49	1.43	1.38	1.38	1.89	1.40	1.38	1.38	

Table 5.3: *Unsaturated soil thermal capacity in [$\text{MJ m}^{-3} \text{K}^{-1}$] at $\psi_{w0}=-1$ [m] for positive temperatures (left) and at $T = -2^\circ\text{C}$ (right), as function the combination (α,n) . In the calculation $\theta_s = 0.4$ and $\theta_r = 0$.*

5.4 Hydraulic conductivity

The hydraulic conductivity is a property soil or rock, that describes the ease with which water can move through pore spaces or fractures. It depends on the intrinsic permeability of the material and on the degree of saturation. Saturated hydraulic conductivity, K_s , describes water movement through saturated media. The saturated hydraulic conductivity K_s is made dependent on soil temperature through viscosity, which increases by a factor 2 from 10°C to 40°C . As temperature and saturation degree come to play, one could say that the hydraulic conductivity is a function of T and ψ_{w0} . For frozen soils, the hydraulic conductivity depends also on the ice content which limits the pore space and thus the flow of water. The hydraulic conductivity of a frozen soil has become an interesting topic for various reasons, among which: (1) the control of frost heave, (2) the environmental concerns related to spillage of petroleum hydrocarbons at fuel sites in permafrost

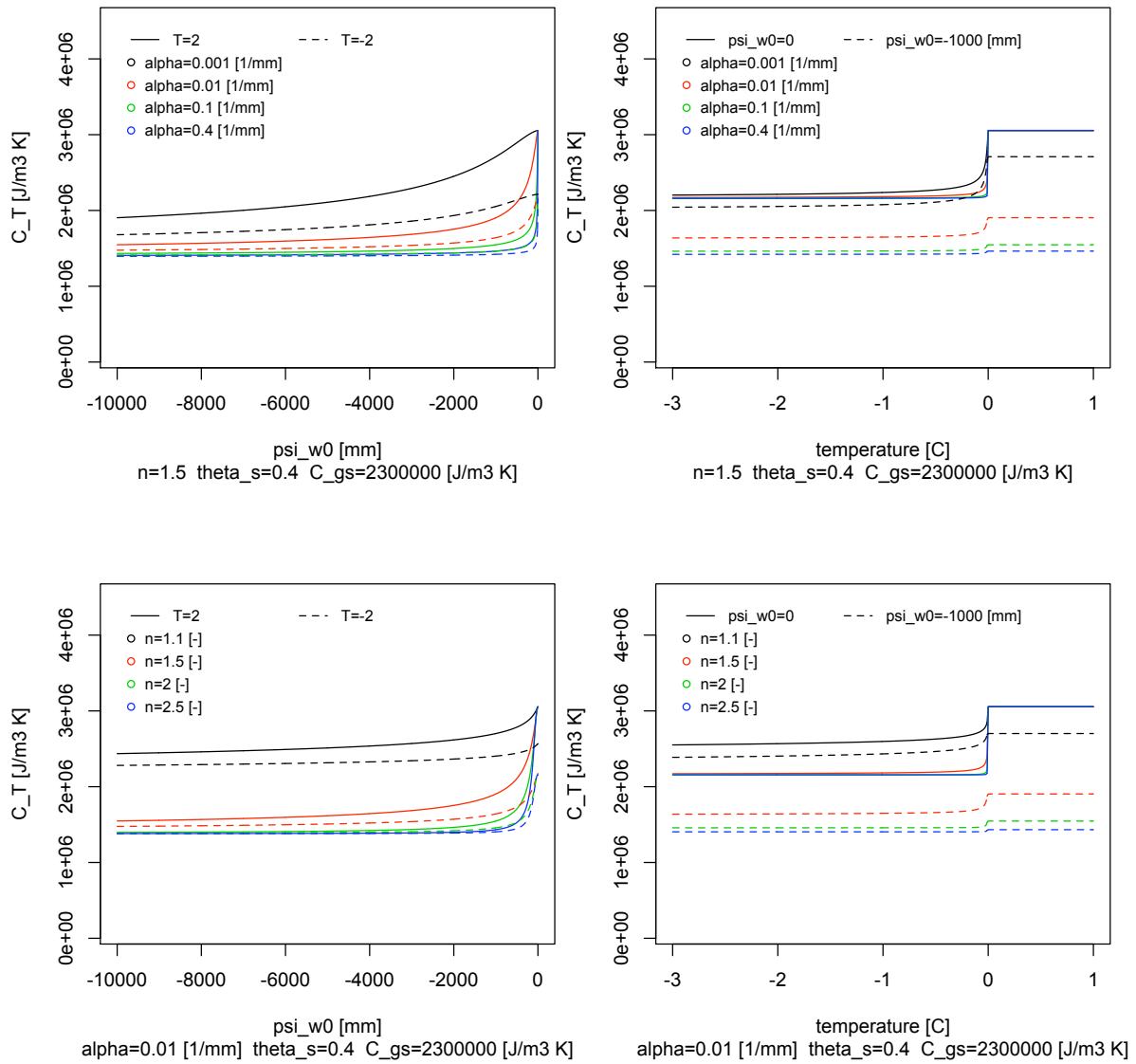


Figure 5.10: Unsaturated thermal capacity. Top left: influence of α and ψ_{w0} . Top right: influence of α and T . Bottom left: influence of n and ψ_{w0} . Bottom right: influence of α and T

5. Thermal and hydraulic parameters of soils and rocks

areas and (3) the sue of sub-surface frozen soil barriers for containment of hazardous liquid waste contaminants (Andersland and Ladanyi, 2003). In table 5.4 is summarized the formulation of the hydraulic conductivity from various authors.

Author	K_H
Harlan (1973)	= $f(\psi)$ experimental functional relationship
Fuchs et al. (1978)	$K_s \left(\frac{\theta_w}{\theta_s}\right)^m$
Guymon and Luthin (1974)	$K_s \frac{1}{(-A_k \psi^3 + 1)}$
Zhao et al. (1997)	$10^{-\omega \theta_i} \cdot K_s S_e^{3 + \frac{2}{\lambda}}$
Hansson et al. (2004), Daanen et al. (2007)	$K_s S_e^l \left[1 - \left(1 - S_e^{\frac{1}{m}} \right)^m \right]^2 \cdot 10^{-\omega Q}$
Lout et al. (2009)	$K_s \frac{\theta_w}{\theta_s}^{2b+3}$
Zhang et al. (2007)	$10^{-E \theta_i} \cdot K_s \frac{\theta_w}{\theta_s}^{2b+3}$
Shoop and Bigl (1997)	$\frac{K_s}{A_k h_p ^{b+1}}$
Watanabe (2008)	$K_s \frac{(w_1 S_1 + w_2 S_2)^l \left(w_1 \alpha_1 \left[1 - \left(1 - S_e^{\frac{l}{m_1}} \right)^{m_1} \right] + w_2 \alpha_2 \left[1 - \left(1 - S_e^{\frac{l}{m_2}} \right)^{m_2} \right] \right)^2}{(w_1 \alpha_1 + w_2 \alpha_2)^2} \cdot 10^{-\omega \frac{\theta_i}{\theta_s}}$

Table 5.4: Unsaturated hydraulic conductivity formulations from various authors.

The dependance on temperature is modeled with a polinomial $\Gamma(T)$ that interpolates the cinematic viscosity at various temperature (Hornberger, 1998):

$$\Gamma(T) = \begin{cases} 1.5869 \cdot 10^{-4} \cdot T^2 + 2.5263 \cdot 10^{-2} \cdot T + 0.7315 & \text{if } T > 0 \\ 0.73 & \text{if } T \leq 0 \end{cases} \quad (5.10)$$

Defining the saturation degree S_r as:

$$S_r := \frac{\theta_w - \theta_r}{\theta_s - \theta_r} = \frac{1}{(1 + (\alpha (-\Psi_{w0}))^n)^m} \quad (5.11)$$

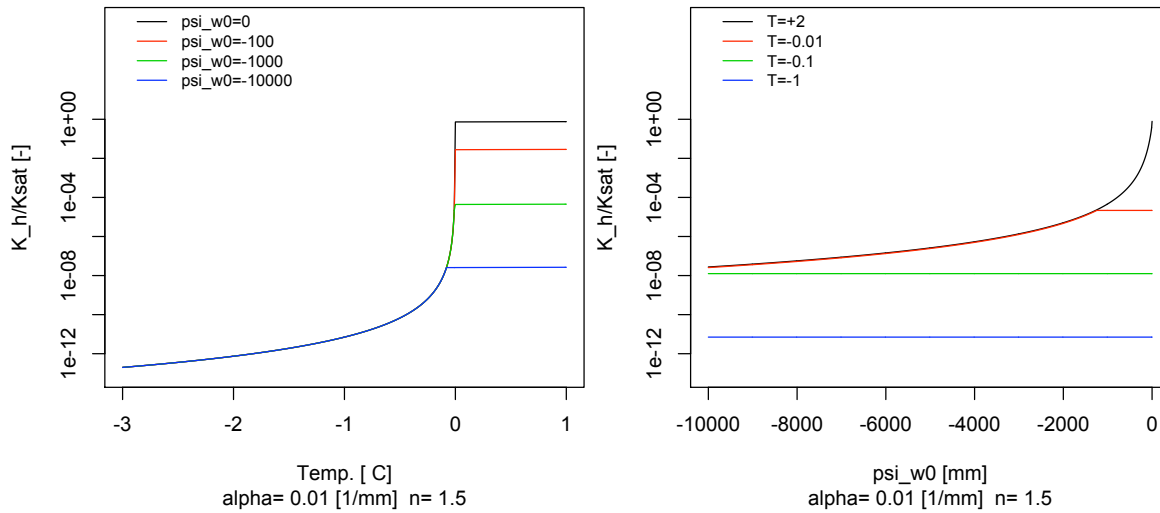


Figure 5.11: Ratio between the unsaturated and saturated hydraulic conductivity [-] as function of temperature at various ψ_{w0} (left); ratio between the unsaturated and saturated hydraulic conductivity [-] at various T (right). In both plots the y axis is in logarithmic scale

where $m \geq 1$ is a parameter (usually one puts $m=1-1/n$). One can apply the formulation of Mualem (1976) to account for the dependance on ψ_{w0} of the hydraulic conductivity:

$$K_H(T, S_r) = K_s \cdot f(T) \cdot S_r^{\frac{1}{2}} \cdot \left[1 - \left(1 - S_r^{\frac{1}{m}} \right)^m \right]^2 \quad (5.12)$$

One can notice that the influence on porosity of the hydraulic conductivity is not in the formulation, as it is embedded in K_s . The dependence on T and ψ_{w0} is visible in Fig. 5.11. On the left is reported the dependance on temperature of the ratio K_H/K_s at various ψ_{w0} : at negative temperatures, the ratio is the same for every ψ_{w0} because the frozen soil is considered completely “desaturated”; at positive temperatures, increasing ψ_{w0} increases also K_H/K_s . On the right is reported the dependance on ψ_{w0} at various temperatures: generally K_H/K_s increases with increasing ψ_{w0} but, as soon as the temperature falls below 0°C , K_H/K_s decreases dramatically and stays constant even if ψ_{w0} increases. According to the *freezing=drying* assumption, the liquid water content falls at negative temperature and so the hydraulic conductivity drops accordingly. However, near the freezing front also the pore water pressure ψ_{w1} increases in modulus due to the freezing, and this would result in a high flow of water towards the freezing front. This flow of water could sometimes overestimate the real flow determined by the freezing process. In order to account for this effect, a reduction was introduced and called “blocking effect” of ice. *Jame and Norum* (1980)

propose a reduction that is proportional to the ice content in the soil:

$$K_{H_v}(\theta_i) = K_{H_v} \cdot 10^{-E \theta_i} \quad (5.13)$$

where E is the impedance factor and may be given by the following relation according to *Shoop and Bigl (1997)* :

$$E = \frac{5}{4}(K_s - 3)^2 + 6 \quad (5.14)$$

Lundin (1990) and later *Hansson et al. (2004)* consider the impedance factor Ω depending on the ice ratio i_r :

$$K_{H_v}(\theta_i) = \begin{cases} K_{H_v}(T) \cdot 10^{-\Omega \cdot i_r} & \text{if } i_r < 0.25 \\ 0.0 & \text{otherwise} \end{cases}, \quad (5.15)$$

where $i_r := \theta_i / (\theta_i + \theta_w)$ is the ice ratio and is defined as the relative quantity of ice with respect to the total water content. The exponential form of the equation implies that even a small value of can have a significant effect on the conductivity of the liquid phase as the ice portion increases.

In table 5.5 is reported a simple calculation of K_H/K_s at $\psi_{w0} = -1$ [m], at both $T = 2$ and $T = -2$ °C. The results show that, given α and n , passing from $T=2$ to $T=-2$ the ratio K_H/K_s decreases between 5 and 14 orders of magnitude. In Fig. 5.12 at the top is reported the influence of the parameters α and n on the ratio K_s/K_H . On the top left is proposed the influence of α and ψ_{w0} : at positive temperatures, given α , increasing ψ_{w0} increases also K_H/K_s because the saturation content increases. Given ψ_{w0} , increasing α means a decrease of K_H/K_s as the saturation content decreases. At negative temperatures, the influence on ψ_{w0} is null and still an increase in α translates in a decrease of K_H/K_s . On the top right is reported the influence of α and T : in general, passing from negative to positive temperatures, means an increase in K_H/K_s . On the bottom is reported the influence of n : in general an increase in n means a decrease in K_H/K_s , yet the decrease is not more constant with ψ_{w0} whereas with α the decrease is much more rapid. Table 5.5 shows the values of K_H of a soil with porosity equal to 0.4 at an unsaturated condition given by $\psi_{w0} = -1$ [m]. According to the specific values of (α, n) , the ratio K_H/K_s may vary of 16 orders of magnitude in the unfrozen state, and of 30 orders of magnitude in the frozen state.

5.5 Apparent heat capacity

The apparent heat capacity, recalling Eq. 4.48 is defined as:

$$C_a := C_T + \rho_w [L_f + (c_w - c_i) \cdot T] \cdot \frac{\partial \theta_w}{\partial \psi} \cdot \frac{\partial \psi_{freez}(T)}{\partial T} = C_T + C_{ph} \quad (5.16)$$

5. Thermal and hydraulic parameters of soils and rocks

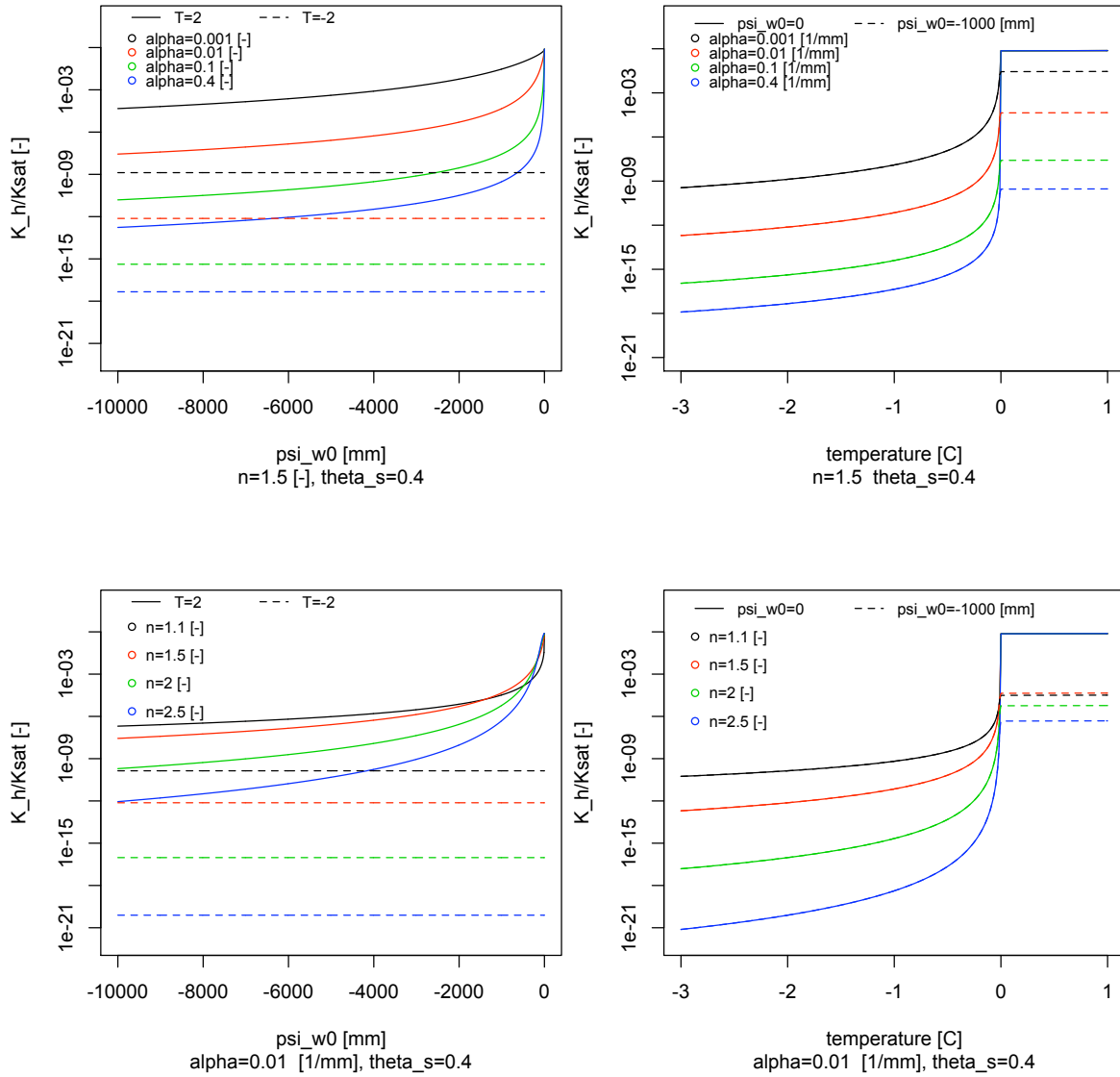


Figure 5.12: Unsaturated hydraulic conductivity. Top left: influence of α and ψ_{w0} . Top right: influence of α and T . Bottom left: influence of n and ψ_{w0} . Bottom right: influence of α and T

5. Thermal and hydraulic parameters of soils and rocks

$\Psi_{w0}=-1[m]$		$T = 2\text{ }^\circ\text{C}$		
$\alpha [mm^{-1}]$				
n	0.001	0.01	0.1	0.4
1.1	2.83E-3	3.33E-5	2.03E-7	9.03E-9
1.5	2.97E-2	4.66E-5	2.74E-8	3.04E-10
2.0	5.65E-2	6.08E-6	2.96E-10	3.82E-13
2.5	7.36E-2	4.98E-7	8.91E-13	3.07E-16

$\Psi_{w0}=-1[m]$		$T = -2\text{ }^\circ\text{C}$		
$\alpha [mm^{-1}]$				
n	0.001	0.01	0.1	0.4
1.1	2.44E-8	1.37E-10	7.74E-13	3.42E-14
1.5	1.32E-9	7.43E-13	4.18E-16	4.62E-18
2.0	3.00E-12	9.50E-17	3.00E-21	5.87E-24
2.5	4.37E-15	7.78E-21	1.38E-26	4.77E-30

Table 5.5: Ratio K_H/K_s [-] between unsaturated and saturated soil hydraulic conductivity at $\Psi_{w0} = -1$ [m] for positive temperatures (top) and at $T = -2\text{ }^\circ\text{C}$ (bottom), as function the combination (α, n) . Eq. 5.12 was used in the calculation

where C_{ph} is the component responsible for phase change. Adopting the *Van Genuchten* (1980) model for the SWC, after some calculations, the C_{ph} may be written as:

$$C_{ph}(T, \Psi_{w0}) = [1 + (-\alpha \Psi_{w1})^n]^{\frac{1}{n}-2} \cdot (-\alpha \Psi_{w1})^{n-1} \cdot \frac{(\theta_s - \theta_r) (n-1) \alpha \rho_w L_f [L_f + (c_w - c_i) T]}{g T_0}$$

Therefore C_a , given the total water pressure Ψ_{w0} , is a function of the negative temperature T and the shape and steepness of the curve depend on Van Genuchten's parameters.

The apparent heat capacity of a soil sample is the sum of the thermal capacity responsible for temperature raise or decrease, and the thermal capacity responsible for phase change and is the derivative of the internal energy U with temperature. As can be seen in Fig. 5.13, at null porosity the apparent heat capacity coincides with the thermal capacity of the soil grain C_{gs} . Then, increasing the porosity, the apparent heat capacity assumes a linear behavior: if the temperature is positive it coincides with the thermal capacity (see Fig. 5.7) as the hydraulic capacity C_{ph} is null. If the temperature is negative (dotted line), differently from the thermal capacity (Fig. 5.7), it increases because the term C_{ph} increases linearly with porosity and compensates the minor thermal capacity of ice compared with C_{gs} .

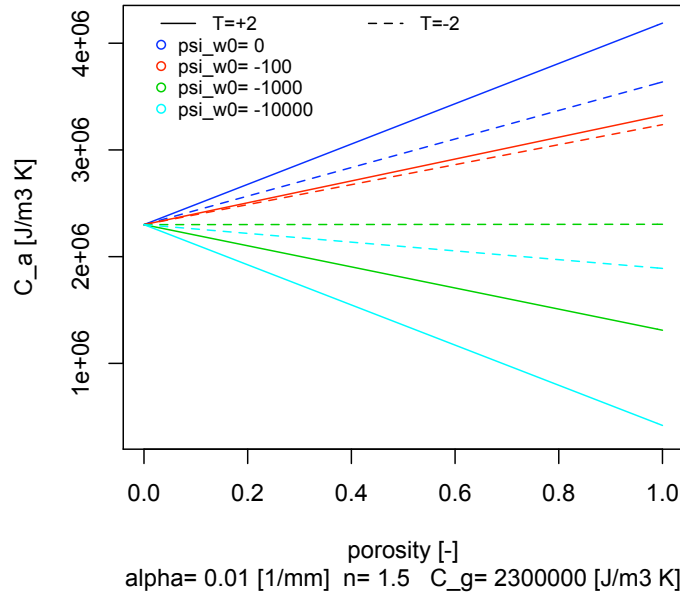


Figure 5.13: Apparent heat capacity variation with porosity at different ψ_{w0} . The plain and dotted lines refer to positive and negative temperatures respectively

dependance on water content and temperature at various porosity As reported in Fig.5.14 on the left, the thermal capacity increases both with porosity θ_s and with ψ_{w0} . Increasing temperature, from negative to positive, the hydraulic capacity increases and so does C_a , reaching the maximum when $T \approx 0$. Near T_0 the curve has enormous gradients. As outlined by *Hansson et al. (2004)*, this may induce numerical oscillation passing from positive to negative temperatures in one time step and therefore has to be treated with proper numerical schemes. At the right is reported the influence of C_a with ψ_{w0} at different porosity levels. Two considerations are important:

- At low total water suctions, the apparent heat capacity is comparable with the thermal capacity C_T , i.e. the term C_{ph} in Eq. 5.16 is not influent. Near saturation, on the other hand, the term C_{ph} becomes dominant.
- the higher the porosity, the higher the apparent heat capacity;
- the maximum of C_a may be found near the melting temperatures

dependance on Van Genuchten parameters at various T and ψ_{w0} In Fig. 5.15 at the top is reported the influence of the parameters α , n , T and ψ_{w0} on the apparent heat capacity. Increasing

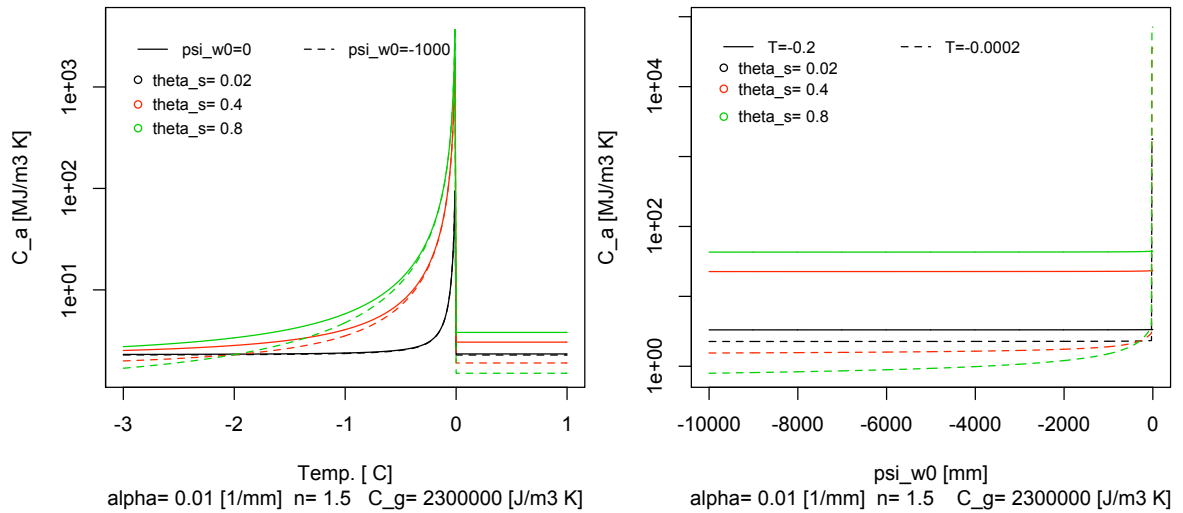


Figure 5.14: Soil bulk apparent heat capacity C_a [$\text{MJ m}^{-3} \text{K}^{-1}$] as function of temperature (left) and ψ_{w0} (right). Different colors correspond to different porosity values

α , as outlined in 3.12, means decreasing the water content for a given ψ_{w0} , and this reflects in a reduction of the capacity (top left). When the saturation is approached, then the apparent heat capacity suddenly increases when the temperature is near the melting temperature (dotted line). Increasing temperatures (top right), the maximum will be become ever bigger, the magnitude depending on α : increasing α the apparent heat capacity decreases as the total water content decreases. Also n is highly linked to the water content. High values of n mean low water content, and therefore low thermal capacity (bottom left). The same is true for increasing temperatures: an increase in n reflects in a reduction of C_a for every saturation level. When $T = 0$ is reached, then $C_a \equiv C_T$.

As visible in table 5.6, at saturation ($\psi_{w0} = 0$), if $T = -0.2^\circ \text{C}$ the apparent heat capacity is comparable with the thermal capacity. At $T = -0.0002^\circ \text{C}$, the apparent heat capacity dramatically increases and, according to the value of (α, n) , may increase of 5 orders of magnitude.

5.6 Conclusions

This section has reported an overview of the modeling techniques for the thermal and hydraulic properties of soil and rock. In particular, special attention was given to the *Johansen* (1975) and *Farouki* (1981) representation for the thermal conductivity, to the *de Vries* (1963) for the thermal capacity and the *Mualem* (1976) - *Van Genuchten* (1980) model for the hydraulic conductivity.

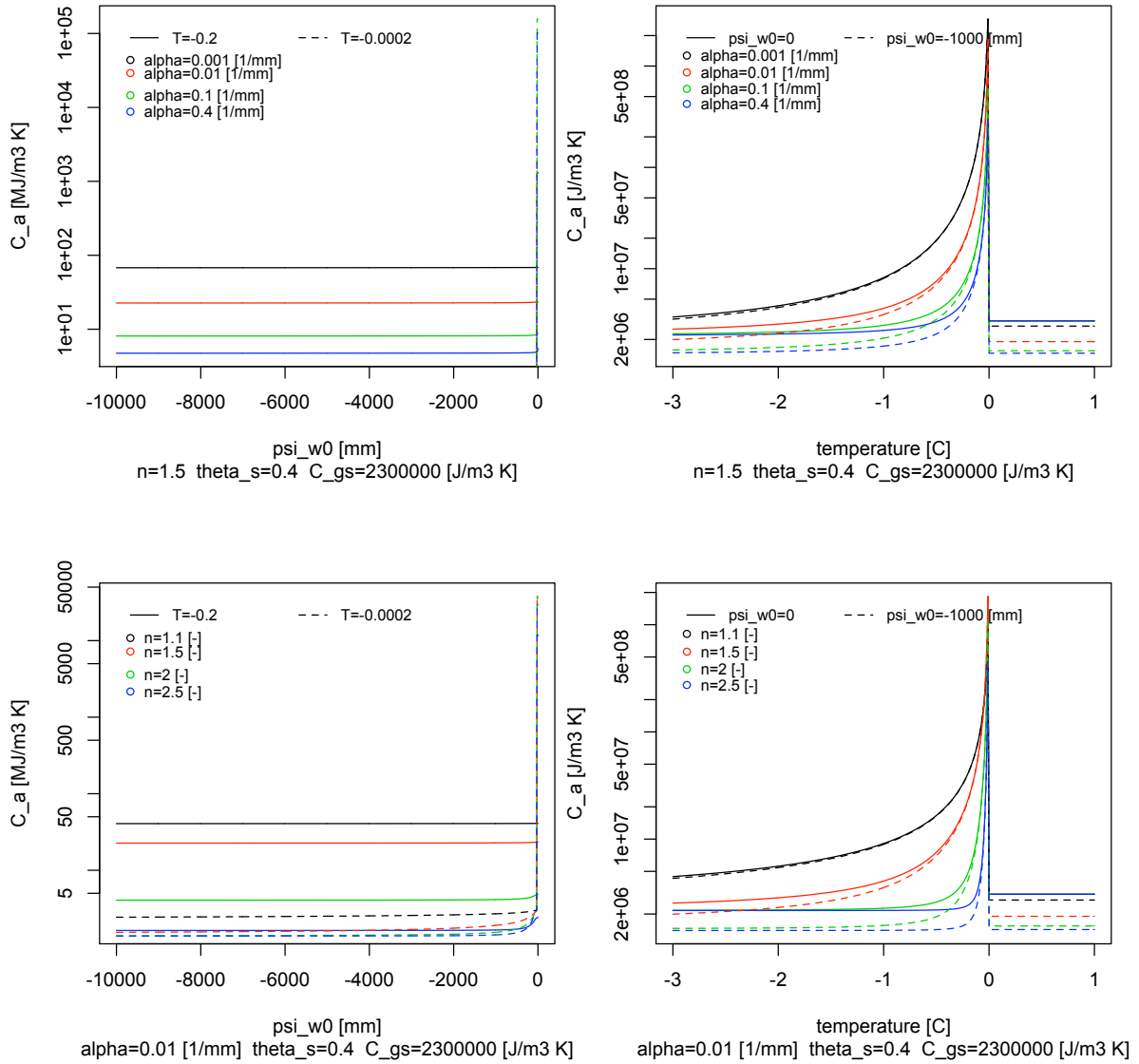


Figure 5.15: Apparent heat capacity. Top left: influence of α and ψ_{w0} . Top right: influence of α and T . Bottom left: influence of n and ψ_{w0} . Bottom right: influence of n and T .

5. Thermal and hydraulic parameters of soils and rocks

n	T=-0.2°C				$\Psi_{w0}=0$	T=-0.0002°C			
	$\alpha [mm^{-1}]$					$\alpha [mm^{-1}]$			
	0.001	0.01	0.1	0.4		0.001	0.01	0.1	0.4
1.1	5.0E1	4.0E1	3.3E1	2.9E1		1.1E3	1.2E4	4.3E4	4.9E4
1.5	6.8E1	2.3E1	8.8E0	5.5E0		1.3E3	3.5E4	1.6E5	1.0E5
2.0	2.9E1	4.8E0	2.4E0	2.2E0		4.1E2	3.8E4	1.6E5	1.0E5
2.5	1.0E1	2.4E0	2.1E0	2.2E0		1.0E2	3.0E4	2.2E5	3.2E4

Table 5.6: Apparent heat capacity [$MJ m^{-3} K^{-1}$] at saturation for $T=-0.2^\circ C$ (left) and at $-0.0002^\circ C$ (right), as function the combination (α, n) . In the calculation $\theta_s=0.4$ and $\theta_r=0$.

For this parameterization, a sensitivity analysis of each property was considered against porosity, temperature, saturation degree and the Van Genuchten parameters. The results show that the thermal conductivity strongly depends on porosity and temperature. The dependance on the saturation degree becomes important near $\Psi_{w0} = 0$, according to the shape of the SWC. The thermal capacity increases with porosity at positive temperatures and decreases with negative temperatures and is maximum at saturated unfrozen conditions. The hydraulic conductivity strongly depends on the saturation degree and on temperature, as the ice acts as an obstacle to the flow of water. According to the shape of the SWC, the hydraulic conductivity may vary of several orders of magnitude, representing the most variable parameter. Finally, the apparent heat capacity depends on temperature and on the shape of the SWC: near $T = T_m$ it increases by several orders of magnitude in very little temperature intervals. This may become an issue when the heat equation has to be numerically solved. The proper approach to deal with this discontinuity will be treated in the next session.

6 The freezing-soil model in GEOtop

6.1 Introduction

In section 3 the equilibrium relations for pressure and temperature have been revisited. The meaning and the consequences of the assumption *freezing=drying* have been highlighted and the relations for the SFC determined. In section 4 the equations for the mass and heat conservation have been thoroughly developed, starting from the continuity equation and thermodynamic equilibrium. The result is a system of two coupled non-linear differential equations on the variables T and Ψ_{w0} . In section 5 the modeling approaches for thermal and hydraulic properties of soils and rocks have been revisited. The high variability of the apparent heat capacity in proximity to $T = T_m$ has suggested the need for a proper numerical approach (*Hansson et al.*, 2004).

This section is intended to give a detailed explanation on the solution strategy for the system of differential equations. First a literary review of the current freezing-soil models will be given. Then the in the decoupling strategy for the equations will be discussed in the 1D case. Then a new numerical method to deal with the strong discontinuity in the apparent heat capacity will be presented. Finally the discretized equations with boundary conditions will be eventually thoroughly outlined.

The overall “*freezing-soil module*” will be eventually inserted in the hydrological model GEOtop (*Rigon et al.*, 2006) to enhance its capabilities in accounting for phase change and water flow in freezing/thawing soils.

6.2 The decoupled solution

Discretizing the mass (Eq. 4.20) and energy (Eq. 4.39) conservation equations in 1D along the vertical z coordinate (see in Fig. 6.1), one obtains:

$$\frac{\partial \Theta(\Psi_{w0})}{\partial t} - \frac{\partial}{\partial z} \left[K_H(\Psi_{w0}, T) \cdot \frac{\partial \Psi_{w1}(\Psi_{w0}, T)}{\partial z} - K_H \cos \beta \right] + S_w = 0 \quad (6.1)$$

$$\frac{\partial U(\psi_{w0}, T)}{\partial t} - \frac{\partial}{\partial z} \left[\lambda_T(\psi_{w0}, T) \cdot \frac{\partial T}{\partial z} - J(\psi_{w0}, T) \right] + S_{en} = 0 \quad (6.2)$$

where β is the slope angle of the surface with respect to the vertical. The above system is coupled as both equations are contemporarily functions of ψ_{w0} and T . *Hansson et al.* (2004) solve the above system in a coupled way in the numerical HYDRUS-1D code (*Simunek et al.*, 1998). In GEOTop the snow module is encapsulated inside the heat conservation equation, and so the number of nodes of the heat equation differs from the number of nodes of the mass conservation equation. Therefore the coupling of the two equations was not possible. Therefore the above system needs to be solved in a decoupled way, as explained in Fig. 6.2. The procedure may be summarized in three steps:

1. **get the initial θ_w and θ_i**

The initial total water content Θ may be simply determined by the SWC and ψ_{w0} . In fact $\Theta = \Theta(\psi_{w0})$. From Clausius Clapeyron equation, given the temperature at the time step T^n , applying Eq. 3.45 one can obtain the pressure ψ_{w1} . Then, through Eq. 3.48, one can calculate the initial liquid water content $\theta_w^n(\psi_{w1})$. The ice content $\theta_i^n(\psi_{w1})$ is the difference between the two, corrected by the water/ice density ratio.

2. **solve Richards' equation**

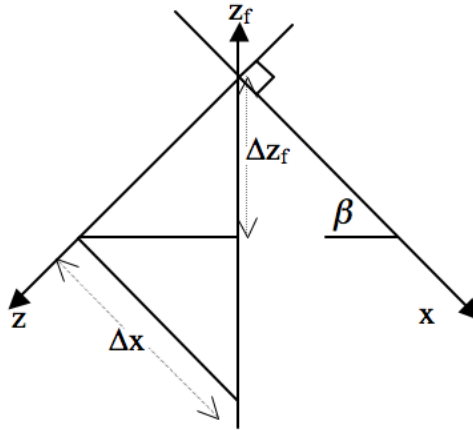


Figure 6.1: Schematization of the geometry along an inclined plane

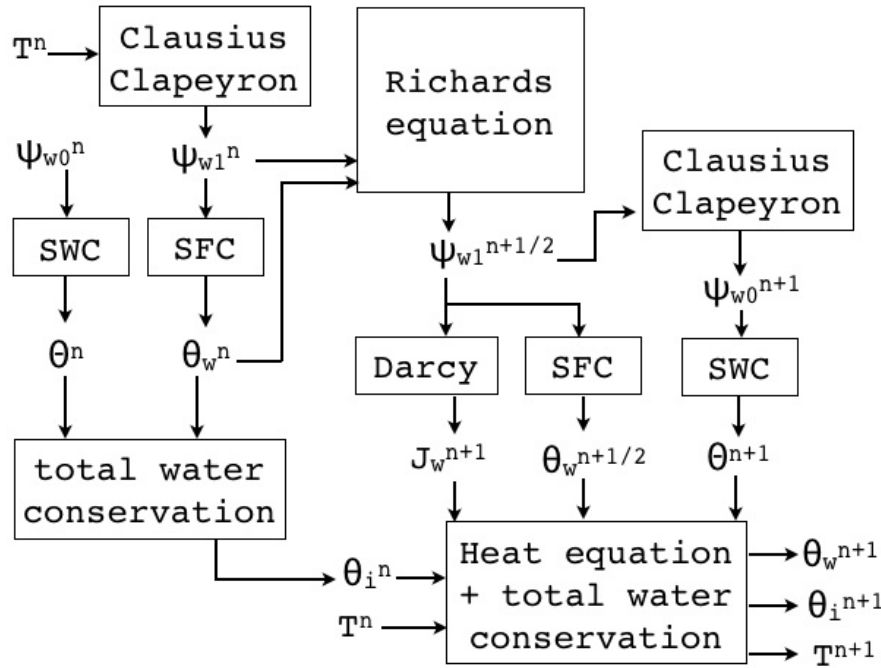


Figure 6.2: Flow chart for the decoupling of the freezing soil system: n means the time at the beginning of the time interval, $n+1$ means the time at the end

Keeping constant the temperature and the ice content at the time step n , Eq. 6.1 becomes:

$$\left\{ \begin{array}{l} T = T^n = \text{const} \\ \theta_i^n = \text{const} \end{array} \right. \Rightarrow \frac{\partial \theta_w(\psi_{w1})}{\partial t} + \frac{\partial J_w(\psi_{w1})}{\partial z} + S_w = 0 \Rightarrow \left\{ \begin{array}{l} \psi_{w1}^{n+1/2} \Rightarrow \theta_w^{n+1/2} \\ \psi_{w0}^{n+1} \Rightarrow \Theta^{n+1} \\ J_w^{n+1} \end{array} \right. \quad (6.3)$$

The above is a partial differential equation on the variable ψ_{w1} whose solution provides the new water pressure $\psi_{w1}^{n+1/2}$ and consequently the liquid water content $\theta_w^{n+1/2}$. These variables are denoted by the superscript $(n+1/2)$ to indicate that are intermediate values. Applying Darcy's law it is possible to calculate the water flux J_w^{n+1} which goes in input to the heat equation for the calculation of the advective flux. From $\psi_{w1}^{n+1/2}$, applying again 3.45, one finds the new ψ_{w0}^{n+1} and consequently the new total water content Θ^{n+1} .

3. solve heat equation

Keeping Θ^{n+1} constant, the ice content θ_i and water content θ_w are just function of tem-

perature. Therefore, the thermal conductivity $\lambda_T = \lambda_T(\theta_i, \theta_w) \equiv \lambda_T(T)$ is just a function of temperature, and so is the conduction flux $G = G(T)$. Also the internal energy becomes just a function of temperature, its value depending on the mix between θ_i and θ_w and on temperature itself. Furthermore, keeping constant the water flux J_w , the advection flux $J = J_w \cdot u_w(T) \equiv J(T)$ is just a function of temperature. Eventually Eq. 6.2 becomes:

$$\left\{ \begin{array}{l} \Theta^{n+1} = \text{const} \\ J_w^{n+1} = \text{const} \end{array} \right. \Rightarrow \frac{\partial U(T)}{\partial t} + \frac{\partial}{\partial z} [G(T) + J(T)] + S_{en} = 0 \Rightarrow \left\{ \begin{array}{l} \theta_w^{n+1} \\ \theta_i^{n+1} \\ T^{n+1} \end{array} \right. \quad (6.4)$$

This equation is now a differential equation on T and may be solved obtaining the new temperature T^{n+1} and the new mix of ice and water content in equilibrium at T^{n+1} given the total water content Θ^{n+1} .

6.3 The numerical scheme

The differential equations of mass and heat conservation share the common structure of *flow and budget equations*, since both include a conserved quantity (internal energy for the heat equation, and volumetric water content for the mass equation) and a flux (Fourier's law plus advection flux for the heat equation, and Darcy's law for the mass equation). Furthermore, both equations are characterized by a strong gradient of the conserved quantity in proximity of the "zero" (energy or mass). In fact, in the mass equation, the volumetric water content passes from relatively low values to complete saturation in proximity of the suction head $\psi = 0$, through the soil water characteristic curve. On the other hand, in the heat equation, the internal energy is subject to a sharp increment in proximity of the temperature $T = 0^\circ\text{C}$, due to the latent heat of fusion in the phase change transition. In this way, the transition unsaturated-saturated and frozen-thawed are analogous.

The budget and flow equations can be expressed as partial differential equations as follows:

$$\frac{\partial \xi}{\partial t} + \frac{\partial q}{\partial z} + S = 0 \quad (6.5)$$

with

$$q = f + u = -k \frac{\partial \eta}{\partial z} + u \quad (6.6)$$

where t is time, z is space, ξ is the conserved quantity expressed per unit of volume, q is the flux (discharge per unit of cross surface) of the conserved quantity, S is a sink term deriving from the

divergence of lateral fluxes or other natural processes like phase change or chemical and physical transformations, η is the potential or a variable (i.e. temperature in case of heat conduction) whose gradient governs the flow, k and u are conductivity coefficients.

The variables ξ , k and u are generally functions of a variable η and space, thus following the mathematical formalism:

$$\xi = \xi(\eta, z) \quad (6.7)$$

$$k = k(\eta, z) \quad (6.8)$$

$$u = u(\eta, z) \quad (6.9)$$

The functions introduced in (6.7), (6.8), (6.9) are assigned by the particular problem. Eq. 6.6 can be put in Eq. 6.5, thus:

$$\frac{\partial \xi}{\partial t} - \frac{\partial}{\partial z} \left[k \frac{\partial \eta}{\partial z} - u \right] + S = 0 \quad (6.10)$$

which can be defined as nonlinear diffusion-advection equation. The comparison between the equation of heat and mass balance can be easily outlined in Table 6.1.

Symbol	Heat	Unit	Mass	Unit
η	T	[°C]	ψ	[mm]
ξ	$U = C_T \cdot T + \rho_w L_f \theta_w$	[J m ⁻³]	$\Theta = \theta_w + \frac{\rho_i}{\rho_w} \theta_i$	[-]
f	$-\lambda_T \frac{\partial T}{\partial z}$	[W m ⁻²]	$-K_H \frac{\partial \psi}{\partial z}$	[mm s ⁻¹]
u	$\rho_w c_w J_w T$	[W m ⁻²]	$K_H \cos \beta$	[mm s ⁻¹]
q	$-\lambda_T \frac{\partial T}{\partial z} + \rho_w c_w J_w T$	[W m ⁻²]	$-K_H \frac{\partial \psi}{\partial z} + K_H \cos \beta$	[W m ⁻²]
$\frac{\partial \xi}{\partial \eta}$	$C_a(\Psi_{w0}, T)$	[J m ⁻³ K ⁻¹]	$C_H(\Psi_{w1})$	[mm ⁻¹]

Table 6.1: Comparison between heat and mass conservation equation as nonlinear diffusion-advection equations

If Eq. 6.10 is seen as Richards' equation, η is pressure head, ξ is water content, the function $\xi(\eta, z)$ corresponds to the soil water retention curve which can vary with space, k is the unsaturated hydraulic conductivity which is a function of water content and then pressure head, u is the unsaturated hydraulic conductivity k multiplied by a factor taking into account gravity, this factor

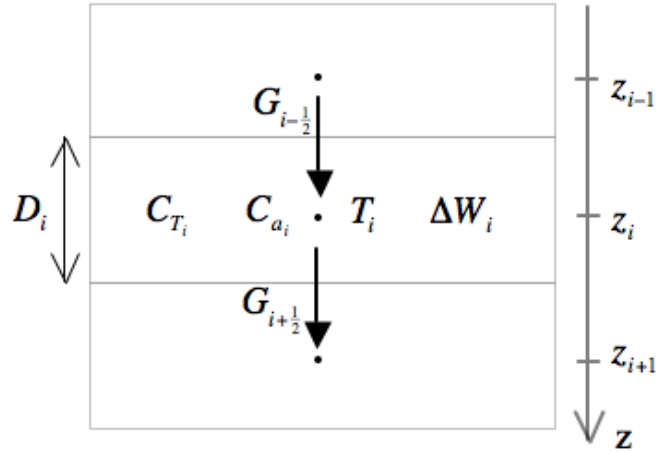


Figure 6.3: 1D discretization scheme for the energy equation in the soil/ rock

depending on surface slope and is 1 in case of a horizontal surface and axis z vertically downward. If Eq. 6.10 is instead seen as heat transfer equation in soils, η is temperature, ξ is the internal energy per unit of soil volume which depends on temperature, k is the thermal conductivity and u is the advection term due to liquid water flow. In both cases t is time, z is depth and S is the sink term depending on lateral flow, phase change.

6.3.1 The discretization

Eq. 6.10 in η can be only solved numerically, except few particular cases depending on the equations 6.7, 6.8 and 6.9. Eq. 6.5 represents the budget in a generic point of the domain and Eq. 6.10 is the 1D representation. One can discretize the system in 1D along the vertical z positive downwards as proposed in the discretization scheme in Fig. 6.3: to do so, the domain is divided into a finite number of cells and the cells are numbered with integer values starting from 1 and increasing with space coordinate z . The size of i -th cell is defined as Δz_i , the center of i -th cell is located at the depth z_i . The budget (6.5) is discretized and applied to the generic i -th cell:

$$\frac{\partial \xi_i(\eta_i, z_i)}{\partial t} + \frac{q_{i+\frac{1}{2}} - q_{i-\frac{1}{2}}}{\Delta z_i} + S_i = 0 \quad (6.11)$$

where $q_{i-\frac{1}{2}}$ and $q_{i+\frac{1}{2}}$ are the fluxes through the interfaces between the $i-1$ -th and i -th cells and between the i -th and $i+1$ -th cells respectively, $\xi_i(\eta_i, z_i)$ and S_i are the variables ξ and S averaged on the i -th cell extension. If ξ is the water content, $\xi_i(\eta_i, z_i)$ is the averaged water content of the i -th cell and S_i are the averaged losses due to lateral fluxes, root uptake and phase change. The variables $q_{i+\frac{1}{2}}$ and η_i are functions of time t and defined for each cell. The partial differential

Equation 6.5 is thus replaced with a system of ordinary differential equations like Eq. 6.11 which are the budgets of each cells. The flux $q_{i-\frac{1}{2}}$ depends on the gradient $\partial\eta/\partial z$ and the conductivities k and u evaluated at the interface between the $i-1$ -th and i -th cells according to Eq. 6.6. In absence of such detailed information, the gradient is replaced with a finite difference quotient and $q_{i-\frac{1}{2}}$ is calculated as follows:

$$q_{i-\frac{1}{2}} = -k_{i-\frac{1}{2}} \frac{\eta_i - \eta_{i-1}}{z_i - z_{i-1}} + u_{i-\frac{1}{2}} \quad (6.12)$$

where z_{i-1} and η_{i-1} are the location and the quantity η evaluated at the center of the $i-1$ -th cell, $k_{i-\frac{1}{2}}$ and $u_{i-\frac{1}{2}}$ are the conductivity evaluated at the interface and are also function of time t . The conductivities $k_{i-\frac{1}{2}}$ and $u_{i-\frac{1}{2}}$ are estimated by a suitable mean (arithmetic, geometric or harmonic, etc.) between the values of k and u evaluated by Eq. 6.8 and 6.9 at the nodes $i-1$ and i .

Replacing the index i with $i+1$ in Eq. 6.12, the flux $q_{i+\frac{1}{2}}$ is obtained as follows:

$$q_{i+\frac{1}{2}} = -k_{i+\frac{1}{2}} \frac{\eta_{i+1} - \eta_i}{z_{i+1} - z_i} + u_{i+\frac{1}{2}} \quad (6.13)$$

where the conductivities $k_{i+\frac{1}{2}}$ and $u_{i+\frac{1}{2}}$ at the interface between the i -th and $i+1$ -th cells and are defined and estimated analogously with $k_{i-\frac{1}{2}}$ and $u_{i-\frac{1}{2}}$.

The Equations 6.12 and 6.13 are the law which govern the flux between two adjacent cells, whereas Eq. 6.6 is the flux law which can applied in the case of a continuous medium. The conductivities $k_{i-\frac{1}{2}}$ and $u_{i-\frac{1}{2}}$ which depends on the values $k(\eta, z)$ and $u(\eta, z)$ applied to the nodes and the type of mean which is used, they might be also affected by the size of the cells. Let us note that the values of $k_{i-\frac{1}{2}}$ and $u_{i-\frac{1}{2}}$ significantly affect the transient dynamics whereas the whole budget is still conserved because of Eq. 6.11. It is recommended to pay much attention on how to estimate the conductivities on the borders between two cells.

After dividing the domain into a finite number of cells in which budget are calculated, Eq. 6.11 requires a discretization of time t to be solved. As a consequence, a time interval between two generic instants t^n and t^{n+1} is considered and Eq. 6.11 is integrated as follows:

$$\frac{1}{\Delta t^n} \int_{t^n}^{t^{n+1}} \frac{\partial \xi_i(\eta_i, z_i)}{\partial t} dt + \frac{1}{\Delta t^n} \int_{t^n}^{t^{n+1}} \frac{q_{i+\frac{1}{2}} - q_{i-\frac{1}{2}}}{\Delta z_i} dt + \frac{1}{\Delta t^n} \int_{t^n}^{t^{n+1}} S_i dt = 0 \quad (6.14)$$

where Δt^n is the considered time interval and it is $\Delta t^n = t^{n+1} - t^n$. Before solving the integrals in (6.14), the following assumptions are needed:

$$\frac{1}{\Delta t^n} \int_{t^n}^{t^{n+1}} q_{i-\frac{1}{2}} dt = q_{i-\frac{1}{2}}^{n+\frac{1}{2}} \approx (1 - \omega) q_{i-\frac{1}{2}}^n + \omega q_{i-\frac{1}{2}}^{n+1} \quad (6.15)$$

and analogously

$$\frac{1}{\Delta t^n} \int_{t_n}^{t^{n+1}} q_{i+\frac{1}{2}} dt = q_{i+\frac{1}{2}}^{n+\frac{1}{2}} \approx (1 - \omega) q_{i+\frac{1}{2}}^n + \omega q_{i+\frac{1}{2}}^{n+1} \quad (6.16)$$

where $q_{i-\frac{1}{2}}^{n+\frac{1}{2}}$ and $q_{i+\frac{1}{2}}^{n+\frac{1}{2}}$ are the averaged fluxes in the time interval Δt^n , $q_{i-\frac{1}{2}}^n$ and $q_{i+\frac{1}{2}}^n$ are the instantaneous values of the fluxes at the instant t^n , and $q_{i-\frac{1}{2}}^{n+1}$ and $q_{i+\frac{1}{2}}^{n+1}$ are the fluxes at the instant t^{n+1} . The parameter ω ranges between 0 and 1 and is defined in function of the numerical scheme used ($\omega = 0$, Explicit Euler Method, $\omega = 0.5$ Crank-Nicholson Method, $\omega = 1$ Euler-Implicit Method). The sink term in the right end side of (6.14) is averaged as follows:

$$\frac{1}{\Delta t^n} \int_{t_n}^{t^{n+1}} S_i dt = S_i^{n+\frac{1}{2}} \approx (1 - \omega_S) S_i^n + \omega_S S_i^{n+1} \quad (6.17)$$

where $S_i^{n+\frac{1}{2}}$ is the averaged sink term S_i within the time interval Δt^n , S_i^{n+1} and S_i^n are the sink term S_i evaluated at the final and initial instants t^{n+1} and t^n , ω_S is a dimensionless parameters between 0 and 1 depending on a chosen numerical approximation analogously with ω .

The budget given by Eq. 6.13 is thus fully discretized as follows:

$$-\omega \frac{q_{i+\frac{1}{2}}^{n+1} - q_{i-\frac{1}{2}}^{n+1}}{\Delta z_i} - (1 - \omega) \frac{q_{i+\frac{1}{2}}^n - q_{i-\frac{1}{2}}^n}{\Delta z_i} = \frac{\xi_i^{n+1} - \xi_i^n}{\Delta t^n} + S_i^{n+\frac{1}{2}} \quad (6.18)$$

This is the discretized budget equation of the i -th cell in a discrete time interval. The goal of of the problem is to predict the profile of the variable η at the time t^{n+1} for each cell, thus all variable referred at time t^n are known whereas all variables must be expressed as functions of η . Eq. 6.18 is rearranged as follows:

$$-\omega \frac{q_{i+\frac{1}{2}}^{n+1} - q_{i-\frac{1}{2}}^{n+1}}{\Delta z_i} = \frac{\xi_i^{n+1} - \xi_i^n}{\Delta t^n} + S_i^{n+\frac{1}{2}} + (1 - \omega) \frac{q_{i+\frac{1}{2}}^n - q_{i-\frac{1}{2}}^n}{\Delta z_i} \quad (6.19)$$

and replacing the unkwon fluxes (Eq. 6.12 and 6.19), it is:

$$\begin{aligned} \frac{\omega}{\Delta z_i} \left[k_{i+\frac{1}{2}}^{n+1} \frac{\eta_{i+1}^{n+1} - \eta_i^{n+1}}{z_{i+1} - z_i} - u_{i+\frac{1}{2}}^{n+1} - k_{i-\frac{1}{2}}^{n+1} \frac{\eta_i^{n+1} - \eta_{i-1}^{n+1}}{z_i - z_{i-1}} + u_{i-\frac{1}{2}}^{n+1} \right] &= \frac{\xi_i^{n+1} - \xi_i^n}{\Delta t^n} + \\ &+ S_i^{n+\frac{1}{2}} + (1 - \omega) \frac{q_{i+\frac{1}{2}}^n - q_{i-\frac{1}{2}}^n}{\Delta z_i} \end{aligned} \quad (6.20)$$

6.3.2 Iterative scheme

Eq. 6.20 is an algebraic nonlinear equation and can be solved by iterations. One common way is to use the fixed point iteration which is a method of computing fixed points of iterated functions.

More specifically, given $\eta = g(\eta)$ the fixed value problem where $v = g(v)$ is the solution, and given a point η_0 in the domain of g , the following succession:

$$\eta^{m+1} = g(\eta^m), \quad m = 0, 1, 2, \dots \quad (6.21)$$

gives rise to the fixed point iteration on the real numbers with real values in η which is hoped to converge to the solution v . This succession is also called *Picard iteration* and converges if $|g'(v_k)| < 1 \quad \forall k = 0, 1, 2, \dots, m-1$ and $v^k \in [v, \eta^k]$ (*Gambolati, 1994*).

To linearize the resulting discrete system of equations, Newton-Raphson or Picard iteration is commonly used. A comparison of Picard and Newton iteration in the numerical solution for similar problems can be found in *Paniconi and Putti (1994)*.

Picard iteration The unknowns η^{n+1} are initialized with empirical values which may be equal to η^n , then the coefficients of Eq. 6.19 are estimated and 6.20 is solved for several levels of reiteration. Therefore, the levels of reiteration are indicated by the second apex m and Eq. 6.19 is rewritten referring the unknowns η^{n+1} and ξ^{n+1} to the $m+1$ -th level of iteration whereas other variables related to the instant t^{n+1} are assumed as known and referred to the m -th reiteration level:

$$\begin{aligned} \frac{\omega}{\Delta z_i} \left[k_{i+\frac{1}{2}}^{n+1,m} \frac{\eta_{i+1}^{n+1,m+1} - \eta_i^{n+1,m+1}}{z_{i+1} - z_i} - u_{i+\frac{1}{2}}^{n+1,m} - k_{i-\frac{1}{2}}^{n+1,m} \frac{\eta_i^{n+1,m+1} - \eta_{i-1}^{n+1,m+1}}{z_i - z_{i-1}} + \right. \\ \left. + u_{i-\frac{1}{2}}^{n+1,m} \right] = \frac{\xi_i^{n+1,m+1} - \xi_i^n}{\Delta t^n} + S_i^{n+\frac{1}{2},m} + (1 - \omega) \frac{q_{i+\frac{1}{2}}^n - q_{i-\frac{1}{2}}^n}{\Delta z_i} \end{aligned} \quad (6.22)$$

where the unknowns are $\eta^{n+1,m+1}$ and $\xi^{n+1,m+1}$ in the left and right hand side respectively. The quantity $\xi_i^{n+1,m+1}$ is calculated with a first-order Taylor series (*Celia et al., 1990*):

$$\xi_i^{n+1,m+1} \approx \xi_i^{n+1,m} + C_i^{n+1,m} (\eta_i^{n+1,m+1} - \eta_i^{n+1,m}) \quad (6.23)$$

where $C_i^{n+1,m}$:

$$C_i^{n+1,m} = \left. \frac{\partial \xi(\eta, z)}{\partial \eta} \right|_{\eta^{n+1,m}} \quad (6.24)$$

is the capacity evaluated at the i -th node at the instant t^{n+1} (previous reiteration level) and is a

function of η and space. Replacing Eq. 6.23 into 6.19, it is:

$$\begin{aligned} & \frac{\omega}{\Delta z_i} \left[k_{i+\frac{1}{2}}^{n+1,m} \frac{\eta_{i+1}^{n+1,m+1} - \eta_i^{n+1,m+1}}{z_{i+1} - z_i} - u_{i+\frac{1}{2}}^{n+1,m} - k_{i-\frac{1}{2}}^{n+1,m} \frac{\eta_i^{n+1,m+1} - \eta_{i-1}^{n+1,m+1}}{z_i - z_{i-1}} + \right. \\ & \left. + u_{i-\frac{1}{2}}^{n+1,m} \right] = C_i^{n+1,m} \frac{\eta_i^{n+1,m+1} - \eta_i^{n+1,m}}{\Delta t^n} + \frac{\xi_i^{n+1,m} - \xi_i^n}{\Delta t^n} + S_i^{n+\frac{1}{2},m} + (1-\omega) \frac{q_{i+\frac{1}{2}}^n - q_{i-\frac{1}{2}}^n}{\Delta z_i} \end{aligned} \quad (6.25)$$

Eventually, the budget of the i -th cell can be rewritten in a tridiagonal form expliciting the unknowns η^{n+1} :

$$\begin{aligned} & \frac{\omega k_{i+\frac{1}{2}}^{n+1,m}}{(z_{i+1} - z_i)} \eta_{i+1}^{n+1,m+1} + \left[-\frac{\omega k_{i+\frac{1}{2}}^{n+1,m}}{(z_{i+1} - z_i)} - \frac{\omega k_{i-\frac{1}{2}}^{n+1,m}}{(z_i - z_{i-1})} - \frac{\Delta z_i}{\Delta t^n} C_i^{n+1,m} \right] \eta_i^{n+1,m+1} + \\ & + \frac{\omega k_{i-\frac{1}{2}}^{n+1,m}}{(z_i - z_{i-1})} \eta_{i-1}^{n+1,m+1} = \frac{\Delta z_i}{\Delta t^n} \left[\xi_i^{n+1,m} - \xi_i^n - C_i^{n+1,m} \eta_i^{n+1,m} \right] \\ & + S_i^{n+\frac{1}{2},m} \Delta z_i + (1-\omega) \left(q_{i+\frac{1}{2}}^n - q_{i-\frac{1}{2}}^n \right) + \omega \left(u_{i+\frac{1}{2}}^{n+1,m} - u_{i-\frac{1}{2}}^{n+1,m} \right) \end{aligned} \quad (6.26)$$

Then, Eq. 6.26 is repeated for each cell and an algebraic system of budget equations related to each cells is then defined after the Eq. 6.26 must be modified in the first and last cells according to boundary conditions.

Newton-Raphson method Given a function $f(\eta) = 0$ and its derivative $f'(\eta)$, we begin with a first guess η^m . A better approximation η^{m+1} would be:

$$f(\eta^m + h) \simeq f(\eta^m) + h f'(\eta^m) = 0 \quad \Rightarrow \quad \eta^{m+1} = \eta^m + h = \eta^m - [f'(\eta^m)]^{-1} \cdot f(\eta^m) \quad (6.27)$$

This scheme may be thought as a particular case of the Picard iteration, in which $g(\eta) = \eta - f(\eta)/f'(\eta)$. The convergence criteria of the Picard iteration requires that:

$$|g'(\eta)| < 1 \quad \Rightarrow \quad \frac{|f(\eta) f''(\eta)|}{[f'(\eta)]^2} < 1 \quad (6.28)$$

which is normally true for continuity reasons in a neighborhood of v , as for $\eta = v$ one has $f(\eta) = 0$. This scheme may not be applied in the case v is a multiple root, i.e. $f'(v) = 0$. The advantage of Newton-Raphson is therefore that it is more easily convergent, and that it is convergent to the second order. One may use Newton's method also to solve systems of k (non-linear)

equations. In this case the procedure may be so described:

$$A \vec{\eta} = \vec{b} \quad \Rightarrow \quad A \vec{\eta} - \vec{b} := \vec{\Gamma}(\eta) = 0 \quad (6.29)$$

$$\vec{\eta}^{m+1} \simeq \vec{\eta}^m - \left[\frac{\partial \vec{\Gamma}^m}{\partial \eta} \right]^{-1} \cdot \vec{\Gamma}(\eta^m) = \vec{\eta}^m - \vec{\Delta}\eta$$

where $\vec{\Gamma}$ is the remainder of the initial linear system, and $\left[\frac{\partial \vec{\Gamma}^m}{\partial \eta} \right]^{-1}$ is the inverse of the k-by-k Jacobian matrix A . One may notice that $A^{-1} \left[\vec{\Gamma}(\eta) \right] = \vec{\Delta}\eta$ is the increment of the solution and can be calculated solving the linear system $A \vec{\Delta}\eta = \vec{\Gamma}$.

Globally convergent Newton method The Newton-Raphson method works fine if the initial guess value η_0 is close enough to the true solution. Typically, a region which is well-behaved is located first with some other method, and Newton's method is then used to "polish" a root which is already known approximately. It may happen that, if the initial value is not close enough, the scheme may not converge (see Fig.6.4). This happens in the heat equation solution this happens during the phase transition, when temperature passes from positive to negative values or viceversa. At positive temperatures the heat capacity is ≈ 2 [MJ m⁻³K⁻¹] and at -0.1°C it assumes more or less the same value. At the latent term of the equation, in fact, is comprised in very small temperature intervals, where the peak of the apparent heat capacity is positioned (see Fig. 5.14) and may reach values $\approx 2E5$ (see Table 5.6). *Hansson et al.* (2004) recommend, in order to converge, to set the value of the heat capacity to its maximum value when passing from positive to negative temperature. However, although necessary, this precaution is not sufficient as we observed that the Newton's scheme was not converging. A considerable improvement was obtained switching to the so-called *globally convergent Newton scheme*. This scheme stems from the fact the the direction of the tangent given by the Newton's scheme is always a "good" direction, in the sense that it always points to the decreasing direction of the remainder. Yet the final point may be too far from the solution, and so the scheme may oscillate. In order to avoid this, the *globally convergent Newton scheme* suggests to put a check on the remainder:

$$\text{if } \|\vec{\Gamma}(\eta)^{m+1}\| > \|\vec{\Gamma}(\eta)^m\| \quad \Rightarrow \quad \vec{\eta}^{m+1} \simeq \vec{\eta}^m - \vec{\Delta}\eta \cdot \delta \quad (6.30)$$

This check means that we are getting far from the solution, then the increment must be multiplied by a reduction factor δ with $0 \leq \delta \leq 1$. If $\delta = 1$ the scheme is the same as the normal Newton-Raphson scheme. This method, together with the maximum heat capacity imposition, has proved to converge (see Section 7). This scheme is also applied by *Tomita* (2009) to solve surface energy balance equation, when the surface temperature shows oscillations caused by the exclusion

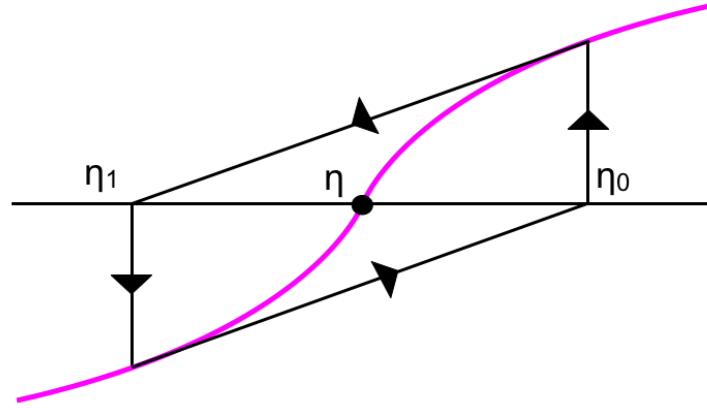


Figure 6.4: Schematization of a non convergent Newton-Raphson method

or poor consideration of the surface temperature dependence of the turbulent transfer coefficient at the surface.

6.3.3 Boundary conditions

The boundary conditions of the equation System 6.5 and 6.6, i.e. 6.10, can be assigned as flux (Neumann conditions) or as fixed value condition (Dirichlet condition). Let us examine the two cases.

6.3.3.1 Neumann condition

$$q = -k \frac{\partial \eta}{\partial z} + u = J_0(t, \eta) \quad z = 0 \quad (6.31)$$

$$q = -k \frac{\partial \eta}{\partial z} + u = J_L(t, \eta) \quad z = L \quad (6.32)$$

where 0 and L are the values of z coordinate at the boundary, $J_0(t, \eta)$ and $J_L(t, \eta)$ are the fluxes at the boundaries assigned as known functions of time and η . The conditions are discretized by replacing the flux J_0 and J_L in the budget equation (6.18) applied to the boundary cells. Therefore the budget equation (6.18) is rewritten for the first cell ($i = 1$):

$$-\omega \frac{q_{i+1/2}^{n+1} - J_0^{n+1}}{\Delta z_i} - (1 - \omega) \frac{q_{i+1/2}^n - J_0^n}{\Delta z_i} = \frac{\xi_i^{n+1} - \xi_i^n}{\Delta t^n} + S_i^{n+1/2} \quad (6.33)$$

where J_0^n and J_0^{n+1} are the incoming fluxes evaluated at the times t^n and t^{n+1} through the interface $i - 1/2$ deriving from the function $J_0(t, \eta)$:

$$\frac{1}{\Delta t^n} \int_{t_n}^{t^{n+1}} J_0 dt = J_0^{n+1/2} \approx (1 - \omega) J_0^n + \omega J_0^{n-1} \quad (6.34)$$

where J_0 is defined upon the interface and is a functions of η_1 , time t and other environmental forcing variables external to the problem. Let us note that no value of η is defined at the border of the domain or between two cells where J_0 with other fluxes and conductivities ($q_{i-1/2}$, $k_{i-1/2}$, $u_{i-1/2}$) are defined.

The boundary conditions at the last cell is analogously reported ($i = N$ where N is the number of cells and $L = \sum_{i=1}^N \Delta z_i$):

$$-\omega \frac{J_L^{n+1} - q_{i-1/2}^{n+1}}{\Delta z_i} - (1 - \omega) \frac{J_L^n - q_{i-1/2}^n}{\Delta z_i} = \frac{\xi_i^{n+1} - \xi_i^n}{\Delta t^n} + S_i^{n+1/2} \quad (6.35)$$

where J_L^n and J_L^{n+1} are the outgoing fluxes evaluated at the times t^n and t^{n+1} through the interface $i + 1/2$ deriving from the function $J_L(t, \eta)$:

$$\frac{1}{\Delta t^n} \int_{t_n}^{t^{n+1}} J_L dt = J_L^{n+1/2} \approx (1 - \omega) J_L^n + \omega J_L^{n-1} \quad (6.36)$$

where J_L is the outgoing flux depending on η_N through a "discretized" form of the function $J_L(t, \eta)$ in Equations 6.31 and 6.32: replacing the unknown fluxes with the definition of q given by Eq. 6.12 in Eq. 6.33 and 6.35 respectively one obtains:

$$\begin{aligned} \frac{\omega}{\Delta z_i} \left[k_{i+1/2}^{n+1} \frac{\eta_{i+1}^{n+1} - \eta_i^{n+1}}{z_{i+1} - z_i} - u_{i+1/2}^{n+1} + J_0^{n+1} \right] &= \frac{\xi_i^{n+1} - \xi_i^n}{\Delta t^n} + \\ &+ S_i^{n+1/2} + (1 - \omega) \frac{q_{i+1/2}^n - J_0^n}{\Delta z_i} \end{aligned} \quad (6.37)$$

and

$$\begin{aligned} \frac{\omega}{\Delta z_i} \left[-J_L^{n+1} - k_{i-1/2}^{n+1} \frac{\eta_i^{n+1} - \eta_{i-1}^{n+1}}{z_i - z_{i-1}} + u_{i-1/2}^{n+1} \right] &= \frac{\xi_i^{n+1} - \xi_i^n}{\Delta t^n} + \\ &+ S_i^{n+1/2} + (1 - \omega) \frac{J_L^n - q_{i-1/2}^n}{\Delta z_i} \end{aligned} \quad (6.38)$$

Then, applying Picard reiterative method, respectively:

$$\frac{\omega}{\Delta z_i} \left[k_{i+1/2}^{n+1,m} \frac{\eta_{i+1}^{n+1,m+1} - \eta_i^{n+1,m+1}}{z_{i+1} - z_i} - u_{i+1/2}^{n+1,m} + J_0^{n+1,m+1} \right] = \frac{\xi_i^{n+1,m+1} - \xi_i^n}{\Delta t^n} + S_i^{n+1/2,m} + (1 - \omega) \frac{q_{i+1/2}^n - J_0^n}{\Delta z_i} \quad (6.39)$$

and

$$\frac{\omega}{\Delta z_i} \left[-J_L^{n+1,m+1} - k_{i-1/2}^{n+1,m} \frac{\eta_i^{n+1,m+1} - \eta_{i-1}^{n+1,m+1}}{z_i - z_{i-1}} + u_{i-1/2}^{n+1,m} \right] = \frac{\xi_i^{n+1,m+1} - \xi_i^n}{\Delta t^n} + S_i^{n+1/2,m} + (1 - \omega) \frac{J_L^n - q_{i-1/2}^n}{\Delta z_i} \quad (6.40)$$

where $J_0^{n+1,m+1}$ and $J_L^{n+1,m+1}$ are the fluxes J_0^{n+1} and J_L^{n+1} evaluated at the $m + 1$ -th level of reiteration.

Analogously to Eq. 6.26, Equations 6.39 and 6.40 are rewritten in a tridiagonal form:

$$\begin{aligned} & \frac{\omega k_{i+1/2}^{n+1,m}}{\Delta z_i (z_{i+1} - z_i)} \eta_{i+1}^{n+1,m+1} + \left[-\frac{\omega k_{i+1/2}^{n+1,m}}{\Delta z_i (z_{i+1} - z_i)} - \frac{C_i^{n+1,m}}{\Delta t^n} \right] \eta_i^{n+1,m+1} = \\ & = -C_i^{n+1,m} \frac{\eta_i^{n+1,m}}{\Delta t^n} + \frac{\xi_i^{n+1,m} - \xi_i^n}{\Delta t^n} + S_i^{n+1/2,m} + \\ & + (1 - \omega) \frac{q_{i+1/2}^n - J_0^n}{\Delta z_i} + \omega \frac{u_{i+1/2}^{n+1,m}}{\Delta z_i} - \omega \frac{J_0^{n+1,m+1}}{\Delta z_i} \end{aligned} \quad (6.41)$$

with $i = 1$ and

$$\begin{aligned} & \left[-\frac{\omega k_{i-1/2}^{n+1,m}}{\Delta z_i (z_i - z_{i-1})} - \frac{C_i^{n+1,m}}{\Delta t^n} \right] \eta_i^{n+1,m+1} + \\ & + \frac{\omega k_{i-1/2}^{n+1,m}}{\Delta z_i (z_i - z_{i-1})} \eta_{i-1}^{n+1,m+1} = -C_i^{n+1,m} \frac{\eta_i^{n+1,m}}{\Delta t^n} + \frac{\xi_i^{n+1,m} - \xi_i^n}{\Delta t^n} + S_i^{n+1/2,m} + \\ & + (1 - \omega) \frac{J_{L_{i+1/2}}^n - q_{i-1/2}^n}{\Delta z_i} - \omega \frac{u_{i-1/2}^{n+1,m}}{\Delta z_i} + \omega \frac{J_L^{n+1,m+1}}{\Delta z_i} \end{aligned} \quad (6.42)$$

with $i = N$.

The fluxes $J_0^{n+1,m+1}$ and $J_L^{n+1,m+1}$ are thus estimated by Taylor's series:

$$J_0^{n+1,m+1} \approx J_0^{n+1,m} + \left. \frac{\partial J_0}{\partial \eta_i} \right|_{\eta_i = \eta_1^{n+1,m}} \left(\eta_1^{n+1,m+1} - \eta_1^{n+1,m} \right) \quad (6.43)$$

and

$$J_L^{n+1,m+1} \approx J_L^{n+1,m} + \left. \frac{\partial J_L}{\partial \eta_i} \right|_{\eta_i = \eta_N^{n+1,m}} \left(\eta_N^{n+1,m+1} - \eta_N^{n+1,m} \right) \quad (6.44)$$

Replacing Eq. 6.43 and 6.44 into Eq. 6.41 and 6.42, one obtains:

$$\begin{aligned} & \frac{\omega k_{1+1/2}^{n+1,m}}{(z_2 - z_1)} \eta_2^{n+1,m+1} + \left[-\frac{\omega k_{1+1/2}^{n+1,m}}{(z_2 - z_1)} + \omega \left. \frac{\partial J_0}{\partial \eta_1} \right|_{\eta_1 = \eta_1^{n+1,m}} - \Delta z_1 \frac{C_1^{n+1,m}}{\Delta t^n} \right] \eta_1^{n+1,m+1} = \\ & = -C_1^{n+1,m} \frac{\eta_1^{n+1,m}}{\Delta t^n} \Delta z_1 + \frac{\xi_1^{n+1,m} - \xi_1^n}{\Delta t^n} \Delta z_1 + S_1^{n+1/2,m} \Delta z_1 + \\ & + (1 - \omega) (q_{1+1/2}^n - J_0^n) + \omega \cdot u_{1+1/2}^{n+1,m} - \omega \left(J_0^{n+1,m} - \left. \frac{\partial J_0}{\partial \eta_1} \right|_{\eta_1 = \eta_1^{n+1,m}} \eta_1^{n+1,m} \right) \end{aligned} \quad (6.45)$$

with $i = 1$ and

$$\begin{aligned} & \frac{\omega k_{N-1/2}^{n+1,m}}{\Delta z_N (z_N - z_{N-1})} \eta_{N-1}^{n+1,m+1} + \left[-\frac{\omega k_{N-1/2}^{n+1,m}}{\Delta z_N (z_N - z_{N-1})} - \frac{\omega}{\Delta z_N} \left. \frac{\partial J_L}{\partial \eta_N} \right|_{\eta_N = \eta_N^{n+1,m}} - \frac{C_N^{n+1,m}}{\Delta t^n} \right] \eta_N^{n+1,m+1} = \\ & -C_N^{n+1,m} \frac{\eta_N^{n+1,m}}{\Delta t^n} + \frac{\xi_N^{n+1,m} - \xi_N^n}{\Delta t^n} + S_N^{n+1/2,m} + \\ & + (1 - \omega) \frac{J_L^n - q_{N-1/2}^n}{\Delta z_N} - \omega \frac{u_{N-1/2}^{n+1,m}}{\Delta z_N} + \omega \frac{J_L^{n+1,m} + \left. \frac{\partial J_L}{\partial \eta_N} \right|_{\eta_N = \eta_N^{n+1,m}} \left(\eta_N^{n+1,m+1} - \eta_N^{n+1,m} \right)}{\Delta z_N} \end{aligned} \quad (6.46)$$

with $i = N$.

6.3.3.2 Dirichlet condition

The Dirichlet conditions allow to fix the value of η on the borders. In this case we suppose the existence of a node in $z_0 = -\Delta z/2$ and in $z_{N+1} = z_N + \Delta z_N = L + \Delta z_N/2$. One obtains:

$$\begin{cases} \eta_0 = \eta_0(t) & z = 0 \\ \eta_{N+1} = \eta_L = \eta_L(t) & z = L \end{cases} \quad (6.47)$$

6. The freezing-soil model in GEOTop

The fluxes $q_{1-\frac{1}{2}}$ and $q_{N+\frac{1}{2}}$ become respectively:

$$\begin{cases} q_{1-\frac{1}{2}} = q_0 = -k_1 \frac{\eta_1 - \eta_0}{\Delta z_1} + u_{1-\frac{1}{2}} \\ q_{N+\frac{1}{2}} = q_L = -k_N \frac{\eta_N - \eta_{N-1}}{\Delta z_N} + u_{N+\frac{1}{2}} \end{cases} \quad (6.48)$$

The values of the fluxes in the two boundary conditions (Neumann and Dirichlet) for the heat equation can be summarized in Table 6.2.

flux	Dirichlet	Neumann
q_0	$-\lambda_{T_1} \frac{T_1 - T_0}{\Delta z_1} + \rho_w u_w(T_{inf}) J_{w_{inf}}$	$R_n + \rho_w u_w(T_{inf}) J_{w_{inf}}$
q_L	$-\lambda_{T_L} \frac{T_L - T_N}{\Delta z_N} + \rho_w u_w(T_L) J_{w_L}$	$-G_{geot} + \rho_w u_w(T_L) J_{w_L}$

Table 6.2: *Boundary fluxes according to Dirichlet and Neumann boundary condition. R_n stands for net radiation and G_{geot} for the geothermal heat flux at the bottom*

If we substitute the first condition of Eq. 6.47 in Eq. 6.20 and suppose $i = 1$:

$$\begin{aligned} \frac{\omega}{\Delta z_1} \left[k_{1+\frac{1}{2}}^{n+1} \frac{\eta_2^{n+1} - \eta_1^{n+1}}{z_2 - z_1} - u_{1+\frac{1}{2}}^{n+1} - k_1^{n+1} \frac{\eta_1^{n+1} - \eta_0^{n+1}}{\Delta z_1} + u_{1-\frac{1}{2}}^{n+1} \right] &= \frac{\xi_1^{n+1} - \xi_1^n}{\Delta t^n} + \\ &+ S_1^{n+\frac{1}{2}} + (1 - \omega) \frac{q_{1+\frac{1}{2}}^n - q_{1-\frac{1}{2}}^n}{\Delta z_1} \end{aligned} \quad (6.49)$$

After few algebraic calculation and applying the Picard iteration one obtains:

$$\begin{aligned} \left[-\frac{\omega k_{1+1/2}^{n+1,m}}{(z_2 - z_1)} - \omega \frac{k_1}{\Delta z_1} - C_1^{n+1,m} \frac{\Delta z_1}{\Delta t^n} \right] \eta_1^{n+1,m+1} &+ \frac{\omega k_{1+1/2}^{n+1,m}}{(z_2 - z_1)} \eta_2^{n+1,m+1} = \\ &= \frac{\Delta z_1}{\Delta t^n} \left(\xi_1^{n+1,m} - \xi_1^n - C_1^{n+1,m} \eta_1^{n+1,m} \right) + S_1^{n+1/2,m} \Delta z_1 + \\ &+ (1 - \omega) (q_{1+\frac{1}{2}}^n - q_0^n) - \omega \frac{k_1}{\Delta z_1} \eta_0^{n+1} + \omega \left(u_{1+1/2}^{n+1,m} - u_0^{n+1,m} \right) \end{aligned} \quad (6.50)$$

If we substitute the second condition of Eq. 6.47 in Eq. 6.20 and suppose $i = N$:

$$\begin{aligned} \frac{\omega}{\Delta z_N} \left[k_N^{n+1} \frac{\eta_{N+1}^{n+1} - \eta_N^{n+1}}{\Delta z_N} - u_{N+\frac{1}{2}}^{n+1} - k_{N-\frac{1}{2}}^{n+1} \frac{\eta_N^{n+1} - \eta_{N-1}^{n+1}}{z_N - z_{N-1}} + u_{N-\frac{1}{2}}^{n+1} \right] &= \frac{\xi_N^{n+1} - \xi_N^n}{\Delta t^n} + \\ &+ S_N^{n+\frac{1}{2}} + (1 - \omega) \frac{q_{N+\frac{1}{2}}^n - q_{N-\frac{1}{2}}^n}{\Delta z_N} \end{aligned} \quad (6.51)$$

After few algebraic calculation and applying the Picard iteration one obtains:

$$\begin{aligned}
& \frac{\omega k_{N-1/2}^{n+1,m}}{\Delta z_N (z_N - z_{N-1})} \eta_{N-1}^{n+1,m+1} + \left[-\frac{\omega k_{N-1/2}^{n+1,m}}{(z_N - z_{N-1})} - \omega \frac{k_N}{\Delta z_N / 2} - C_N^{n+1,m} \frac{\Delta z_N}{\Delta t^n} \right] \eta_N^{n+1,m+1} = \\
& \frac{\Delta z_N}{\Delta t^n} \left(\xi_N^{n+1,m} - \xi_N^n - C_N^{n+1,m} \eta_N^{n+1,m} \right) - S_N^{n+1/2} \Delta z_N + \\
& + (1 - \omega) (q_L^n - q_{1+\frac{1}{2}}^n) - \omega \frac{k_N}{\Delta z_N} \eta_L^{n+1} + \omega \left(u_{L-1/2}^{n+1,m} - u_L^{n+1,m} \right) \quad (6.52)
\end{aligned}$$

6.4 Conclusions

This section has reported a description of the *freezing soil* developed in the hydrological model GEOtop. The equations of mass and heat conservation results in a coupled system of nonlinear diffusion-advection equations on the unknown T and ψ_{w0} . The system in GEOtop may not be solved coupled, as the number of nodes in the energy equation differs from the number of nodes in the heat equation, due to the presence snow module just in the heat equation. Therefore the system was solve in a decoupled way in three steps: (1) get initial water and ice content, (2) solve Richards' equation and (3) solve heat equation. The apparent heat capacity is characterized by a peak in proximity of T_m . When passing from positive to negative temperatures, the numerical scheme was subject to high oscillations, and did not converge. The convergence was found to be improved by the use of two precautions: (1) when passing from positive to negative temperatures (or vice-versa), the value of the heat capacity must be assigned to the maximum apparent heat capacity; (2) the Newton scheme must be modified to the *globally convergent Newton scheme*, characterized by a check on the remainder. This scheme has proved to be robust, as will be demonstrated in the following session.

7 Model validation

7.1 Introduction

In the previous section the *freezing soil module* developed in GEOtop was presented, and the numerical method thoroughly outlined. This section is meant to apply the model and to prove its numerical stability and precision. The validation of the model has been performed in successive steps with increasing complexity: first pure conduction with constant λ_T and C_T ; then pure conduction with variable λ_T , and then conduction with phase change without water movement (Stefan problem). Eventually, conduction with phase change with water movement. The test has been accomplished against the analytical solution for the first three cases, and against experimental results deriving from inherent publications for the last case.

7.2 Pure conduction

Considering a pure conduction case Eq. 6.2 becomes:

$$C_T \frac{\partial T}{\partial t} - \frac{\partial}{\partial z} \left(\lambda_T \frac{\partial T}{\partial z} \right) = 0 \quad (7.1)$$

This equation, under proper assumptions, admits the analytical solution $T(z, t)$ for every z, t . Let us consider two cases: linear case, in which the thermal coefficients are constants ($C_T = 1$, $\lambda = 1$) and non-linear case in which the thermal conductivity is function of the solution ($C_T = 1$, $\lambda = \lambda(T)$).

7.2.1 Linear conduction equation

Equation 7.2 in the case of $C_T = 1$ and $\lambda = 1$ becomes the classical diffusion equation:

$$\frac{\partial T}{\partial t} - D \frac{\partial^2 T}{\partial z^2} = 0 \quad (7.2)$$

7. Model validation

where $D = \lambda/C_T \equiv 1$ in this case. Considering an homogeneous initial temperature profile characterized by a discontinuity given by:

$$T(x,0) = \begin{cases} T_R & \text{if } z < z_0 \\ T_L & \text{if } z \geq z_0 \end{cases} \quad (7.3)$$

one obtains the following analytical solution:

$$\begin{aligned} T(z,t) &= \frac{1}{\sqrt{4\pi Dt}} \left[T_L \int_{-\infty}^{z_0} \exp\left(-\frac{(z-z_0-\xi)^2}{4Dt}\right) d\xi + T_R \int_{z_0}^{\infty} \exp\left(-\frac{(z-z_0-\xi)^2}{4Dt}\right) d\xi \right] = \\ &= \frac{T_L + T_R}{2} - \frac{T_L - T_R}{2} \operatorname{erf}\left(\frac{z-z_0}{\sqrt{4Dt}}\right) \end{aligned} \quad (7.4)$$

The problem has been numerically solved considering a Dirichlet boundary condition with $T_0 = T_L$ and $T_{N+1} = T_R$. The domain is a 10 Km profile with 100 nodes of grid size $\Delta z=100\text{m}$ and integration interval $\Delta t=60\text{sec}$. The upper boundary condition was set to $T_L=1000^\circ\text{C}$ and bottom boundary condition $T_R = 1^\circ\text{C}$. In Fig. 7.1 on the left is reported the behavior of the simulated temperature against the analytical solution of Eq. 7.6 after a simulation time of 1 day, 2 days, 3 days, 5 days and 10 days. In Fig. 7.1 on the right is reported the absolute error of the simulation.

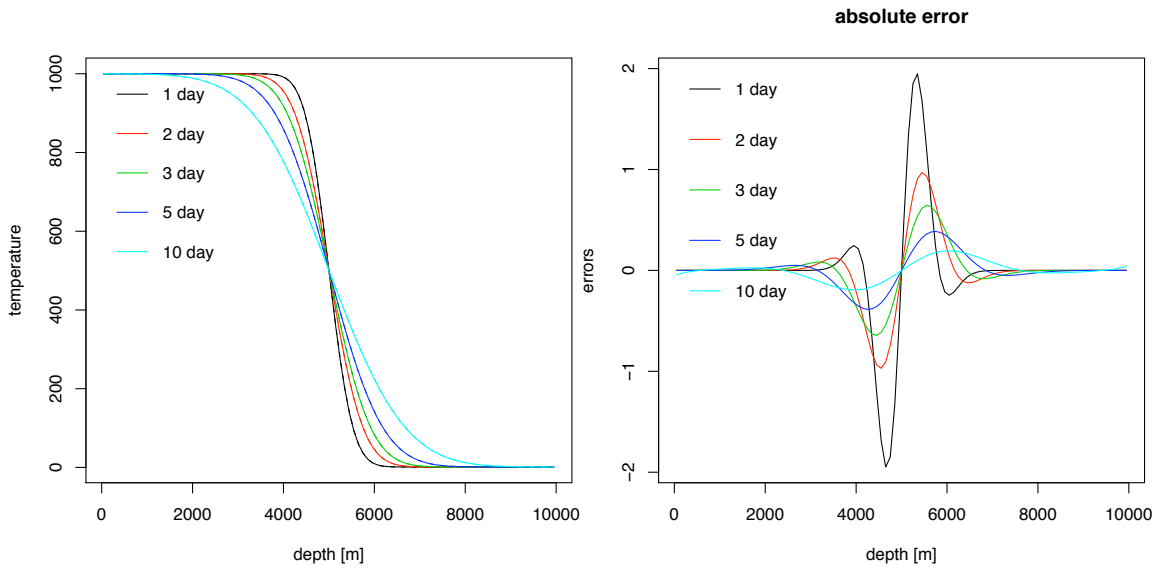


Figure 7.1: *Left: comparison between the numerical and analytical solution of the linear conduction example. The colors represent different time frames. Right: absolute error at different time frames*

7.2.2 Non-linear conduction equation

Eq. 7.2 in the case of $C_T = 1$ and $\lambda = \lambda(T)$ yealds again the diffusion equation but with diffusivity as a function of temperature. One obtains:

$$\frac{\partial T}{\partial t} - \frac{\partial}{\partial z} \left(D(T) \cdot \frac{\partial T}{\partial z} \right) = 0 \quad (7.5)$$

where $D = \lambda(T)/C_T$. Considering an homogeneous initial temperature profile characterized by a discontinuity given by:

$$T(z, 0) = \begin{cases} 1 - \delta & \text{if } z < z_0 \\ \delta & \text{if } z \geq z_0 \end{cases} \quad (7.6)$$

where δ is a parameter, and the variation of the thermal conductivity λ as:

$$\lambda(T) = \varepsilon T (1 - T) \quad (7.7)$$

with ε as a parameter, one obtains the following analytical solution (*Dumbser et al.*, 2008):

$$T(z, t) = \min \left\{ 1, \max \left[0, \frac{1}{2} \left(1 - \frac{z - z_0}{\sqrt{\varepsilon t}} \right) \right] \right\} \quad (7.8)$$

The problem has been numerically solved considering a Dirichlet boundary condition with $T_0 = 1 - \delta$ and $T_{N+1} = \delta$. The domain is a 10Km profile with 500 nodes of grid size $\Delta z = 20\text{m}$ and integration interval $\Delta t = 60\text{sec}$. The discontinuity is located at the middle of the domain at 5Km. In the simulation the parameter $\delta = 1E - 3$ and the parameter $\varepsilon = 1.0$.

In Fig. 7.2 on the left is reported the behavior of the temperature at different time frame and on the right is reported the absolute error of the simulation.

7.3 Conduction and phase change without water movement

Quoting *Carslaw and Jaeger* (1959), “[...] the problem of freezing is frequently referred to as the ”problem of Stefan”, as Stefan was the first to publish a discussion of problems of phase change in a study of the thickness of polar ice. The essential new feature of such problems is the existence of a moving surface of separation between the two phases, where heat is liberated or absorbed on it, and the thermal properties of the two phases on different sides of it may be different”.

A simple case of a moving boundary is often referred to as the Neumann problem, of which *Nakano and Brown* (1971), following the approach described by *Carslaw and Jaeger* (1959) for a homogeneous substance, give the analytical solution for an initially frozen soil bound to a constant

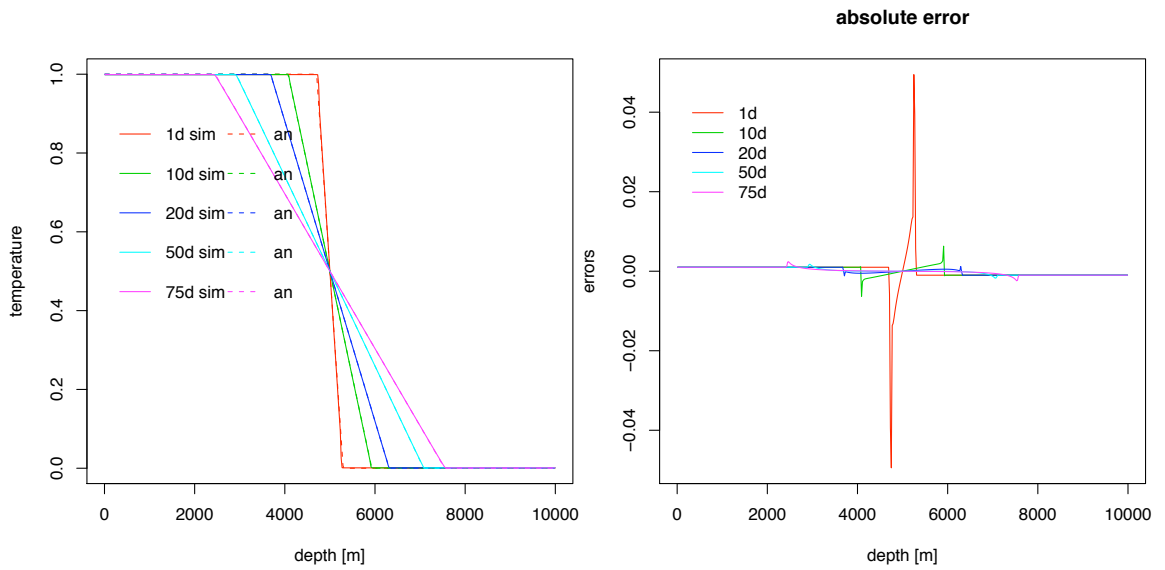


Figure 7.2: *Left: comparison between the numerical and analytical solution of the non-linear conduction example. The colors represent different time frames. Right: absolute error at different time frames*

Dirichlet boundary condition at the top. The approximations made are the following:

- the heat flow between the surface $z = 0$ and the surface of separation $z = Z(t)$ is of steady type;
- the change of volume is neglected: $\rho_w = \rho_i$
- the phase change is instantaneous, i.e. no unfrozen water at temperatures less than the melting temperature T_m is allowed. Therefore when the temperature is greater than the melting temperature T_m then all the present water is liquid, whereas when the temperature is lower than T_m then all the water is solid.

$$\left\{ \begin{array}{l} \text{if } T < T_m \Rightarrow \Theta \equiv \theta_i \\ \text{if } T \geq T_m \Rightarrow \Theta \equiv \theta_w \end{array} \right. \quad (7.9)$$

7.3.1 Freezing case

Referring to the scheme illustrated in Fig. 7.3, the system of equations in this case becomes:

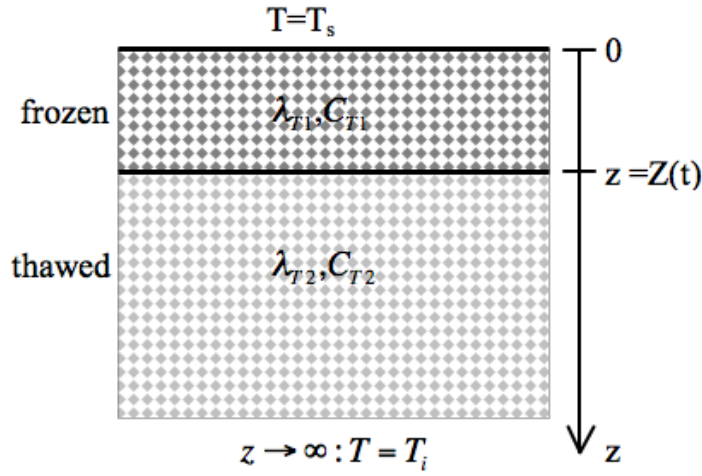


Figure 7.3: The problem of Neumann

$$\left\{ \begin{array}{ll}
 v_1 = v_2 = T_{ref} & (t > 0, z = Z(t)) \\
 v_2 \rightarrow T_i & (t > 0, z \rightarrow \infty) \\
 v_1 = T_s & (t > 0, z = 0) \\
 \lambda_1 \frac{\partial v_1}{\partial z} - \lambda_2 \frac{\partial v_2}{\partial z} = L_f \rho_w \theta_s \frac{dZ(t)}{dt} & (t > 0, z = Z(t)) \\
 \frac{\partial v_1}{\partial t} = k_1 \frac{\partial^2 v_1}{\partial z^2} & (t > 0, z < Z(t)) \\
 \frac{\partial v_2}{\partial t} = k_2 \frac{\partial^2 v_2}{\partial z^2} & (t > 0, z > Z(t)) \\
 v_1 = v_2 = T_i & (t = 0, z)
 \end{array} \right. \quad (7.10)$$

where the index 1 refers to the "frozen state" whereas the index 2 refers to the "thawed state" above and below the moving surface respectively, z is the space coordinate, positive downwards, v_1 and v_2 are the temperature of the frozen and thawed soil and T_{ref} is the temperature of phase change ($0^\circ C$ in this case). The first and second Equations in 7.10 give the boundary conditions at bottom ($T = T_i$) and at the surface ($T = T_s$) of the domain respectively (Dirichlet condition);

the third and fourth equations refer to the boundary conditions at the interface between the two substances, indicating that the temperatures of the two states are equal to the temperature of phase change on the surface and that the energy derived by the difference of the heat fluxes is exploited for phase change. The fifth and sixth equations refer to the approximation of steady state conduction behavior of the temperature in the two states, where $k = \lambda_T / C_T$ is the thermal diffusivity. Finally the last equation reports the initial condition in which the whole system is set at $T = T_i$. Considering a "saturation" condition, the thermal parameters are modeled according to Eq. 5.3 and 5.7:

$$C_{T1} = C_{gs} (1 - \theta_s) + c_i \rho_w \theta_s \quad (7.11)$$

$$C_{T2} = C_{gs} (1 - \theta_s) + c_w \rho_w \theta_s$$

$$\lambda_{T1} = \lambda_{gs}^{1-\theta_s} \cdot \lambda_i^{\theta_s}$$

$$\lambda_{T2} = \lambda_{gs}^{1-\theta_s} \cdot \lambda_w^{\theta_s}$$

If we make the following change of variable: $v_1^* = v_1 - T_s$ and $v_2^* = v_2$, the first and third Equations in 7.10 become:

$$\left\{ \begin{array}{ll} v_1^* + T_s = T_{ref} \Rightarrow v_1^* + T_s = T_{ref} & \text{if } z = Z(t) \\ v_2^* = T_{ref} & \text{if } z = Z(t) \\ v_1^* + T_s = T_s \Rightarrow v_1^* = 0 & \text{if } z = 0 \end{array} \right. \quad (7.12)$$

therefore we obtain a homogeneous Dirichlet condition at the surface. We can realize that:

$$v_1^* = A \cdot \operatorname{erf} \frac{z}{2\sqrt{k_1 t}} \quad (7.13)$$

$$v_2^* = T_i - B \cdot \operatorname{erfc} \frac{z}{2\sqrt{k_2 t}} \quad (7.14)$$

satisfy the fifth and third and the sixth and second equations in Eq. 7.10 respectively. Combining Eq. 7.13 and 7.14 with the first and second Equations in 7.12 one obtains:

$$A \cdot \operatorname{erf} \frac{z}{2\sqrt{k_1 t}} + T_s = T_{ref} = T_i - B \cdot \operatorname{erfc} \frac{z}{2\sqrt{k_2 t}} \quad (7.15)$$

The only formulation admitted for the advance of the moving boundary is $z \propto \sqrt{k_1 t}$ and, substituting $z = 2\zeta\sqrt{k_1 t}$ in Eq. 7.15 one obtains the formula of A and B :

$$A = \frac{T_{ref} - T_s}{\operatorname{erf} \zeta} \quad (7.16)$$

$$B = \frac{T_i - T_{ref}}{\operatorname{erfc}\left(\zeta\sqrt{\frac{k_1}{k_2}}\right)} \quad (7.17)$$

Combining Eq. 7.16 and 7.17 in the the fourth equation in 7.10 one obtains:

$$\frac{\exp(-\zeta^2)}{\zeta \cdot \operatorname{erf}\zeta} - \frac{\lambda_{T2} \sqrt{k_1} (T_i - T_{ref})}{\lambda_{T1} \sqrt{k_2} (T_{ref} - T_s) \zeta \cdot \operatorname{erfc}\left(\zeta\sqrt{\frac{k_1}{k_2}}\right)} \cdot \exp\left(-\frac{k_1}{k_2} \zeta^2\right) = \frac{L_f \rho_w \theta_s \sqrt{\pi}}{C_{T1} (T_{ref} - T_s)} \quad (7.18)$$

which is a function of ζ that can be solved. Eventually the analytical solution of v_1 and v_2 becomes:

$$\begin{cases} v_1(t, z) = T_s + \frac{T_{ref} - T_s}{\operatorname{erf}\zeta} \cdot \operatorname{erf}\frac{z}{2\sqrt{k_1 t}} & \text{if } z \leq Z(t) \\ v_2(t, z) = T_i - \frac{T_i - T_{ref}}{\operatorname{erfc}\left(\zeta\sqrt{\frac{k_1}{k_2}}\right)} \cdot \operatorname{erfc}\frac{z}{2\sqrt{k_2 t}} & \text{if } z > Z(t) \end{cases} \quad (7.19)$$

Assigning the following values to the parameters and initial/boundary conditions: $\theta_s = 0.4$, $T_i(0, z) = 2^\circ\text{C}$ and $T_s(t > 0, 0) = -5^\circ\text{C}$, $\lambda_{gs} = 2.5 \frac{\text{W}}{\text{m K}}$ and $C_{gs} = 2.30E6 \frac{\text{J}}{\text{m}^3 \text{K}}$, we obtain a behavior of a freezing front as depicted in Fig. 7.4.

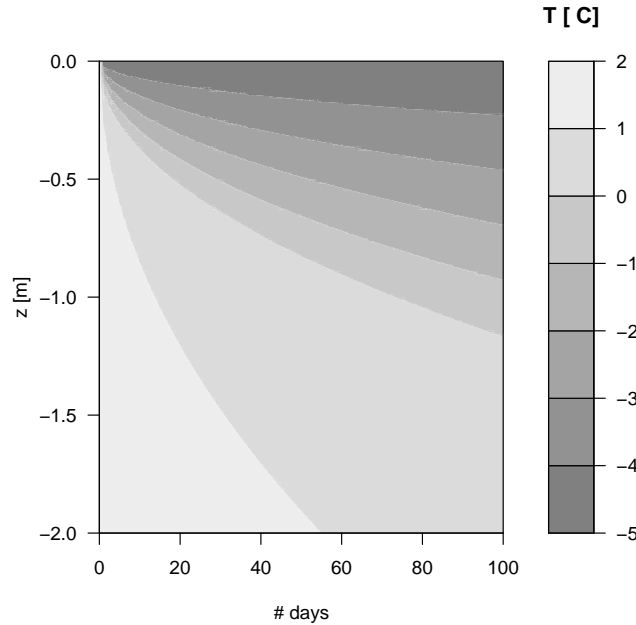


Figure 7.4: Freezing front advancing according to the analytical solution of the Neumann problem (see eq. 7.19)

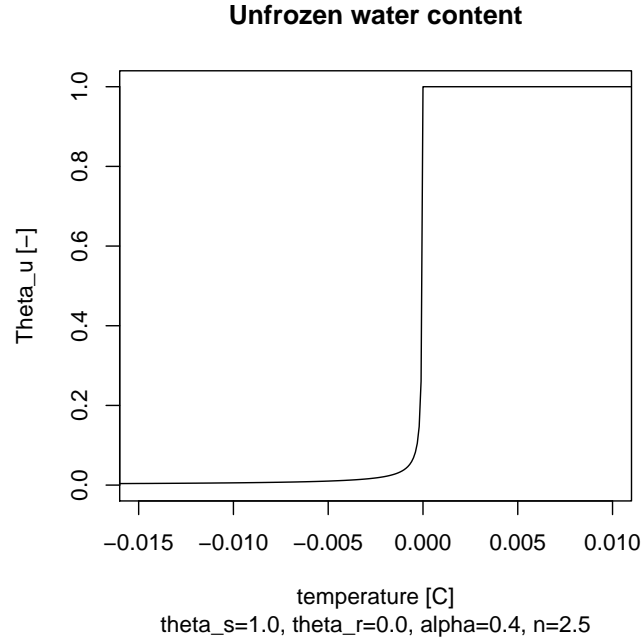


Figure 7.5: *Parameterization of a very steep SFC to resemble a homogeneous substance with instantaneous phase change*

7.3.2 Comparison between the numerical and the analytical solution

Let us apply the analytical solution to a domain composed of a homogeneous substance (pure water), initially thawed at temperature $T_i(0, z) = +2.0$ and let us force the surface to a constant temperature of $T_s(t > 0, 0) = -5^\circ\text{C}$. One of the hypothesis of the analytical solution is that phase change completely occurs at $T = T_m$ and that the substance is solid if $T < T_m$ and liquid if $T \geq T_m$. In order to do this, one has to consider a SFC very steep similar to a step function with no residual water content. As visible in Fig. 3.12, the higher the parameters α and n , the steeper the SFC. For this example, we have set $\alpha = 0.4$ [mm^{-1}] and $n=2.5$. Furthermore, in order to have a pure substance as in the analytical solution, a porosity of 100% was assumed (i.e. $\theta_s = 1$). The resulting SFC may be seen in Fig. 7.5. The initial and boundary conditions, and the soil parameters that satisfy these requests may be written as:

$$\left\{ \begin{array}{ll} T_\infty = +2^\circ\text{C} & (t > 0, z \rightarrow \infty) \\ T_s = -5^\circ\text{C} & (t > 0, z = 0) \\ \theta_w(z) = 1.0 ; \theta_i(z) = 0.0 ; \lambda(z) = \lambda_w ; C_T(z) = \rho_w c_w & \text{if } T \geq T_m \\ \theta_w(z) = 0.0 ; \theta_i(z) = 1.0 ; \lambda(z) = \lambda_i ; C_T(z) = \rho_i c_i & \text{if } T < T_m \\ \alpha = 0.4 ; n = 2.5 ; \theta_r = 0.0 ; \theta_s = 1.0 & \end{array} \right. \quad (7.20)$$

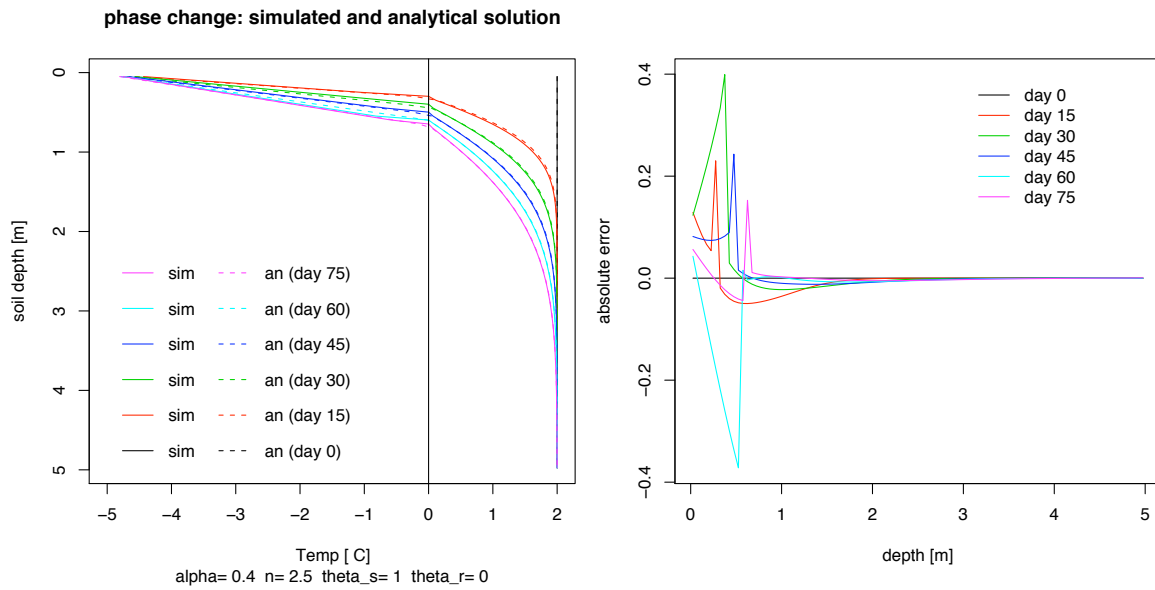


Figure 7.6: Left: numerical and analytical solution of the Neumann problem in the freezing case. The colors represent different time frames. Right: absolute error

The model was tested in a domain composed by 100 layers of 50 [mm] depth and with an integration time $\Delta t=60$ [sec]. The comparison between the analytical solution and the numerical solution and the error may be seen in Fig. 7.6. One can see that the maximum error appears at the point in the domain where the phase change is occurring, and the maximum error decreases as the simulation time increases.

In Fig.7.7 it is possible to compare the simulated (dotted line) with the analytical solution (plain line) at different depths. One can the following observations:

- the temperature behavior shows a change in the slope that coincides with the separation point between the upper thawed part with the frozen below;
- the slope of the frozen part is higher than the slope of the thawed part because the thermal diffusivity of ice is higher than the thermal diffusivity of water: $D_i=1.13E-6 > D_w=1.43E-7$ [$m^2 s^{-1}$];
- the numerical solution shows some oscillations after the temperature reaches the freezing point. These are due to the fact that the interface $Z = Z(t)$ where $T = 0^\circ C$ can move just in a discrete way and not in a continuous way as in the analytical solution. This means that the interface thawed-frozen can be either on the cell i or on the cell $i+1$ but not in between. In fact, the numerical solution starts decreasing the temperature only once all the water in the grid has been frozen, and this depends on the grid size. Furthermore, T_i is influenced by

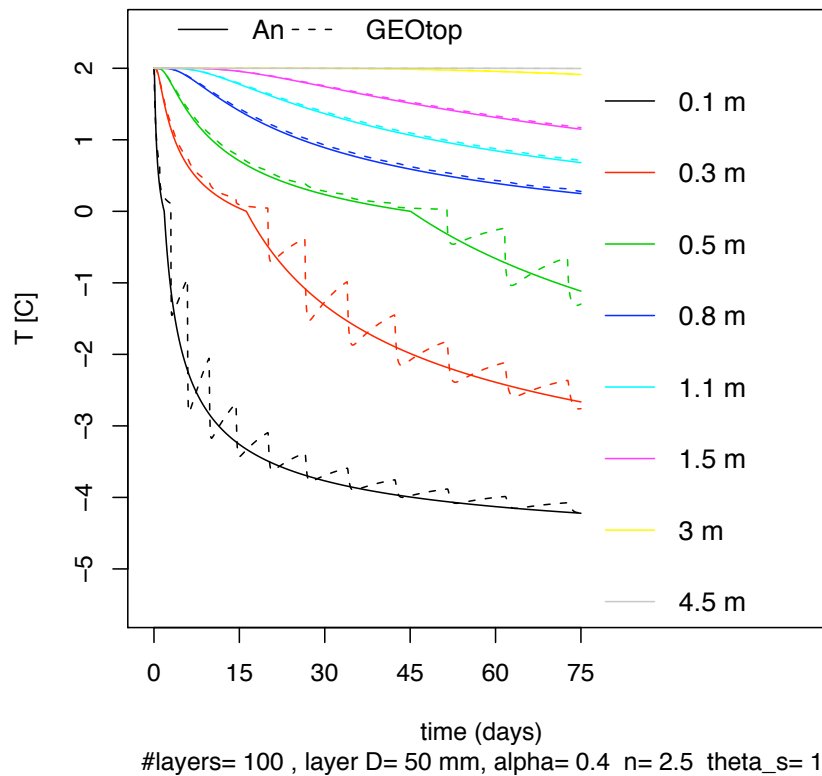


Figure 7.7: Comparison between the numerical (dotted line) and the analytical solution (plain line) for the Neumann problem. Δt of integration is 60 [sec]

the phase change of T_{i+1} by the release of latent heat and thus the temperature oscillation continues also in the frozen state. Therefore oscillation amplitude is both linked to the grid size and to the time, as reported in Fig.7.8. Increasing the grid size, the oscillation amplitude increases, as increases the mass of water to freeze before the temperature may decrease. The oscillations amplitude dampens with time as the freezing front moves away from z_i . The oscillations amplitude may be reduced but not eliminated, as it is embedded with the fixed-grid Eulerian method, where the freezing front may move in a discrete way and not in a continuum as in the reality. The only way to avoid oscillations is to use a Lagrangian method.

Also *McKenzie et al.* (2007) have compared their model (SUTRA code) against the analytical solution. They used the *Lunardini* (1985) solution, different from the Neumann problem as it divides the region into three zones: fully frozen (with only the residual amount of unfrozen water), “mushy” (with both ice and water) and fully thawed. Their results show a good agreement with the analytical solution, however no mention is given about the grid space and integration time used with the comparison.

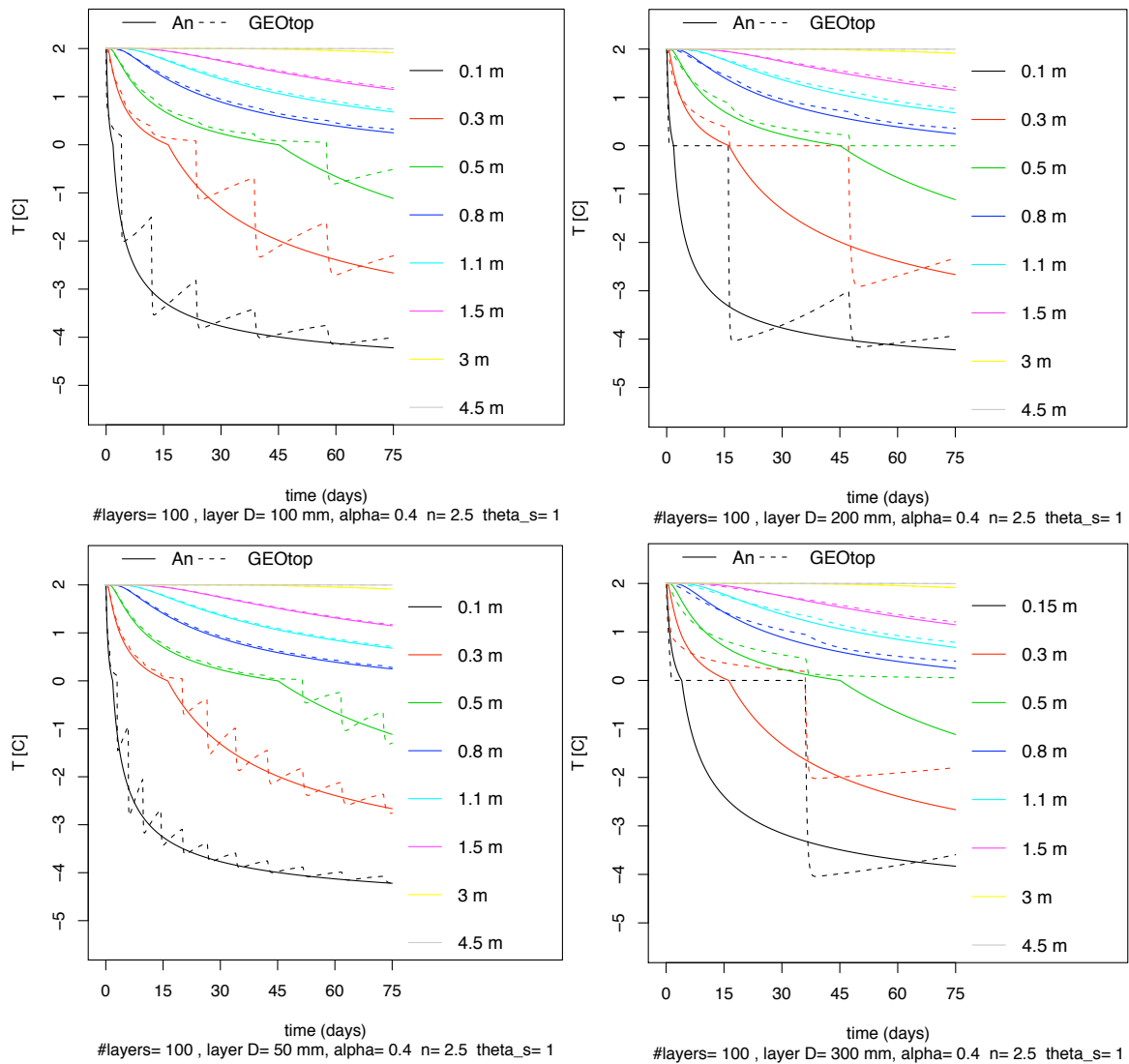


Figure 7.8: Comparison between the numerical (dotted line) and the analytical solution (plain line) for the Neumann problem at different grid size discretization [mm]: 50 (bottom left), 100 (top left), 200 (top right), 300 (bottom right). Increasing the grid size, the oscillations amplitude increases

7.4 Conduction and phase change with water movement

In order to verify the goodness of the model with water movement, the comparison was made against the measured data from Fig. 5 of *Hansson et al. (2004)* as shown in Fig. 7.9. The same model validation was also performed by *Daanen et al. (2007)*. The plot shows the profile of the total water content Θ (liquid + solid) at different time frames: after 12 hours on the bottom left, after 24 hours at the top left and after 50 hours at the top right. It is visible that the freezing of the soil sucks water from below, due to the increase in soil water suction. The increase in total water content reveals the position of the freezing front: after 12 hours it is located about 40mm from the soil surface, after 24 hours at 80mm and finally after 50 hours at 140mm. Similar to *Hansson et al. (2004)*, the results were improved by adding an impedance factor Ω to decrease the hydraulic conductivity close to the freezing front. It was found that the value of Ω that best resembles the results is 2. At the bottom right of Fig. 7.9 is shown the profile of the liquid water content at the same time frames: starting from a uniform water content $\theta_w = 0.33$, the liquid water content decreases from above due to the increase of ice content. Then the liquid water content starts decreasing also from below, showing that the flow of water affects the lower part of the soil.

The use of the impedance factor has been debated in the literature. *Newman and Wilson (1997)* argue that they obtained better results excluding the impedance factor for calibrating the permeability function at and behind the freezing front. In their simulations, the ice content was computed using the permeability versus suction relationship, predicted with the *Fredlund and Xing (1994)* equation for unsaturated soil permeability functions. *Watanabe (2008)* highlights that soil water flows not only through the unfrozen area but also through the frozen area. In fact he points out that a better estimation of the hydraulic conductivity of frozen soils is needed in future, especially in dealing with the impedance factor: if $\Omega = 0$ a huge pressure difference between the frozen and unfrozen regions induce water flow to the freezing front, where the soil quickly reaches ice saturation so that water can no longer pass through. However, increasing Ω to decrease the hydraulic conductivity results in a reduced water flow and decrease of ice formation at the freezing front. Therefore the impedance factor should be described in accordance with the unfrozen liquid water content instead of the ice content.

7.5 Conclusions

In this section the validation of the *freezing soil model* inside GEOtop has been performed in successive steps with increasing complexity. First the model was subject to pure conduction, then to conduction and phase change and eventually also water flow in freezing soil was added. The model has shown a good agreement with the analytical solution. In particular, when dealing

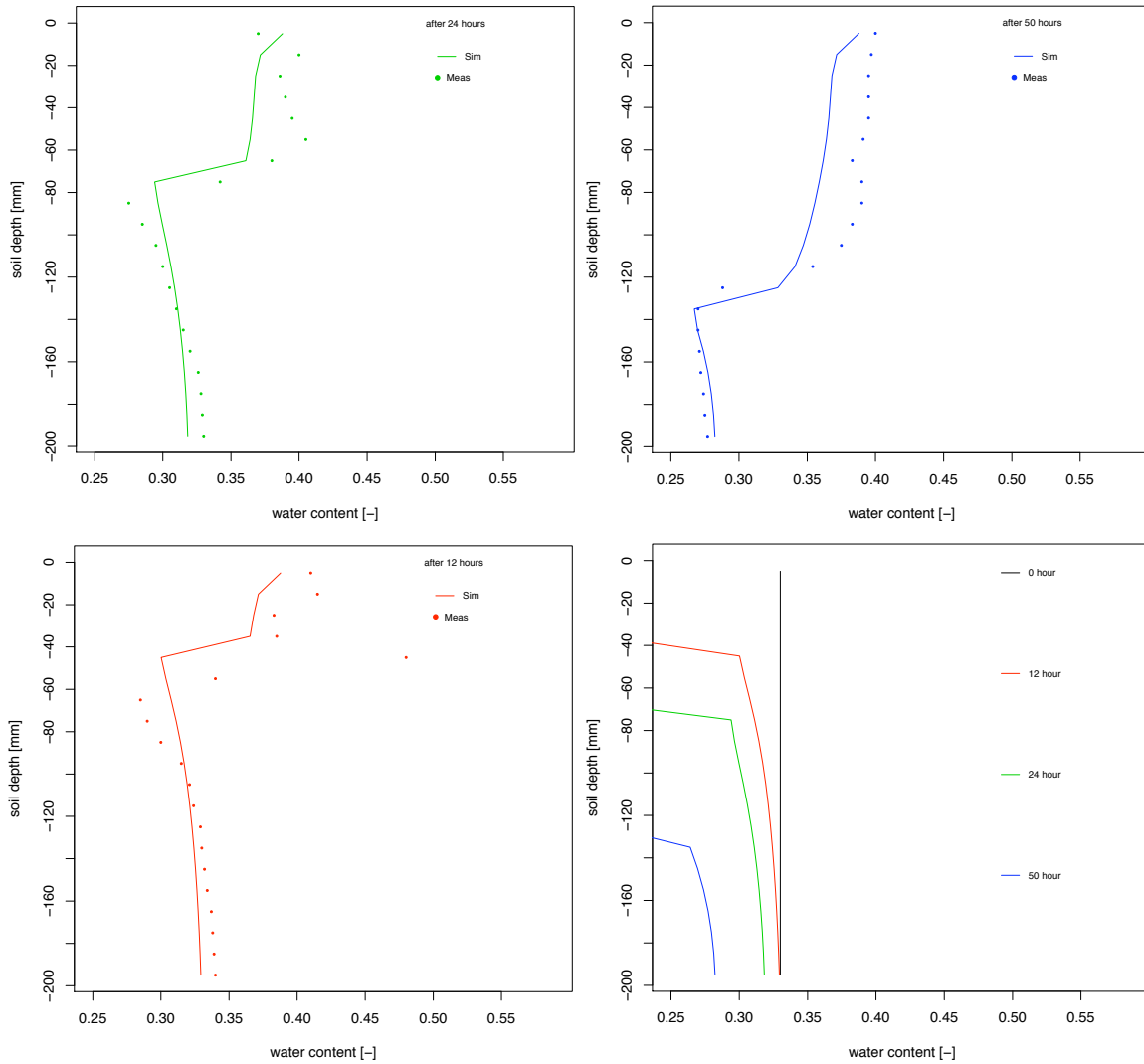


Figure 7.9: Comparison between the numerical (plain line) and the experimental results (points) obtained by Hansson et al. (2004). Situation after 12 hours (bottom left), 24 hours (top left) and 50 hours (top right). The liquid water content profile at the same time frames is shown in the bottom right figure

7. Model validation

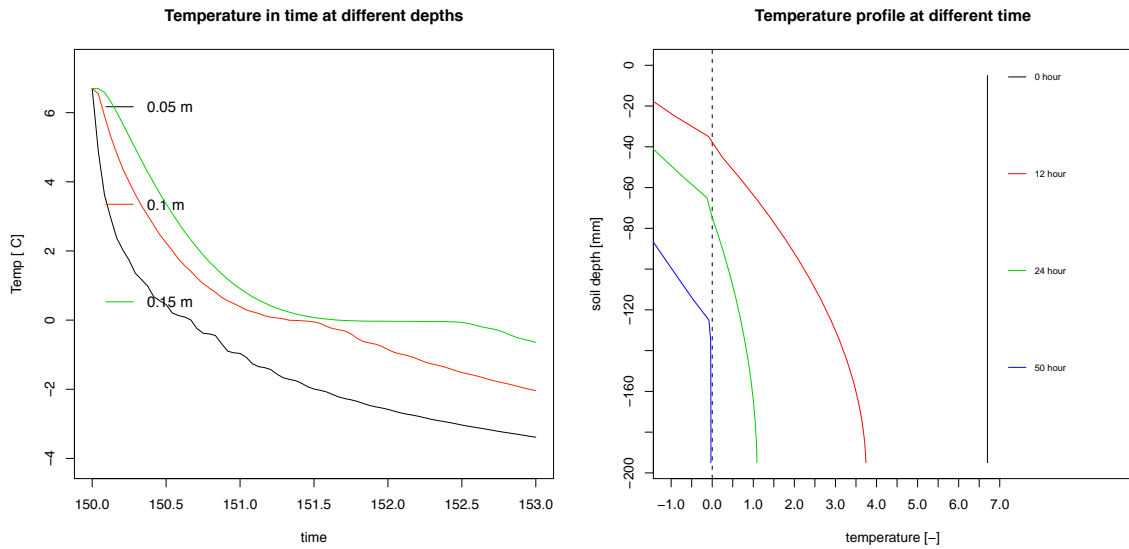


Figure 7.10: *Hansson et al. (2004) experiment. Left: temperature of the soil sample at different depths. Right: temperature profile of the soil at different time frames*

with phase change, it shows oscillations around the analytical solution. The amplitude of the oscillations depends on the domain discretization: the bigger the grid size, the bigger the amplitude of oscillations. However, the amplitude may be reduced but not eliminated, as they are embedded with the fixed-grid Eulerian method. The model was then applied to simulate the water flow in a freezing soil, and the results were compared to the experimental findings of *Hansson et al. (2004)*. The model results have shown a high sensitivity to the impedance factor Ω of the hydraulic conductivity. A value of $\Omega = 2$ has given the best performance.

8 Case study 1: water- and frost-table evolution

8.1 Introduction

In the previous section the *freezing soil model* of GEOtop has been thoroughly described and validated against analytical solutions and laboratory experiments. These applications were propaedeutical to prove the validity of the model under fixed boundary conditions and simple test cases, in order to debug possible errors in the code. In this section the *freezing soil model* will be applied on the field, to test its behavior under variable and complex situations, and verify its capabilities to simulate thermal and hydraulic interactions in permafrost affected soils.

GEOtop (*Rigon et al., 2006*), a physically based hydrological model that solves the energy and mass balance of the ground. This model is conceived to deal with complex topographies, as it accounts for the topographical characteristics of the basin and allows heterogeneous input parameters in the form of maps. GEOtop, given the meteorological data and soil parameters in input, allows to simulate the evaporation of the soil (*Bertoldi et al., 2006*), the transpiration of the vegetation, the pore water pressure in the soil, the water discharge in an outlet, the height and density of the snow and the mass balance of a glacier. GEOtop includes a snow module that calculates accumulation-melting of snow through a multilayer discretization of the snowpack (*Zanotti et al., 2004* and *Endrizzi, 2007*). For saturated and unsaturated subsurface flow, GEOtop makes use of a numerical solution of the 3D Richards' equation in order to properly model, besides the lateral flow, the vertical structure of water content and the suction dynamics. Furthermore, it calculates the proneness to instability of a slope and its evolution during a precipitation event (*Simoni et al., 2008*).

The objective of this study is to investigate the energy-based runoff generation theory for organic-covered permafrost. This will be accomplished by the following: 1) model the soil thaw for a small test area of the study basin where there is a relatively high concentration of thaw depth measurements; 2) evaluate frequency distributions of simulated ground thaw depths with field observations for the test area; 3) model the distributed ground thaw throughout the study basin in the form of topographic maps of the frost table representing different stages of active layer thaw; 4) evaluate the relative importance of vertical heat conduction and lateral heat advection with subsurface drainage, in controlling ground thaw; and 5) identify the key factors (e.g. peat thickness,

ground surface slope and aspect) that control the latter.

This section has been conducted in collaboration with Dr. Stefano Endrizzi, from the Centre for Hydrology, University of Saskatchewan, Saskatoon, Canada, Prof. Phil Marsh from the National Hydrology Research Centre, Saskatoon and Dr. William (Bill) Quinton from the Department of Geography and Environmental Studies, Wilfred Laurier University, Waterloo, Canada.

8.2 Factors influencing hydrology in organic permafrost terrains

There has been relatively little application of runoff generation theory to cold regions, particularly to the expansive treeless environments where tundra vegetation, permafrost, and organic soils predominate. Here, the hydrological cycle is heavily influenced by 1) snow storage and release, 2) permafrost and frozen ground that restrict drainage, and 3) the water holding capacity of organic soils. While ground surface topography obviously plays an important role in the assessment of contributing areas, the close coupling of energy to the hydrological cycles in arctic and alpine tundra environments dictates a new paradigm (*Quinton and Carey, 2008*). Spatial permafrost models have been a suitable choice to evaluate geographic trends and variability in permafrost parameters, and to simulate permafrost evolution with the recent warming (*Zhou et al., 2009; Anisimov et al., 2007; Yi et al., 2007*). However, *Woo et al. (2008)* suggested that more effort should be directed to improve hydrological modelling with respect to the spatial variability of ground freeze-thaw, moisture input, storage and release in permafrost areas. One attempt can be seen in the model by *Zhang et al. (2000)*, a spatially distributed hydrological and thermal model developed for Arctic regions that includes a spatially distributed thawing/freezing subroutine by *Hinzman et al. (1998)*, and the pan-Arctic water balance model by *Rawlins et al. (2003)* which incorporates a thaw-freeze model.

The energy-based runoff generation theory, for organic-covered permafrost terrains should encompass three main topics:

- **peat and hydraulic conductivity**

Since the saturated, horizontal hydraulic conductivity in the peat, K_s , decreases several orders of magnitude with depth (*Quinton et al., 2008*), the depth of the relatively impermeable frost table is critically important in controlling the rate of subsurface drainage from hill-slopes. Proper estimation of this flux therefore requires that the depth of thaw be known, so that an appropriate value of K_s can be assigned. A strong correlation between the cumulative ground heat flux (or indices of the latter, such as cumulative ground surface temperature) and the depth of thaw was demonstrated (*Quinton et al., 2005*).

- **topography**

While traditional theories of runoff generation may apply to flat, homogeneous tundra, any degree of topographic complexity introduces stark variations in radiation and aerodynamic energy, which in turn affects the accumulation and melt of snow, active layer thaw, soil moisture, evapotranspiration, and therefore, the volume and timing of runoff. Since the ground surface of arctic tundra is so highly permeable, the topography of the frost table strongly influences both the rate and direction of runoff (*Quinton and Pomeroy, 2006*). Defining the frost table topography as it evolves throughout the thaw season is therefore necessary for proper routing of subsurface drainage in the tundra environment.

- **water- and frost-table**

The definition of water table is the set of points in the soil where the total water pressure (considering the sum of liquid water and ice) is equal to zero. At the same manner, the frost table may be defined as the set of points where the temperature is equal to zero. This simple definition allows to have two main configurations of water- and frost-tables. As outlined in Fig. 8.1, when the water table is over the frost table, the soil among the tables is unfrozen and saturated (configuration on the left), when the water table is under the frost table, the soil among the two lines is frozen unsaturated (configuration on the right). The two configurations are important to be taken into account when the coupled water and heat transfer is to be analyzed. In fact, depending on the saturation content, the thermal parameters of the soil vary (see Chapter 5) and therefore the corresponding thermal profile. Having the at the top very unsaturated soil results in a faster warming or cooling, and therefore a faster movement of the frost table.

During thawing, the frost table (by assuming negligible freezing point depression, the frost table depth can be approximated by the depth of the zero-degree isotherm) coincides closely with the cryo-front since the soil below the frost table is typically saturated with ice and a small amount of unfrozen water. The frost table acts as a semi-impermeable aquitard and represents the lower boundary of the sub-surface flow zone, the thawed portion of the saturated soil that conducts runoff (*Quinton and Carey, 2008*). As the frost table, and the water table perched above it, descend due to the thawing active layer, the horizontal hydraulic conductivity of the flow zone decreases by orders of magnitude as a result of the fact that in organic soils, hydraulic conductivity decreases with depth (*Quinton et al., 2008*).

Unlike temperate environments, the subsurface fluxes of water and energy are closely coupled in tundra environments (*Quinton and Carey, 2008*). The ground thaw depth is strongly correlated with cumulative ground heat flux (*Quinton et al., 2005*), and thus the spatial pattern of thaw mirrors the pattern of snowcover removal (*Obradovic and Sklash, 1987*). With the onset of snowmelt, the soil profile is usually saturated or nearly saturated with ice, creating a relatively impermeable

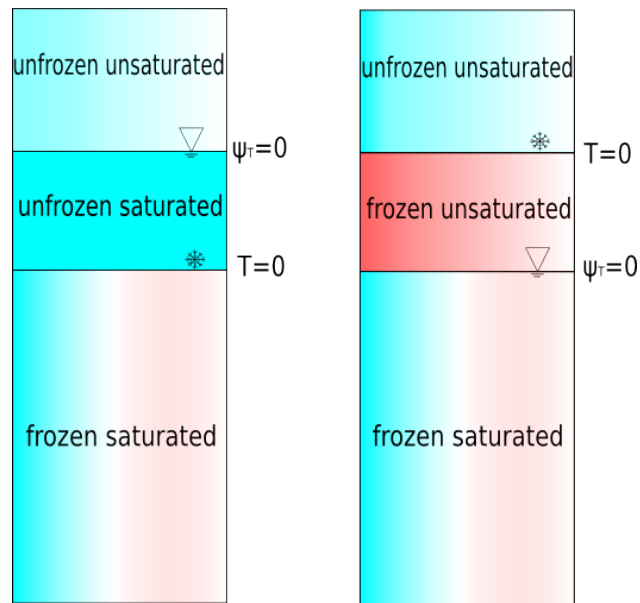


Figure 8.1: *Different configurations of frost and table depth. Left: water table over frost table; right: frost table over water table*

boundary close to the ground surface (Quinton *et al.*, 2009). The ground begins to thaw once it has become snow-free and continues if sufficient energy is supplied. Given the depth-dependancy of K_s , this topography defines the spatial distributions of K_s and hydraulic gradients, and reveals preferential pathways and local drainage directions (Quinton and Marsh, 1998; Hinzman *et al.*, 1993; Carey and Woo, 2000). Given the depth-dependancy of K_s , knowing the frost table topography also defines the spatial distributions of K_s and hydraulic gradients.

8.3 Study site

Modelling and field studies were focused on Trail Valley Creek (TVC), a 68 Km² arctic tundra basin 50 Km north of Inuvik, gauged since 1977. TVC has one of the most extensive data records of any arctic tundra basin in Canada, including hydro-meteorological station data since 1990, and well-documented measurements of active layer, permafrost and snow-cover properties.

The study was conducted at Siksik Creek (68°440N, 133°280W) located approximately 55 Km north-northeast of Inuvik, and 80 Km south of Tuktoyaktuk on the Arctic Ocean (see Fig. 8.2). The watershed is located at the northern fringe of the forest tundra transition zone (Bliss *et al.*, 1992), and is within continuous permafrost (Heginbottom and Radburn, 1992). Siksik Creek drains a 95.5 ha area with elevations ranging between approximately 60 and 100 m a.s.l.

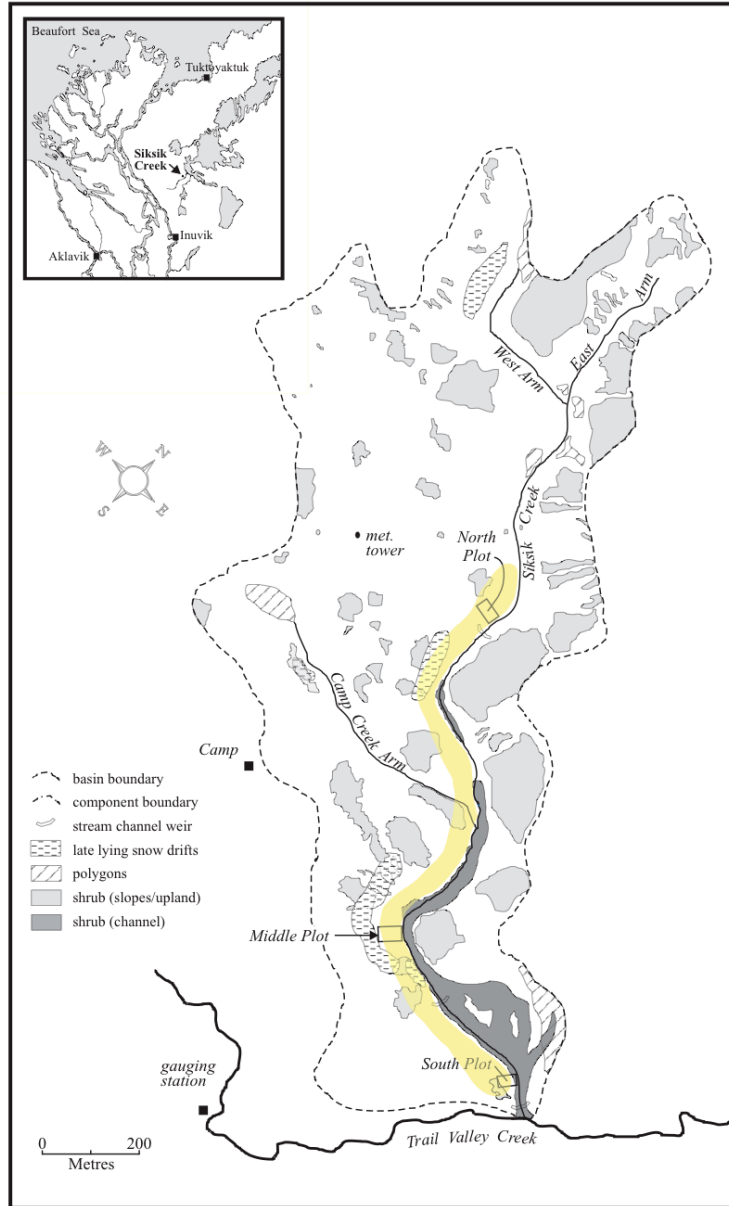


Figure 8.2: Study area of Siksik creek. North-, middle- and south-plot of peat and thaw depth measurements are shown together with the location of the meteo tower. The yellow stripe represents the west river bank where the simulation output are computed

8.3.1 The climate at Siksik

Siksik creek, as inferred from the climate normals for Inuvik and Tuktoyaktuk (AES, 1982a,b), is characterized by short, cool summers and long cold winters, with 8 months of snow cover. The mean daily temperature rises above 0°C in early June and falls below 0°C in early October, with a mean annual air temperature of -9.5°C at Inuvik and -10.5°C at Tuktoyaktuk. The mean annual precipitation totals 275 mm at Inuvik and 125-200 mm at Tuktoyaktuk, of which 45% and 44% fall as snow respectively. Monthly precipitation is greatest in August, September and October, with most precipitation falling as rain in August and September, and as snow in October.

Mineral earth hummocks occur throughout the study basin, covering between 30% and 70% of hillslope surfaces (reference). Their diameters range between 0.4 and 1 m, with their crests rising 0.1 to 0.4 m above the surrounding interhummock surface. The hummock surfaces are bare or support a thin layer of lichen (*Alectoria* and *Cladina* spp.). The interhummock vegetation consists of sedges (*Eriophorum* and *Carex* spp.) and small vascular plants (*Empetrum*, *Vaccinium*, *Ledum* and *Rubus* spp.) rooted in a continuous cover of moss (*Sphagnum* spp.). The peat in the interhummock area is ≈ 0.3 to 0.4 m thick. The upper 0.1 to 0.2 m is composed of living vegetation and lightly decomposed peat. Below this, the peat is moderately to strongly decomposed (*Quinton and Marsh, 1998*). Water moves preferentially through the interhummock area, since the hummocks are raised, and the hydraulic conductivity of the organic soil is three to six orders of magnitude higher than that of the clay-rich hummocks (*Quinton and Marsh, 1998*). By late summer, the average frost table depth was ≈ 0.3 m in the interhummock area, compared with 0.6 m in the hummocks (*Quinton and Marsh, 1998*). Fine-grained, frost-susceptible soils underlie the organic cover throughout the basin.

At the onset of snowmelt runoff in the spring, the soil profile in the interhummock area is usually saturated or nearly saturated with ice, creating a relatively impermeable boundary close to the ground surface. Previous hydrological studies on this hillslope (*Quinton and Marsh, 1998; Quinton et al., 2000*) demonstrated that, during soil thawing, the upper surface of the frozen, saturated soil coincides closely with the elevation of the 0°C isotherm, i.e. the frost table. The frost table, therefore, approximates the lower boundary of the thawed, saturated layer through which subsurface water drains from the hillslope. The saturated, horizontal hydraulic conductivity K_s decreases from 10 mm/s to 10^{-3} mm/s between 0.1 and 0.3 m depth increments in the interhummock area (*Quinton et al., 2000*). Given the depth dependency of K_s and the impermeable nature of the frost table in this environment, the frost table elevation is a major factor controlling the timing and magnitude of hillslope subsurface drainage.

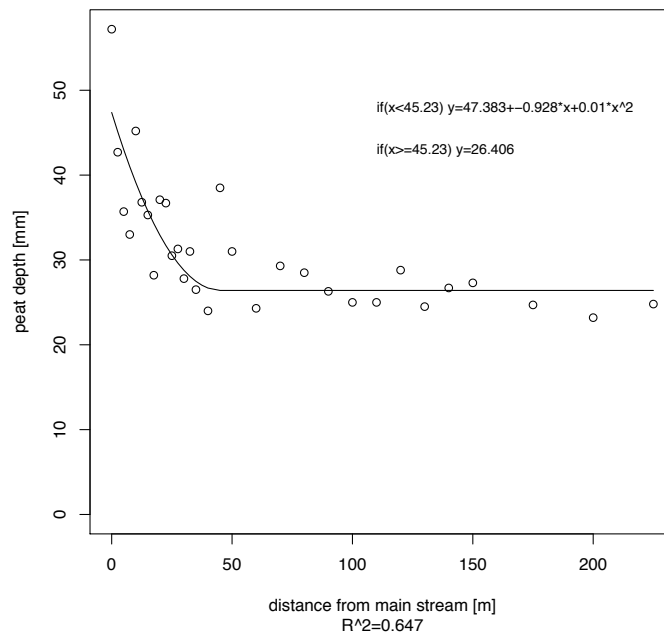


Figure 8.3: Peat depth at Siksik as a function of the distance from main stream. The peat depth measured in the field and the interpolated line are shown

8.4 Field measurements

During the summer 1993 numerous transects have been performed to measure the thaw depth along the west riverbank of Siksik creek, both in mineral (hummock) and organic soil (peat). The peat depth was measured in three plots: North Plot (NP), South Plot (SP) and Middle Plot (MP) along transect from the main stream towards the interior in the west riverbank (see yellow stripe in Fig. 8.2). The measurements, as depicted in Fig. 8.3, reveal that the peat depth decreases as the distance from the mainstream increases. The decrease, however, is more evident in the first 40 m, then the peat depth remains constant at a value ≈ 25 cm. A regression line was then calculated to interpolate the measurements through a quadratic line until 45 m and then a constant value onwards.

In the same transect the frost depth (or equivalently the thaw depth) was also measured by a thermistor probe on average three times a week during the summer 1993. Table 8.1 reports the results of frost depth averaged on a weekly basis. It was also interesting to investigate the presence of a trend in thaw depth (TD) measurements with time and distance from the main channel. The distance from the main channel was divided into intervals of 5 m and then the TD measurements were grouped if belonging to the same distance interval, and then averaged on a weekly basis within this interval. The results are shown in Fig. 8.4 where on the x axis is reported the week

8. Case study 1: water- and frost-table evolution

number, on the y axis the distance from the main channel and the colors represent the thaw depth. It is visible that, advancing with the summer, the thaw depth increases until it reaches the maximum of about 50 cm at the end of the summer (week 9). The location of the maximum thaw table depth along the transect, however, changes according to the time of the summer. In the first part of the summer the maximum of thaw depth is located at 20 m of distance; then, proceeding with the summer, this maximum fades and a new maximum is formed far from the channel. /A possible explanation could be that, at the beginning of the summer, the nearer to the channel, the more water is present, i.e. more energy is available to thaw the ground (deeper thaw depth). At the end of the summer, on the other hand, the drainage of water becomes more important and so the heat advected becomes dominant. Far from the channel the peat becomes shallower and so part of the mineral soil is affected by the thaw, which increases the thaw rate and therefore the thaw depth increases. Comparing Fig. 8.3 and Fig. 8.4, one realizes that at the end of the summer there is a relation between peat depth and thaw depth. In fact, getting farther from the main stream, the peat becomes shallower and the ground thaw deeper, highlighting an inverse proportion between peat depth and thaw depth.

week #	period
week1	from 24/05/1993 to 31/05/1993
week2	from 02/06/1993 to 08/06/1993
week3	from 09/06/1993 to 16/06/1993
week4	from 17/06/1993 to 23/06/1993
week5	from 25/06/1993 to 01/07/1993
week6	from 02/07/1993 to 09/07/1993
week7	from 10/07/1993 to 24/07/1993
week8	from 25/07/1993 to 31/07/1993
week9	from 09/09/1993 to 15/09/1993

Table 8.1: *Weekly aggregation of measured data*

As expected, the thaw depth increases as the summer advances. It is thus possible to find the frequency distribution of thaw depth in the various weeks, in the same way as in Fig. 4 in *Wright et al.* (2009). The results are shown in Fig. 8.5: with the advancing of the summer, the mean thaw depth increases, passing from 15 cm in week 1 to about 35 cm in week 9. At the same time, however, also the variance of the measures increases, indicating that at the end of the summer the measures are highly variable from point to point.

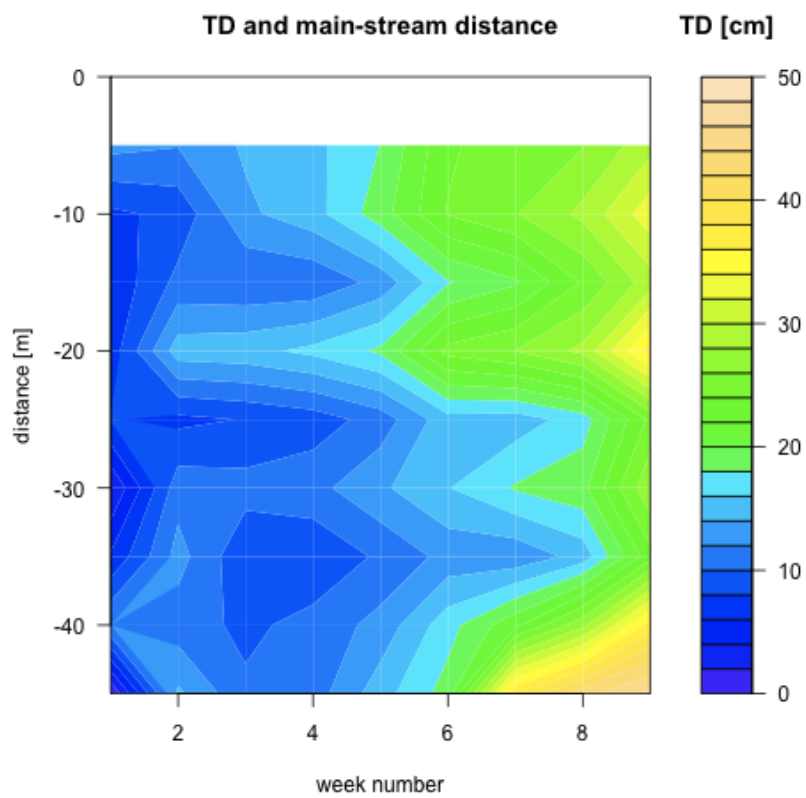


Figure 8.4: Frost table depth in organic soil at siksik west river bank as a function of time and distance from main stream

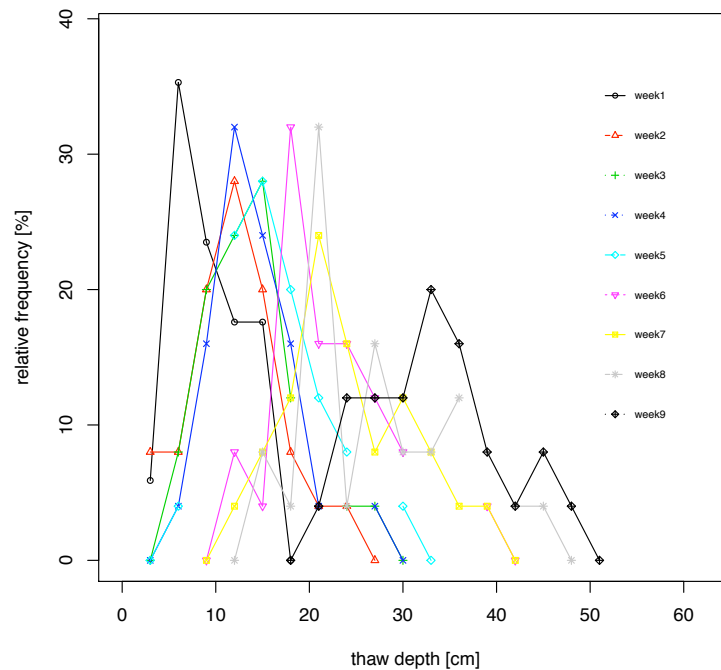


Figure 8.5: Weekly-averaged frequency distribution of thaw depth during the 9 weeks. Both the mean and the variance of the distribution increase with the advancing of the summer

8.5 Thaw depth simulation

GEOtop requires a detailed description of the forcing (meteorological data), initial conditions (temperature and moisture content), soil thermal and hydraulic parameters, topographic and hydrographic maps, and soil cover parameters (roughness, vegetation) to calculate the turbulent fluxes. The meteo data in input refer to the data recorded in a meteo station located in the basin and include air temperature, relative humidity, global short wave radiation, wind direction, wind speed. The topographic input maps (elevation, aspect, slope, laplacian) and the hydrographic input maps (drainage directions and channel network) derive from a 10 m resolution DEM, and were obtained by the routines embedded in JGrass (www.jgrass.org), an open source GIS dedicated to geomorphologic calculations. The soil has been discretized into 80 layers until a depth of 4 m, considering a profile composed by a surface layer of peat and then a uniform layer of mineral soil (see Table 8.2). The hydraulic conductivity, according to *Quinton et al.* (2008), has been given in input as a profile ranging from $3.0 \text{ [mm s}^{-1}\text{]}$ at the surface, to $1.0 \text{ E-2 [mm s}^{-1}\text{]}$ at 30 [cm] depth. The thermal conductivity of the peat was assigned to $0.21 \text{ [W m}^{-1}\text{K}^{-1}\text{]}$ as outlined in Table 1 of *Quinton and Gray* (2003). The initial condition on temperature is a uniform profile equal to 0°C and the initial water table was set at the surface level, hypothesizing a saturated condition.

Depth [mm] from surface	θ_s [-]	θ_r [-]	K_H [mm s ⁻¹]	α [mm ⁻¹]	n [-]	λ_T [W m ⁻¹ K ⁻¹]	C_{gs} [MJ m ⁻³ K ⁻¹]
0 (peat)	0.95	0.21	3	0.01	1.6	0.21	7.500 E-2
100 (peat)	0.95	0.21	1.82	0.01	1.6	0.21	1.000 E-1
200 (peat)	0.85	0.21	5 E-2	0.01	1.6	0.21	1.800 E-1
300 (peat)	0.85	0.21	1 E-2	0.01	1.6	0.21	1.800 E-1
mineral soil	0.5	0.1	1 E-4	0.004	1.4	2.5	1.157

Table 8.2: Hydraulic and thermal parameters of peat. α and n are Van Genuchten (1980) parameters

8.5.1 Point simulation

The first set of simulations were directed to understand and calibrate the thermal profile in one point, in order to verify the goodness of the thermal and hydraulic parameters of the peat. This was done applying the 1D version of GEOtop at the meteo station, where sensors of soil temperature were available. The sensors are located at 5, 17, 27 and 30 cm in the ground. As can be seen in Fig. 8.6, the model represents the temperature in the soil along the whole simulation period. The active layer, as visible in Fig. 8.7 on the left, gets deeper with time until the depth of 50 cm at the end of the summer, whereas the water table at the beginning coincides with the frost depth, and later in the summer stays above the frost depth (see Fig. 8.7 on the right). This means that the soil is desaturating due to the evaporation fluxes. This means that the evaporation and drainage velocity is lower than the velocity of warming, and this creates a positive feedback as an unsaturated peat warms faster than a saturated one.

8.5.2 Distributed simulation

The next step of simulations was directed to analyze the thaw depth in the basin, in order to understand the influence of the topographical characteristics (slope, aspect, curvature) and peat thickness to the temporal and spatial evolution of the active layer. As the measures of thaw depth were available in three plots along the west riverbank, the validation of the results was performed comparing the measured thaw depth frequencies, as outlined in Fig. 8.5, with the average of the modeled thaw depth obtained along the yellow stripe highlighted in Fig. 8.2. The results reported in Fig. 8.8 show a reasonably good agreement. The higher variability in modelled results could be probably imputed to the larger domain of simulation.

In Fig. 8.9 on the top is reported the map of thaw depth simulated at the end of the summer 1993 (11 september), considering an infinite peat thickness in all the basin and neglecting the lateral subsurface flow, thus leaving the only source of spatial variability to the surface energy balance (slope and aspect). One can notice that the thaw depth at the end of the summer is uniform in

8. Case study 1: water- and frost-table evolution

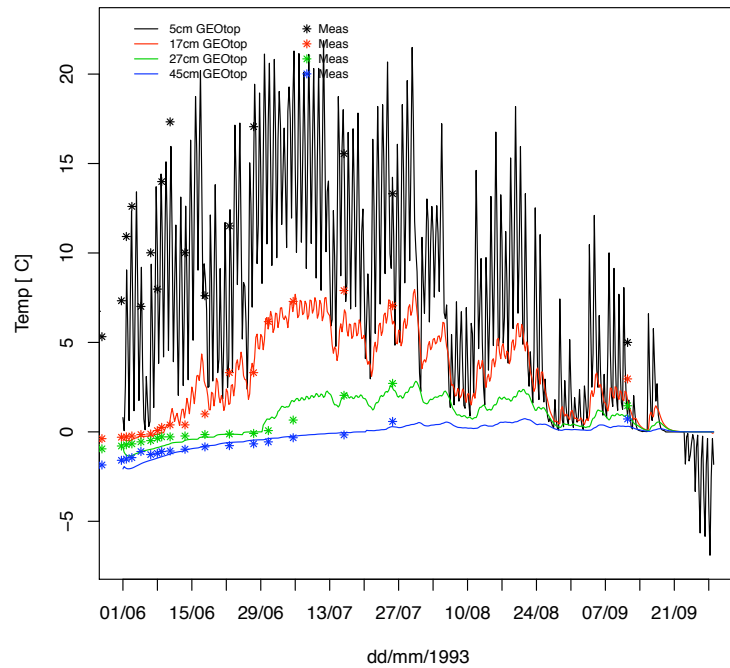


Figure 8.6: Simulated and measured temperature at the meteo tower

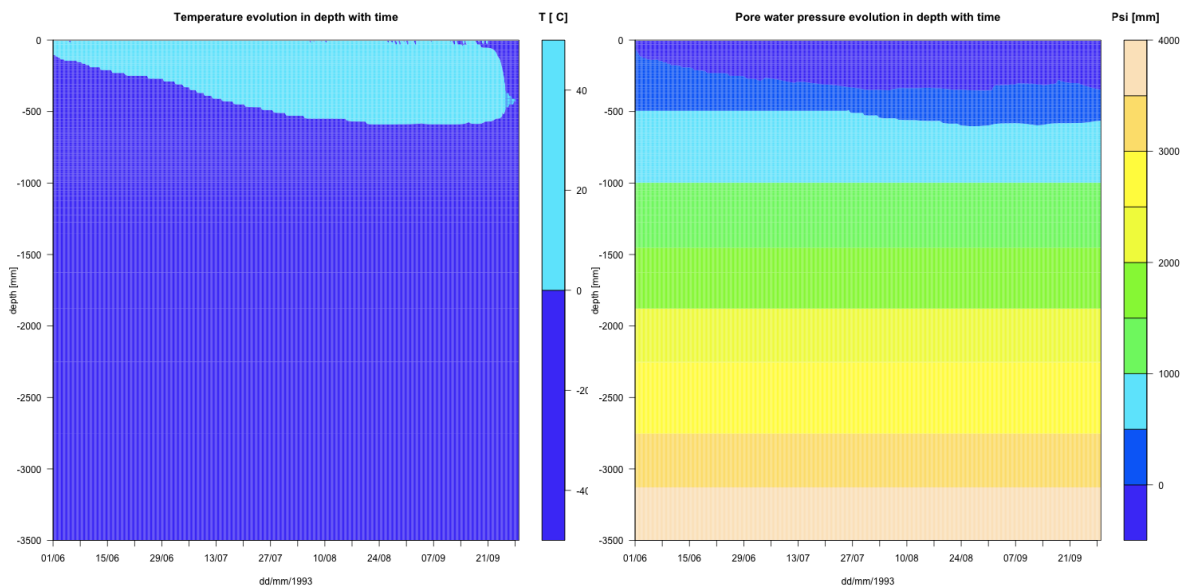


Figure 8.7: Left: soil temperature during the summer: light blue represents positive temperature, dark blue represents negative temperatures. Right: total water pressure [mm] during the summer: the violet color represents the depth of the "zero" pressure, coinciding with the water table

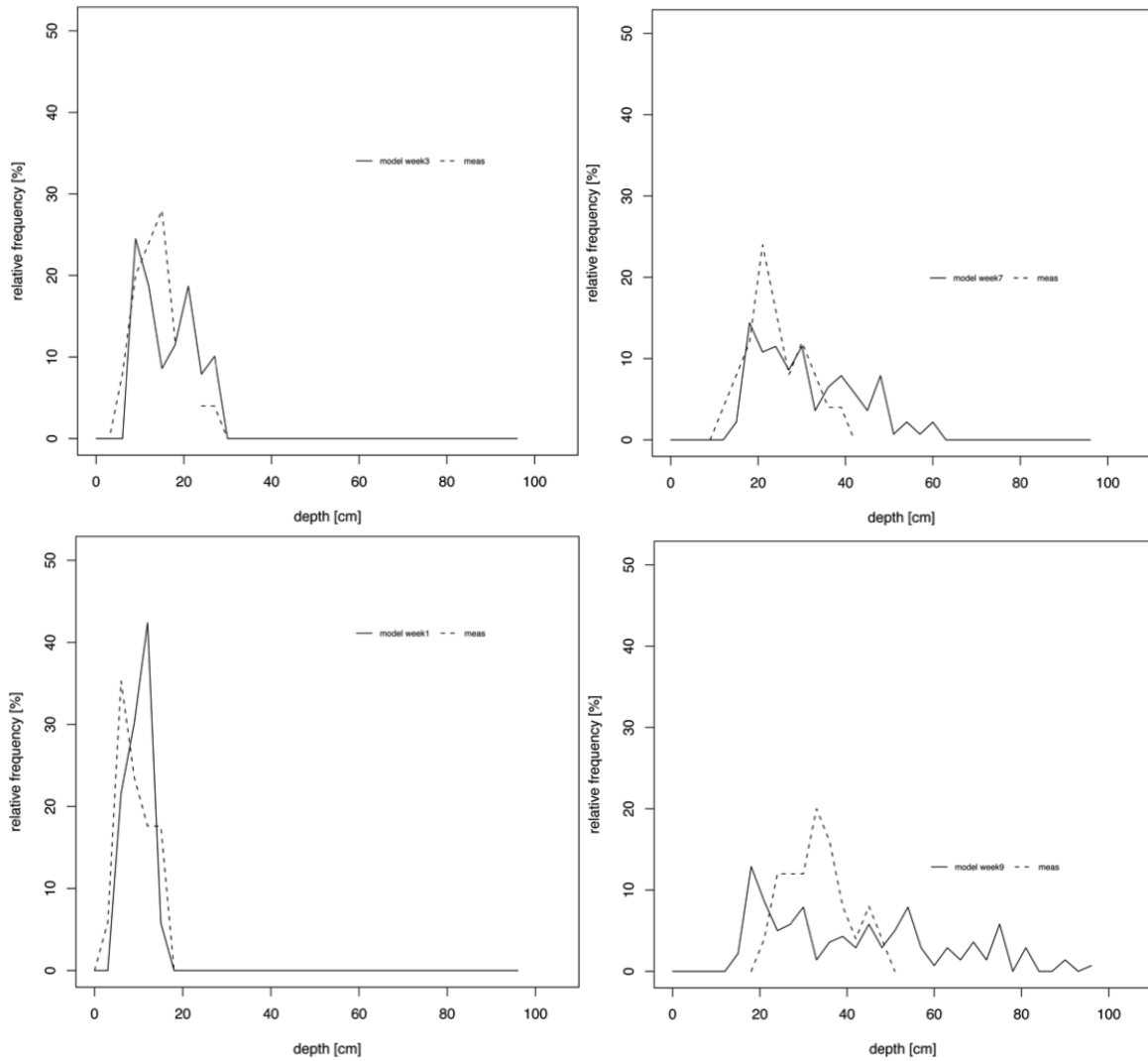


Figure 8.8: Thaw depth frequencies measured on the west riverbank (yellow stripe). On the x axis is the thaw depth [cm], on the y axis is the relative frequency of thaw depth observation [%]. The plain line and dotted line represent the measured and the modeled frequency distribution respectively. Bottom left: week 1; top left: week 3; top right: week 7; bottom right: week 9

all the basin, indicating that the measured spatial variability of the frost table is not controlled by the surface energy balance. In Fig. 8.9 on the bottom is reported the map of thaw depth simulated at the same day. This map was obtained considering a variable peat thickness, a variable surface energy balance and neglecting the lateral subsurface flow. The yellow stripe coincides with the main stream, where the peat thickness is deeper than the interior (see Fig. 8.3). It is visible that the peat thickness influences the thaw depth (deeper peat, shallower frost table depth), as the high water content of peat insulates the ground and therefore "protects" the permafrost in summer. However the very low spatial variability of the frost table depth indicates that the spatial variability of peat thickness and surface energy balance does not control the spatial variability of the frost table depth. Finally Fig. 8.10 reports the map of thaw depth, considering a variable peat thickness and admitting the lateral subsurface flow. One can notice now a very high spatial variability: very low frost table depth is measured where water flow diverges (higher slopes), and very high frost table depth where water flow converges (lower slopes). This is coherent with the fact that the thermal conductivity of the peat strongly depends on water content (see Fig. 5.4 on the right).

8.6 Conclusions

In this section a case study of the freezing model of GEOtop has been performed in a small peat-covered arctic catchment. First the 1D version of the model was applied at the meteorological station where thermistor sensors at depth were available. The model was able to reproduce the thermal pattern of the ground during the whole summer. This test provided a good example for tuning the thermal and hydraulic parameters of peat. Then a distributed simulation was performed with the objective to model the topography-induced spatial variability of the frost table depth. The results show that the main source of spatial variability is related to the effect of the high subsurface flow as a result of the high hydraulic conductivity of the organic soil, which leads to significant variability of the water content and in turn greatly affects the effective thermal conductivity in the peat.

The model allows to analyze complex situations, where a combination of factors influence the thermal and hydraulic pattern of the ground. In this case study the snow was not considered, as the simulation was spanning from the beginning of summer to the end of summer. The snow-soil thermal interactions will be the objective of the case study presented in the following section.

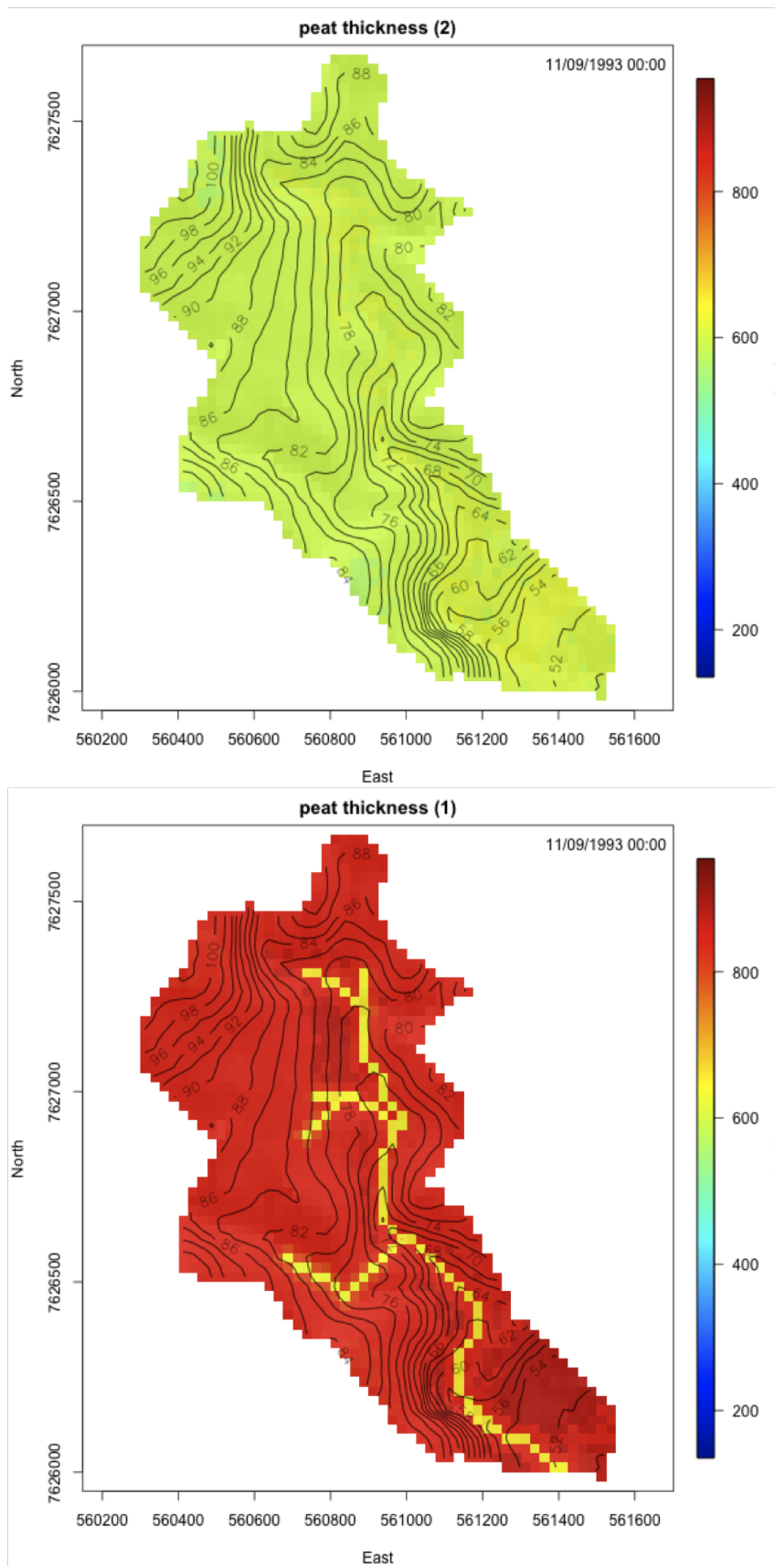


Figure 8.9: Top: effects of spatial variability of surface energy balance on thaw depth map (no lateral subsurface flow, infinite peat thickness). Bottom: effects of spatial variability of peat thickness on thaw depth map (no lateral subsurface flow, variable peat thickness)

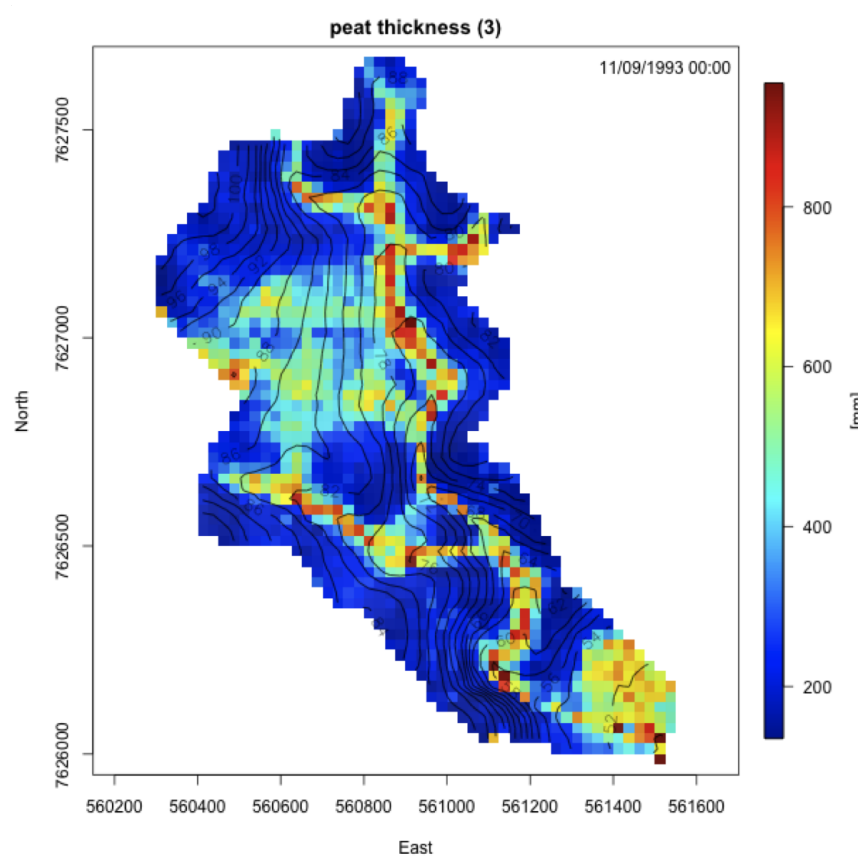


Figure 8.10: *Effects of subsurface water flow induced by topography on thaw depth map (lateral subsurface flow, variable peat thickness)*

9 Case study 2: snow-soil thermal interactions

9.1 Introduction

Thanks to its high insulating properties and high albedo, the snow has great effects on the thermal behavior of soil and rocks during winter. In particular, snow depth and density influence the thermal conductivity of the snow pack, and thus dictate the heat transfer between the air and the ground surface. However, also modeling details come into play in this context. For example, the number of grid points and grid size of the snow pack and the thermal conductivity at the snow-soil interface may influence the heat transfer mechanism with the underlying terrain. The snow module of GEOTop has been thoroughly described and validated by *Zanotti et al.* (2004) and *Endrizzi* (2007). The objective of this case study is to evaluate the impact of the snow layer discretization in modeling the snow cover and the underlying ground temperatures, and to give some hints on the thermal interactions between the snow and the soil. The simulations will be performed with GEOTop in an alpine permafrost site in the Swiss alps, where the oldest temperature time series of alpine permafrost are present (*Vonder Mühll and Haerberli*, 1990 and *Hoelzle et al.*, 1999).

9.2 Interface problem

Commonly, in alpine climates the soil exchanges heat directly with the atmosphere only in a short time window, roughly coinciding with summer months, whereas during winter and early spring heat transfer between soil and atmosphere is mediated by the snowpack, and, consequently, the heat flux reaching the soil surface is strongly reduced, due to the high snow albedo, which reduces net energy input, and to snow insulating properties, which cause heat conduction to be very small below the upper snow layers. In fact, the surface energy balance can be written as follows (*Oke*, 1990):

$$\Delta E_b = R_n + P - H - L \quad [\text{W m}^{-2}] \quad (9.1)$$

where R_n is the net all-wave radiation, P the sensible heat flux supplied by precipitation, H and L are respectively the sensible and latent heat fluxes exchanged between the surface (be it snow or soil) and the atmosphere. ΔE_b represents the net heat flux in input at the separation surface. In

case snow is present, this term may be written as:

$$\Delta E_b = \Delta Q_S + \Delta Q_M + G \quad (9.2)$$

where ΔQ_S and ΔQ_M are the heat storage rate in the snowpack due to sensible and latent heat (melting, freezing and rain on snow) respectively, and G is the heat flux reaching the soil surface acting as soil energy input. When the ground is snow free, ΔQ_S and ΔQ_M are null, and G is equal to the net energy flux exchanged with the atmosphere:

$$G \equiv \Delta E_b \quad (9.3)$$

On the other hand, for snow covered ground, G is proportional to the temperature gradient at the snow-soil interface, namely:

$$G \equiv G_{sn-g} = -\lambda_{int} \frac{T_{sn} - T_g}{\frac{1}{2}(D_{sn} + D_g)} \quad (9.4)$$

where λ_{int} is the thermal conductivity at the snow-soil interface, T_{sn} is snow temperature in the layer close to the soil surface, T_g is the soil surface temperature, and D_{sn} and D_g are the depths of the snow and surface layer respectively.

9.2.1 Snow-soil interface thermal conductivity

The snow-soil interface thermal conductivity (λ_{int}) may be calculated as a weighted harmonic mean between the snow and soil thermal conductivities, where the weights coincide with the snow and soil layer depths:

$$\lambda_{int} = \frac{D_{sn} + D_g}{\frac{D_{sn}}{\lambda_{sn}} + \frac{D_g}{\lambda_g}} \quad (9.5)$$

The snow thermal conductivity is modeled in GEOtop according to the *Yen* (1981) formulation:

$$\lambda_{sn} = \lambda_i \left(\frac{\rho_{sn}}{\rho_w} \right)^{1.88} \quad (9.6)$$

where ρ_{sn} is the snow density [Kg m^{-3}]. Observed values of newly fallen snow densities can range from 4 to 340 [Kg m^{-3}] (*McKay*, 1970), with lower values occurring under calm and very cold conditions and higher values under higher winds and higher temperature. In fact, high wind speeds break and pack together the snowflakes into denser layers (*Dingman*, 1994). Snow density has also been associated with snow grain diameter according to considerations about the age of the snow

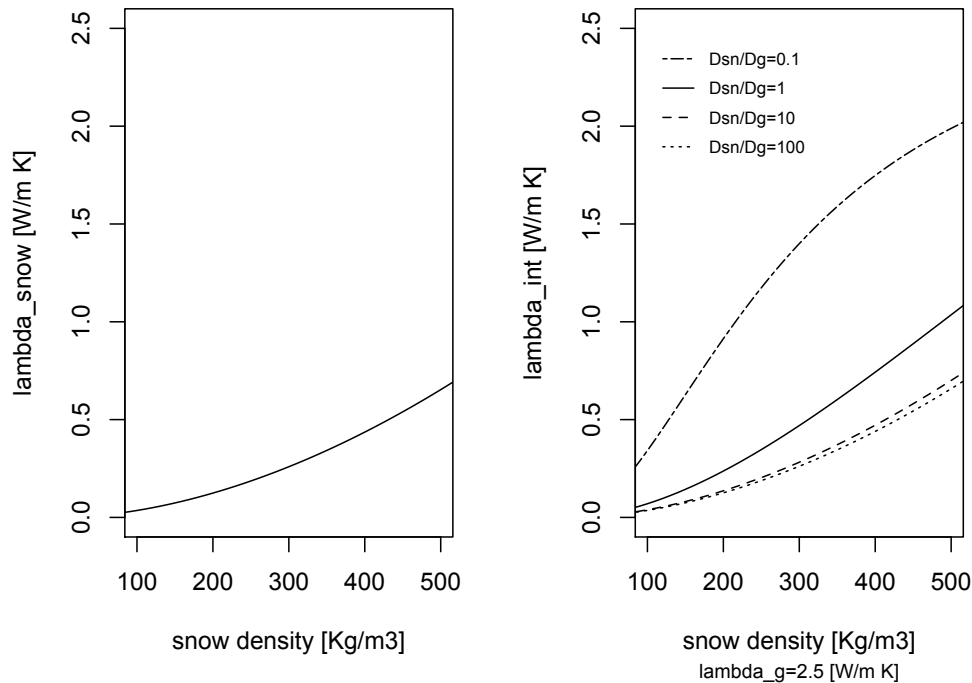


Figure 9.1: *Left: snow thermal conductivity as a function of snow density according to (Yen, 1981). Right: thermal conductivity at the snow-soil interface calculated as a weighted harmonic mean of soil and snow thermal conductivity. The different lines respect different ratio of soil layer and snow layer depth*

(new, old) and the metamorphism (constructive, destructive), reaching also values of more than $500 \text{ [Kg m}^{-3}\text{]}$ (Jordan, 1991). In Fig. 9.1 on the left is reported the thermal conductivity of snow as a function of snow density. One can notice that a newly fallen snow with density equal to $100 \text{ [Kg m}^{-3}\text{]}$ is characterized by a thermal conductivity of $0.035 \text{ [W m}^{-1}\text{K}^{-1}\text{]}$, which is comparable to pure air. Fresh snow, in fact, is considered a very efficient insulator. When the snow is subject to metamorphism, it becomes more dense and consequently increases its thermal conductivity. A snow of $500 \text{ [Kg m}^{-3}\text{]}$, may reach a thermal conductivity of $0.653 \text{ [W m}^{-1}\text{K}^{-1}\text{]}$, which is similar to the thermal conductivity of water.

Applying the formulation in Eq. 9.5 one can derive the thermal conductivity at the interface between the snow and the soil considering different values of soil and snow layer depths (see Fig. 9.1 on the right). If the snow layer is as deep as the soil layer, then the weighted harmonic mean coincides with the arithmetic mean. If the snow layer depth is bigger than the soil layer depth (e.g. 10 times bigger), then the low thermal conductivity of the snow prevails, and the thermal

conductivity at the interface becomes half of the arithmetic mean. If, on the other hand, the snow layer is thinner than the soil layer, than the soil thermal conductivity prevails and the conductivity at the interface is much higher than the arithmetic mean. Table 9.1 reports the calculations of the thermal conductivity at the interface for different snow density values and various ratios D_{sn}/D_g . It is visible that, if the ration between the snow layer depth and the soil layer depth passes from 1 to 10, the thermal conductivity at the interface becomes half.

D_{sn}/D_g	snow density [Kg m ⁻³]		
	100	300	500
0.1	3.42E-1	1.40E0	1.99E0
1	7.00E-2	4.69E-1	1.04E0
10	3.90E-2	2.82E-1	7.00E-1
50	3.62E-2	2.64E-1	6.63E-1
200	3.56E-2	2.60E-1	6.55E-1

Table 9.1: Thermal conductivity at the snow-soil interface calculated as a weighted harmonic mean between soil thermal conductivity $\lambda_g=2.5 [W m^{-1}K^{-1}]$ and snow thermal conductivity λ_{sn} according to Yen (1981). Depending on the snow density and on the ratio between snow layer depth (D_{sn}) and soil layer depth (D_g), the thermal conductivity at the interface changes

9.2.2 Snow layer modeling

The snow cover commonly exhibits large vertical gradients in terms of temperature, density, and water content. In order to take into account such variability many models represent the snow-pack with multilayer schemes, normally using thinner layers near the surface, and thicker layers downwards, since the largest gradients occur at the atmosphere interface. However, if the thermal conductivity at the layer interfaces is modelled with a harmonic mean, having a deep snow layer and a neighboring thin soil layer may result in a very small interface thermal conductivity, and, consequently, a strong underestimation of the snow-soil heat flux. This heat flux component has actually a very important implication in the thermal and hydraulic regime of permafrost and seasonally frozen ground, especially during the melting season, when the snow disappearance time should be carefully described. In Fig. 9.2 two different snow layer schematizations are shown: on the left is reported the SNTHERM model schematization (Jordan, 1991), characterized by layer thickness decreasing from the snow bottom layer to the atmosphere. In the following of the text this schematization will be referred to as the “old” schematization. On the right is reported a “new” proposed schematization, characterized by a asymmetrical arrangement with shallow snow layers at both the boundaries. In fact the bottom snow layer (next to the soil) and the top snow layer (next to the atmosphere) are thin, comparable with the top soil layer, and the inner snow layers are thick.

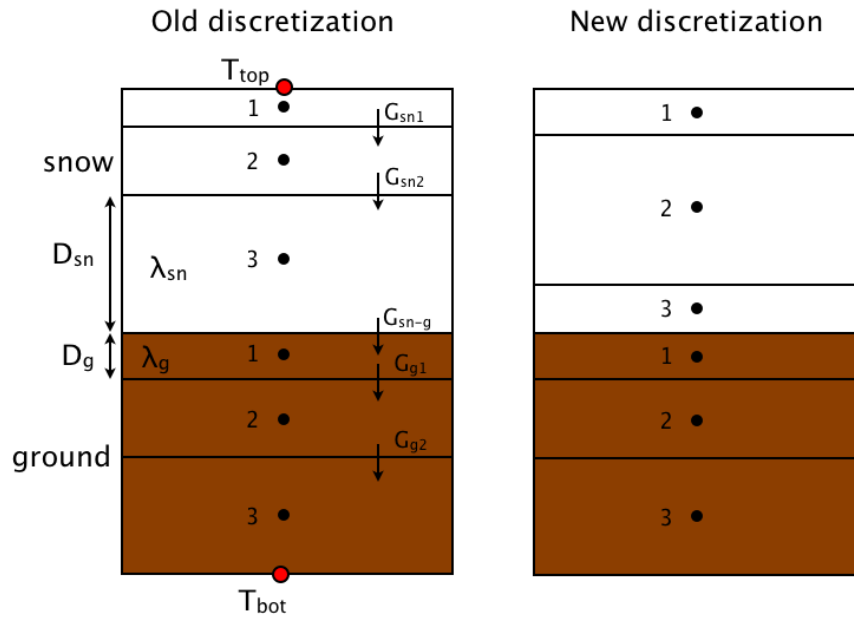


Figure 9.2: Left: *SNTHERM* model (Jordan, 1991) snow schematization, with layer thickness decreasing from the snow bottom layer to the atmosphere. Right: "new" snow schematization with thin bottom and top snow layers, and thick layers in between

Let us assess the influence of the snow-soil interface problem through a numerical experiment between a "synthetic snow" material where phase change is inhibited, and soil below. Let us consider domain composed of $N=6$ layers, of which 3 layers of snow and 3 layers of soil, as shown in Fig. 9.2. For this example let us exclude phase change, and let us concentrate on the thermal differences resulting from the pure conduction in the bottom snow layer and top soil layer. The heat equation applied to the column considering just conduction fluxes is:

$$C_T \frac{\partial T}{\partial t} + \frac{\partial G}{\partial z} = 0 \quad (9.7)$$

Discretizing the above equation in finite differences for both spatial and temporal domain, and considering a fully implicit scheme for the flux G one obtains:

$$D_i C_{T_i} \frac{T_i^{n+1} - T_i^n}{\Delta t} + G_i^{n+1} - G_{i-1}^{n+1} = 0 \quad (9.8)$$

where:

$$G_i^{n+1} = -\lambda_{int_i} \frac{T_{i+1}^{n+1} - T_i^{n+1}}{\frac{D_i + D_{i+1}}{2}} \quad ; \quad G_{i-1}^{n+1} = -\lambda_{int_{i-1}} \frac{T_i^{n+1} - T_{i-1}^{n+1}}{\frac{D_{i-1} + D_i}{2}} \quad (9.9)$$

λ_{int_i} is the thermal conductivity at the interface calculated as a harmonic weighted mean between

λ_{T_i} and $\lambda_{T_{i+1}}$. These thermal conductivities may be derived by Eq. 5.6 for the soil and 9.6 for the snow. For the inner layers (from layer 2 of snow to layer 2 of soil) the system of equations becomes:

$$-2 \frac{\lambda_{int_{i-1}}}{D_i + D_{i-1}} T_{i-1}^{n+1} - \left(\frac{D_i C_{T_i}}{\Delta t} + 2 \frac{\lambda_{int_{i-1}}}{D_i + D_{i-1}} + 2 \frac{\lambda_{int_i}}{D_i + D_{i+1}} \right) T_i^{n+1} - 2 \frac{\lambda_{int_i}}{D_i + D_{i+1}} T_{i+1}^{n+1} = \frac{D_i C_{T_i}}{\Delta t} T_i^n \quad (9.10)$$

The boundary condition is obtained considering a Dirichlet constant temperature of T_{top} and T_{bot} for the top snow surface temperature and bottom soil boundary condition respectively. Eventually the first and last equation become:

$$\begin{cases} - \left(\frac{D_1 C_{T_1}}{\Delta t} + \frac{\lambda_1}{D_1} + 2 \frac{\lambda_{int_1}}{D_1 + D_2} \right) T_1^{n+1} - 2 \frac{\lambda_{int_1}}{D_1 + D_2} T_2^{n+1} = \frac{D_1 C_{T_1}}{\Delta t} T_1^n + \frac{\lambda_1}{D_1} T_{top} \\ - 2 \frac{\lambda_{int_{N-1}}}{D_{N-1} + D_N} T_{N-1}^{n+1} - \left(\frac{D_N C_{T_N}}{\Delta t} + \frac{\lambda_N}{D_N} + 2 \frac{\lambda_{int_{N-1}}}{D_{N-1} + D_N} \right) T_N^{n+1} = \frac{D_N C_{T_N}}{\Delta t} T_N^n + \frac{\lambda_N}{D_N} T_{bot} \end{cases} \quad (9.11)$$

Let us suppose to have a snow and soil column with initial temperature $T^n = (-1.0^\circ\text{C}, -1.0^\circ\text{C}, -0.5^\circ\text{C})$ for the snow column and $(-0.5^\circ\text{C}, 0.0^\circ\text{C}, 0.5^\circ\text{C})$ for the soil column. For the soil column let us suppose a domain geometry of (1 cm, 10 cm, 100 cm). For the snow column let us consider a geometry of (1 cm, 10 cm, 100 cm) for the old discretization, and (1 cm, 109 cm, 1 cm) for the new discretization. Furthermore let us suppose $T_{top} = -1^\circ\text{C}$, $T_{bot} = 1^\circ\text{C}$ as boundary conditions. The thermal conductivity of soil depends on the soil type, moisture content and temperature. For the thermal conductivity the soil, a rock with with the following parameters is assumed: $\theta_s = 0.02$, $\theta_r = 0$, $\alpha = 0.001$ [mm^{-1}], $n = 1.5$ and $\lambda_g = 2.5$ [$\text{W m}^{-1} \text{K}^{-1}$]. For the snow thermal conductivity, a density of 300 [Kg m^{-3}] was assumed. As reported in table 9.2, after one day of simulation, the temperature of bottom snow layer and the top soil layer are $(-0.483^\circ\text{C}, 0.297^\circ\text{C})$ and $(0.245^\circ\text{C}, 0.257^\circ\text{C})$ for the old and new schematization respectively (please notice that the positive temperatures in the ‘‘synthetic snow’’ material are admitted because in this example phase change is not considered). Therefore, passing from the old to the new schematization, the difference between the bottom snow layer and top soil layer passes from $\approx 0.78^\circ\text{C}$ to $\approx 0.01^\circ\text{C}$.

9.3 Applications

Simulations have been carried out in proximity of the active rock glacier Murt el (Upper Engadin, Swiss Alps: $46^\circ 26' \text{N}$, $9^\circ 49.5' \text{E}$, 2670 m a.s.l., 15° slope with NW aspect) which represents the Alpine Permafrost site for which the longest temperature time series (Vonder M uhll and Haeblerli 1990 and Hoelzle et al., 1999) is available. In addition, data derived from the Meteo Swiss station

Layer	T^n	λ_T [W/m K]	D_{old} [m]	T_{old}^{n+1} [°C]	D_{new} [m]	T_{new}^{n+1} [°C]
sn1	-1.0	0.26	1.00E-2	-0.992	1.00E-2	-0.999
sn2	-1.0	0.26	1.00E-1	-0.946	1.09E0	-0.938
sn3	-0.5	0.26	1.00E0	-0.483	1.00E-2	0.245
g1	-0.5	2.49	1.00E-2	0.297	1.00E-2	0.257
g2	0.0	2.43	1.00E-1	0.307	1.00E-1	0.271
g3	0.5	2.43	1.00E0	0.494	1.00E0	0.490

Table 9.2: *Interface problem: a simple conduction model has been applied to a snow-soil column forced to $T_{top}=-1$ [°C] and $T_{bot}=1$ [°C]. The snow layer depth is different between the old and new discretization. The new temperature of the column is reported after one day of simulation with an integration interval of $\Delta t=60$ [sec]. For the thermal conductivity the soil is assumed to be a rock with $\theta_s=0.02$, $\theta_r=0$, $\alpha=0.001$ [mm^{-1}], $n=1.5$ and $\lambda_g=2.5$ [$W m^{-1} K^{-1}$]. The thermal capacity of the soil grain was set to $C_g=2.3$ [$MJ m^{-3} K^{-1}$]. For the snow thermal conductivity, a density of 300 [$Kg m^{-3}$] was assumed*

at the nearby Corvatsch summit have been used and extrapolated to the rock glacier location. They include incoming shortwave radiation, incoming longwave radiation, air temperature, wind speed, air pressure, and precipitation. The 1D version of model GEOtop was applied for a period of eight hydrological years, beginning from October 1997 to July 2005. As the first snowfall normally occurs in November, this choice allows to avoid the problem of the determination of the initial condition of snow on the surface. Most of the parameters used by the snow model of GEOtop were simply taken from literature, e.g. snow reflectance, and snow thermal and hydraulic properties. As only total precipitation was available, the calibration was reduced to the definition of the threshold air temperatures above (below) which precipitation is considered to occur as rain (snow), and on the correction factor for total precipitation.

Fig. 9.3 on the top reports the simulated Vs measured snow depth (black line). The grey line, instead, shows the heat flux G reaching the soil surface. It is visible that it depends on the snow presence: when soil is snow free, the flux is of the order of 50 [$W m^{-2}$], but it can drop by an order of magnitude, or more, when snow is present. This consideration highlights the importance of a correct snow modeling to simulate soil temperatures, especially during the ablation time. In fact a delay (anticipation) in the estimation of the snow cover complete ablation date may lead to an underestimation (overestimation) of the ground input flux, with consequent false estimation of soil surface and subsurface temperature. For example, Fig. 9.3 on the bottom reports the temperature behavior at the soil surface and 55 cm depth during the snow melting period, considering two scenarios: a "proper" snow simulation (full grey line), with correct snow model. A "poor" snow simulation, with delayed snow melting (dotted grey line). In general surface temperature starts

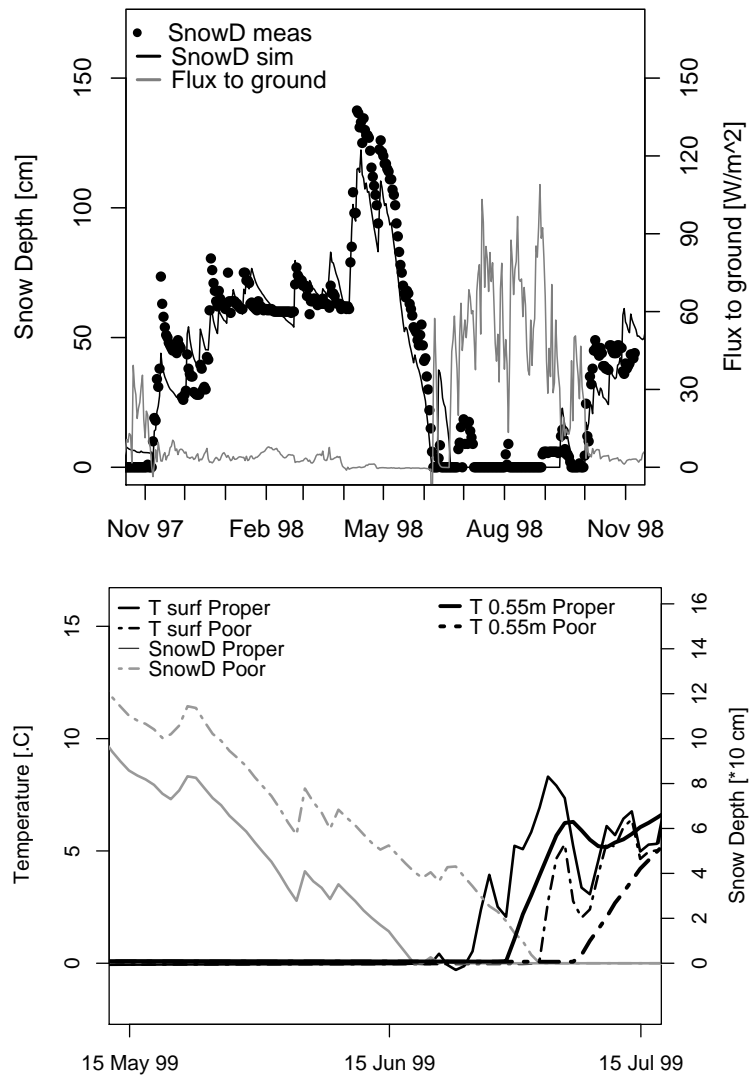


Figure 9.3: Top: Black line: simulated Vs measured snow depth. Grey line: energy flux input to the ground. Snow depth modeled with 9 layers according to the “new” schematization. Bottom: the error in temperature profile depends on the snow modeling and becomes bigger the deeper in the ground. “Proper” and “Poor” refer to real measures and delayed modelling respectively

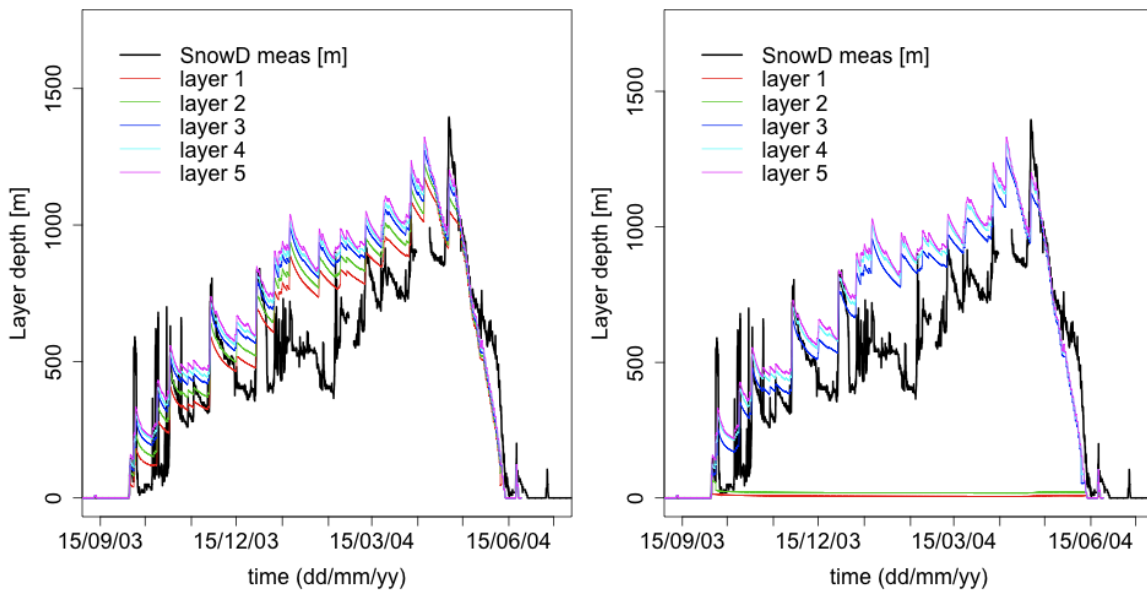


Figure 9.4: Comparison between the "old" (left) and "new" (right) snow schematizations. Different colors represent the thickness of different layers

increasing as soon as the snow is melted, and shortly after also the subsurface soil temperature starts increasing. A poor snow modeling has scarce influence on surface temperature (black thin line): in fact, the proper (plain) and poor (dotted) surface temperatures converge very quickly. The situation is fairly different at 55 cm depth (thick black line). In fact the delay in the temperature evolution is still visible after one month, indicating that the error in snow model will propagate and increase with the increase of soil depth. A correct snow model, especially in the estimation of the ablation time, is therefore crucial for soil temperature modeling.

Fig. 9.4 reports a plot with the two schematizations with a total of 5 layers: on the left is the "old" discretization, with snow layer depths decreasing from the soil surface upward and the thickest layer being the first; on the right the "new" parameterization, the "new" asymmetrical parameterization with the thickest layer being in the middle of the snowpack.

The temperature of the bottom snow layer and the top soil layer are reported in Fig. 9.5: as can be seen, the old discretization provokes a decoupling of the two temperatures. The soil surface temperature (red line) is higher than the snow bottom temperature (black), indicating that the snow temperature decreases without transferring the heat to the soil. The new discretization, on the other hand, shows a much improved coupling. This depends on two aspects: first, the higher snow-soil thermal conductivity at the interface for the new compared with the old: with the ratio $D_{sn}/D_g \approx 1$ for the new and ≈ 200 for the old. Considering a snow density of ≈ 300 [Kg m⁻³] for the new and ≈ 400 [Kg m⁻³] for the old (see 9.5 grey line), the thermal conductivity at the interface is about

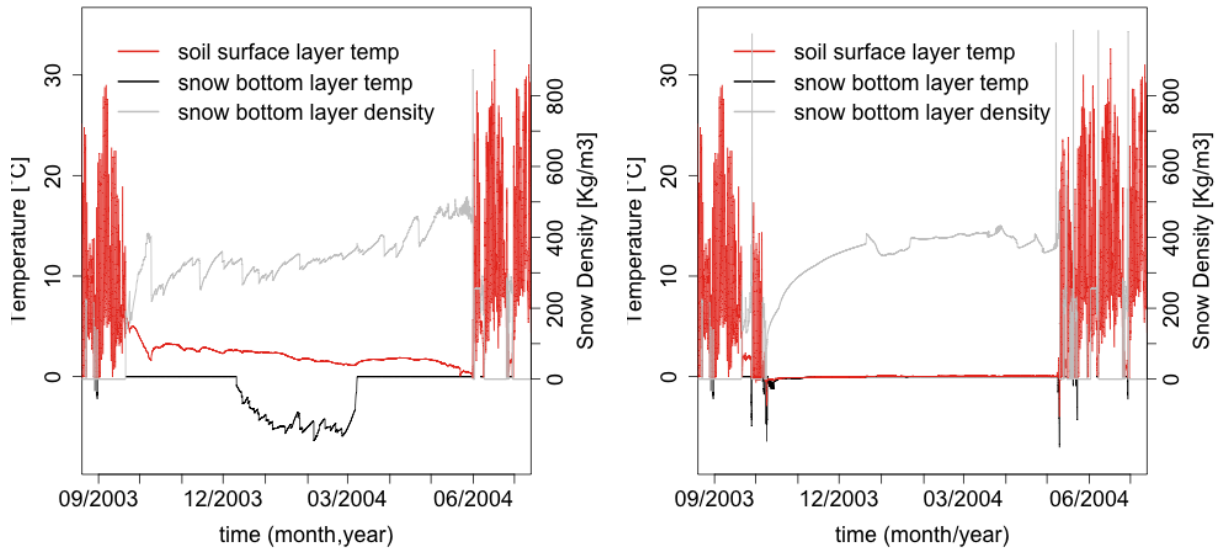


Figure 9.5: Comparison between the "old" (left) and "new" (right) snow schematizations with 5 layers. The decoupling of the temperatures of the bottom snow layer and top soil layer is clearly visible in the old schematization

0.74 [$\text{W m}^{-1}\text{K}^{-1}$] and 0.26 for the old (see table 9.1). Second, the shallower snow layer depth in the new discretization (≈ 1 [cm]), compared to the deeper snow depth of the old (≈ 100 [cm]). This results in a different internal energy decomposition of the whole snow cover, with consequent different snow temperature change.

9.4 Conclusions

In this section the snow-ground thermal interactions have been analyzed through the 1D version of the model GEOtop applied on a permafrost site based on the Swiss alps. The "old" discretization coherent to the *Jordan* (1991) model with snow layer depth decreasing from the atmosphere surface to the ground, was compared to the "new" soil discretization, with shallow snow layer at both the snow-ground and snow-atmosphere interfaces. The result show that the new symmetrical snow discretization is not as efficient as the classical snow discretization if the same number of snow layers is used. This is due to the fact that the snow cover behaviour is mainly driven by the atmosphere, and, therefore, shallow layers are required at the snow-atmosphere interactions. Shallow layers far from the surface are quite an useless computational effort if the interest is only on snow. However, the classical snow discretization, with deep layers at the snow-soil interface, produces a decoupling of soil and snow temperatures, which becomes even more evident when the snowpack is deeper, when soil surface temperature can still be up to few degrees above 0°C . This

decoupling is due to the fact that the thermal conductivity at the ground-snow interface is modeled with a weighted harmonic mean. If the snow layer depth is bigger than the soil layer depth (e.g. 10 times bigger), then the low thermal conductivity of the snow prevails and the thermal conductivity at the interface is very low, inhibiting the heat transfer with the soil and causing a decoupling on the temperature of the snow and soil layers.

Furthermore, the simulations highlighted the importance of a proper representation of the snow melting time. An advance or a delay in the estimation of the time of snow disappearance would cause a strong error in the calculation of the energy balance at the soil surface, altering the ground heating or freezing, and, therefore, affecting the soil temperature profile for the whole summer.

10 Conclusions

In this work the freezing soil module of GEOtop has been presented and applied to some case studies. The freezing module of GEOtop solves the mass and energy conservation in a soil/rock. It includes water flow in freezing soils thanks to the solution of Richards' equation, and allows the treatment of ice and water content in the ground through the inclusion of latent heat term in the heat equation as an apparent heat capacity. GEOtop also provides proper numerics for transient of the incoming radiation, the snow cover, surface water fluxes and convective fluxes at the terrain surface. The model has been developed starting from the basic principles of thermodynamics, in order to understand the limits of the assumptions and the extent of the possible applications. The version implemented is based on the common assumption usually known as *freezing=drying* (Miller, 1963) and the soil freezing characteristic curve is based on the *Van Genuchten* (1980) model and the generalized Clausius-Clapeyron equation. The mass and energy conservation equations, written for a "rigid volume" scheme, result in a coupled system of differential equations. This system is solved decoupled and the equations are discretized according to a finite volume representation. The fluxes are given by Darcy's law for the mass equation, and by Fourier law and advection for the heat equation. The derivation of the internal energy and of the mass with the time are derived evolving to (Celia *et al.*, 1990). A semi-implicit time discretization is used to solve the equation numerically and to linearize the resulting discrete system of equations, the globally convergent Newton-Raphson iteration scheme is used. The boundary conditions in input may be of Dirichlet or Neumann type. In the latter case, they are coupled inserted in the set of equations to be dynamically evaluated, as the surface temperature influences the turbulent fluxes (e.g. Tomita, 2009).

The revision of the freezing soil theory and the testing of the numerical model to experimental results and to field applications may lead to draw the following conclusions:

1. The assumption *freezing=drying* (Miller, 1963) is a "convenient" hypothesis, often tacitly used in literature, that allows to represent the freezing process as a desaturation process. This assumption, however, has important implications: (a) the pressure at the ice-water interface is equal to the air-water interface; (b) the pressure at the ice-air interface and (c) the ice

pressure is equal to the atmospheric pressure, usually set to zero. Therefore in the Gibbs-Duhem equation the term $v_i(\)dp_i = 0$ and so, in the resulting Clapeyron equation, there is no evidence of the ice density. However, the limitation of the *freezing=drying* assumption is that phenomena like frost heave cannot be modeled. In this case a more complete approach should be used (*Rempel et al. 2004, Rempel, 2007*) and the ice pressure should not be put to zero (*Christoffersen and Tulaczyk, 2003*). Despite this was not done in the present work, the theoretical part provides the fundamentals for a straightforward generalization of this case.

2. A freezing suction ψ_{freez} may be defined, as the negative pressure due to negative temperature T . This suction is added to the negative pressure ψ_{w0} due to the saturation degree and gives the total suction of the water phase. Inserting this pressure in a retention curve, it is possible to derive a formulation for the soil freezing characteristic curve under unsaturated conditions. According to the Van Genuchten model, results show that different combinations of α and n may result in a variation of the liquid water content of more than eight orders of magnitude.
3. The work due to freezing expansion is often neglected in literature as in the present work. This assumption, however, implies that (a) the density of water and ice are considered equal, and (b) the ice pressure is null.
4. The thermal conductivity strongly depends on porosity and on temperature. The dependence on the saturation degree becomes important near $\psi_{w0} = 0$, according to the shape of the SWC. The thermal capacity increases with porosity at positive temperatures and decreases with negative temperatures and is maximum at saturated unfrozen conditions. The hydraulic conductivity strongly depends on the saturation degree and on temperature, as the ice acts as an obstacle to the flow of water. According to the shape of the SWC, the hydraulic conductivity may vary of several orders of magnitude, representing the most variable parameter. Finally, the apparent heat capacity depends on temperature and on the shape of the SWC: near $T = T_m$ it increases by several orders of magnitude in very little temperature intervals.
5. The apparent heat capacity is characterized by a peak in proximity of T_m which may inhibit the convergence of the numerical model when passing from positive to negative temperatures. The convergence was found to be improved by the use of two precautions: (a) when passing from positive to negative temperatures (or vice-versa), the value of the heat capacity must be assigned to the maximum apparent heat capacity (*Hansson et al., 2004*); (b) the Picard scheme does not converge; (c) the Newton scheme, in order to converge, should be modified to the *globally convergent Newton scheme*, characterized by a check on the

remainder.

6. The model has shown a good agreement with the analytical solution typical of heat equation problems. Oscillations around the analytical solutions have been noticed when the model includes the apparent heat capacity term in the heat equations. The oscillation amplitude may be reduced by reducing the grid size but not eliminated, as it is embedded with the fixed-grid Eulerian method.
7. The model has shown a good agreement with the experimental findings of *Hansson et al.* (2004). It also shows a high sensitivity to the impedance factor of the hydraulic conductivity. A value of the impedance equal to 2 has given the best performance.
8. The model was able to reproduce the ground temperature measures of the arctic catchment during the whole simulation. The main source of spatial variability of the frost depth in a peat-covered arctic basin is related to the effect of the high subsurface flow, as a result of the high hydraulic conductivity of the organic soil, which leads to significant variability of the water content and in turn greatly affects the effective thermal conductivity in the peat.
9. The number of grid points and the grid size of the snow discretization has large influence on the coupling of the snow-soil thermal interactions. A snow discretization with deep layer at the snow-soil interface, provokes a decoupling between the snow and soil temperature, due to the fact that the thermal conductivity at the ground-snow interface is modeled with a weighted harmonic mean. A snow discretization with shallow layer at both the snow-soil and snow-atmosphere interface allows to improve the thermal coupling.
10. A proper representation of the snow melting time is crucial to correctly simulate ground temperatures. An advance or a delay in the estimation of the time of snow disappearance would cause a strong error in the calculation of the energy balance at the soil surface, altering the ground heating or freezing, and, therefore, affecting the soil temperature profile.

References

- Andersland, O., and B. Ladanyi (2003), *Frozen ground engineering*, John Wiley & Sons Inc.
- Anisimov, O., S. N.I., and N. E. (2002), Variability of seasonal thaw depth in permafrost regions: A stochastic modeling approach, *Ecol. Modell.*, 153, 217–227.
- Anisimov, O., V. Lobanov, S. Reneva, N. Shiklomanov, T. Zhang, and F. Nelson (2007), Uncertainties in gridded air temperature fields and effects on predictive active layer modeling, *Journal of Geophysical Research-Earth Surface*, 112(F2), F02S14.
- Arenson, L., and S. Springman (2000), Slope stability and related problems of alpine permafrost, in *Proceedings of the International Workshop on Permafrost Engineering*, pp. 183 – 196, Longyearbyen, Svalbard.
- Armstrong, R., and E. Brun (2008), Snow and climate: physical processes, surface energy exchange and modeling, *Snow and Climate: Physical Processes, Surface Energy Exchange and Modeling*, Edited by RL Armstrong and E. Brun. Cambridge: Cambridge University Press, 2008.
- Bentley, W., and W. Humphreys (1962), *Snow Crystals: By WA Bentley and WJ Humphreys*, Courier Corporation.
- Bertoldi, G., R. Rigon, and T. M. Over (2006), Impact of watershed geomorphic characteristics on the energy and water budgets, *J. Hydromet.*, 7, 389–403.
- Bliss, L., N. Matveyeva, et al. (1992), Circumpolar arctic vegetation, *Arctic ecosystems in a changing climate: an ecophysiological perspective*, pp. 59–89.
- Bohren, C., and B. Albrecht (1998), *Atmospheric Thermodynamics*, 402 pp.
- Brooks, R. H., and A. T. Corey (1964), Hydraulic properties of porous media, *Hydrology paper*, 3, Colorado State University, Fort Collins.
- Callen, H. (1985), *Thermodynamics and an Introduction to Thermodynamics*, John & Sons.

- Carey, S., and M. Woo (2000), Within-slope variability of ground heat flux, subarctic Yukon, *Physical Geography*, 21(5), 407–417.
- Carslaw, H., and J. Jaeger (1959), *Conduction of heat in solids*, Clarendon Press Oxford.
- Cary, J., and H. Mayland (1972), Salt and Water Movement in Unsaturated Frozen Soil, *Soil Science*.
- Celia, M., E. Bouloutas, and R. Zarba (1990), A General Mass-Conservative Numerical Solution for the Unsaturated Flow Equation, *Water Resources Research*, 26(7), 1483–1496.
- Christoffersen, P., and S. Tulaczyk (2003), Response of subglacial sediments to basal freeze-on: 1. Theory and comparison to observations from beneath the West Antarctica Ice Sheet, *J. Geophys. Res.*, 108, 2222.
- Clapp, R. B., and G. M. Hornberger (1978), Empirical equations for some hydraulic properties, *Water Resour. Res.*, 14, 601–605.
- Daanen, R., D. Misra, and H. Epstein (2007), Active-Layer Hydrology in Nonsorted Circle Ecosystems of the Arctic Tundra, *Vadose Zone Journal*, 6(4), 694.
- Davies, M., O. Hamza, and C. Harris (2001), The effect of rise in mean annual temperature on the stability of rock slopes containing ice-filled discontinuities, *Permafrost and Periglacial Processes*, 12, 137–144.
- de Vries, D. A. (1963), Thermal properties of soils.
- Dingman, L. S. (1994), *Physical Hydrology*, Prentice Hall.
- Dumbser, M., C. Eaux, and E. Toro (2008), Finite volume schemes of very high order of accuracy for stiff hyperbolic balance laws, *Journal of Computational Physics*, 227(8), 3971–4001.
- Edlefsen, N., and A. Anderson (1943), Thermodynamics of soil moisture, *Hilgardia*, 15(2), 31–298.
- Endrizzi, S. (2007), Snow cover modelling at local and distributed scale over complex terrain, Ph.D. thesis, Ph. D. dissertation, Institute of Civil and Environmental Engineering, Università degli Studi di Trento, Trento. Available from <http://www.ing.unitn.it/~endrizzi/PhDthesis.pdf>.
- Etzelmuller, B., M. Hoelzle, E. Heggem, K. Isaksen, C. Mittaz, D. Muhll, R. Odegard, W. Haerberli, and J. Sollid (2001), Mapping and modelling the occurrence and distribution of mountain permafrost, *Norwegian Journal of Geography*, 55(4), 186–194.

- Farouki, O. T. (1981), The thermal properties of soils in cold regions, *Cold Regions Sci. and Tech.*, 5, 67–75.
- Flerchinger, G. (1987), Simultaneous heat and water model of a snow-residue-soil system, Ph.D. thesis, Washington State University.
- Flerchinger, G. (1991), Sensitivity of soil freezing simulated by the SHAW model, *Transactions of the ASAE*, 34(6), 2381–2389.
- Flerchinger, G., and F. Pierson (1991), Modeling Plant Canopy Effects on Variability of Soil Temperature and Water, *Agricultural and Forest Meteorology AFMEEB*, 56(3/4).
- Flerchinger, G., and K. Saxton (1989), Simultaneous Heat and Water Model of a Freezing Snow-Residue-Soil System I. Theory and Development, *Transactions of the ASAE TAAEJ*, 32(2).
- Flerchinger, G., M. Seyfried, and S. Hardegee (2006), Using Soil Freezing Characteristics to Model Multi-Season Soil Water Dynamics, *Vadose Zone Journal*, 5(4), 1143.
- Fredlund, D., and A. Xing (1994), Equations for the soil-water characteristic curve, *Canadian Geotechnical Journal*, 31(4), 521–532.
- Fuchs, M., G. Campbell, and R. Papendick (1978), An analysis of sensible and latent heat flow in a partially frozen unsaturated soil, *Soil Sci. Soc. Am. J.*, 42(3), 379–385.
- Gambolati, G. (1994), *Lezioni di Metodi Numerici per ingegneria e scienze applicate*, Edizione Libreria Cortina.
- Gantmacher, F. (1975), *Lectures in Analytical Mechanics*, second ed., MIR, Moscow.
- Gardner, W. (1958), Some steady-state solutions of the unsaturated moisture flow equation with application to evaporation from a water table, *Soil Sci.*, 85(4), 228–232.
- Gray, W., and C. Miller (2007), Consistent thermodynamic formulations for multiscale hydrologic systems: Fluid pressures, *Water Resources Research*, 43(9), W09,408.
- Gruber, S., and M. Hoelzle (2008), The cooling effect of coarse blocks revisited, Proceedings of the Ninth International Conference on Permafrost, Fairbanks, Alaska, USA, Institute of Northern Engineering, University of Alaska, Fairbanks.
- Gruber, S., M. Peter, M. Hoelzle, I. Woodhatch, and W. Haeberli (2003), Surface temperatures in steep alpine rock faces—A strategy for regional-scale measurement and modelling, in *Proceedings of the 8th International Conference on Permafrost*, vol. 1, pp. 325–330.

- Gruber, S., M. Hoelzle, and W. Haeberli (2004a), Permafrost thaw and destabilization of Alpine rock walls in the hot summer of 2003, *Geophysical Research Letters*, 31(13), L13,504.
- Gruber, S., M. Hoelzle, and W. Haeberli (2004b), Rock-wall temperatures in the Alps: modelling their topographic distribution and regional differences, *Permafrost and Periglacial Processes*, 15(3), 299–307.
- Guymon, G., and J. Luthin (1974), A coupled heat and moisture transport model for arctic soils, *Water Resources Research*, 10(5), 995–1001.
- Haeberli, W., G. Cheng, A. Gorbunov, and S. Harris (1993), Mountain permafrost and climatic change, *Permafrost and Periglacial Processes*, 4(2), 165–174.
- Hansson, K., J. Simunek, M. Mizoguchi, L. Lundin, and M. van Genuchten (2004), Water Flow and Heat Transport in Frozen Soil Numerical Solution and Freeze-Thaw Applications, *Vadose Zone Journal*, 3(2), 693–704.
- Harlan, R. (1973), Analysis of coupled heat-fluid transport in partially frozen soil, *Water Resources Research*, 9(5), 1314–1323.
- Harris, C., et al. (2003), Warming permafrost in European mountains, *Global and Planetary Change*, 39(3-4), 215–225.
- Harris, S., and D. Pedersen (1998), Thermal regimes beneath coarse blocky materials, *Permafrost and Periglacial Processes*, 9(2), 107–120.
- Hayhoe, H. (1994), Field testing of simulated soil freezing and thawing by the SHAW model, *Can. Agric. Eng.*, 36(4), 279–285.
- Heginbottom, J., and L. Radburn (1992), Permafrost and ground ice conditions of northwestern Canada, *Geological Survey of Canada, Map 1691A, scale, 1(1), 000.*
- Hinzman, L., D. Kane, and K. Everett (1993), Hillslope hydrology in an Arctic setting, in *Proceedings, Sixth International Conference on Permafrost*, pp. 257–271.
- Hinzman, L., D. Goering, and D. Kane (1998), Special Section: ARCSS/LAII Flux Study-A distributed thermal model for calculating soil temperature profiles and depth of thaw in permafrost regions (Paper 98JD01731), *Journal of Geophysical Research-Part D-Atmospheres-Printed Edition*, 103(22), 28,975–28,992.
- Hoelzle, M., M. Wegmann, and B. Krummenacher (1999), Miniature Temperature Dataloggers for Mapping and Monitoring of Permafrost in High Mountain Areas: First Experience from the Swiss Alps, *Permafrost and Periglacial Processes*, 10(2), 113–124.

- Hornberger, D. (1998), *Elements of Physical Hydrology*, Johns Hopkins University Press.
- Hudson, J. (1996), *Thermodynamics of materials: a classical and statistical synthesis*, Wiley-Interscience.
- Ingersent, K. (2000), Callen's thermodynamic postulates. available at <http://www.phys.ufl.edu/kevin/teaching/3513/handouts/postulates.pdf>.
- IPCC (2007), Wg1 ar4 final report, in *Intergovernmental Panel on Climate Change*, Paris.
- Jame, Y., and D. Norum (1980), Heat and mass transfer in a freezing unsaturated porous medium, *Water Resources Research*, 16(4).
- Jansson, P. (1998), Simulation Model for Soil Water and Heat Conditions-Description of the SOIL model. Commun. 98: 2, 81pp, *Swed. Univ. of Agric. Sci., Dept. of Soil Sci. Uppsala, Sweden*.
- Johansen, O. (1975), Thermal conductivity of soils, Ph.D. thesis, Ph. D. dissertation, Norwegian Technical University, Trondheim.
- Jordan, R. (1991), A one-dimensional temperature model for a snow cover: Technical documentation for SNTHERM 89, *Tech. rep.*, US Army Cold Regions Research and Engineering Laboratory, Hanover, NH, USA.
- Juliussen, H., and O. Humlum (2007), Towards a TTOP ground temperature model for mountainous terrain in central-eastern Norway, *Permafrost and Periglacial Processes*, 18(2), 161–184.
- Kääb, A., R. Frauenfelder, and I. Roer (2007), On the response of rockglacier creep to surface temperature increase, *Global and Planetary Change*, 56(1-2), 172–187.
- Kasten, F., and G. Czeplak (1980), Solar and terrestrial radiation dependent on the amount and type of cloud, *Sol. Energy*, 24, 177–189.
- Keller, F. (1992), Automated mapping of mountain permafrost using the program PERMAKART within the geographical information system ARC/INFO, *Permafrost and Periglacial Processes*, 3(2), 133–138.
- Keller, F., and H. Gubler (1993), Interaction between snow cover and high mountain permafrost, Murtel-Corvatsch, Swiss Alps, in *Proceedings of the Sixth International Conference on Permafrost*, vol. 1, pp. 332–337.
- Koren, V., J. Schaake, K. Mitchell, Q. Duan, F. Chen, and J. Baker (1999), A parameterization of snowpack and frozen ground intended for NCEP weather and climate models, *Journal of Geophysical Research-Atmospheres*, 104(D16).

- Loch, J. (1978), Thermodynamic equilibrium between ice and water in porous media, *Soil Science*, 126(2), 77.
- Lukyanov, V., and M. Golovko (1957), Calculations of the depth of freeze in soils. (In Russian), *Union of Transp. Constr., Moscow*, 23.
- Lunardini, V. (1981), *Heat transfer in cold climates*, Van Nostrand Reinhold, New York.
- Lunardini, V. (1985), Freezing of soil with phase change occurring over a finite temperature difference, in *Proceedings of the 4th offshore mechanics and arctic engineering symposium*, The American Society of Mechanical Engineers.
- Lundin, L. (1990), Hydraulic Properties in an Operational Model of Frozen Soil, *Journal of Hydrology JHYDA* 7,, 118(1/4).
- Luo, L., et al. (2003), Effects of frozen soil on soil temperature, spring infiltration, and runoff: Results from the PILPS 2 (d) experiment at Valdai, Russia, *Journal of Hydrometeorology*, 4(2), 334–351.
- Luo, S., S. Lü, and Y. Zhang (2009), Development and validation of the frozen soil parameterization scheme in Common Land Model, *Cold Regions Science and Technology*, 55(1), 130–140.
- McCumber, M., and R. Pielke (1981), Simulation of the effects of surface fluxes of heat and moisture in a mesoscale numerical model. 1. Soil layer, *J. Geophys. Res.*, 86(C10), 9929–9938.
- McKay, G. A. (1970), Precipitation, in *Handbook on the principles of hydrology*, edited by D. M. Gray, Port Washington, NY, USA.
- McKenzie, J., C. Voss, and D. Siegel (2007), Groundwater flow with energy transport and water–ice phase change: Numerical simulations, benchmarks, and application to freezing in peat bogs, *Advances in Water Resources*, 30(4), 966–983.
- Miller, R. (1963), Phase-equilibria and soil freezing. p 193-197 In: International Conference on Permafrost. Lafayette, Ind) ana, *National Academy of Science*.
- Miller, R. (1973), Soil freezing in relation to pore water pressure and temperature, in *Permafrost: North American Contribution [to The] Second International Conference*, pp. 344–352, Pearson Education.
- Miller, R. (1980), Freezing phenomena in soils, *Applications of soil physics*, pp. 254–299.
- Mualem, Y. (1976), A new model for predicting the hydraulic conductivity of unsaturated porous media, *Water Resour. Res.*, 12, 513–522.

- Muller, I., and W. Weiss (2005), Entropy and Energy: A Universal Competition.
- Nakano, Y., and J. Brown (1971), Effect of a freezing zone of finite width on thermal regime of soils, *Water Resources Research*, 5, 1226–1233.
- Nakaya, U. (1956), Properties of single crystals of ice, revealed by internal melting.
- Nassar, I., R. Horton, and G. Flerchinger (2000), SIMULTANEOUS HEAT AND MASS TRANSFER IN SOIL COLUMNS EXPOSED TO FREEZING/THAWING CONDITIONS1., *Soil Science*, 165(3), 208.
- Newman, G., and G. Wilson (1997), Heat and mass transfer in unsaturated soils during freezing, *Canadian Geotechnical Journal*, 34(1), 63–70.
- Niessner, J., and S. Hassanizadeh (2009), Non-equilibrium interphase heat and mass transfer during two-phase flow in porous media—Theoretical considerations and modeling, *Advances in Water Resources*, 32(12), 1756–1766.
- Niu, G., and Z. Yang (2006), Effects of frozen soil on snowmelt runoff and soil water storage at a continental scale, *Journal of Hydrometeorology*, 7(5), 937–952.
- Obradovic, M., and M. Sklash (1987), An isotopic and geochemical study of seasonal snowmelt runoff in the Apex River watershed, *NATO ASI series. Series C, Mathematical and physical sciences*, 211, 643–659.
- Oke, T. R. (1990), *Boundary Layer Climates*, Routledge.
- Paniconi, C., and M. Putti (1994), A comparison of Picard and Newton iteration in the numerical solution of multidimensional variably saturated flow problems, *Water Resources Research*, 30(12), 3357–3374.
- Phukan, A. (1985), *Frozen Ground Engineering*.
- Pihlainen, J., and G. Johnston (1963), Guide to a field description of permafrost for engineering purposes, *Assoc. Com. Soil and Snow Mechanics Tech. Man*, 79, 23.
- Quinton, W., and S. Carey (2008), Towards an energy-based runoff generation theory for tundra landscapes, *Hydrological Processes*, 22(23), 4649–4653.
- Quinton, W., and D. Gray (2003), Subsurface drainage from organic soils in permafrost terrain: the major factors to be represented in a runoff model, in *Proceedings of the Eighth International Conference on Permafrost, Davos, Switzerland*, 6pp.

- Quinton, W., and P. Marsh (1998), The influence of mineral earth hummocks on subsurface drainage in the continuous permafrost zone, *Permafrost and Periglacial Processes*, 9(3), 213–228.
- Quinton, W., and J. Pomeroy (2006), Transformations of runoff chemistry in the Arctic tundra, Northwest Territories, Canada, *Hydrological Processes*, 20(14), 2901–2919.
- Quinton, W., D. Gray, and P. Marsh (2000), Subsurface drainage from hummock-covered hillslopes in the Arctic tundra, *Journal of Hydrology*, 237(1-2), 113–125.
- Quinton, W., T. Shirazi, S. Carey, and J. Pomeroy (2005), Soil water storage and active-layer development in a sub-alpine tundra hillslope, southern Yukon Territory, Canada, *Permafrost and Periglacial Processes*, 16(4), 369–382.
- Quinton, W., M. Hayashi, and S. Carey (2008), Peat hydraulic conductivity in cold regions and its relation to pore size and geometry, *Hydrological Processes*, 22(15), 2829–2837.
- Quinton, W., R. Bemrose, Y. Zhang, and S. Carey (2009), The influence of spatial variability in snowmelt and active layer thaw on hillslope drainage for an alpine tundra hillslope, *Hydrological Processes*, 23(18).
- Rawlins, M., R. Lammers, S. Frohling, B. Fekete, and C. Vorosmarty (2003), Simulating pan-Arctic runoff with a macro-scale terrestrial water balance model, *Hydrological Processes*, 17(13), 2521–2539.
- Rempel, A. (2007), Formation of ice lenses and frost heave, *J. Geophys. Res.*, 112.
- Rempel, A., J. Wettlaufer, and M. Worster (2004), Premelting dynamics in a continuum model of frost heave, *Journal of Fluid Mechanics*, 498, 227–244.
- Richards, L. A. (1931), Capillary conduction of liquids in porous mediums, *Physics*, 1, 318–333.
- Rigon, R., G. Bertoldi, and T. M. Over (2006), GEOtop: a distributed hydrological model with coupled water and energy budgets, *J. Hydromet.*, 7, 371–388.
- Riseborough, D., N. Shiklomanov, B. Etzelmuller, S. Gruber, and S. Marchenko (2008), Recent advances in permafrost modelling, *Permafrost and Periglacial Processes*, 19(2), 137–156.
- Roth, K., and J. Boike (2001), Quantifying the thermal dynamics of a permafrost site near Ny-Aalesund, Svalbard, *Water Resources Research*, 37(12), 2901–2914.
- Safran, S. (1994), *Statistical thermodynamics of surfaces, interfaces, and membranes*, Addison-Wesley, Reading, Massachusetts.

- Schaap, M., F. Leij, and M. van Genuchten (2001), rosetta: a computer program for estimating soil hydraulic parameters with hierarchical pedotransfer functions, *Journal of Hydrology*, 251(3-4), 163–176.
- Schofield, R. (1935), The pF of the water in soil, *Transactions of the 3rd International Congress on Soil Science, Oxford, UK*, 2, 37–48.
- Shoop, S., and S. Bigl (1997), Moisture migration during freeze and thaw of unsaturated soils: modeling and large scale experiments, *Cold Regions Science and Technology*, 25(1), 33–45.
- Simoni, S., F. Zanotti, G. Bertoldi, and R. Rigon (2008), Modelling the probability of occurrence of shallow landslides and channelized debris flows using GEOtop-FS, *Hydrological Processes*, 22(4), 532–545.
- Simunek, J., M. Sejna, and M. T. van Genuchten (1998), The hydrus 1d software package for simulating the one-dimensional movement of water, heat, and multiple solutes in variably-saturated media. version 2.0, *Technical report*, US Salinity Laboratory, ARS/USDA.Riverside,, California.
- Smirnova, T., J. Brown, S. Benjamin, and D. Kim (2000), Parameterization of cold-season processes in the MAPS land-surface scheme, *Journal of Geophysical Research*, 105(D3), 4077–4086.
- Spaans, E., and J. Baker (1996), The Soil Freezing Characteristic: Its Measurement and Similarity to the Soil Moisture Characteristic, *Soil Science Society of America Journal*, 60(1), 13.
- Stahli, M., P. Jansson, and L. Lundin (1996), Preferential water flow in a frozen soil - A two-domain model approach, *Hydrological Processes*, 10, 1305–1316.
- Stocker-Mittaz, C., M. Hoelzle, and W. Haeberli (2002), Modelling alpine permafrost distribution based on energy-balance data: a first step, *Permafrost and Periglacial Processes*, 13(4), 271–282.
- T., G. W. (2008), *Entropy and the Time Evolution of Macroscopic Systems*, International Series of Monographs in Physics, Oxford Science Publications, Oxford, New York.
- Tomita, H. (2009), Analysis of Spurious Surface Temperature at the Atmosphere–Land Interface and a New Method to Solve the Surface Energy Balance Equation, *Journal of Hydrometeorology*, 10(3), 833–844.
- Van Genuchten, M. T. (1980), A closed-form equation for predicting the hydraulic conductivity of unsaturated soils., *Soil Sci. Soc. Am. J.*, 44, 892–898.

- Vereecken, H., J. Maes, J. Feyen, and P. Darius (1989), Estimating the soil moisture retention characteristic from texture, bulk density and carbon content, *Soil Science*, 148, 389–403.
- Viterbo, P., A. Beljaars, J. Mahfouf, and J. Teixeira (1999), The representation of soil moisture freezing and its impact on the stable boundary layer, *Quarterly Journal of the Royal Meteorological Society*, 125(559), 2401–2426.
- Vonder Mühl, D., and W. Haeberli (1990), Thermal characteristics of the permafrost within an active rock glacier (Murtel/Corvatsch, Grisons, Swiss Alps), *Journal of Glaciology*, 36(123), 151–158.
- Watanabe, K. (2008), Water and heat flow in a directionally frozen silty soil, pp. 15–22, Proceedings of the third HYDRUS Workshop, June 28, 2008, Tokyo University of Agriculture and Technology, Tokyo, Japan, ISBN 978-4-9901192.
- Williams, P. (1964), Unfrozen water content of frozen soils and soil moisture suction, *Geotechnique*, 14(3), 231–246.
- Williams, P. (1967), Unfrozen water in frozen soils, *Norwegian Geotechnical Institute, Oslo, Publication*, 72, 37–48.
- Williams, P., and M. Smith (1989), *The frozen earth: fundamentals of geocryology*, Cambridge University Press.
- Woo, M., D. Kane, S. Carey, and D. Yang (2008), Progress in permafrost hydrology in the new millennium, *Permafrost and Periglacial Processes*, 19(2), 237–254.
- Wright, J., C. Duchesne, and M. Côté (2003), Regional-scale permafrost mapping using the TTOP ground temperature model, in *Proceedings 8th International Conference on Permafrost. Swets and Zeitlinger, Lisse*, pp. 1241–1246.
- Wright, N., M. Hayashi, and W. Quinton (2009), Spatial and temporal variations in active layer thawing and their implication on runoff generation in peat-covered permafrost terrain, *Water Resources Research*, 45(5), W05,414.
- Yen, Y. (1981), Review of thermal properties of snow, ice and sea ice.
- Yi, S., M. Woo, and M. Arain (2007), Impacts of peat and vegetation on permafrost degradation under climate warming, *Geophysical Research Letters*, 34(16), L16,504.
- Zanotti, F., S. Endrizzi, G. Bertoldi, and R. Rigon (2004), The GEOTOP snow module, *Hydrol. Proc.*, 18, 3667–3679. DOI:10.1002/hyp.5794.

- Zhang, X., S. Sun, and Y. Xue (2007), Development and testing of a frozen soil parameterization for cold region studies, *Journal of Hydrometeorology*, 8(4), 690–701.
- Zhang, Y., S. Carey, and W. Quinton (2008), Evaluation of the algorithms and parameterizations for ground thawing and freezing simulation in permafrost regions, *J. Geophys. Res.*, 113.
- Zhang, Z., D. Kane, and L. Hinzman (2000), Development and application of a spatially-distributed Arctic hydrological and thermal process model (ARHYTHM), *Hydrological Processes*, 14(6), 1017–1044.
- Zhao, L., D. Gray, and D. Male (1997), Numerical analysis of simultaneous heat and mass transfer during infiltration into frozen ground, *Journal of Hydrology*, 200(1-4), 345–363.
- Zhou, F., A. Zhang, R. Li, and E. Hoeve (2009), Spatio-temporal simulation of permafrost geothermal response to climate change scenarios in a building environment, *Cold Regions Science and Technology*, 56(2-3), 141–151.
- Zia, R., E. Redish, and S. McKay (2009), Making sense of the Legendre transform, *American Journal of Physics*, 77, 614.
- Zimmermann, M., and W. Haeberli (1992), Climatic change and debris flow activity in high mountain areas: a case study in the Swiss Alps, *Catena Supplement*, 22, 59–72.